TECHNISCHE UNIVERSITÄT MÜNCHEN
MAX-PLANCK-INSTITUT FÜR ASTROPHYSIK

Analysis of spectra of Type I supernovae with radiative transfer models

Stephan Hachinger

Vollständiger Abdruck der von der Fakultät für Physik der Technischen Universität München zur Erlangung des akademischen Grades eines

Doktors der Naturwissenschaften (Dr. rer. nat.)

genehmigten Dissertation.

Vorsitzender: Univ.-Prof. S. Bishop, PhD

Prüfer der Dissertation:

1. Hon.-Prof. Dr. W. Hillebrandt
2. Univ.-Prof. Dr. W. Weise

Die Dissertation wurde am 01.06.2011 bei der Technischen Universität München eingereicht und durch die Fakultät für Physik am 08.07.2011 angenommen.

Contents

1 Introduction **13**
- 1.1 SN observations . . . 14
  - 1.1.1 Light curves and cosmological application of SNe . . . 14
  - 1.1.2 Spectra . . . 21
- 1.2 Theory of Type Ia SNe (thermonuclear SNe) . . . 28
  - 1.2.1 Observational constraints . . . 28
  - 1.2.2 Progenitor systems: some details; evolution prior to explosion . 31
  - 1.2.3 Final stages, explosion and nucleosynthesis . . . 34
- 1.3 Theory of Type Ib, Ic and II SNe (core-collapse SNe) . . . 38
  - 1.3.1 Observational constraints . . . 39
  - 1.3.2 Progenitor star models . . . 43
  - 1.3.3 Explosion models and nucleosynthesis . . . 44
- 1.4 SN ejecta after explosion – force-free, homologous expansion . . . 50

2 Analysing spectra with radiative transfer models **53**
- 2.1 Radiative transfer in SN atmospheres . . . 53
  - 2.1.1 Radiative transfer: basic quantities and equations . . . 53
  - 2.1.2 Opacity and emissivity in SNe . . . 55
  - 2.1.3 The state of the plasma . . . 63
- 2.2 Radiative transfer / spectrum synthesis code . . . 66
  - 2.2.1 Concept of the code . . . 66
  - 2.2.2 Main loop of the code and MC transport loop . . . 68
  - 2.2.3 Formal integral procedure . . . 72
  - 2.2.4 The NLTE extension to the code . . . 72
  - 2.2.5 Spectral models: principles, modelling, abundance tomography 78

3 SNe Ia: spectral analysis of peculiar objects **83**
- 3.1 SN 2005bl . . . 83
  - 3.1.1 Density profiles . . . 84
  - 3.1.2 Models . . . 85
  - 3.1.3 Discussion . . . 95
  - 3.1.4 Summary – analysis of the 1991bg-like SN 2005bl . . . 106
- 3.2 SN 2009dc . . . 108
  - 3.2.1 Introduction . . . 108
  - 3.2.2 Observations and observational parameters . . . 108
  - 3.2.3 Density profile & rise time – early time models . . . 109
  - 3.2.4 Tomography models . . . 118

3.2.5 Discussion 129
3.2.6 Summary – analysis of the "Super-Chandrasekhar" SN 2009dc . 136

4 SNe IIb/Ib/Ic: a sequence of spectral models for stripped CC SNe 139
4.1 Models for the SNe 2008ax and 1994I 139
4.1.1 SN 2008ax – a SN IIb 142
4.1.2 SN 1994I – a SN Ic 148
4.2 Model sequence 152
4.2.1 Setup 152
4.2.2 Results 160
4.3 Discussion 164
4.3.1 He atom, rate equilibria in a He I/He II-dominated plasma in SNe 164
4.3.2 He state in the SN 2008ax model; evolution of the lines 166
4.3.3 Tests: modifications of the "SN Ib/Ic" model 169
4.3.4 Summary – our results and SN Ib/Ic progenitor models 170

5 Conclusions and outlook 173

Astrophysical terms and notation

In this thesis, we follow the usual terminology in astrophysics and supernova physics. Terms less common in general physics, or used in a different sense than in other branches of physics, are printed *italic* the first time they are used. Terms which cannot be guessed from the context and which are easily misinterpreted or for which it is hard to find a clear definition in a basic textbook (Unsöld & Baschek 2001), are explained below in Table 1. We kindly ask the reader to consult this table when in doubt. Equations are always written in cgs units (gaussian units, cf. Jackson 1998). Other units are used only if common in astrophysics. Unusual symbols and non-cgs units which appear in our formulae are listed in Table 2. Usage of one symbol for more than one quantity has been allowed in a few cases.

Table 1: Technical terms in astrophysics and supernova physics.

term	meaning
atomic line	line of an atom *or ion*, corresponding to a transition between discrete energy levels
co-moving, lagrangian	refers to the *co-moving frame*
co-moving frame, lagrangian frame	A coordinate system moving locally with the hydrodynamic flow; the transformation from the static (*eulerian*) to the co-moving frame changes with time such that each fluid element retains its coordinate. A transformation from a global static to a global co-moving system need not be linear.
dust extinction	see *reddening*
envelope	outer layers of a star (often used as an opposite to the term *core*)
extragalactic	not within the Milky Way
Fe-group elements	scandium (Sc) and heavier elements up to nickel (Ni)
IME / intermediate-mass elements	elements heavier than oxygen (O) and lighter than scandium (Sc)
galactic	within the Milky Way
He (giant) star	a star which has lost its H envelope (usually as a result of binary evolution), but retained its He
LTE	local thermodynamic equilibrium

Table 1: (contd.) Technical terms in astrophysics and supernova physics.

term	meaning
NLTE, non-LTE	non – local-thermodynamic-equilibrium, i.e. a state (of the plasma and the radiation field) out of LTE
metal	any element heavier than helium
observed wavelength	wavelength at which line radiation is observed by an observer immersed in air – this wavelength will differ from the *rest wavelength* (see below) if emitting material moves with respect to the observer
optical spectrum	spectrum of an astronomical source of light covering at least the optical wavelength range (but normally also extending into the near infrared)
rest wavelength	atomic line wavelength measured in a laboratory (in air)
reddening	Attenuation of light from an astrophysical source by dust; usually leads to a particularly strong suppression of blue radiation. When needed we assume a Cardelli et al. (1989) extinction curve with $R_V = 3.1$ (standard Milky-Way-like dust).
scattering	in radiative transfer: absorption and re-emission of a photon, preserving the photon's energy in the rest frame of the absorber – only the energy-preserving nature is relevant here; the exact properties of the physical process is irrelevant and also the target (atom, free electron, ...)

Table 2: Less common symbols and non-cgs units used in this thesis.

symbol	meaning
Å	Ångstrom, 1 Å $= 10^{-8}$cm. Whenever wavelengths of spectral features are mentioned, a notation like "1234.5 Å" implies that 1234.5 is the *observed wavelength*
B	B filter band [$\sim$3700 – 5500 Å; for detailed shapes of filter bandpasses see e.g. Bessell (1990)]
Δ...	Δ prefixes denote small quantities, or increments of quantities.
d_L	luminosity distance, i.e. the distance inferred from the ratio of the *radiation flux* F sent out and received from an object
foe	10^{51}erg [(ten to the) **f**ifty-**o**ne **e**rg]

Table 2: (contd.) Less common symbols and non-cgs units used in this thesis.

symbol	meaning
F, F_ν, F_λ, f, ...	radiation flux ($F_\nu = \frac{\mathrm{d}F}{\mathrm{d}\nu}$: flux per unit frequency; F_λ: analogous): energy transported by a beam of radiation per unit time and per unit area perpendicular to the beam
λ1234.5	1234.5Å. Whenever wavelengths of spectral features are denoted like this, 1234.5 is to be taken as the *rest wavelength*.
I	I filter band [$\sim$7000 – 8750 Å; for detailed shapes of filter bandpasses see e.g. Bessell (1990)]
I, I_ν	intensity ($I_\nu = \frac{\mathrm{d}I}{\mathrm{d}\nu}$: frequency-dependent specific intensity)
...I, ...II, ...	Ionisation stages (e.g. Si I, Si II, ...) – I refers to a neutral atom, II to a ion with a charge of $+e$, III to a ion with a charge of $+2e$. Negative ions are denoted in the standard notation, e.g. OH^-.
L	luminosity: power [erg/s] of a radiation source
$...\lambda$	analogous to $...\nu$, see there
ly	light year – $1\ \mathrm{ly} = c \times 365.25\ \mathrm{d} \times 86400\ \mathrm{s/d} \sim 9.461 \times 10^{17}\mathrm{cm}$.
M	total mass
M, m, mag	Magnitudes, a logarithmic measure for the brightness of a source of light. The relative magnitude m of an astrophysical source of light – as seen from earth – is defined using the star Vega as a reference: $m[\mathrm{mag}] = -2.5\log(\frac{F}{F_{\mathrm{Vega}}})$, where F is the measured flux of the radiation. The absolute magnitude M is the relative magnitude at which an object would appear if it would be 10 pc away from the observer. It is equivalent to a luminosity, and can be calculated as: $M[\mathrm{mag}] = -2.5\log(\frac{F}{F_{\mathrm{Vega}}}) - 5\log(\frac{r}{10\mathrm{pc}})$.
M_X, m_X	magnitude in the filter band X
$...\nu$	ν as subscript to a function denotes the frequency as an argument to the function. This notation is commonly used in radiative transfer, where e.g. a frequency-dependent intensity is denoted as $I_\nu(...)$.
pc	Parsec – the distance (perpendicular to the orbital plane) from which the mean radius of the Earth's orbit around the Sun is observed to subtend an angle of 1". 1 pc $\sim$ 3.26 ly.
R	R filter band [$\sim$5600 – 8500 Å; for detailed shapes of filter bandpasses see e.g. Bessell (1990)]

Table 2: (contd.) Less common symbols and non-cgs units used in this thesis.

symbol	meaning
U	U filter band [$\sim$3100 – 4100 Å; for detailed shapes of filter bandpasses see e.g. Bessell (1990)]
V	V filter band [$\sim$4800 – 6600 Å; for detailed shapes of filter bandpasses see e.g. Bessell (1990)]
Z	metallicity: abundance of *metals* (see Table 1)
$...^*$	An superscript asterisk attached to some quantity denotes the value of this quantity in local thermodynamic equilibrium (at temperature T).
$...\odot$	A subscript $\odot$ attached to a quantity denotes the value for the sun (e.g. sun mass: $M_\odot$).
$\sim$ or $\approx$	approximately equal to
$\doteq$	equal to first order (of some quantity, e.g. v/c – used only if it is obvious which quantity is meant)
$\propto$	proportional to

Functions of $\vec{r}$, t and other common arguments are sometimes written without explicit mention of their arguments.

Preface

Supernovae – very bright transient stars visible for some weeks to months – have attracted the attention of astronomers since the middle ages and even before. Unambiguous historical records date back to the years 185, 1006, 1054, 1572, 1604 and 1885 AD. The first Europeans describing supernovae were Brahe (1573) and Kepler (1606) with their books "De nova et nullius aevi memoria prius visa stella" and "De stella nova".

Up to the 20th century, not much was understood about the physical nature of "guest stars". They were generally called *novae*, and only in the 1930s W. Baade and F. Zwicky recognised that these guest stars do not form a homogeneous group. They began to distinguish "super-novae", i.e. very bright new stars as seen by the first astronomers, from novae (e.g. Shore et al. 1993). Supernovae, sometimes outshining entire galaxies, seemed to result from a dramatic transition in the life of a star (Baade & Zwicky 1934a). Minkowski (1941) collected a number of spectroscopic observations, and was able to separate supernovae into two classes, *Type I* and *Type II*. Type II objects differed from the others by showing spectral lines of Hydrogen. A more sophisticated classification system with five types was later used by F. Zwicky, but today supernovae of his classes *III* to *V* are either classified as completely different transients or as *Type II peculiar*.

In the 1960s, '70s and '80s, significant progress was made in understanding the mechanisms by which stars can explode as supernovae. The results [for reviews see Wheeler 1981 and Woosley & Weaver (1986)] form the basis of today's supernova theory. It was recognised that at least two ways exist to produce a supernova: explosive nuclear fusion of elements lighter than Fe, and the collapse of a stellar object in its own gravitational field. The majority of the Type I supernovae were recognized as *thermonuclear explosions* of carbon-oxygen white dwarf stars with masses $\lesssim 1.4 M_\odot$ (Hoyle & Fowler 1960; Whelan & Iben 1973; Chevalier 1981; Arnett 1982; Woosley & Weaver 1986). If a nuclear flame can be initiated and sustained in such a white dwarf star, it can release enough energy to unbind the object, and no remnant is left behind. Type II supernovae proved consistent with a gravitational collapse scenario: the core of a star with a mass $\gtrsim 8 M_\odot$ stops to burn and collapses due to gravitational pressure (Colgate & White 1966; Grasberg et al. 1971; Chevalier 1976; Falk & Arnett 1977; Weaver & Woosley 1980). Part of the energy gained in this *core collapse* is transferred to the intermediate and outer layers of the star, which are ejected as a supernova.

On the observational side, it was found in the later '80s that Type I supernovae can be split into three subclasses (Types *Ia/Ib/Ic*; Elias et al. 1985, Branch 1986, Wheeler & Harkness 1986). These classes are distinguished by the presence or absence of certain spectral features: Type Ia supernovae show strong silicon lines, Type Ib objects show clear helium lines, and Type Ic objects fulfil none of these two criteria. Only Type Ia supernovae – or at least most of them – are explosions of white dwarfs; the other types can be explained by a core collapse of stars which have lost their hydrogen

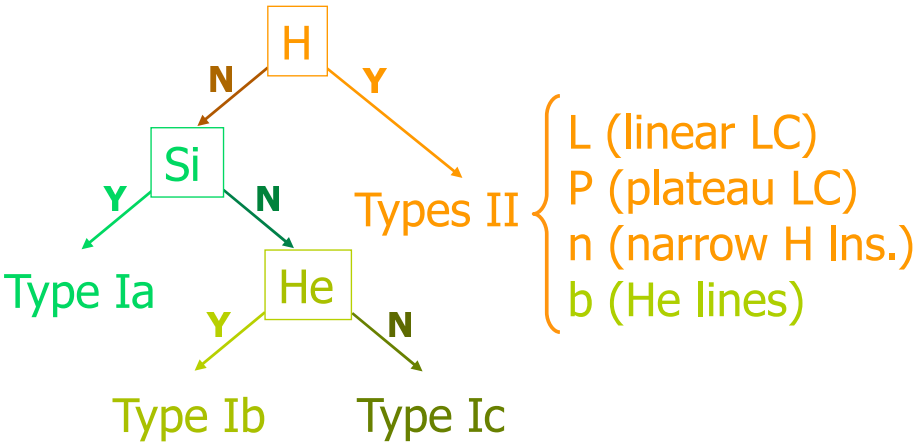

Figure 1: Basic supernova classification scheme, taking into account prominent properties of the spectra (lines of different elements – H, He, Si) and light curves (LCs, in the case of Type II-L/II-P supernovae). Less common subclasses, especially those for highly peculiar supernovae, are not taken into account here (cf. Turatto et al. 2007).

envelope. Also, different subtypes of Type II supernovae can be distinguished: Following Barbon et al. (1979), objects which show a plateau in their post-maximum light curve are called Type *II-P* (plateau), while other objects are classified as *II-L* (linear decline of the magnitude with time). Some Type II objects with spectroscopic peculiarities are nowadays termed *IIb* (H and He lines, Woosley et al. 1988) or *IIn* (narrow H lines, Schlegel 1990). Practically all Type II supernovae are believed to result from core collapse. An overview over the classification criteria for supernovae as outlined here is given in Fig. 1.

Detailed hydrodynamic simulations for both core-collapse and thermonuclear explosions were developed with time. The simulations now succeed in reproducing a significant part of the observed events (Hillebrandt & Niemeyer 2000; Janka et al. 2007; Marek & Janka 2009; Bruenn et al. 2009; Kasen et al. 2009). Yet, there are many riddles to be solved before we will have a comprehensive and detailed physical picture of supernovae. Some aspects of the explosion mechanisms are still unclear or too expensive to simulate (Hillebrandt & Niemeyer 2000; Janka et al. 2007). In addition, the processes generating the optical light are not easy to reproduce with computational models (Kromer & Sim 2009). And last but not least, there are large uncertainties in the initial assumptions of the simulations. The properties of the progenitor systems are inferred from stellar evolution and population synthesis calculations (e.g. Yoon et al. 2010; Ruiter et al. 2011), which certainly need to be refined.

Despite all problems, however, lots of advances are made in understanding individual objects and the supernova subclasses they represent. A central method contributing to our progress is the comparison of observed light curves and spectra with *synthetic observables*, which are calculated from explosion models with the help of *radiative transfer* codes or *spectral synthesis* codes (Mazzali & Lucy 1993; Baron et al. 1993; Fisher et al. 1997; Kasen et al. 2004; Kromer & Sim 2009; Maurer 2010). Synthetic observables help us to decline or accept different explosion models for an observed supernova, or to optimise the physical parameters of an explosion model so as to match the observations. Thus, information on the explosions can be obtained. Recent supernova searches (e.g. Palomar Transient Factory – Rau et al. 2009, SkyMapper supernova

search – Keller et al. 2007) and follow-up observations will provide more high-quality data than ever before. This will be a good basis for a better understanding of supernovae.

In this thesis, we develop radiative transfer models for Type I and IIb supernovae. We set up models with a number of free parameters representing important supernova properties (e.g. abundances), and optimise these so as to match observed with synthetic spectra. Thus, we infer the characteristics of supernovae not well understood as yet, and obtain hints on the origin of these explosions. With our work, we hope to contribute to the solution of the puzzle "Which stars explode in what manner, and what do these explosions look like?".

We first analyse the properties of two extraordinary supernovae Ia. For one of these supernovae, the subluminous object SN 2005bl (Taubenberger et al. 2008), we find that it can be explained by an explosion scenario involving a detonation at low densities, such as a white dwarf merger. The merger scenario had classically been considered unable to produce supernovae Ia (Nomoto & Iben 1985; Saio & Nomoto 1985, 1998), but some aspects of it had not been sufficiently studied. After our study, Pakmor et al. (2010, 2011) have indeed been able to show that mergers of roughly-equal-mass white dwarfs can produce subluminous supernovae. The other supernova we investigate (SN 2009dc; Silverman et al. 2011, Taubenberger et al. 2011a) is extreme in the opposite way: it is so superluminous that it also must have a non-standard progenitor. Up to now, we have however not been able to definitively suggest a progenitor scenario for this object. We find that rotating white dwarfs, which have been suggested as progenitors for such supernovae (Howell et al. 2006), can be excluded unless asymmetries have a surprisingly extreme effect.

In a second part of the thesis, we study spectra of Type Ic, Ib and IIb supernovae. The parameter space for these supernovae is much wider, and the hydrodynamic models are probably not as mature as standard Type Ia models (Nordhaus et al. 2010). Yet, interesting possibilities for spectral analyses open up as the ejecta of core-collapse supernovae are less reprocessed by nuclear burning. Information on the progenitor star can be obtained directly from the observed spectra. We investigate how much of its helium envelope a progenitor must have lost in order for the supernova not to show He lines in the photospheric spectrum (i.e. for the supernova to be classified as a Ic, as opposed to a Ib or a IIb). This question is highly relevant for the validation of progenitor models for Type Ic, Ib and IIb supernovae (Smartt 2009; Yoon et al. 2010), which have to explain the absence of the He envelope in Type Ic objects. As a first step, we present an analysis of such SNe with a low to normal ejecta mass and explosion energy. We find that for such SNe may not contain more than $\sim 0.1 M_{\odot}$ of He if they show a Type Ic spectrum. This corresponds to an almost complete loss of the He envelope prior to explosion, which can probably only be achieved in binary systems. For our study, which requires accurate modelling of the H and He lines in supernovae IIb and Ib, we have developed a *non-LTE* (non - local-thermodynamic-equilibrium) extension to the radiative transfer code of our group.

This thesis is organised as follows: We first give an introduction to observational and astrophysical aspects of supernovae, and outline current developments in supernova physics (Chapter 1). Afterwards, we discuss radiative transfer in supernova atmospheres and describe our code with the non-LTE extension (Chapter 2). We then analyse Type Ia (Chapter 3) and Type Ic/Ib/IIb (Chapter 4) supernovae. Our results are summarised in Chapter 5, where we give conclusions and a brief outlook on possible extensions of the work presented here.

Chapter 1

Introduction

Supernovae (SNe) play an prominent role in astrophysics, and also in fundamental physics and cosmology. Large efforts are made to study the *mechanisms* of the catastrophic explosions in detail (Hillebrandt & Niemeyer 2000; Janka et al. 2007), and to investigate the evolution of the *progenitor stars* (e.g. Nomoto et al. 2007; Yoon et al. 2010).

In the last decade, increasing emphasis has been put on obtaining high-quality observations of SNe with a good temporal coverage. Several large collaborations (e.g. the European Supernova Collaboration, EURTN2-2001-00037), but also smaller groups and individual observers have obtained excellent data. With upcoming SN surveys (e.g. Keller et al. 2007) and observational follow-up programmes (e.g. ESO Large Programme 184.D-1140, Padova group), the situation is still getting better. More and more objects of relatively rare types are observed, such as SNe Ia with an extremely low kinetic energy (Narayan et al. 2010) or SNe Ic connected with a *long /soft gamma-ray burst* (Cobb et al. 2010). Modellers try to interpret the data using *radiative transfer* codes (Nugent et al. 1995; Fisher et al. 1997; Stehle et al. 2005; Mazzali et al. 2008). Ab-initio theoretical models are developed (Röpke et al. 2007; Fink et al. 2010; Marek & Janka 2009; Hammer et al. 2010) and tested against the observations (Kasen et al. 2009; Sim et al. 2010).

Besides detailed data on individual objects, statistical data on the nature and the rates of SNe (e.g. Greggio et al. 2008; Hayden et al. 2010; Li et al. 2011a,b) can give constraints on the explosion mechanisms and the characteristics of the progenitors. *Population synthesis* codes (e.g. Ruiter et al. 2009) predict the evolution of a statistical sample of stars based on the current paradigms for the evolution and explosive death of stars. The predicted consequences of these paradigms can then be compared against the observed SN statistics.

In this introduction, we will review the various observational constraints on different SN types. In particular, we discuss observed light curves and spectra, as they are used for the analyses in this thesis. After this part emphasising the observations, we give some basics of SN theory type by type.

We try to convey a general impression of the relevance of SNe in astrophysics and beyond. Some details are given on the application of SNe as *standard candles* in cosmology, which has been crucial for inferring the *accelerated expansion* of the universe (e.g. Perlmutter et al. 1997, Riess et al. 1998, Perlmutter et al. 1999, Astier et al. 2006, Wood-Vasey et al. 2007, Hicken et al. 2009). Furthermore, we briefly discuss core-

collapse SNe as emitters of neutrinos and gravitational waves, and as production sites of the *metals* we find in our Universe today.

1.1 SN observations

SNe show a large diversity in the observations, for which we sketch a basic physical interpretation below. We discuss the *bolometric light curves* and *optical spectra* (sometimes extending into the near-UV/IR) of "normal" SNe in detail.

In recent years, more and more efforts have been started in order to find and explain "weird" SNe and transients (e.g. Fryer et al. 1999; Bond et al. 2009; Wood-Vasey et al. 2007; Fryer et al. 2009; Rau et al. 2009; Kawabata et al. 2010; Perets et al. 2010). These objects, as well as Type IIn SNe (Schlegel 1990; Chevalier & Fransson 1994), are interesting, but too special in their physics to be discussed in this thesis.

1.1.1 Light curves and cosmological application of SNe

The light curves of different SN Types (Fig. 1.1) are physically determined by the mechanisms which produce and store the energy which finally escapes in the optical bands.

If the explosion is driven by a hydrodynamic shock wave (Weaver 1976), radiation from the *shock break-out* (Chevalier 1976; Ensman & Burrows 1992; Waxman & Loeb 2001, and references therein) may be observed within $\sim$ 1 d after explosion, in particular in the higher-energy bands (UV, X-ray).

The focus here is however on two processes which can provide energy for SN light curves on the timescale of days to months. One of them is heating of the ejecta in the explosion process (Imshenik & Nadëzhin 1965; Grasberg & Nadëzhin 1970; Arnett 1971; Chevalier 1976; Wilson et al. 1985). Whether or not significant light can be gained in this way depends strongly on hydrodynamic details of the model, which influence the conversion of heat and radiative energy to kinetic energy and back again. The other one is the decay of freshly synthesised radioactive material after the explosion (Borst 1950; Burbidge et al. 1956). The most relevant species in this respect is ^{56}Ni (Pankey 1962; Colgate & McKee 1969), whose production is followed by the decays

$$^{56}\mathrm{Ni} \overset{t_{1/2}=6.077\,\mathrm{d}}{\longrightarrow} {}^{56}\mathrm{Co} \overset{t_{1/2}=77.27\,\mathrm{d}}{\longrightarrow} {}^{56}\mathrm{Fe},$$

in which positrons and gamma rays are released. The gamma rays undergo Compton scattering, accelerating electrons, which heat the plasma. Also the positrons deposit kinetic energy before they annihilate; however the heating due to gamma rays dominates until the ejecta become transparent to these (a few hundred days after explosion, (Cappellaro et al. 1997)). The relative importance of heating by radioactivity on the one hand, and by the explosion process itself on the other hand depends on the SN type and the epoch the SN is in.

Before released, radiation can be trapped for some weeks in optically thick regions (Arnett 1982). The radiation field usually stores much more energy than the ejecta do via their ionisation/excitation state and their thermal motion. The opacity of the optically thick zones – depending on the SN type – is usually dominated by *atomic lines* of *Fe-group elements* or also by *free electrons* (for zones where H II is abundant, as H releases many electrons per unit mass when ionised).

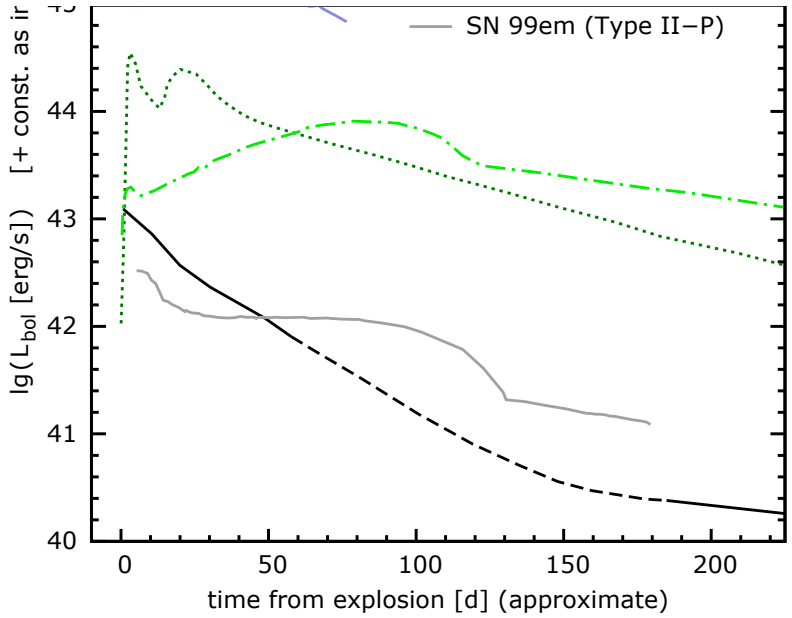

Figure 1.1: Bolometric light curves of SNe of different types (from top to bottom: Pastorello et al. 2007a; Taubenberger et al. 2006; Iwamoto et al. 1994; Taubenberger et al. 2011b and references therein; Catchpole et al. 1989; Bartunov & Tsvetkov 1986; Bersten et al. 2011). The SN Ic curves represent SNe Ib and Ic. Core-collapse SNe have a large spread even within each subclass; the data shown are only examples. The time axis is approximate due to uncertainties in the estimated explosion dates.

1.1.1.1 Type I SNe

Type Ia

In Type Ia SNe, freshly synthesised ^{56}Ni constitutes between 10% and 90% of the ejected mass, which is between 0.7 and $1.4 M_{\odot}$ (Stritzinger et al. 2006[a)]). Compared to the radioactive energy production, little heat from the explosion process itself is stored in Type I SNe, corresponding to the fact that their progenitors do not have an extended envelope. Thus, their light curve is entirely dominated by radioactivity (Arnett 1979; Meyerott 1980; Colgate et al. 1980; Chevalier 1981). Exceptions to this could occur within the first $<$ 10 d past explosion, if a shock breakout, an impact of the ejecta onto a companion star, or interaction of the ejecta with a circumstellar medium generated significant radiation. However signatures of these processes have not been observed yet.

Most of the ^{56}Ni in a SN Ia is produced in the core where densities are relatively

[a)]The analysis in this paper is known to be somewhat flawed, but accurate enough for a rough estimate.

high. The core remains optically thick for about one month after the explosion, and traps significant amounts of radiation. The light curve rises and reaches a maximum ~ 15 – 20 d after explosion (Fig. 1.1; Conley et al. 2006; Hayden et al. 2010). At this time, the envelope is dilute enough for photons to stream outwards, while the energy input by ^{56}Ni and ^{56}Co decreases due to the ongoing decay of the parent nuclei. Around maximum light, the instantaneous energy generation by radioactivity roughly equals the luminosity ["Arnett's rule"; this is somewhat model-dependent – Arnett (1982); Pinto et al. (2000)]. Afterwards, the trapped radiation continues to escape, with the emitted energy per unit time being larger than the energy input. When the reservoir is exhausted, the light curve drops back to a level with a heating-cooling equilibrium[b)]. This occurs within some weeks past maximum light, when the energy generation is already dominated by ^{56}Co decay. The slope of the light curve is somewhat steeper than what would be expected considering the half-life of ^{56}Co. The reason for this deviation is the increasing transparency of the ejecta to gamma rays. When full transparency to gamma rays is reached about 150 – 300 d after explosion, the ejecta are still opaque to positrons. Up to very late times ($\gtrsim$ 600 d, Seitenzahl et al. 2009), the light-curve then follows a slope corresponding to ^{56}Co decay, with an absolute light output proportional to the mass of radioactive material times the fraction of decay energy emitted in positrons.

The bulk of SNe Ia [*normal* SNe Ia, Branch et al. (1993)] have ^{56}Ni masses of $\sim 0.3 - 1.0 M_\odot$ (Mazzali et al. 2007). Therefore their light curves differ about a factor of $\lesssim 4$ in maximum luminosity. Furthermore, the curves show an uniform behaviour in the sense that objects with higher maximum luminosities on average have broader light curves. The physical mechanism behind this is that both the luminosity and the opacity (which determines the width of the light-curve) are modulated by Fe-group elements (e.g. Mazzali et al. 2001). The brightness of a SN Ia can therefore be guessed from its light-curve shape (Phillips 1993; Phillips et al. 1999), which is the basis of the application of SNe Ia in cosmology (Sec. 1.1.1.3).

Type Ib/Ic

The light curves of Type Ib/Ic SNe share the characteristics of the Type Ia ones. Although Type Ib/Ic SNe are core-collapse events (with a few exceptions perhaps), their progenitors have not retained a large H or H/He envelope, respectively. Therefore the light curves are dominated by ^{56}Ni decay (Arnett 1982), except for the earliest times when a shock break-out and cooling of the envelope may be observed in some objects (Soderberg et al. 2008).

SNe Ib/Ic have strongly varying ejecta masses $\gtrsim 1.0 M_\odot$ (Nomoto et al. 2009) and a significant, but not too large mass of Fe-group elements such as ^{56}Ni ($\lesssim 15\%$ of the ejecta mass, e.g. Tanaka et al. 2009). The light curves mostly evolve faster than those of SNe Ia, and show more strongly varying luminosities and widhts. These depend on the abundances of ^{56}Ni and other elements, the kinetic energies and the ejecta masses. In contrast to SNe Ia, width and peak luminosity do not correlate strongly. For some objects, the evolution of the light curve turns out to be particularly slow around $\sim$50 d past maximum, almost perfectly following the ^{56}Co decay (Clocchiatti & Wheeler 1997).

[b)] There may be further modulations due to processes abruptly releasing stored energy: e.g. at $\sim$ 50 d, the infrared light curves often exhibit a second peak, slowing down the decline in bolometric luminosity (Kasen 2006).

This may indicate a very efficient trapping of gamma rays due to clumping or a large ejecta mass.

1.1.1.2 Type II

Type II SNe (with Type IIn objects as a possible exception) have retained at least part of their H envelope. Their ejecta masses vary from object to object, with the smallest values ($\gtrsim 2.5 M_\odot$) in Type IIb SNe (Zampieri 2005; Taubenberger et al. 2011b). Also the explosion energies show a large scatter (Zampieri 2005). All this reflects in the different light curves (Fig. 1.1) of SNe IIb (small H mass), II-L and II-P (large H mass).

With its early time emission after shock breakout, a Type II SN radiates the energy that has been deposited in the outer layers as the explosion shock has passed them (see Sec. 1.3.3). The initial light curve peak tends to be stronger for more extended envelopes (Arnett 1989), and probably also for more massive ones. In addition, the envelope properties modulate the width of the peak.

Some days after the first maximum, the light curve may show a plateau (SNe II-P), a second delayed peak (peculiar SNe II-P, SNe IIb) or a quasi-linear decline (SNe II-L).

A plateau corresponds to the gradual release of photons produced in the explosion phase. The photons generated are trapped for some time in optically thick layers dominated by H II and free electrons. The opacity is largely due to *Thomson scattering*, but also *free-free* processes (and *bound-bound* or *bound-free* processes if atoms or ions other than H II are abundant) are relevant, depending on the wavelength range (Eastman et al. 1994; cf. Chapter 2). During the plateau phase, more and more of the stored photons can escape as the plasma becomes transparent when H II recombines [*recombination wave* – Kirshner & Kwan (1975); Falk & Arnett (1977); Litvinova & Nadëzhin (1983)]. During this period, SNe II have a relatively well-defined *photosphere*, i.e. a thin layer behind which the ejecta are optically thick at practically all wavelengths (due to the ionised state), and above which optical depths are small at most wavelengths.

SNe II without a plateau either have too small an opacity in the H II layers due to a small density, or too small a volume in which energy is stored – i.e. their progenitor star was less massive and/or has had a less extended H envelope.

A second, delayed light curve peak occurred in the famous, nearby SN 1987A (a peculiar Type II-P SN – Fig. 1.1) and is a usual feature in Type IIb light curves. The reason for this can either be found in the time evolution of the ejecta (extent, opacities, energy content), or in their ^{56}Ni content (especially for Type IIb objects). The second maximum can, in fact, be stronger than the first one, which is sometimes also missed when observations start too late.

Most Type II SNe, including those for which ^{56}Ni did not significantly contribute to the early light curve, show a late-time decline which follows more or less the decay of ^{56}Co. In this respect, Type I and Type II SNe are similar, but the ^{56}Ni masses and thus the late-time luminosities of Type II SNe are rather low ($\lesssim 2\%$ of the ejecta mass, Zampieri 2005).

1.1.1.3 SNe as standard candles in cosmology

Since the 1970s (Wagoner 1977; Colgate 1979), there has been the idea of using SNe as *standard candles* (i.e. objects with known intrinsic luminosity) for measuring *extragalactic luminosity distances* (i.e. distances corresponding to the ratio of emitted and

received flux). In the last 20 years, this has been made a reality, and "supernova cosmology" studies have become extremely popular (Schmidt et al. 1992, Perlmutter et al. 1997, Riess et al. 1998, Hamuy 2001). Especially in the case of Type Ia SNe, the cosmological application has become an important motivation for studies on the SNe themselves and their funding, following the paradigm that the cosmological studies can only be as reliable as our knowledge on the SNe.

Why are distances so important for astrophysics and cosmology? – Luminosity distances d_L to extragalactic objects with known *cosmological redshift* z (i.e. an apparent "Doppler-shift" of spectral lines of extragalactic objects) can be used to determine the expansion history of the Universe. Also, better distances to remote galaxies are useful for accurate estimates of the luminosity of stars and other astrophysical objects in them.

Cosmology and extragalactic distances

Within the standard model of cosmology (cf. Carroll 2004), part of the properties of our Universe are fixed by basic theoretical assumptions. These basic assumptions are the *cosmological principle* (homogeneity, and isotropy for *co-moving* observers) and our theory of *gravitation* (general theory of relativity). The exact geometric evolution of the Cosmos however depends on the (time-dependent) energy-momentum tensor and the *cosmological constant* Λ.

Assuming the cosmological principle and the *Einstein field equations of general relativity* with a perfect-fluid energy-momentum tensor, one obtains a *Friedmann-Robertson-Walker Universe*, described by a *Robertson-Walker metric* and the *Friedmann equations*. Here, we will not describe these equations and their solution, but are just concerned with parameters characterising a universe.

The Robertson-Walker metric has two free quantities fixing the geometry: a constant *curvature* $\kappa \in \mathbb{R}$ and a free *scale factor* $a(t)$. The scale factor function $a(t)$ can imply an expansion or contraction of space. As it is normally defined, distances within an Universe at one point of time t will be proportional to a (note that a measurement at $t =$ const. is not possible in reality). The evolution of a with time is coupled to the (time-dependent) *energy/matter density* and *pressure* due to different components of our universe [visible and *dark* matter (e.g. Papantonopoulos 2007), radiation and the cosmological constant Λ]. The cosmological constant acts like a positive energy density and a negative pressure in the Einstein equations, and its density remains constant with time. Due to the invisibility of this "energy" with its strange properties, Λ is often referred to as *dark energy*.

How can one measure $a(t)$ and gain knowledge about the components of our universe? – Within a Friedmann-Robertson-Walker universe, radiation emitted by remote objects at a time t_e, and received at a time t_r experiences a positive or negative redshift in wavelength $z = (\lambda_r - \lambda_e)/\lambda_e$, which is given by

$$z = a(t_r)/a(t_e) - 1. \tag{1.1}$$

Here, t_e and t_r are the values of the cosmological time at which the light is emitted and received, respectively.

The equation implies a relation between luminosity distance d_L and redshift z for extragalactic objects: If one for example assumes a monotonically increasing $a(t)$, a larger distance – corresponding to a larger light travel time – implies a stronger deviation

of $a(t_r)/a(t_e)$ from 1. Information on $a(t)$ can thus be derived from measurements of luminosity distancs and redshifts.

To make this more obvious, we consider an expansion of $d_L(z)$ about $z = 0$:

$$d_L = H_0^{-1}\left[z + \frac{1}{2}(1 - q_0)z^2 + \ldots\right] \tag{1.2}$$

The leading-order term on the right hand side is *Hubble's law* (cf. Hubble 1929), which states that the redshift (or the apparent recession velocity of an object[c)]) is proportional to the distance. The constant of proportionality is H_0 (*Hubble constant*), which is today's value of the *Hubble parameter*

$$H(t) = \dot{a}/a. \tag{1.3}$$

The quantity q_0 is today's value of the *deceleration parameter*

$$q(t) = -a\ddot{a}/\dot{a}^2. \tag{1.4}$$

Both H_0 and q_0 can be determined from fitting a $d_L - z$ relation with free parameters to observations. Perlmutter et al. (1997) and Riess et al. (1998) were the first to reliably determine – with the help of data on SNe Ia – that q_0 is negative and the Universe is currently undergoing accelerated expansion. As mentioned, the dynamics of our Universe depend on the relative importance of the different components (matter, radiation, cosmological constant). Therefore, the current measurements of the properties of our Cosmos imply that $\sim$70% of the density in today's Universe is due to dark energy (e.g. Spergel et al. 2007).

Distance determination step by step - the cosmic distance ladder

The measurement of d_L between us and some location in space requires objects at that location for which one knows the intrinsic luminosity. However, knowledge about the luminosity of objects of a certain type can only be built through studies of representative samples. For this, enough objects of the respective type have to exist for which we know the distance. This "chicken-egg problem" is resolved in astronomy by inferring distances step by step. Suppose distances are known up to a certain redshift, and within the current bounds one finds a sample of special galaxies with roughly uniform luminosity. Then, after inferring their mean luminosity, one uses these galaxies to obtain distances to locations further out.

The step-by-step system for the determination of extragalactic distances is known as the *cosmic distance ladder* (Fig. 1.2, cf. Webb 1999). New methods are continuously invented to extend the ladder, and redundant measurements are added in order to reduce statistical and systematic errors. Below we discuss how SNe are used in this context.

SNe Ia as distance indicators - light curve calibration methods

Data on Type Ia SNe have been used to obtain the first spectacular results of SN cosmology (Riess et al. 1998; Perlmutter et al. 1997, 1999). Since the 1990s, several new

[c)]The interpretation of cosmological redshifts as an "apparent Doppler effect" is very common, even if the cosmological redshift has a completely different origin – the dynamical evolution of space-time.

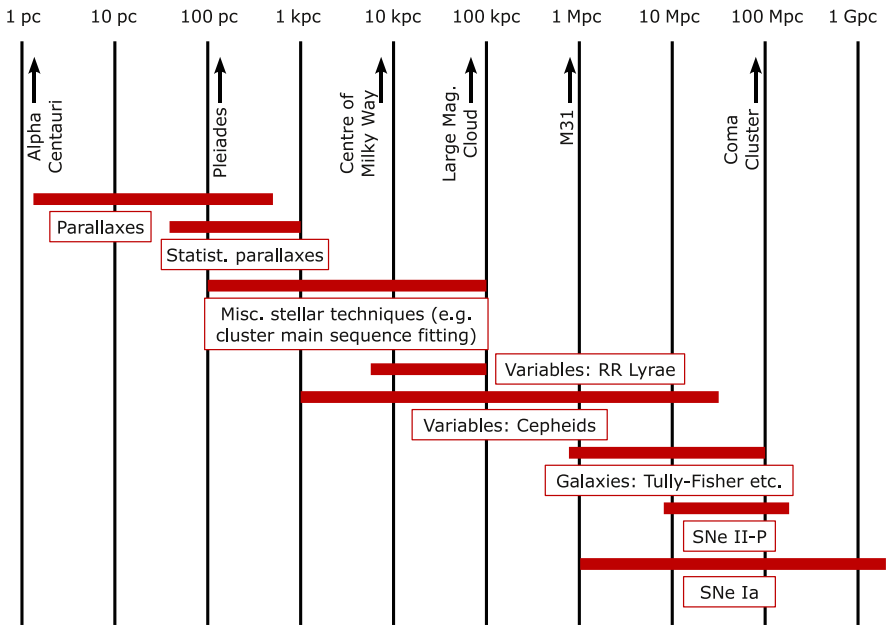

Figure 1.2: The cosmic distance ladder. The sketch gives some methods/objects used to determine *galactic* and extragalactic distances step by step. For each method a red bar gives the range in which it is most suitable for distance determination (numerical scale see top of the figure, with widely known objects at these distances mentioned). Adapted from lecture notes of D. J. Jeffery and F. Kupka; reflects the state of measurements in the early 2000s, except for the SNe II-P bar which corresponds to the data of Jones et al. (2009).

data compilations methods have been issued and analysed with sophisticated techniques (e.g. Astier et al. 2006; Wood-Vasey et al. 2007; Hicken et al. 2009).

SNe Ia are not exactly standard candles, but rather *standardisable candles*: the ^{56}Ni masses of Type Ia SNe show some dispersion, and so does the luminosity of the objects. However, the light-curve shape of the objects, and in particular the "speed" with which the (logarithmic) light curve declines, can be measured independent of distance. The decline speed is in turn an indicator for the intrinsic brightness of the SN (Sec. 1.1.1.1). The accuracy of this indicator depends on the spectral range in which the light curve is recorded. Different bandpasses are affected by different peculiarities in the flux redistribution within the SN, and also by different observational errors. A quite reliable luminosity calibration is empirically possible measuring the change in magnitude in the B-band during the first 15 days past B maximum, $\Delta m_{15}(B)$ (Phillips 1993; Phillips et al. 1999). $\Delta m_{15}(B)$ is used as a proxy for luminosity ("larger luminosity - smaller $\Delta m_{15}(B)$") also in non-cosmological studies on SNe (e.g. Mazzali et al. 2007).

Modern light-curve fitters (e.g. MCLS2k2, Jha et al. 2007) broaden this concept, evaluating data in several bands to infer the brightness of a SN Ia. In principle, this makes SN Ia cosmology more accurate. However, the light-curve fitters are still based on luminosity-shape relations which must be calibrated using a local sample of SNe Ia. The systematic errors which may result from differences between the local sample and the "cosmology sample" (due to intrinsic differences, or differences in the average *dust extinction*) have therefore remained a problem limiting the precision of SN Ia cosmology.

SNe II-P as distance indicators - expanding photosphere method

Type II-P SNe can be used as standard(isable) candles using the *expanding photosphere method* (*EPM*, Kirshner & Kwan 1974, Jones et al. 2009). The idea of this method is to infer the luminosity from basic physical assumptions, without relying on a calibration sample of objects. In principle, EPM is therefore more appealing than the SN Ia calibration methods. However, up to now EPM distances have often been affected by oversimplifications exactly in the basic physical assumptions. Therefore, a number of improvements (e.g. Schmidt et al. 1992) or also alternative methods (Hamuy et al. 2002) have been proposed. In the following, we want to explain the principles of EPM. For this purpose, it suffices to describe the simplest form (without improvements).

During the plateau phase, Type II-P SNe have a quite well-defined photosphere (Sec. 1.1.1.2). The large optical depth below this photosphere at practically all wavelengths allows for a thermalisation of the radiation field, so that the photosphere radiates approximately like a "spherical black body" according to the Stefan-Boltzmann law:

$$L = \sigma \times 4\pi r_{\text{ph}}^2 \times T_{\text{ph}}^4 = \sigma \times 4\pi v_{\text{ph}}^2 t^2 \times T_{\text{ph}}^4 \tag{1.5}$$

where $\sigma = \frac{2\pi^5 k_{\text{B}}^4}{15h^3c^2}$ is the Stefan-Boltzmann constant, and r_{ph}, v_{ph} and T_{ph} are the radius, expansion velocity and temperature at the photosphere, respectively. t is the time from explosion.

The photospheric velocity can roughly be determined from an observed spectrum (see Section 1.1.2) by line velocity measurements or model fitting. Also, the temperature T can be derived from the spectral energy distribution. Therefore, we only need the time t from explosion in order to calculate the luminosity of the SN. If we estimate the date of explosion as t_{estim}, and call the difference between real and estimated explosion date Δt, then

$$\begin{aligned} t_{\text{real}} &= t_{\text{estim}} + \Delta t \text{ and} \\ L &= \sigma \times 4\pi\, v_{\text{ph}}^2\, (t_{\text{estim}} + \Delta t)^2 \times T_{\text{ph}}^4. \end{aligned}$$

From measurements of v_{ph} and T_{ph} at two different points of time $t_{\text{estim,1}}, t_{\text{estim,2}}$ during the plateau phase (where L is either assumed constant or the luminosity *difference* has been observed) , we can therefore infer the luminosity $L(t_{\text{estim,2}})$ as well as Δt.

Unfortunately, the photospheric picture is not a perfect physical description[d)] for SNe, and Type II-P SN are not a complete exception to this rule. Thermalisation happens not abruptly, but gradually with increasing depth, in the zone where H II and electrons are abundant. The determination of a "photospheric velocity" therefore depends on the theoretical assumptions on the radiating SN envelope. In addition, the real $L - v - T$ relation will not exactly be a simple Stefan-Boltzmann law. Appropriate radiative transfer models for a reliable application of the EPM are therefore still a subject of active research (e.g. Jones et al. 2009).

1.1.2 Spectra

The spectra of SNe show a huge diversity. Here, we give an overview focused on early-time spectra as they are used for our thesis project.

[d)] A spherical body emitting radiation is obviously not a closed system in undisturbed thermal equilibrium; thus it is not surprising that "spherical blackbodies" are an approximate concept with limitations.

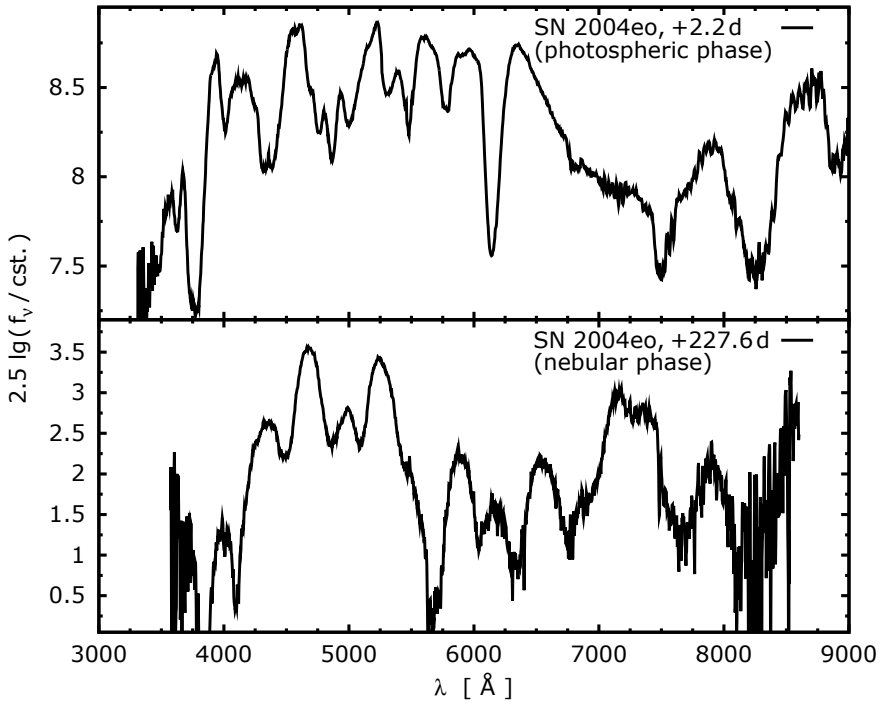

Figure 1.3: Photospheric (+2.2 d after B maximum) vs. nebular (+227.6 d) spectrum of a SN Ia (SN 2004eo, Pastorello et al. 2007b). The photospheric spectrum can be thought of as a continuous flux distribution eroded by a multitude of broad absorption *features* corresponding to *atomic lines*. The nebular spectrum is an emission spectrum – it has a larger dynamic range (cf. scale), and the flux decreases to practically zero at a couple of wavelengths.

1.1.2.1 Photospheric versus nebular spectra

In general one distinguishes two phases in the observed evolution of a SN: the photospheric and the nebular phase. Example SN Ia spectra for both phases are plotted in Figure 1.3.

During the early, *photospheric* phase, some core region of the ejecta is optically thick (e.g. Kirshner & Kwan 1975; Branch et al. 1983). In Type II-L/II-P SNe, the opaque core includes the part of the H envelope which is ionised at early times. It contains photons generated in the explosion process and releases them with time. In Type I (and also Type IIb) objects, the situation is different: these SNe have a core which is opaque mostly due to line opacity of Fe-group elements (e.g. Sauer et al. 2006), and which does not store much energy from the explosion process. At early epochs, this core includes the majority of the ^{56}Ni-rich zone where the light is generated.

In SNe of all types, radiation first diffuses through the central zone until it reaches the outer layers and finally escapes. Normally, no strong heating (e.g. by radioactivity) occurs in the outer ejecta, and thus these layers do not generate many additional photons. They merely reprocess the radiation field coming from the inner part in approximate *radiative equilibrium* (energy is transported only by radiation, and the radiation field has no net energy win/loss). In effect, the outer layers therefore leave their imprint in strong and wide *P-Cygni features* ("blueshifted absorption + redshifted reemission" features), imposed on a relatively continuous spectrum which has formed in the inner ejecta (Fig. 1.3, upper panel).

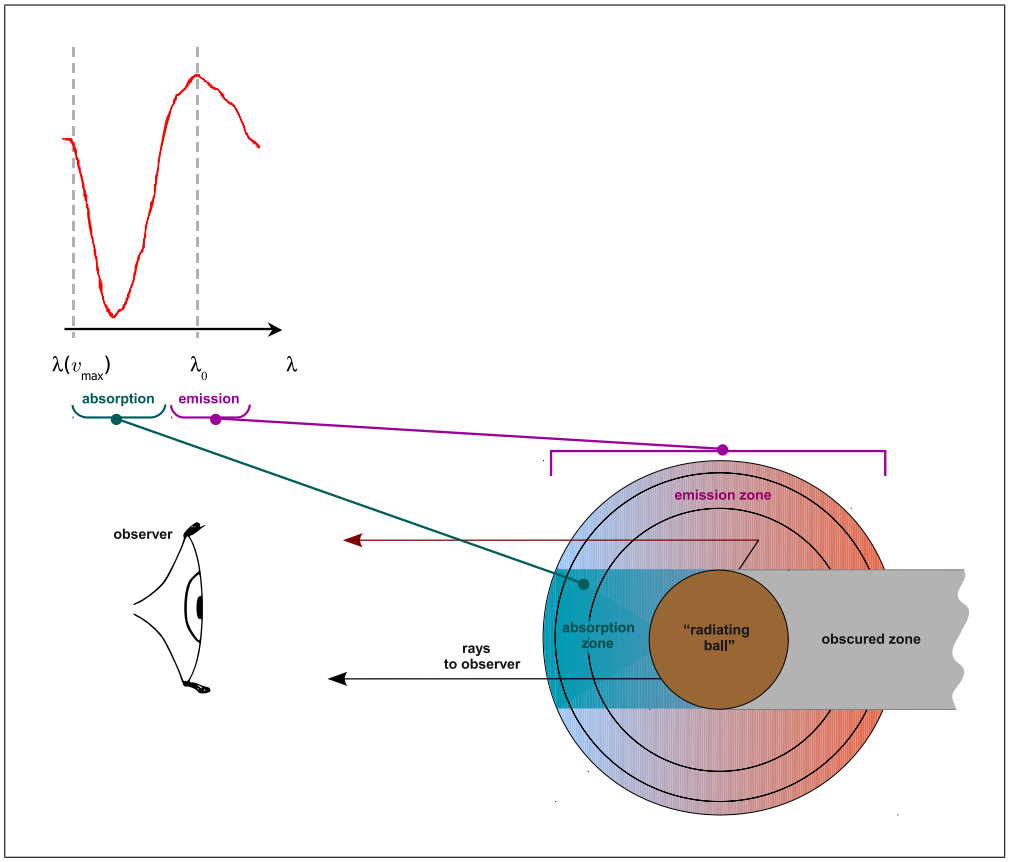

Figure 1.4: Formation of P-Cygni line profiles in the photospheric spectrum (*upper left corner*) of a SN. Different zones (absorption zone, emission zone) in the SN (*lower right corner*; the region inside the photosphere is referred to as "radiating ball") with respect to the observer's position (*lower left corner*) correspond to different parts of the line profile. The resulting line shape in the spectrum is typical for fast-expanding scattering atmospheres.

When sufficiently expanded (i.e. 100 – 300 d past maximum light, depending on the initial densities and abundances), SN ejecta become transparent in the optical and the SN enters the *nebular* phase (e.g. Taubenberger et al. 2009). The optical luminosity emitted by each spatial region, which balances the energy deposited by gamma rays and positrons per unit time, contributes quite directly to the nebular spectrum. Radiation, once emitted, is often unaffected by the outer ejecta layers it has to pass (Axelrod 1980), with the exception of some line interactions especially in the blue and UV. Due to the overall weak reprocessing of radiation, the continuum level in the spectrum is small. One therefore sees a spectrum of broad *emission features* (Fig. 1.3, lower panel), through which the ejecta cool. Remarkably, the transitions in which the emission takes place are often forbidden ones, due to a strongly non-thermal occupation of metastable levels which can be filled up until emission starts (Axelrod 1980).

1.1.2.2 Spectral features: Line broadening in fast-expanding ejecta and P-Cygni shape

The large width of all line features in SN spectra is a consequence of the expansion of the ejecta, which makes atoms/ions absorb and emit at Doppler-shifted wavelengths.

Because of the high (but not strongly relativistic; mostly $0.001c \lesssim v \lesssim 0.1c$) velocities, the Doppler effect due to the global motion is the only line broadening effect relevant for the spectra; all other mechanisms generate negligibly small broadening (e.g. the thermal velocities of the material are much smaller than the expansion velocities). At epochs of a few days after explosion, at which the earliest spectra are recorded, most objects have entered a phase of *force-free*, *homologous* expansion (Woosley et al. e.g. 1994; Röpke & Hillebrandt e.g. 2005; Sec. 1.4). This means that $r = v \times t$ holds for each particle with respect to the centre-of-mass of the ejecta, where t is the time from explosion onset and v is the velocity of the particle gained in the explosion. All particles are moving in radial direction, as their initial offsets $\vec{r}_0$ from the centre-of-mass can be neglected ($|\vec{r}_0| \ll r$ for $v \times t$ sufficiently large).

Basic characteristics of nebular emission features (Fig. 1.3, lower panel) are easy to understand. If one assumes, for simplicity, a feature to be due to one atomic line active throughout the ejecta, the emission will be centred about the line's rest wavelength. Each part of the ejecta contributes to the emission at a Doppler-shifted frequency determined by its velocity projected onto the line-of-sight towards the observer. The blue and red wings of the feature correspond to the largest expansion velocities of the ejecta. The exact profile shape depends on the spatial emissivity distribution of the ejecta, and on the observer's point of view. In reality, *blending* (i.e. line overlap) occurs very often and one does not see single line features, but features mixed into each other. This makes detailed analyses more difficult, especially when the ejecta are fast, causing a lot of blending.

In the photospheric phase (Fig. 1.3, upper panel), line features are combined absorption-emission features, whose formation is a more complicated process. They have a P-Cygni shape typical for *fast-expanding atmospheres* in which a continuous distribution of photons coming from deep, optically thick layers undergoes *scattering* (i.e. absorption and reemission without energy loss; other processes in the SN shall be temporarily ignored). In the case of a SN envelope, a line feature consists of a blueshifted absorption part and an emission part centred roughly about the rest wavelength (Fig. 1.4, left-hand side). This can be understood in terms of a division of the envelope into different zones (right-hand side of Fig. 1.4) with respect to an observer. Rays coming from the deep layers towards the observer can be scattered by material in between (Fig. 1.4, *absorption zone*). The opaque material moves towards the observer, who therefore sees the atoms "absorbing" at wavelengths blue-shifted with respect to their laboratory line wavelengths. The radiation is, however, not lost – it has only been scattered into another direction. For our observer, in turn, this means that he will notice additional radiation scattered towards him. This radiation has been re-emitted by atoms moving either away from him or in his direction (Fig. 1.4, *emission zone*). The observed re-emission thus peaks, just as a nebular profile, at the rest wavelength of the line if one neglects that a part of the atmosphere is obscured due to the optically thick core (Fig. 1.4, *obscured zone*). Line blending is extremely strong in the photospheric phase. Therefore, only a few lines in a real SN spectrum exhibit a P-Cygni shape clear enough to give direct information on the absorbing and re-emitting material. Also, line absorption in practice often is not followed by re-emission of photons at the same (co-moving frame) wavelength. Instead, atoms can for example emit a cascade of photons when de-exciting over a "ladder" of intermediate states. Because of such effects and/or because of the shape of the underlying flux distribution, the P-Cygni re-emission peaks are usually weak or hard to identify in real SN spectra.

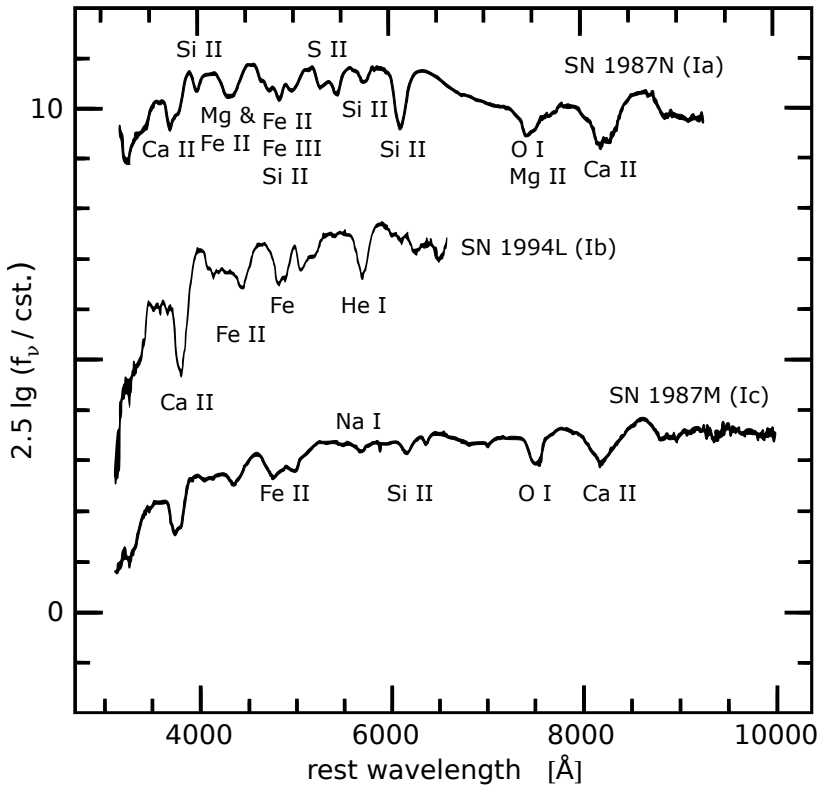

Figure 1.5: Spectra of Type I SNe $\sim$ 1 week past maximum light. Adapted from Filippenko (1997). Major spectral features are marked with element/ion designations.

1.1.2.3 Type I SNe

The spectra of Type I SNe around maximum light (Fig. 1.5) show P-Cygni features due to C, O, *intermediate-mass elements* (*IME*: Mg, Si, S, Ca, ...) and Fe-group elements. In SNe Ib, also He lines are very prominent. Some features which appear to be similar among Type Ia, Ib or Ic SNe are in fact due to different lines depending on the SN type (Fig. 1.5 – e.g. at 5800 Å). In SNe Ia, the most prominent lines are made by IME and Fe-group elements, which indicates an efficient nucleosynthesis. In SNe Ib, only the strongest lines due to IME (Ca II H&K, for example) and Fe-group elements (several Fe II lines) appear. This points towards a less pervasive nucleosynthesis in the outer layers – especially taken together with the evidence for He lines. SNe Ic have no He lines, but their IME and Fe-group lines are relatively weak as well. Their progenitors also undergo a quite limited nuclear reprocessing in the explosion, but are more He-deficient than Type Ib progenitors (which obviously depends on the history of the progenitor star, cf. Chapter 4). SN Ic spectra are sometimes relatively similar to SN Ia ones, but the weaker or absent Si II $\lambda 6355$ line in SNe Ic can be used to distinguish them from SNe Ia.

With a little imagination, one can distinguish a continuous flux contribution underlying the photospheric spectra of Type I SNe (Fig. 1.5). This continuous flux is difficult to quantify as it is strongly eroded by line absorption. It is not a true continuum in the sense of a blackbody radiation field, as it would be generated if the emitting matter was in thermal equilibrium with the radiation field due to a full-spectrum coupling of matter and radiation (via free-bound, free-free and/or Thomson scattering processes).

Line opacity and emissivity, which is dominant in Type I SN ejecta (Sauer et al. 2006), allows for a coupling of radiation to the gas only in certain wavelength regions. The resulting radiation field does not follow a Planck distribution, and the plasma state will also deviate from a Saha-Boltzmann equilibrium (cf. Chapter 2). The strongest line coverage (in Type I SNe) occurs in the UV and in the blue, where many lines of Fe-group elements overlap each other. Where emissivities are large, a *pseudo-continuum* or *quasi-continuum* forms[e)]. This extends into the optical, but breaks down at $\gtrsim$ 6400 Å, where the number of lines is low (Sauer et al. 2006).

The spectra of Type Ia SNe have been subject to intense observational and theoretical analyses especially in the last two decades (Branch et al. 1993; Mazzali & Lucy 1993; Nugent et al. 1995; Fisher et al. 1997; Benetti et al. 2005; Stehle et al. 2005; Hachinger et al. 2006; Kromer & Sim 2009). Due to the large uncertainties in explosion models and in radiative transfer calculations, direct hints on the explosion mechanisms have, however, only quite recently been obtained (Mazzali et al. 2007; Kasen et al. 2009; Sim et al. 2010; Maeda et al. 2010).

1.1.2.4 Type II SNe

The early-time spectra of Type II SNe show a strong time evolution; Fig. 1.6 shows spectra for three epochs in order to give an impression. Initially, a relatively undisturbed continuum is observed (cf. Sections 1.1.1.2 and 1.1.1.3), which strongly distinguishes these spectra from Type I ones. The only features at the early epochs are due to H and (sometimes) He (Fig. 1.6, upper panel); the outer atmospheres of Type II SNe practically consist only of these elements. This is consistent with the picture that an ionised H plasma creates a large continuous opacity within the ejecta of Type II SNe, leading to the formation of an approximately Planckian spectrum below some photosphere (near the border between neutral and ionised material).

The further evolution of the spectrum depends on the H mass and the influence of ^{56}Ni on the luminosity. In classical SNe II-P and II-L, the H mass is large and the influence of ^{56}Ni is small at photospheric epochs. The spectrum first keeps to be dominated by H lines, and the continuum remains intact (Fig. 1.6, middle panel). As the photosphere recedes (first in the *enclosed-mass coordinate*, later in radius), other elements leave their lines in the spectrum. Quite late, the continuum is eroded by lines, and the spectra look qualitatively similar to Type I ones (Fig. 1.6, lower panel).

Type IIb objects have a low H mass, and H recombination in them finishes within hours or days after explosion. From the very beginning, their spectra show He lines. Soon in the further evolution, these He lines become dominant. Oxygen, IME and Fe-group lines get strong, and only an H_α P-Cygni profile remains to distinguish the SN from a Type Ib one. Some 15 d past explosion, a Type IIb SN usually shows its bluest spectrum (Taubenberger et al. 2011b; Fig. 1.6, middle panel), roughly coincident with the (secondary) maximum of the light curve, which is due to radioactivity of ^{56}Ni.

[e)] The region where this quasi-continuum forms in Type I SNe may be quite extended in radius, covering zones where the ionisation/excitation conditions vary – another factor which disfavours the creation of a blackbody continuum.

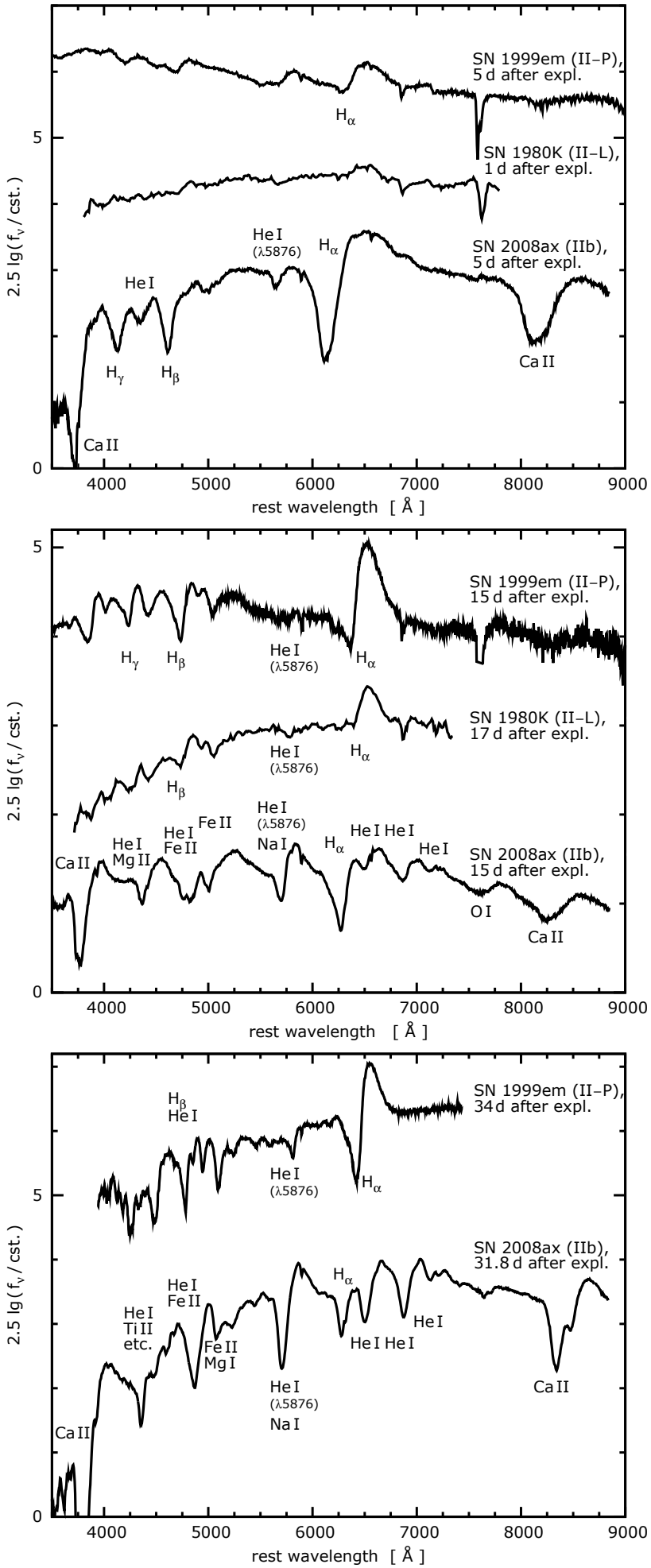

Figure 1.6: Spectra of different Type II SNe at ≤ 5 d, ~ 15 d and > 30 d after explosion [upper, middle and lower panel, respectively; objects: SN 1980K – Uomoto & Kirshner (1986), SN 1999em – Hamuy et al. (2001), SN 2008ax – Taubenberger et al. (2011b)]. Major spectral features are marked with element/ion designations.

1.2 Theory of Type Ia SNe (thermonuclear SNe)

Type Ia SNe show a larger observational homogeneity than other SN types, which has motivated the development of unified SN Ia models which aim at explaining the whole class (e.g. Mazzali et al. 2007). The scenario most favoured in the last decade is certainly the *single-degenerate-Chandrasekhar-mass* (*SD-*$M_{\rm Ch}$) scenario – the word *degenerate* here is used synonymously to the term *white dwarf star* (*WD*), referring to the state of the electron gas in a WD. The SD-$M_{\rm Ch}$ scenario involves a system in which a WD in a *binary system* grows by *accretion* of matter from a non-degenerate *companion*. A *thermonuclear explosion* is then triggered when the mass of the WD has increased (almost) to the stability limit, known as the *Chandrasekhar mass* [$M_{\rm Ch,non\text{-}rot} \sim 1.38 M_\odot$ without rotation – e.g. Kippenhahn & Weigert (1994); original work: Chandrasekhar (1931)].

However, as more and more diversity has been discovered in precision observations of SNe Ia, recent theoretical developments have become very diverse. Explosion scenarios which had gotten out of focus are reconsidered, and new scenarios are developed (Plewa et al. 2004; Fink et al. 2007; Bravo et al. 2009; Kasen et al. 2009; Rosswog et al. 2009; Pakmor et al. 2010; Sim et al. 2010). Mergers of two WDs (*double-degenerate* or *DD* scenario) had classically been thought to not lead to SNe Ia (Nomoto & Iben 1985), but this opinion has now been disproved for some configurations (Pakmor et al. 2010). Another interesting possibility are explosions of WDs which have accumulated He shells, but are somewhat lighter than a Chandrasekhar mass [*SD sub-*$M_{\rm Ch}$*/edge-lit/ double-detonation* scenario, Fink et al. (2007) and further references given below].

Below, we discuss constraints on Type Ia SN models which can be derived from the observations. Afterwards, we give a summary on the possible progenitor systems of SNe Ia and on the most important theoretical models in terms of hydrodynamics and nucleosynthesis.

1.2.1 Observational constraints

1.2.1.1 Abundances of IME, ^{56}Ni and other elements, and total ejecta mass

Observations show that normal Type Ia SNe typically yield substantial amounts of IME [$\sim 0.2 - 0.9 M_\odot$, Mazzali et al. (2007); the exact amounts depend on the model assumptions]. The picture of a very efficient nucleosynthesis – affecting a much larger fraction of the ejecta than in other SN types – is completed by a large mass of ejected ^{56}Ni [$\sim 0.3 - 1.0 M_\odot$ in normal objects, Mazzali et al. (2007)]. These values for the ^{56}Ni mass can be inferred from luminosities or, more accurately, from spectral models in the nebular phase (Bowers et al. 1997; Mazzali et al. 2007). Alternatively, they can be derived from the maximum luminosity (Arnett 1982; Pinto et al. 2000); here the model assumptions play a larger role again. Some amount of O (and sometimes also C) is seen in photospheric spectra, but lighter elements have never been identified.

Despite the large masses of nucleosynthesis products, the entire ejecta of SNe Ia are quite light [roughly $1 M_\odot$, Stritzinger et al. (2006)], and no compact remnant has ever been found where such a SN exploded. The combination of these constraints is fully consistent with a scenario in which white dwarfs undergo a thermonuclear explosion.

1.2.1.2 Kinetic energy

The line velocities in photospheric spectra of SNe Ia do not correlate with the luminosity, with very subluminous (*1991bg-like*, Filippenko et al. 1992) events as an exception (Hachinger et al. 2006). This suggests that the bulk of SNe Ia have a "kinetic energy over mass" ratio (roughly corresponding to a mean ejecta velocity) independent of luminosity. Standard explosion models (Nomoto et al. 1984) have a kinetic energy somewhat in excess of 10^{51} erg. Note that among normally-looking SNe Ia there are some with exceptionally high line velocities and a steep velocity decline with time, the so-called *HVG* (*high-velocity-gradient*, Benetti et al. 2005) objects. The observed HVG objects have luminosities similar to other SNe Ia. The reasons for the distinct velocity evolution are relatively unclear. HVG objects may just have a somewhat different opacity distribution, globally or towards the observer (Tanaka et al. 2008; Maeda et al. 2010).

1.2.1.3 Asphericity and polarisation

Most Type Ia SNe show a low overall polarisation in spectropolarimetric studies (Leonard et al. 2005). This suggests that the objects are only mildly aspherical. In SNe Ia with high line velocities, significant line polarisation is observed. However, this does not indicate a global asymmetry, but rather a production of IME in clumps (Leonard et al. 2005).

Significant overall polarisation is found in subluminous, 1991bg-like SNe Ia (Howell et al. 2001), indicating an extraordinary explosion mechanism for these objects.

1.2.1.4 Signatures of the progenitor systems

No progenitor or companion star of a SN Ia has been unambiguously identified so far, but a few hints on the progenitor systems have been obtained in different ways.

Observations of potential progenitor systems

Some binary systems which may potentially end up in a SN Ia explosion have been identified and observed.

Most prominently, part of the so-called *supersoft* (X-ray) *sources* are expected to be binaries in which a WD accretes mass (Di Stefano et al. 2006, and references therein). It turns out that neither the detected number (Di Stefano 2010), nor the accumulated luminosity (Gilfanov & Bogdán 2010) of these sources within several galaxies is enough to be compatible with typical SN Ia rates per galaxy, if it is assumed that all progenitors are accreting WDs radiating as supersoft sources. As yet it is somewhat unclear whether this is an argument against the SD-M_{Ch} scenario, or if it merely means that for most of the time an accreting WD is no supersoft source (Di Stefano 2010; Hachisu et al. 2010).

Also, numerous white dwarfs in binaries have been directly observed with extreme-UV instruments (Parthasarathy et al. 2007). WDs in binaries which produce *nova* outbursts can be analysed by modelling the novae (Hachisu & Kato 2001). For surprisingly many of the WDs analysed the mass could be constrained to be $\gtrsim 1.0 M_{\odot}$, which seems to support the idea that at least some SNe Ia are produced by a single-degenerate (but not necessarily M_{Ch}) scenario.

Early-time emission from the explosions

Observations of SNe Ia at early epochs have not detected early-time bursts of X-ray to UV radiation. Such bursts may result from shock breakout (for recent – contradictory – predictions, see Höflich & Schaefer 2009; Piro et al. 2010); somewhat different signals are expected if the ejecta interact with a circumstellar medium (Fryer et al. 2010). Likewise, X-ray and UV emission would be expected if an exploding white dwarf interacted with a companion star (Kasen 2010). Kasen (2010) has been able to derive interesting constraints on the companion stars, based on the non-detection of luminosity from interaction. He concludes that WDs fed by an extended, *red giant* (RG) companion are disfavoured as progenitors, as the interaction with an extended companion star generates a high luminosity [as a caveat, (Justham 2011) has recently put forward the claim that that a RG companion can significantly shrink during the accretion process].

H lines from the companion material in nebular spectra

Another constraint on progenitor systems where a WD accretes from a RG or a *main-sequence* (MS) companion comes from the absence of H lines in the nebular spectra. Mattila et al. (2005) and Leonard (2007) concluded from the absence of H lines in two SNe Ia that these objects may not contain more than $0.01 - 0.03 M_{\odot}$ of H. Depending on the companion star, such values may well be reached in the explosion process (Marietta et al. 2000; Pakmor et al. 2008). Further observations and theoretical improvements may be valuable in order to derive limits on progenitor systems consisting of a WD and a MS star. An explosion with an extended (RG) companion, however, is strongly disfavoured by the available simulations.

He lines or other signatures of an accreted He shell

The sub-M_{Ch} scenario has often been considered incompatible with SN observations, as the primary ignition happens within a He shell the WD has accreted and this shell may show up in various ways in the SN spectra. Possible signatures, none of which are observed in actual SNe Ia, would either be He lines, or lines due to burning products of the shell [Fe-group elements – Hoeflich & Khokhlov (1996), or IME – Sim et al. (2010), with exact abundances depending on the burning conditions]. Lately, however, it is considered possible that the He shells in Nature are just light enough not to have a strong observed effect (Fink et al. 2010; Sim et al. 2010).

Circumstellar Na lines in the spectra

Patat et al. (2007), Blondin et al. (2009) and Simon et al. (2009) found signatures of material possibly expelled by the progenitor star in spectra of three SNe Ia. Most of the spectra were recorded with exceptionally high resolution. The high-resolution spectra show several narrow, clear absorption components within the Na I D spectral region, which vary with time. Usually, such varying absorption is thought to be caused by interstellar material moving perpendicular to the line of sight. Patat et al. (2007), however, found that Ca II H&K lines due to the same clouds of material remain constant. They concluded that the time variation of only the Na I lines is caused by a time variation of the ionisation in the clouds. The behaviour of Ca II is different because of the different ionisation potential. The ionisation change can be attributed to the UV flux of the SN.

Under these assumptions, Patat et al. (2007) were able to constrain the distance between the SN and the clouds. They suggested that they can be interpreted as part of the wind of the donor star in a binary with an accreting WD. These findings point towards a RG star as a donor; a MS donor would not have such a strong wind.

Time variability in interstellar absorption lines is only shown by a minority of SNe Ia (Blondin et al. 2009; Simon et al. 2009), and Chugai (2008) heavily attacked the interpretation of Patat et al. (2007). Yet, the findings are interesting, and it remains to be seen whether the idea of a RG donor star can be reconciled with the evidence against extended progenitors mentioned above (cf. Justham 2011).

Companion stars

Nearby *remnants* of SNe Ia (Tycho's SN 1572; SN 1604) are being scanned for stars which have a peculiar motion and peculiar abundances, as they would be expected for companion stars of exploded white dwarfs. However, the results are not conclusive so far (Ruiz-Lapuente et al. 2004; Kerzendorf et al. 2009).

1.2.1.5 Host galaxies

Normal SNe Ia appear in all types of galaxies (Gallagher et al. 2005): in spirals, which are usually assumed to be quite active in star formation, and in ellipticals, which are rather passive. Thus, some SNe Ia probably have younger, and others have older progenitor systems (Mannucci et al. 2006). Subluminous (1991bg-like) SNe Ia, in contrast, show a strong preference towards ellipticals (Taubenberger et al. 2008). The recently discovered "Super-Chandrasekhar" objects, which are extremely luminous Type Ia SNe, seem to prefer low-mass galaxies, sometimes of irregular galaxy type (Taubenberger et al. 2011a). These findings again support the idea that some peculiar SNe Ia have progenitors different from normal ones.

1.2.1.6 Summary diagram

SNe Ia are objects with well-known observational properties. Yet, quite some theoretical aspects are unclear, and manifold ideas on how SNe Ia be produced cannot be proved or disproved. Current observational work may finally bring significant progress. Some evidence for and against different explosion scenarios obtained up to now has been compiled by Howell (2010) into a diagram, which we show here to conclude our discussion on the observational constraints (Fig. 1.7).

1.2.2 Progenitor systems: some details; evolution prior to explosion

All proposed progenitor systems for the bulk of SNe Ia include at least one C/O WD star. Why is that? – Judging from SN Ia spectra and other constraints, the progenitor systems must not contain large amounts of H or He (unless this is completely burned, which is however improbable). A significant amount of O has to be present at least after the explosion, as it is seen in the spectra. In a few SNe Ia, also C II lines are seen. The composition must be the result of nuclear burning in a stellar object. Therefore, only C/O or O/Ne/Mg mixes remain as possibilities. In order to make a violent explosion with such fuel, disrupting the progenitor and synthesising heavier nuclei, the matter must be degenerate, i.e. so dense that the electron gas is in a degenerate state (cf. Sec. 1.2.3.1).

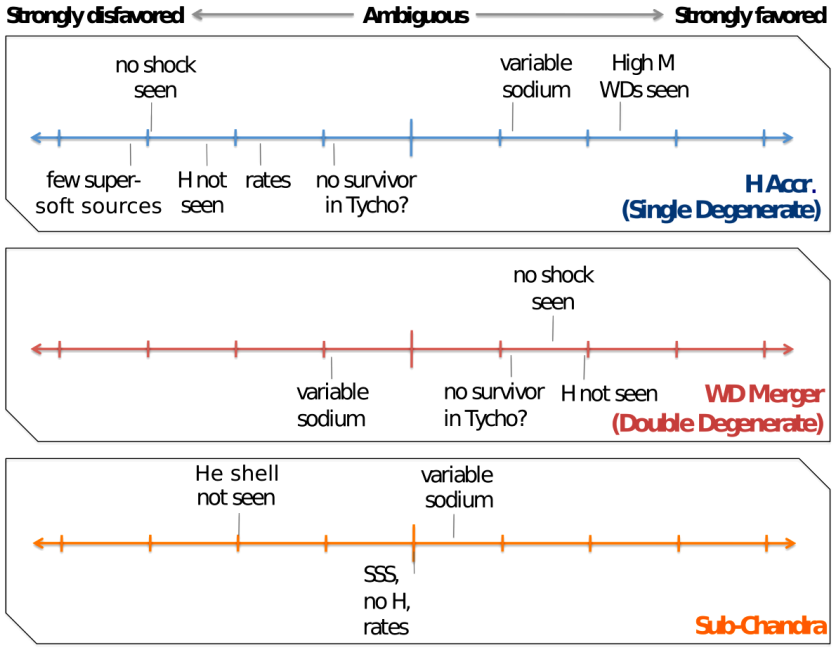

Figure 1.7: Observational evidence for and against three popular progenitor scenarios for SNe Ia (adapted from Howell 2010). The scenarios considered are SD-$M_{\rm ch}$ explosions from H accretors with compact or extended companions (top), WD mergers (middle), and sub-Chandrasekhar explosions from He accretors (bottom). For each scenario, some important observational constraints are given; all constraints mentioned are discussed in different parts of Sec. 1.2.1.

Thus, C/O WDs are obvious progenitor candidates for SNe Ia. O/Ne /Mg WDs probably do not explode, but undergo accretion-induced collapse (Saio & Nomoto 1985). He white dwarfs, even if fully burned, would not be adequate as they are usually very light and would need to accrete for an extremely long time (Benvenuto & De Vito 2005). Explosions of degenerate stellar cores (Ergma & Paczynski 1974; Iben & Renzini 1983) – if possible at all – may show signatures of H or He in the spectrum, and could probably not explain the observed SN Ia rate. Core-collapse explosions, finally, would on average not generate enough ^{56}Ni and would produce either H and He lines, or at least nebular O lines, which are not observed (cf. Taubenberger et al. 2011a).

Therefore, the progenitor discussion is usually constrained to a SD channel (C/O WDs in a binary with a non-compact star, respectively), and a DD channel (binaries of two C/O WDs; binaries involving one O/Ne/Mg WD are neglected here for simplicity).

1.2.2.1 Results from binary evolution and population synthesis

The production of SNe Ia progenitors is investigated in *binary evolution* and *population synthesis* studies. The SD progenitor systems which can form through the various channels of binary evolution can be roughly divided (e.g. Marietta et al. 2000) into *H cataclysmic(-like) variables* (MS star or subgiant + C/O WD), *symbiotic stars and H Algols* (RG + C/O WD), *He cataclysmic variables and AM CVn systems* (*He star* + C

/O WD) and *He Algols* (*He giant star* + C/O WD). The alternative are DD progenitor systems (C/O WD + C/O WD).

Detailed simulations of binary evolution (e.g. Yoon et al. 2010) are used to study the paths towards SNe Ia. They involve a calculation of the evolution of both stars within the binary (similar to simulations of *stellar evolution*[f)]), taking into account the influence of the stars on one another. The main uncertainty here is usually introduced by the very crude prescriptions used to calculate the evolution through *common-envelope* (CE) phases (i.e. phases where the stellar cores are so close that the envelopes merge).

Population synthesis simulations then use typical results of stellar and binary evolution in order to simulate the evolution of a statistical sample of stars and its outcome. In this way, they are able to predict the relevance of different evolution channels to SNe Ia (and other SNe). In the following, we give as an example the channels considered and their characteristics obtained by Ruiter et al. (2011):

SD-$M_{\rm Ch}$, H accretion: The initial binary systems becoming progenitors of this type typically consist of two stars with a *zero-age-main-sequence* (ZAMS) mass of $> 3.5 M_\odot$ and $< 3.5 M_\odot$, respectively. When the primary (more massive) star is in the RG phase or on the asymptotic giant branch, a CE phase occurs. After the CE period, the primary has lost mass, burns its He and becomes a C/O-WD. The secondary eventually donates H-rich matter to the WD, and a $M_{\rm Ch}$ explosion occurs if mass accretion is efficient enough (fine-tuning of the SD scenario, see Sec. 1.2.3.1).

SD-$M_{\rm Ch}$, He accretion: Binaries of He-rich donors and WD accretors start out differently from the H-accreting ones. Ruiter et al. (2009, 2011) calculate that usually the ZAMS mass of the (final) accretor is higher ($\gtrsim 5 M_\odot$) than that of the companion ($\lesssim 3 M_\odot$). The evolution always involves two CE events, and the donor in the final stage is a He-star or a He/He-shell WD. If mass accretion is fast enough so that only small amounts of He accumulate and are burned on the accretor's surface, the system will make a SN Ia explosion only when the accretor reaches $M_{\rm Ch}$.

SD-sub-$M_{\rm Ch}$: The previously-described (single C/O WD, $M_{\rm Ch}$, He accretion) channel is in principle also responsible for sub-$M_{\rm Ch}$ SNe Ia resulting from the edge-lit scenario. If in the last stage of evolution (accretion onto the WD) the mass transfer rate is small enough for He to accumulate on the C/O WD, a sub-$M_{\rm Ch}$/edge-lit explosion may occur if a detonation is ignited in the He.

DD: Ruiter et al. (2009, 2011) assumed all pairs of WDs (also pairs involving He WDs) getting into contact due to gravitational wave emission to make SNe Ia if they had a total mass $> M_{\rm Ch}$. These systems typically originate from binaries of two stars with roughly equal ZAMS mass. They on average undergo

[f)] For an introduction to stellar evolution models, we refer to Kippenhahn & Weigert (1994). Here, all we need to know is that more massive stars generally evolve faster than less massive ones.

one CE event. Note that only for a minority of these systems it has been shown that they can actually make a SN Ia (e.g. Pakmor et al. 2010).

The common trend in population synthesis studies appears to be that the SD-$M_{\rm Ch}$ scenario alone produces too little SNe to explain the full SN Ia rate (Han & Podsiadlowski 2004; Ruiter et al. 2009). They thus advocate a DD scenario or a SD-sub-$M_{\rm Ch}$ scenario for normal SNe Ia (Ruiter et al. 2011).

1.2.3 Final stages, explosion and nucleosynthesis

We now discuss some details of SN Ia explosion models, beginning with the classical SD-$M_{\rm Ch}$ scenario. Even if this scenario has shortcomings, it is still favoured by some research groups. Furthermore, it provides a good context to explain some basics of thermonuclear explosions in general. Afterwards, we describe alternative scenarios.

1.2.3.1 Single-degenerate Chandrasekhar-mass scenario; general concepts

In the SD-$M_{\rm Ch}$ scenario, a WD accretes mass from a MS or RG companion until it is close to $M_{\rm Ch}$. In case of a non-rotating WD, $M_{\rm Ch}$ roughly equals $1.38 M_\odot$; for rotators the mass is larger (up to $\sim 2 M_\odot$ if differential rotation is allowed) as the centrifugal forces stabilise the WD. When approaching this mass limit, the WD eventually explodes.

Progenitor evolution: final accretion phase

In the phase where the WD accretes the mass to reach the Chandrasekhar limit, the accretion rate has to be suitable for the WD to successfully retain the accreted material. The rate has to be in the right range for the material to be burned to He and then to C/O while accreted. If accretion is too slow, lots of material will accumulate until burning commences explosively. This will either lead to a nova outburst removing mass on top of the WD, or to a sub-Chandrasekhar explosion (Hachisu & Kato 2001). If accretion is too fast, a common envelope will form and strong mass loss through winds occurs (Hachisu & Kato 2001). Thus, critics argue that the SD-$M_{\rm Ch}$ scenario needs *fine-tuning*.

If the WD gains enough mass, it develops towards very high central temperatures and densities. The nuclear reaction rate increases and the heating becomes stronger than the cooling by plasmons and neutrinos. The white dwarf then probably undergoes a convective period of roughly 1000 years, in which rising bubbles of hot, burning material transport heat outwards. Finally, with temperatures increasing still, the nuclear burning happens on such short timescales ($\tau \propto T^{-11}$ at $T \sim 10^{10}$ K!) that convective bubbles burn in place (Hillebrandt & Niemeyer 2000, and references therein). In this stage, a *thermonuclear flame* forms – i.e. a thin reaction zone where burning takes place.

Explosion – detonations, deflagrations and delayed detonations

Within a WD close to the $M_{\rm Ch}$, the electron gas is practically fully degenerate, and changes in temperature have, to first order, no effect on the pressure. If energy is generated at a spot, the gas does not quickly respond via expansion. Thus, the flame – once it has formed – runs through the entire star without being quenched. The star explodes.

The flame front can, in principle, propagate either supersonically (*detonation*) or subsonically (*deflagration*). Pure detonations of Chandrasekhar-mass WDs lead to a high burning efficiency, leaving almost only iron-group nuclei behind, which contradicts observations (Arnett et al. 1971). Pure deflagrations tend to produce relatively low kinetic energies and a more strongly mixed structure of burned, partly burned and unburned material than inferred from observations (Stehle et al. 2005; Röpke & Hillebrandt 2005). In modern full-star 3-D models with realistic turbulence, these problems have been cured to some degree, but not completely (Röpke et al. 2007).

Therefore the discussion has focused on *delayed-detonation* models (Blinnikov & Khokhlov 1986, 1987; Khokhlov 1991a,b). In these models, burning starts as a deflagration. At some point, however, a transition to a detonation (DDT – deflagration-detonation-transition) happens in the exploding star, which has already expanded somewhat. Thus, the detonation runs through lower densities compared to a pure detonation model, and large amounts of IME are produced. Compared to a pure deflagration, a delayed detonation leads to a larger explosion energy and less mixing. Thus, two major shortcomings of the deflagration models are removed.

In the SD-$M_{\rm Ch}$ scenario, the uniform ejecta mass explains the "leading-order" homogeneity in SN Ia observations. The observed "next-order" diversity, as we know it nowadays (Phillips 1993; Benetti et al. 2005; Mazzali et al. 2007), can be understood if one invokes DDTs and assumes a varying strength of the initial deflagration (Mazzali et al. 2007; Kasen et al. 2009). The main shortcoming of the SD-$M_{\rm Ch}$ delayed-detonation scenario is the lack of a fully self-consistent physical description of DDTs in SN explosion models. The circumstances under which DDTs can happen are still a matter of active research (Schmidt et al. 2010). In simulations, the detonation is usually artificially started according to criteria on the physical conditions at the flame front.

Other (less popular) models which feature a pre-expansion of the star by a deflagration and a subsequent detonation are *gravitationally confined detonations* (Plewa et al. 2004) and *pulsating reverse detonations* (Bravo et al. 2009).

1.2.3.2 Single-degenerate sub-Chandrasekhar scenario

In a system where a WD accretes matter such that He accumulates on its surface, it may explode as a SN Ia even before reaching the Chandrasekhar mass (Nomoto 1980; Woosley et al. 1980; Nomoto 1982; Livne 1990; Woosley & Weaver 1994). Accreted He shells may detonate if the conditions are suitable. In this case, a shock front is driven into the WD; this almost inevitably causes the core to detonate (Fink et al. 2010). A main question regarding such models is, whether or not one would be able to see clear signatures like high-velocity nickel or remainders of the helium in spectra (Sim et al. 2010), which would contradict observations.

1.2.3.3 Double-degenerate *collision* scenario

Rosswog et al. (2009) have argued that collisions of two C/O white dwarfs may be responsible for about $\sim 1\%$ of the observed SNe Ia. Such collisions may happen in the centres of galaxies and in globular clusters. Simulations show that a collision of two WDs with $0.6 M_{\odot}$ each may well look "SN Ia-like". Also collisions involving non-C/O WDs may lead to explosions (Rosswog et al. 2009).

1.2.3.4 Double-degenerate *violent merger*, *unstable accretion/merger* and *stable accretion* scenarios

Mergers of two C/O WDs in a binary system are an alternative scenario in which a $\sim M_{\mathrm{Ch}}$ object may be created and undergo thermonuclear explosion. The mass ratio q between the two WDs plays a crucial role in deciding the outcome of a merger (D'Souza et al. 2006; Dan et al. 2009), which will eventually happen due to gravitational wave emission.

For $q \gtrsim 0.8$, both white dwarfs are significantly deformed and undergo a violent merger, during which the ignition of a detonation is likely (Pakmor et al. 2011). The detonation burns practically the entire merging object and disrupts it. The burning products depend on the initial density distribution; for low densities, the ^{56}Ni mass generated will be small. Therefore, a merger of two $0.9M_{\odot}$ white dwarfs makes a subluminous SN with only $\sim 0.1M_{\odot}$ of ^{56}Ni (Pakmor et al. 2010). If at least one of the WDs is significantly heavier, larger amounts of ^{56}Ni are expected to be produced.

If $q_{\mathrm{crit}} < q \lesssim 0.8$, mass transfer is unstable as soon as it sets in, i.e. the secondary (lighter) WD is accreted onto the more massive, more compact primary WD. The value of q_{crit} depends on the efficiency of tidal locking (Motl et al. 2007), and may be between 0.2 and 0.67. In contrast to the violent merger scenario, the accretion scenario does not involve large distortions of the primary, and the temperatures and densities reached are not high enough for a detonation to be ignited in the accretion phase. A deflagration may however start, such that the primary is converted to an O/Ne/Mg WD (Nomoto & Iben 1985; Saio & Nomoto 1998). This must be avoided for a SN Ia explosion to occur (Yoon et al. 2007), as an accreting O/Ne/Mg WD would probably undergo accretion-induced collapse (Saio & Nomoto 1985).

Finally, for $q \leq q_{\mathrm{crit}}$, accretion is a self-stabilising and inefficient process: The separation of primary and secondary gets larger when mass is accreted, stopping the accretion. Such systems may make M_{Ch} SNe Ia, if the primary ever grows sufficiently.

1.2.3.5 Nucleosynthesis in SN Ia explosions

Through explosive nuclear burning, SNe Ia produce a significant part of the *metals*[g)] found in the Universe today. Nuclei up to the Fe group, for which the absolute binding energy per nucleon is largest, are synthesised by fusion of C and O atoms and by capture of α-particles. Processes from which heavier nuclei result are not relevant in SNe Ia.

A significant fraction of the ejecta of a typical SN Ia consists of IME and C/O. Counting total cosmic rates, however, the IME and C/O mass ejected by core-collapse SNe is larger (Iwamoto et al. 1999), also because they are more frequent (Li et al. 2011a). SNe Ia are more important when it comes to the synthesis of Fe-group elements – Iwamoto et al. (1999) have crudely estimated that $\sim 55\%$ of the Fe-group nuclei in the Cosmos are due to SNe Ia.

The explosive nucleosynthesis in SNe Ia proceeds in several stages, depending on the peak temperatures T_{peak} and the peak densities ρ_{peak} which are reached before the gas manages to expand and cool (Woosley et al. 1973; Thielemann et al. 1986; Iwamoto et al. 1999). The burning stages reached from the most to the least dense and hot zones, and their characteristics (Woosley et al. 1973; Thielemann et al. 1986), shall

[g)] In astrophysics: elements heavier than He, the heaviest element abundantly produced in primordial nucleosynthesis.

be briefly described in the following. With respect to the nomenclature we remark that, for example, *O burning* or *Si burning* may happen within an initial C/O mixture, if only (over a sufficiently long period of time) the conditions are extreme enough.

NSE + normal freeze-out: For $\rho_{\rm peak} \gtrsim 2 \times 10^8$ g cm^{-3} **and** $T_{\rm peak} \gtrsim 5 \times 10^9$ K, *nuclear statistical equilibrium* (NSE) is reached, i.e. a rate equilibrium in which detailed balance between every production rate (of some nucleus) and the respective destruction (photodissociation) rate holds. The equilibrium composition (in SNe Ia) is dominated by Fe-group nuclei. At large densities, electron captures decrease the electron fraction, which leads to the production of neutron-rich isotopes such as ^{56}Fe, ^{54}Fe and ^{58}Ni at the expense of ^{56}Ni. As temperatures and densities decrease with time, a *freeze-out* occurs, i.e. some forth-/back-reactions quickly cease to be balanced. The resulting composition depends on which reactions stop first. For large enough densities (normal freeze-out), the α-particles crucial for building up heavier nuclei are used up when temperatures are too low to produce new α's by photodissociation. This overproportionately affects the *triple-alpha process* ("$3\alpha \rightarrow {}^{12}$C"), so that a low ^{12}C abundance results. In addition, nuclei with relatively low masses (^{16}O, ^{20}Ne, ...) will be overproduced, as they cannot be converted into heavier nuclei.

NSE + α*-rich freeze-out*: For lower densities, but the same $T_{\rm peak} \gtrsim 5 \times 10^9$ K, the conditions in NSE are different. ^{56}Ni is the dominant element produced; nuclei with a neutron excess are less favoured. If the WD was, however, born in a high-metallicity environment, it usually contains a relatively large amount of ^{22}Ne, which provides neutrons so that some neutron-rich nuclei result. In any case, α-particles remain highly abundant during freeze-out: the triple-α-process occurs at a larger than normal rate (but, of course, not fast enough to use up the α-particles). Inversely to normal freeze-out, ^{12}C and heavy nuclei are overabundant compared to a NSE composition.

Incomplete Si burning: If $T_{\rm peak}$ remains lower than $\sim 5 \times 10^9$ K, but exceeds $\sim 4.5 \times 10^9$ K, two quasi-equilibrium clusters of heavier nuclei form with $28 \lesssim A \lesssim 45$ and $A \gtrsim 46$. Equilibrium **between** these clusters is not reached due to a rate bottleneck. The result of this nucleosynthesis are roughly equal amounts of IME and Fe-group elements; the Fe-group abundance decreases with decreasing $T_{\rm peak}$. The composition of the Fe-group elements in this zone is extremely dependent on the metallicity; ^{54}Fe can be more abundant than ^{56}Ni in the solar metallicity case (Iwamoto et al. 1999).

Explosive O burning: For 3.5×10^9 K $\lesssim T_{\rm peak} \lesssim 4.5 \times 10^9$ K, quasi-equilibrium is reached in the $28 \lesssim A \lesssim 45$ cluster. Mostly typical IME (Si, S) are produced.

Explosive Ne & C burning: At still lower temperatures, lighter and lighter are produced. First, burning stops with an O/Mg mixture, and for the lowest temperatures ($T_{\rm peak} \sim 2 \times 10^9$ K) with Ne and Mg. In any case, if one assumes a ∼1:1 C/O ratio to begin with, O will however be the most abundant product by far.

In Fig. 1.8, we show nucleosynthesis results for the radially symmetric "fast deflagration" SN Ia model *W7* (Nomoto et al. 1984; Iwamoto et al. 1999), and for its zero-metallicity modification W70 (lacking ^{22}Ne prior to burning). The models have a parametrised, partly unphysical prescription for flame propagation, chosen such that the resulting structure is in excellent agreement with observational constraints. Therefore, W7 and W70 certainly must be taken with a grain of salt. Yet, they are somewhat representative of observed SNe Ia and hence have become *de-facto standard* models for studies involving these SNe.

1.3 Theory of Type Ib, Ic and II SNe (core-collapse SNe)

Type Ib/Ic/II SNe are a very diverse group of objects, even if one only considers one of the subtypes (e.g. Elmhamdi et al. 2006 vs. Mazzali et al. 2008; Iwamoto et al. 1998; Pastorello et al. 2004). All these objects can probably be explained by models of stellar collapse and subsequent explosion, which happens when the degenerate Fe (or O/Ne/Mg) core of a massive star grows close to its Chandrasekhar mass [$\sim 1.44 M_\odot$ for an iron core; fast rotation is usually not expected, Janka et al. (2007)]. The observable features of the explosion are strongly influenced by the structure of the progenitor star and also by the type of compact remnant left behind (neutron star or black hole, rotating or not).

The reversal of the collapse to an explosion is not a trivial process. As the core is compressed and converted to a compact object, nuclear densities are reached. At this point, further compression is practically impossible, and an outwards-running shock

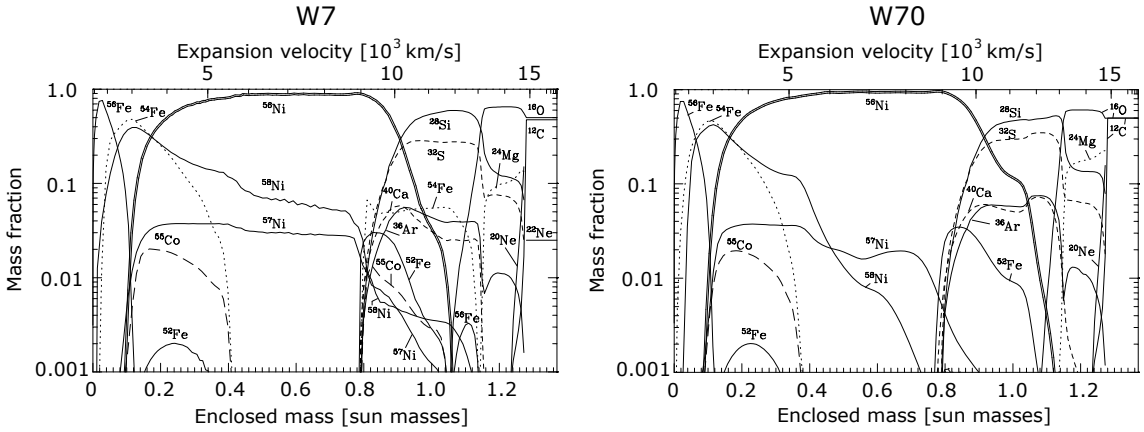

Figure 1.8: Nucleosynthesis in the W7 standard 1-D explosion model for SNe Ia, and in its zero-metallicity variant W70 (plot from Iwamoto et al. 1999).

wave forms (*core bounce* phase). Per se, this shock wave is, however, not strong enough to promptly unbind the outer layers; eventually it stalls and matter continues to fall inwards. Additional mechanisms heating the matter behind the shock have then to be invoked to explode the star. Implementing all important effects in simulations is extremely difficult and computationally expensive. As a result, simulations of core-collapse SNe constructed to be realistic have become infamous for often not even succeeding to explode. This situation is improving now at last (Kitaura et al. 2006; Burrows et al. 2007; Marek & Janka 2009; Bruenn et al. 2009). Yet, the mere fact that the models now explode does not mean that they predict realistic kinetic energies of the ejecta. Therefore, studies which aim at explaining observed objects mostly reach this aim with strongly simplified, parametrised explosion models.

Below, we give – as in the thermonuclear case – an introduction to the observational constraints and explosion models for core-collapse SNe. Because of the extremely large diversity of these SNe, the discussion will however not be as deep as for SNe Ia, and focus on some aspects which are already well established.

1.3.1 Observational constraints

1.3.1.1 Masses of the progenitor, of the ejecta and of ^{56}Ni; abundances; explosion energies

Photometric data and of spectra of core-collapse SNe have been analysed with different radiation hydrodynamics and radiative transfer codes, depending on the SN type and epoch (e.g. Utrobin 1997; Dessart & Hillier 2005; Mazzali et al. 2008; Tsvetkov et al. 2009; Maurer & Mazzali 2010).

^{56}Ni masses, ejecta masses and kinetic energies can often be inferred from these models with reasonable accuracy, and interestingly enough, core-collapse SNe seem to prefer characteristic values for these quantities. Nomoto et al. (2006, 2009) and Smartt (2009) have studied the relations of the kinetic energy and the ^{56}Ni mass to the ZAMS progenitor mass, respectively. In both their $M_{\text{Ni-56}} - M_{\text{ZAMS}}$ and their $M_{\text{Ni-56}} - M_{\text{ZAMS}}$ diagrams (Fig. 1.9), the objects cluster somewhat in three locations. We summarise the characteristic properties of objects in the three clusters in the following. One should keep in mind here that a calculation of ZAMS masses as performed by Nomoto et al. (2009) involves detailed modelling of the explosions and/or the progenitors. Only ejecta masses can "directly" be inferred from observations using radiative transfer models.

Low ZAMS mass cloud: These SNe, coming from stars with a ZAMS mass of $\lesssim 10$ $M_\odot$, have kinetic energies of $\sim 10^{51}$ erg and Ni masses of $< 0.1 M_\odot$. The ejecta masses are roughly $1-18 M_\odot$ (Zampieri 2005; Iwamoto et al. 1994). SNe II-P are most massive; SNe II-L and II-b prefer ejecta masses lower than $8\,M_\odot$(down to $M_{\text{ej}} \sim 2 M_\odot$, Taubenberger et al. 2011b). SNe Ib/Ic (in the low ZAMS mass cloud) have still lower masses due to the envelope stripping [$1-7 M_\odot$, Iwamoto et al. (1994); Mazzali et al. (2008)].

Hypernova (HN) branch: Hypernovae, as defined here, have a kinetic energy of $\sim 1 - 5 \times 10^{52}$ erg. Due to high expansion velocities, they show broad spectral lines, and are thus called *broad-lined* SNe by

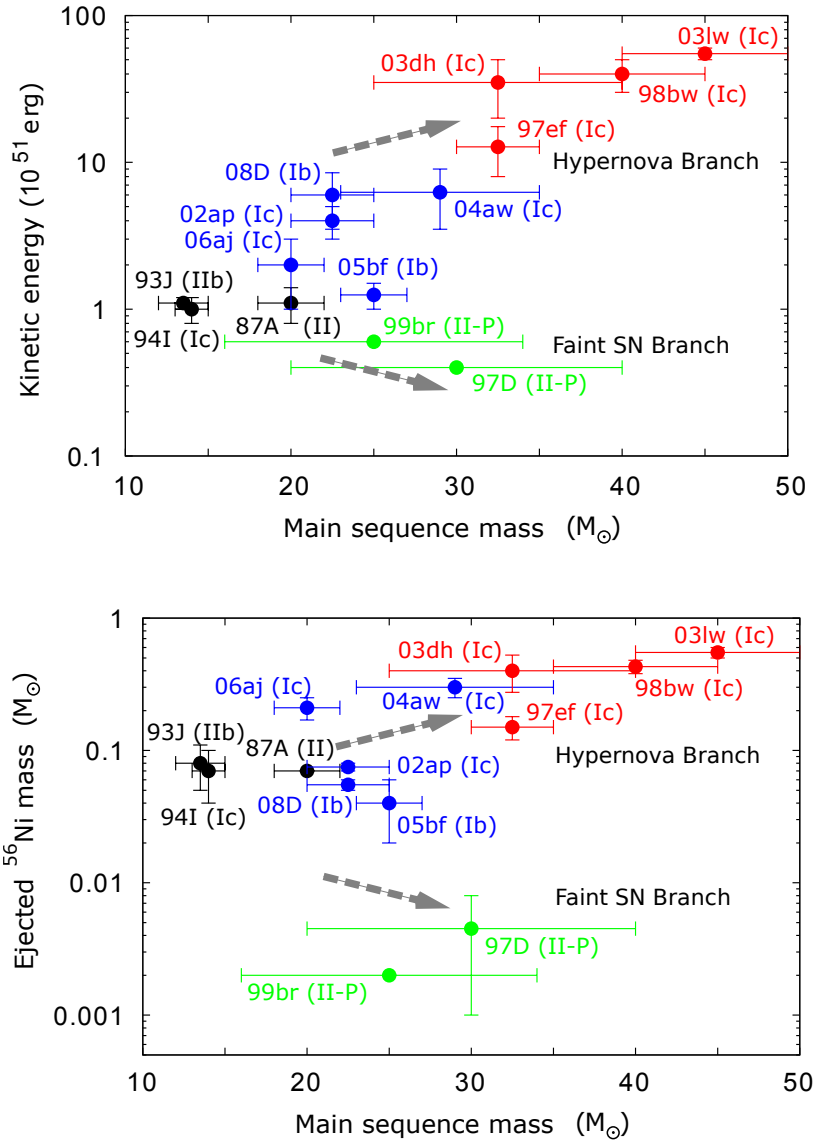

Figure 1.9: Core-collapse SNe: ejected ^{56}Ni mass (upper panel) and kinetic energy of the ejecta (lower panel) plotted against the ZAMS mass of the progenitor (calculated on the basis of models). Adapted from Nomoto et al. (2006, 2009).

other authors. HNe eject a relatively large average ^{56}Ni mass. Typical ejecta masses are $> 7M_{\odot}$ (Tanaka et al. 2009).

Faint SN branch: "Faint SNe" supposedly come from massive stars, in which a black hole is formed during explosion and which experience significant fallback onto this compact remnant. The ejecta masses are often even larger than for objects on the HN branch (Pastorello et al. 2004), but most of the ^{56}Ni produced has been swallowed by the black hole and therefore cannot contribute to the luminosity.

The difference between ZAMS-progenitor and ejecta mass for a core-collapse SN is a sum of two components. One component is the loss due to stellar winds produced in the late phases of stellar evolution. With increasing metallicity, winds play a stronger and stronger role due to *line driving* (Vink 2011). The other component is the mass of the compact remnant. **For a neutron star** this is between the Chandrasekhar mass limit of the progenitor's core, i.e. $\sim 1.44M_{\odot}$, and the maximum mass of neutron stars (theoretically $\lesssim 3.0M_{\odot}$, Bombaci 1996 – cf. observations, e.g. Lattimer & Prakash 2010; first calculations by Tolman 1939 and Oppenheimer & Volkoff 1939 resulted in a limit of $0.7M_{\odot}$). **If** the remnant has a larger mass, it will be a black hole, and a large part of the ejecta may be lost by fallback.

1.3.1.2 Asphericity and polarisation

Leonard & Filippenko (2005) and Leonard et al. (2006) have measured polarisation in different core-collapse SNe. They found that SNe with a large H envelope (SNe II-P) show little polarisation in the first place. As soon as the plateau phase ends, and the core is exposed, however, the polarisation can increase dramatically (Leonard et al. 2006). Type Ib and Ic SNe, with lack a H envelope, tend to be significantly polarised from early phases on (Leonard & Filippenko 2005). This indicates that most core-collapse SNe have somewhat asymmetric cores, sometimes obscured by a relatively symmetric envelope.

1.3.1.3 Observations of progenitor stars, companion stars and compact remnants

For core-collapse SNe, there have been various successful identifications of progenitors and companions. Only for the relatively rare Type Ib/Ic SNe and very rare Type II-L SNe there have not been any detections as yet. Smartt (2009) mention the following results:

SN 1987A: The progenitor of this famous, peculiar SN II has been identified as the star "Sanduleak -69° 202a" (Walborn et al. 1989; Trundle et al. 2007) of spectral/luminosity class B3 I (blue supergiant) in pre-explosion observations. Binarity may be a key ingredient in the evolution of this star as single-star evolution models have problems reproducing its properties (Smartt 2009 and references therein).

SNe IIb: For SN 1993J, the "prototype" SN IIb, extensive information on the progenitor system could be obtained. Besides the stripped K-type supergiant progenitor ($\sim 4-5M_{\odot}$) detected in pre-explosion images, observers also

found hints of a binary companion (a B-type supergiant) at the explosion site (Maund et al. 2004; Smartt 2009). The observed properties of the system can be reproduced with binary evolution models, starting from two stars with ZAMS masses of $\sim$ 14 and $15 M_{\odot}$ (Podsiadlowski et al. 1992; Maund et al. 2004). Another direct progenitor detection from pre-explosion observations was reported for SN 2008ax (Crockett et al. 2008). The images in this case are compatible with a single Wolf-Rayet star as progenitor, or with a binary system if neighbouring stellar systems contribute to the observed light.

SNe II-P: SN II-P explosions are very frequent. Therefore, at least 3 SN II-P progenitors have been detected with high significance. In all unambiguous cases, these progenitors were identified as red supergiants, consistent with the notion that SN II-P light curves require an extended envelope.

More and more compact remnants of core-collapse SNe (in most cases of detection *pulsars* – rotating neutron stars emitting radio pulses) are detected and observed in detail. Chevalier (2005, 2010) and Lattimer & Prakash (2010) have given a comprehensive overviews over the observations and their interpretation, with the Crab (Staelin & Reifenstein 1968) and Vela (Large et al. 1968) pulsars being two classical examples. Detections together with extended remnant structures confirm that Type II SNe leave neutron stars behind – a suggestion already made by Baade & Zwicky (1934b). For at least one SN remnant with a compact object detected, it is suspected that the SN was of Type Ib/Ic. Relatively recently, there have also been claims that a stellar-mass black hole may have been been found in a SNR (Patnaude et al. 2009).

1.3.1.4 SNe Ib/Ic, X-ray flashes and gamma-ray bursts

Type Ib/Ic Hypernovae are known to sometimes be accompanied by X-ray flashes or gamma-ray bursts (of the *long/soft* type) in the earliest phases after explosion (Galama et al. 1998; Woosley & Bloom 2006; Mazzali et al. 2008; Soderberg et al. 2008; Gehrels et al. 2009). While an interpretation of X-ray flashes has been controversial, at least a significant fraction of the long gamma-ray bursts are believed to result from relativistic jets being emitted during core-collapse events. Some of these events may not be visible as a SN, if a black hole is formed and swallows most of the ^{56}Ni produced. In a "long" gamma-ray burst, $\sim 10^{51}$ergs of radiation are sent out in a short time (within $\sim$35 s in the observer's frame on average, MacFayden 2004). According to standard suggestions, this outburst must be explained by the structure of the jet flow. The radiation sent out by a jet depends on internal shocks, the density of electromagnetic fields and electrons/positrons, the interaction of the jet with an external medium, and other features; all this is still a matter of active research (e.g. Gehrels et al. 2009).

In any case, it is believed that a prerequisite for a SN to produce a jet, and thus a gamma-ray burst, is extensive stripping of the progenitor's envelope prior to explosion. Otherwise a jet-like flow in the core of the exploding star may just help to accelerate the ejecta (Heger et al. 2003, e.g.).

1.3.1.5 Host galaxies

The host galaxies of core-collapse SNe – as compared to those of Type Ia supernovae – must have been forming stars relatively recently before the explosion: massive stars, which produce these SNe, have a short live. Hence, core-collapse SNe are mostly found in spiral galaxies (Li et al. 2011b).

Comparisons have been performed between the distribution of core-collapse SNe, sorted by type, and e.g. the distribution of long gamma-ray bursts within galaxies or among different galaxy types (Fruchter et al. 2006; Kelly et al. 2008). One main result is that the distribution of core-collapse SNe in general does not agree with that of long gamma-ray bursts, but reasonable agreement is found if only type Ic SNe are considered. This seems to confirm that long gamma-ray bursts and Type Ic Hypernovae are phenomena linked to each other.

1.3.2 Progenitor star models

We briefly recap the typical evolution of massive stars, as it has immediate consequences for the structure of core-collapse SNe.

The behaviour of a star at the end of its life – in terms of the last stages of burning, and in terms of its death – depends critically on its mass. Low mass stars ($M_{\mathrm{ZAMS}} < 8M_{\odot}$) are thought to end up as He, C/O or O/Ne/Mg white dwarfs, usually after having ejected their outer layers in the late evolutionary stages. They are not able to ignite the burning to heavier elements (for which larger Coulomb barriers must be overcome). For core-collapse to occur, a star must at least have developed a O/Ne/Mg core (Kitaura et al. 2006) and thus have had a ZAMS mass of $\sim 8-10M_{\odot}$ (Kippenhahn & Weigert 1994). Most of the observed core-collapse SNe are probably made by heavier stars, which develop a degenerate Fe core. However, too heavy stars[h)] are thought to directly collapse to black holes without a SN explosion, unless they lose enough mass by stellar winds or they rotate fast. The limit above which this direct collapse will happen has been estimated as $M_{\mathrm{ZAMS}} \sim 40M_{\odot}$ for zero metallicity and rotation (Heger et al. 2003). At solar metallicity, stars with any ZAMS mass may in fact have large enough wind losses to make a SN (Heger et al. 2003). Fast-rotating progenitors are possibly responsible for the existence of Hypernovae.

Stars initially consist of H, with a primordial abundance of He ($\sim 25\%$ by mass) and other elements up to Li. H is burned, and the ash (i.e. He) accumulates especially in the centre. In order to ignite the He core, high temperatures are needed. These are reached as the star contracts for a short time when it has burned a significant part of its H. Subsequent burning stages are always ignited in the centre, while H burning continues in the outermost layers even late in a star's evolution, unless these layers have been lost due to stellar winds. In any case, one can think of an evolved star having an *onion-shell* structure, in which one finds heavier and heavier nuclei going from the outer into the inner layers. During the explosion of such a star, significant parts of the stellar abundance structure are preserved despite the nucleosynthesis processes which take place (see Sec. 1.3.3.5).

Traditional stellar evolution models calculate the star in 1 D and employ parametrised prescriptions to describe the mixing of material (Kippenhahn & Weigert

[h)] Stars with $M_{\mathrm{ZAMS}} > 100M_{\odot}$ may make pair-instability SNe (e.g. Fryer et al. 2001) and are not discussed here.

1994). In these models, a clear separation of different elements is found (despite all mixing processes). Subsequent shells contain H, He, C, Ne, O, Si and Fe (as far as the star can synthesise these elements). Recently, first 2-D calculations of late stages of stellar evolution have been attempted (Arnett & Meakin 2011). The authors find that violent bursts of nuclear burning induce significant mixing between different (Si, O, Ne) layers. It may be that parts of the onion picture have to be revised in the future.

Part of the progenitors of core-collapse SNe are believed to result from binary evolution. In particular, some of the *stripped-envelope* core-collapse SNe (i.e. SNe of the Types Ic, Ib and IIb) are probably due to stars in binaries (cf. Sec. 1.3.1.3). Binary evolution may explain why some of these SNe (e.g. SN 1994I, see Chapter 4) have no H/He envelope, even when their progenitor mass is low, implying weak stellar winds. Therefore, not only single-star evolution, but also binary evolution (e.g. Podsiadlowski et al. 1992; Maund et al. 2004; Yoon et al. 2010) is relevant for explaining the nature of core-collapse SNe.

All progenitor models on the market probably still need refinement in order to make better predictions on the mass stripping and the internal structure of the progenitor stars. In order to make progress here, key features of the progenitor models need to be compared against SN observations; we will contribute to this with our work on the He layers of stripped-envelope SNe (Chapter 4).

1.3.3 Explosion models and nucleosynthesis

Before explaining explosion models, we give a step-by-step description below on how a core-collapse explosion proceeds, and briefly digress on observable features of the earliest explosion phases (neutrinos and gravitational wave emission). Then we discuss detailed simulations as well as parametrised ones which we use to analyse observations. Finally, we give a summary on nucleosynthesis in core-collapse SNe.

1.3.3.1 Stages of core collapse

In a simplified picture, the process of core collapse and explosion of a star can be divided into four characteristic stages. We follow the discussion of Janka et al. (2007) here.

Collapse

The Fe or O/Ne/Mg core of a star can be stabilised by the electron degeneracy pressure only up to its Chandrasekhar mass ($\sim 1.44 M_\odot$ for a Fe core). Before this limit is reached, however, the high Fermi energy of the electron gas already suffices for electron capture reactions to set in on Fe-peak nuclei (or on ^{20}Ne and ^{24}Mg for O/Ne/Mg cores). This decreases the electron fraction and thus the degeneracy pressure, initiating the collapse. For the collapse of Fe cores, also other reactions such as photodisintegration of Fe-group nuclei play a major role.

In any case, electron captures and β-decays lead to a *neutronisation* of the core in the course of the collapse. The lepton number is conserved through the generation of neutrinos while electrons vanish. As soon as densities of $\sim 10^{12}$ g cm^{-3} are reached, these neutrinos are trapped due to scattering on nuclei. The core now has a mass of $\sim 1 M_\odot$, but a radius of only 100 km.

Bounce and shock formation

The collapse stops at nuclear densities ($\sim 10^{14}$ g cm^{-3}), when the *equation of state stiffens* (i.e. the material gets less compressible). The sudden deceleration of the infalling material leads to the generation of a shock wave (for a review on the properties of shocks in SNe, see Weaver 1976). While the shock travels to larger radii, infalling matter is decelerated (i.e. accelerated outwards), and nuclei are partially photodissociated. The free protons generated by photodissociation can efficiently capture electrons, further neutronising the star and generating neutrinos. As soon as the shock wave is near the *neutrinosphere* (i.e. the radius where the optical depth to neutrinos, as seen from outside, is ~ 1), a burst of ν_e leaves the star.

Stalled shock

The photodissociation of nuclei by the shock consumes energy. Thus, around 0.2 s after the onset of core collapse, the shock stalls at a radius of some hundreds of kilometres. It turns into an *accretion shock*, which decelerates the infalling matter but does not reverse its movement into an outwards direction.

Explosion

Meanwhile, neutrinos and antineutrinos of all flavours are generated in the core, carrying the energy deposited by the infalling matter. This leads to a steady outwards neutrino flux from the neutrinosphere, which is below (i.e. closer to the centre than) the shock. Due to the large neutrino flux, a *gain layer* behind the shock forms, where the gas is effectively heated by deposited neutrino energy. Due to this energy, which in effect comes from the infall of material in the gravitational field, the shock wave may eventually be revived to travel outwards and explode the star (*neutrino mechanism*). If this does not happen, the shock revival may take place later due to heating by sound waves, which the nascent neutron star may emit while matter falls onto it [*acoustic mechanism*, Burrows et al. (2006, 2007)].

1.3.3.2 Neutrino and gravitational wave emission in the earliest explosion phases

With the prompt neutrino burst (and also the later emission), core-collapse SNe are very interesting neutrino sources (e.g. Raffelt 2010). SN 1987A (e.g. Immler et al. 2007) in the Large Magellanic Cloud (a satellite of the Milky Way) has become famous as the first SN for which neutrinos were actually detected by the Kamiokande II (Japan), IMB (US) and Baksan (USSR) detectors (for a review see Raffelt 1996). SNe far away from our galaxy are, unfortunately, much harder to observe in neutrinos, but the detection thresholds decrease with every detector generation.

Furthermore, core-collapse SNe are prominent targets for gravitational wave astronomy. During the formation of the compact remnant object, a strong signal is thought to be emitted (Thorne 1980; Scheidegger et al. 2010). Current-sensitivity or better detectors are already able to measure gravitational waves from a galactic core-collapse SN (Sathyaprakash & Schutz 2009), as it happens every few centuries.

1.3.3.3 Detailed numerical models

A full discussion of current explosion models is impossible here as these simulations have become extremely complicated (e.g. Janka et al. 2007). Some interesting features of old and current model calculations shall, however, be mentioned.

One of the first hydrodynamic model calculations for core-collapse SNe was set up by Imshenik & Nadëzhin (1965). Initially, the core bounce and shock formation was thought to trigger a prompt explosion of the star, due to the shock running outwards. However, detailed simulations showed that the shock dissociates nuclei, which leads to the loss of kinetic energy. Today, almost all simulations agree that the prompt explosion mechanism fails. Note that this conclusion not only depends on the simulation accuracy and the microphysical details included (nuclear reaction rates...), but also on the equation of state assumed – especially for the degenerate Fe core and the nascent neutron star.

Neutrino-driven explosion mechanism

Already Colgate & White (1966) concluded that neutrinos may play a significant role for core-collapse SNe and that neutrino-transport calculations must be coupled with hydrodynamic codes in order to obtain adequate explosion simulations. When it became clear that prompt explosions fail (cf. Wilson et al. 1985), the neutrino-driven mechanism became the favoured explosion scenario for core-collapse SNe. Neutrinos are supposed to deposit their energy preferentially a bit above the neutrinosphere. This leads to a convective zone behind the shock, where the material is heated, until explosion occurs.

Although simulations including neutrino transport are getting more and more sophisticated (e.g. non-grey transport is implemented), the deposition by neutrinos is often insufficient to trigger explosions. Only recent simulations in 2 D [and possibly future simulations in 3 D (Nordhaus et al. 2010)] are able to explode the star. One important point found in 2-D studies is that the global shape of the stalling shock is unstable to oscillations [standing accretion shock instability, Blondin et al. (2003)], which leads to a significant deformation of the shock front. This not only generates a huge asymmetry, but also helps the explosion as it increases the mean shock radius and the width of the layer (behind the shock) where energy from neutrinos is absorbed.

Alternative explosion scenarios

In the acoustic explosions proposed by Burrows et al. (2007), the shock is revived by sound waves depositing energy. Such waves can be sent out by the nascent neutron star if its g-modes are excited by the infall of material. The acoustic mechanism becomes relevant with a large delay ($\sim$ 1 s after bounce), and thus is only works if the neutrino mechanism fails.

Furthermore, magnetic fields have been invoked in various different ways in order to explain core-collapse explosions and their features. The majority of SN explosions has probably too weakly-rotating progenitors for the fields to be relevant for the explosion (Janka et al. 2007); however there are probably some SNe in which rotation is crucial such as Hypernovae. Magnetic forces and rotation may either generate to a completely different flow pattern, such as in a *jet SN* (Wheeler et al. 2002; Yamada & Sawai 2004), or lead to viscous heating behind the shock (Thompson et al. 2005). They may also contribute to the pressure, influence the development of fluid instabilities in the core region, and alter the weak interactions in the core (Mezzacappa 2005).

1.3.3.4 Parametrised explosion models

Due to the mixed success of self-consistent simulations of core-collapse explosions, "parametrised" explosion models are used for studies of nucleosynthesis (Arcones & Janka 2011) or of radiative transfer (Woosley et al. 1994). In some of the models, neutrino luminosities are artificially enhanced so as to generate explosions. In other models, the explosion is triggered directly by energy input at the inner boundary of the hydrodynamic simulation (*thermal bomb* method, e.g. Iwamoto et al. 1994), or by setting up a piston at the inner boundary which retracts and then abruptly moves forward, generating a shock wave (e.g. Woosley & Weaver 1995).

In this way, explosion models have been constructed mostly in 1 D to fit all kinds of observed core-collapse SNe (Ensman & Woosley 1988; Nomoto et al. 1993; Iwamoto et al. 1994; Woosley et al. 1994, 1995; Iwamoto et al. 1998; Kasen & Woosley 2009). We will also use such models in our studies here. However, one must be careful in order not to overinterpret model-dependent features. Simulations with neutrino heating, for example, can produce density distributions with details different from those obtained using piston simulations for the same progenitor star (M. Ugliano, private comm.).

1.3.3.5 Nucleosynthesis and late-time structure

The ejecta composition of core-collapse SNe is determined by the progenitor abundances, nuclear reprocessing during the explosion, and by the explosion dynamics which may lead to mixing. The reprocessing in core-collapse SNe tends to be less pervasive than in SNe Ia, preserving more of the progenitor material. Yet, nucleosynthesis in core-collapse objects is by no means uninteresting. Besides the "usual" burning with temperature- and density-dependent results as in the SN Ia case, characteritic nucleosynthesis processes – including processes which generate elements heavier than Fe – may happen in different zones. We first discuss the nucleosynthesis and then mention some recent efforts to calculate the final structure of core-collapse SNe envelopes in 3 D.

Nucleosynthesis

In the SN explosion, the outer layers (at least the H and He envelope) of the progenitor star are mostly ejected as they are (Hashimoto 1995). The abundances within the intermediate layers are changed by explosive nucleosynthesis, but the overall abundance zoning of the stellar progenitor (in mass space) can be preserved as long as limited mixing occurs. To visualize this, we have plotted an example SN Ib nucleosynthesis calculation and the respective abundance stratification of the progenitor star in Figure 1.10. Only in the inner layers, a complete reprocessing of nuclei occurs. The innermost core of the SN is heated and the nuclei are photo-dissociated already before the shock stalls. Neutrino and antineutrino irradiation can induce distinct processes here. Some of the material in the inner zones, including some of the ^{56}Ni generated, will however experience fall-back and will never be observable.

We now summarize what happens in different parts of the SN (Woosley & Hoffman 1992, Woosley & Weaver 1995, Janka et al. 2007 and references below):

Early hot bubble material: When the shock stalls, a hot convective zone forms behind it. This zone consists of free nucleons; in the outer part,

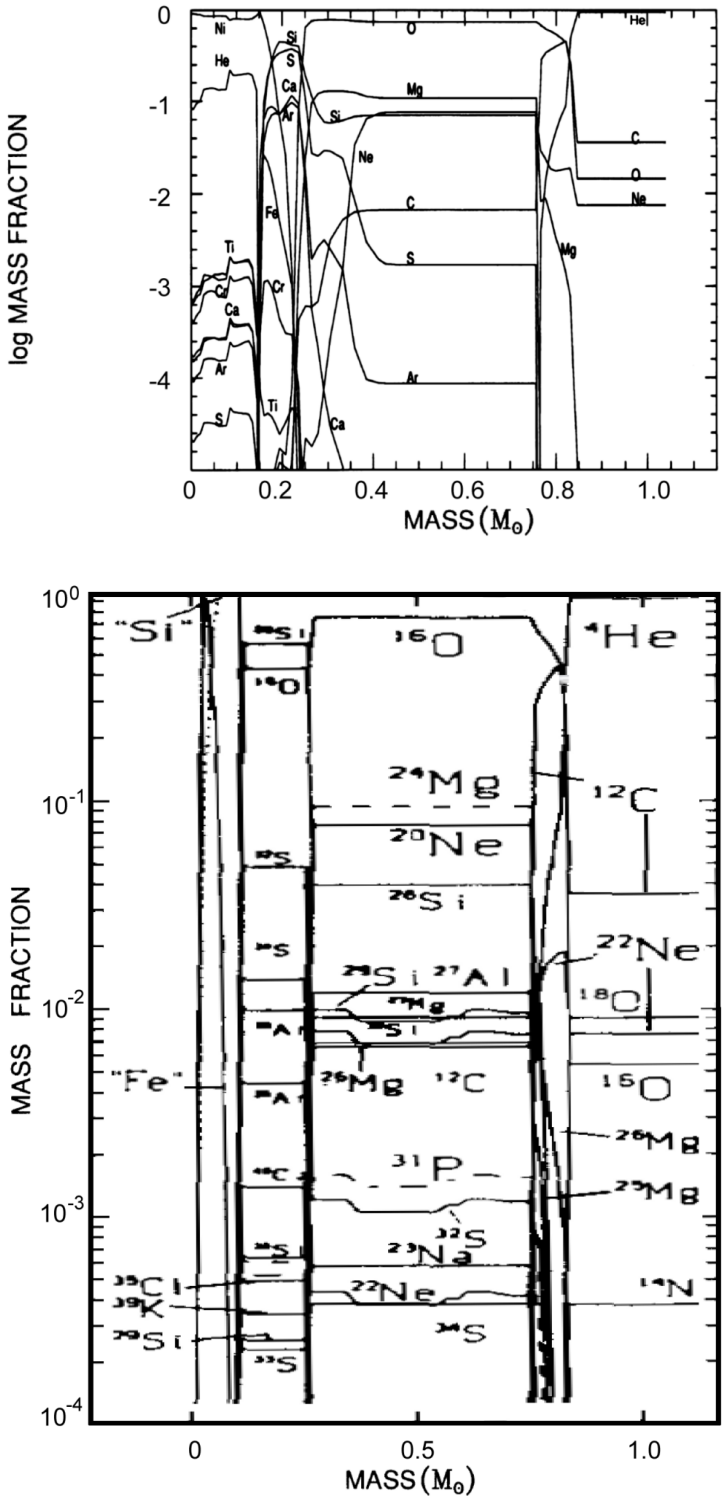

Figure 1.10: Abundances in the ejecta of a SN Ib model (upper panel) and abundances in the respective progenitor star (lower panel) vs. enclosed mass – shown are the inner $\sim 1.0 M_{\odot}$ of the ejecta; the remnant ($\sim 1.3 M_{\odot}$) is cut out in both plots (**also in the axis scale**). Note the strong correspondence between the progenitor's abundance zones and the final abundance zones. From Shigeyama et al. (1990) and Nomoto & Mashimoto (1988), adapted – reader, please excuse the bad reproduction quality.

nucleons recombine into α-particles, first building up light atoms like C. Depending on the conditions (neutron/proton excess, etc.), nuclei up to the Fe group can be built up.

Early ν-driven wind: Somewhat later, material is accelerated which comes from zones closer to the nascent neutron star and is driven out by neutrinos. This material is strongly irradiated by neutrinos and has a large entropy. As a result of the luminosity and mean energy ratios of neutrinos vs. antineutrinos, the material is proton-rich when it assembles into nuclei. In this situation, antineutrinos play a strong role in generating neutrons out of protons, enabling the build-up of heavier nuclei (νp-process). The proton and neutron flux can be large enough to build up relatively heavy nuclei like ^{64}Zn.

α-process, r-process: The late neutrino-driven wind can exhibit a neutron excess (again depending on the conditions of neutrino irradiation). The material affected is initially in NSE at very large temperatures ($T \gtrsim 7 \times 10^9$ K), where the NSE composition is dominated by α particles. Afterwards, an alpha-rich freeze-out occurs in neutron-rich conditions. The resulting nucleosynthesis process is called *α-process*. The nuclei produced by the α-process, can – in the case of large enough neutron excess – be well beyond the iron group. Later, depending on the neutron flux, the nuclei yielded may act as a seed for the r-process, in which massive nuclei can be produced.

γ-process: Under certain conditions ($T \sim 2...3 \times 10^9$ K, expansion timescale $\sim$1 s), a strong gamma-ray field can induce photodisintegration processes stopping at so-called p-nuclei (γ-process). The origin of these proton-rich isotopes has been unclear for quite a long time; other processes such as the p-process (cf. Woosley & Howard 1978) are probably unable to explain the respective cosmic abundances. The γ-process can occur, for example, in the O/Ne layers of Type II-P SNe (Woosley & Howard 1978; Howard et al. 1991).

General explosive burning: As the shock is revived and runs through the ejecta, the material is burned in different regimes, depending on the peak temperatures and densities attained (cf. SN Ia case, Sec. 1.2.3.5). Burning to NSE (usually with an α-rich freeze out and/or an α-process) takes place in the innermost layers. Incomplete Si burning, and explosive Ne and C burning commence in the layers further out. The burning efficiency decreases towards the outer layers, so that the H/He envelope and – depending on the conditions – also deeper (C, Ne) layers of the original star are mostly preserved as they are (Hashimoto 1995). Details, such as the ratio of IME synthesised in the star vs. in the explosion, depend heavily on the explosion dynamics (Woosley & Weaver 1995).

Hydrodynamics and late-time structure

In order to obtain accurate predictions for the "late-time" structure, which can be tested against observations, one needs to evolve hydrodynamic models out to homologous expansion. Due to computational limitations, only a few such simulations have been performed; these show that also late-time mixing within the ejecta due to hydrodynamic instabilities is important and has to be simulated in 3 D (Hammer et al. 2010). When synthetic spectra are to be be predicted from explosion models [such as in the SN Ia case, e.g. Kromer & Sim (2009)], these and similar simulations will play a larger and larger role. The mixing of the outer stellar layers with ^{56}Ni and other elements in the explosion has important effects for the formation of spectra and light curves in the photospheric phase (cf. Chapter 4).

1.4 SN ejecta after explosion – force-free, homologous expansion

A few days after explosion, i.e. at the epochs treated in this work, the ejecta have expanded a lot, with typical mean expansion velocities being around 10000 km s^{-1}. The velocity change of a fluid element due to interactions with other fluid elements becomes negligible soon [$\sim$ 10 s after explosion for SNe Ia, e.g. Röpke & Hillebrandt (2005)]. The SN is in a state of free expansion and each fluid element moves (almost) radially with respect to the centre-of-mass of the ejecta, with

$$r \approx v \times t. \tag{1.6}$$

Here, v is the radial velocity at the onset of force-free expansion, r the radius to which the fluid element has propagated, and t is the time from explosion onset. This simple law, constituting a special case of *homologous expansion*, is a good approximation for $v \times t$ sufficiently large such that $|\vec{r}_0| \ll r$ (where $|\vec{r}_0|$ is the location at the time when forces become negligible). In fact, supernovae even at late epochs show some deviation from $r = v \times t$ because of ongoing acceleration of fluid elements by radiation. The velocity increase over time is, however, only a few per cent for the most-affected parts of the envelope (e.g. Blinnikov et al. 2006; Woosley et al. 2007), which are usually those with a high opacity **and** a large radiation flux. Therefore, the effect on our calculations is insignificant[i)], especially because the variations from one hydrodynamic model to another (for the same SN type) are relatively large.

Assuming a movement according to Equation (1.6), the velocity can be used as a convenient co-moving coordinate (*lagrangian* coordinate) instead of radius; the mass profile in velocity space $\frac{\mathrm{d}m}{\mathrm{d}v}(v)$ remains time-invariant. This profile can be transformed into the spherically-symmetric spatial density ρ (and vice versa) at any given time via:

$$\rho(r) = \frac{1}{4\pi r^2 t} \frac{\mathrm{d}m}{\mathrm{d}v}\bigg|_{v=r/t} = \frac{1}{4\pi v^2 t^3} \frac{\mathrm{d}m}{\mathrm{d}v} \,. \tag{1.7}$$

Some typical density profiles which are the outcome of hydrodynamic simulations are shown in Fig. 1.11. SN Ia and SN Ic profiles are usually relatively smooth.

[i)] In contrast, in Type II-P (and perhaps also II-L) SNe the strong radiation field stored after explosion can have a non-negligible effect on the hydrodynamics out to relatively late epochs.

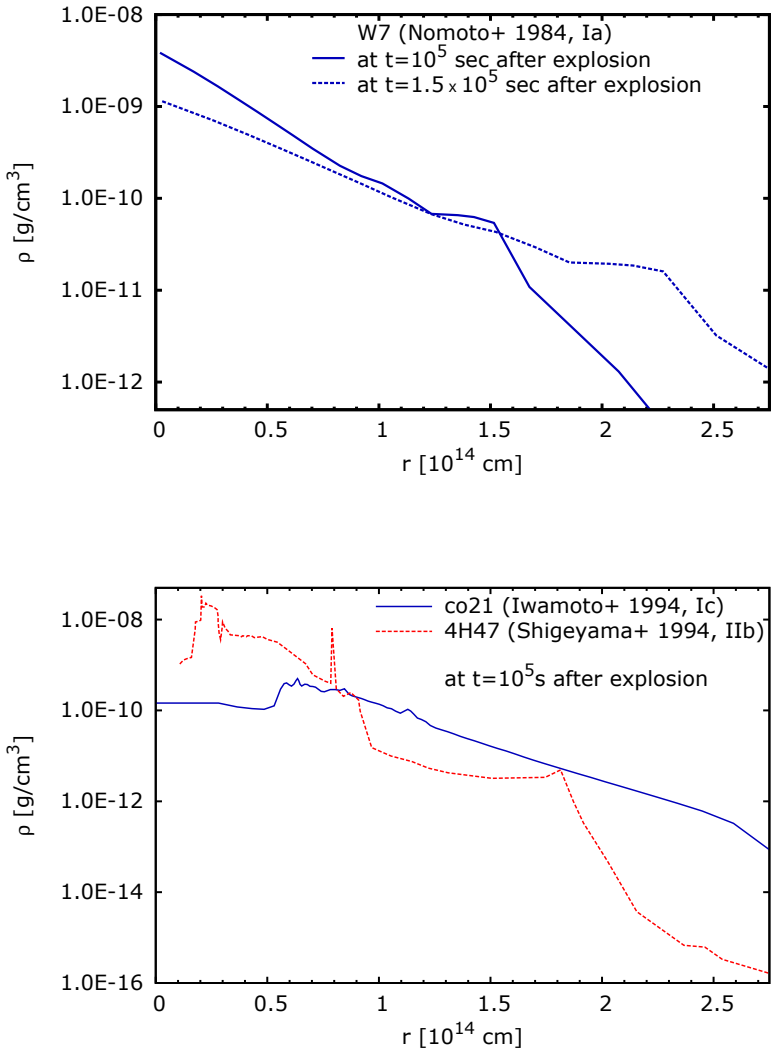

Figure 1.11: Density profiles of simulated SNe after entering the homologous expansion phase (radially symmetric models). The upper panel shows the W7 model of (Nomoto et al. 1984) at two different points of time. The lower panel shows density profiles of type Ic (Iwamoto et al. 1994) and IIb (Shigeyama et al. 1994) core-collapse explosions, with a fully stripped star (bare C /O core) and a somewhat stripped star (some H left, large He layer) as progenitors, respectively.

Type II/Ib profiles can be expected to show significant structure due to abrupt changes in the density gradient which progenitor stars with different composition zones exhibit. The changes in the star's density gradient lead to an acceleration or deceleration of the outwards-moving shock wave; this determines the final density profile (e.g. Matzner & McKee 1999).

Chapter 2

Analysing spectra with radiative transfer models

Astrophysical analyses are often triggered by puzzling observations, showing a light source of unknown nature. Theoretical models are then developed in order to explain what is observed. This involves a specification of the expected components (matter, photons, ...), state and evolution of the system, and a description of all important physical interaction processes.

Radiative transfer codes simulate the propagation of radiation through media and the respective interactions, and thus predict the radiation to be expected from theoretical models for an astrophysical object. If the predictions match the observations, the model is considered valid. Therefore, radiative transfer plays a key role for the validation of astrophysical models today. In some simulations, it is also crucial to couple hydrodynamics and radiative transfer (*radiation hydrodynamics*) in order to consistently model the effect of the radiation on the flow. This can, however, be neglected here (cf. Section 1.4).

In this chapter, we explain basic concepts of radiative transfer and their application in our group's radiative transfer code for SN atmospheres. We also describe the additions to the code programmed for the present thesis project. Finally, we discuss some general principles of our radiative transfer models (input data, important radiative transport effects).

2.1 Radiative transfer in SN atmospheres

Radiative transfer theory is concerned with the evolution of a radiation field in situations where global thermodynamic equilibrium breaks down. To begin with, we discuss quantities and equations which are used in common formulations of this theory. Our discussion crudely follows Mihalas (1978) and Hachinger (2007); only when we turn to more special aspects references to other work are given.

2.1.1 Radiative transfer: basic quantities and equations

2.1.1.1 Intensity and transfer equation

The most basic quantity in radiative transfer is the (specific) intensity I_ν, which contains the full information about the flow of radiation energy at arbitrary points in space. The

intensity is a function of frequency, space, direction and time. It is defined such that the amount of energy δE, which is transported through a surface $\delta\vec{A}$ into a solid angle element $\delta\omega$ in direction of the unit vector $\hat{n}$ is:

$$\delta E = I_\nu(\vec{r}, \hat{n}, \nu, t)\ \delta\vec{A} \cdot \hat{n}\ \delta\omega\ \delta\nu\ \delta t.$$

The angle between $\delta\vec{A}$ and $\hat{n}$ is commonly called θ and its cosine is called μ, i.e. $\delta\vec{A} \cdot \hat{n} =: \delta A \times \cos\vartheta =: \delta A \times \mu$. For many purposes one needs an angle average J_ν of the intensity:

$$J_\nu(\vec{r}, \nu, t) = (4\pi)^{-1} \int_{4\pi} d\omega\ I_\nu(\vec{r}, \omega, \nu, t). \tag{2.1}$$

The basic equation of radiative transfer (*transfer equation*, TEQ) describes the evolution of the photon field in space-time:

$$\frac{\partial}{\partial(ct)} I_\nu(r, \hat{n}, t) + \frac{\partial}{\partial s} I_\nu(r, \hat{n}, t) = \eta_\nu(r, \hat{n}, t) - \chi_\nu(r, \hat{n}, t) I_\nu(r, \hat{n}, t). \tag{2.2}$$

Here, $\frac{\partial}{\partial s}$ is the derivative along the photon path in the direction of $\hat{n}$ parametrised by pathlength s. The notation in terms of the quantities η and χ (*emissivity* and *opacity*) makes it simple to interpret the equation as a statement of energy conservation. These quantities are defined as follows:

- The emissivity $\eta_\nu(\vec{r}, \hat{n}, t)$ is the amount of radiation energy produced (by material, i.e. some medium, at $\vec{r}$) per volume element $\delta\vec{A} \cdot \delta\vec{s}$, unit time, frequency, and target plane angle and emitted through δA in the direction of $\hat{n} \parallel \delta\vec{s}$:

  $\delta E_{\text{em}} = \eta_\nu \delta\vec{A} \cdot \delta\vec{s}\ \delta\omega\ \delta\nu\ \delta t$

- The opacity $\chi_\nu(\vec{r}, \hat{n}, t)$ is the fraction of intensity absorbed from a ray per path element $|\delta\vec{s}|$ which the radiation propagates through a medium. $\delta\vec{s}$ is parallel to $\hat{n}$:

  $\delta E_{\text{abs}} = \chi_\nu I\ \delta\vec{A} \cdot \delta\vec{s}\ \delta\omega\ \delta\nu\ \delta t.$

The TEQ can also be regarded as a special case of the *Boltzmann equation* of kinetic theory, if one identifies the absorption and emission terms with the *collision integral* (e.g. Mihalas 1978). Therefore, it can mathematically be derived (under appropriate assumptions; e.g. Lifshitz & Pitaevskii 1984, Sections 1.3 and 1.16) from the *Liouville equation* which describes the evolution of a many-particle system in phase space.

A common compact notation of the TEQ which specifies the intensity change along a ray in the stationary case ($\frac{\partial}{\partial t} I_\nu = 0$) can be obtained using two quantities called *optical depth* (or *optical pathlength*)

$$\tau_\nu(s) := \int_s^\infty \chi_\nu\ \mathrm{d}\tilde{s} \tag{2.3}$$

and *source function*

$$S_\nu := \eta_\nu / \chi_\nu. \tag{2.4}$$

It reads:

$$\frac{\partial}{\partial \tau_\nu} I_\nu^{+,\text{ray}}(\tau_\nu) = -S_\nu(\tau_\nu) + I_\nu^{+,\text{ray}}(\tau_\nu). \tag{2.5}$$

Here, $I_\nu^{+,\text{ray}}$ is the intensity in the direction of photon propagation ($\theta = 0$), which carries photons of frequency ν. Note that τ_ν **decreases** in the direction of propagation.

The solution of the TEQ requires the "material-dependent functions" η_ν and χ_ν to be specified (or, equivalently, the optical depth τ_ν and source function S_ν). However, in most practical cases η_ν and χ_ν depend on the intensity I_ν itself. This can be due to the re-emission of absorbed intensity, which appears as a contribution to η_ν and/or due to the influence of the intensity on the ionisation and excitation state of the medium.

2.1.1.2 Formal solution

Before discussing absorption and emission processes in SNe (and expressions for the optical depth and source function), we introduce the "formal solution" of the TEQ along a ray (Eq. 2.5). This is the solution obtained if one assumes the source function to be known and specifies an appropriate initial value $I_\nu^{+,\text{ray}}(\tau_{0,\nu})$:

$$I_\nu^{+,\text{ray}} = I_\nu^{+,\text{ray}}(\tau_{0,\nu})\, e^{-(\tau_{0,\nu}-\tau_\nu)} + \int_{\tau_\nu}^{\tau_{0,\nu}} S_\nu(\tilde{\tau})\, e^{-(\tilde{\tau}-\tau_\nu)}\, \mathrm{d}\tilde{\tau}. \tag{2.6}$$

The first term represents the intensity emitted from $\tau_{0,\nu}$ towards τ_ν, which is attenuated depending on the optical depth difference between the boundary and the point considered (note again that τ_ν decreases along the propagation direction for which the intensity is calculated). In the second term, all radiation emitted by matter along the ray is "summed up", multiplied by the appropriate attenuation.

2.1.2 Opacity and emissivity in SNe

Absorption and emission processes couple the radiation field to the medium. These processes can be divided into four categories:

- *Radiative bound-bound (bb) processes*
- *Radiative bound-free and free-bound (bf/fb) processes*
- *Radiative free-free (ff) processes*
- *Scattering processes on free electrons*

Each of the process types has its characteristic effects on the radiation field and the medium (we will often call this *plasma* below, referring to the standard case in astrophysics). We describe these effects in the following.

2.1.2.1 Radiative bound-bound processes - line formation in the Sobolev approximation

Bound-bound processes are *line transitions* of atoms from one energy level to another.

The probability of a line to absorb incoming radiation, and to emit a photon depends strongly on frequency – it peaks sharply at the line's rest-frame frequency ν_0. We usually express the frequency dependence in terms of a line profile

$$\phi(\nu - \nu_0) \;\text{ with }\; \int_{\mathbb{R}} \phi(\nu - \nu_0)\; \mathrm{d}\nu = 1$$

The frequency response, i.e. ϕ, is considered to be the same for absorption and emission in this work, which holds under the approximate assumption of *complete redistribution*. It is determined by *line broadening* mechanisms, which are

- *intrinsic line broadening = radiation broadening = natural damping* (due to the intrinsic uncertainty in the energy levels),
- *thermal/Doppler broadening* (due to the velocity of the atoms at finite temperature), and
- *collisional broadening* (due to collisions of the atoms).

The opacity due to a bound-bound process in the rest frame of the plasma is then:

$$\begin{aligned} \chi_\nu^{bb} &= \chi_0^{bb}\,\phi(\nu-\nu_0) \quad \text{with} \\ \chi_0^{bb} &= \frac{\pi e^2}{m_e c} f_{lu}(n_l - n_u\frac{g_l}{g_u}) = \frac{h\nu}{4\pi}B_{lu}(n_l - n_u\frac{g_l}{g_u}) \end{aligned} \tag{2.7}$$

Here, as usual, χ_0^{bb} includes a correction for stimulated emission (i.e. stimulated emission is treated as negative absorption – see the second term in the bracket). The two notations for χ_0^{bb} are equivalent, as $B_{lu} \propto f_{lu}$ with a proportionality constant evident from the formula. The following symbols are used:

m_e: electron mass

f_{lu}: *oscillator strength*, proportional to the cross section of the atomic line to photons

n_l,n_u: number density of atoms/ions in the lower and upper level of the respective atomic line; we will also call these quantities *occupation numbers* sometimes

g_l,g_u: *statistical weights* of the lower and upper level, respectively

B_{lu}: *Einstein B-coefficient* ($B_{lu} \propto f_{lu}$). Note that the stimulated emission term is often written analogous to the absorption as $\frac{h\nu}{4\pi}B_{ul}n_u$; our expression is then obtained using $B_{ul} = \frac{g_l}{g_u}B_{lu}$ (one of the two so-called *Einstein relations*).

$e, h, ...$ have their common meaning.

The (spontaneous) emissivity is:

$$\eta_\nu^{bb} = \eta_0\,\phi(\nu-\nu_0) \text{ with} \tag{2.8}$$

$$\eta_0^{bb} = n_u\frac{h\nu}{4\pi}A_{ul} \tag{2.9}$$

Here, A_{ul} is the Einstein coefficient for spontaneous emission, which is related to B_{lu} via the other *Einstein relation* $A_{ul} = \frac{2h\nu^3}{c^2}\frac{g_l}{g_u}B_{lu}$. The source function is then

$$S_\nu = \frac{\eta_\nu^{bb}}{\chi_\nu^{bb}} = \frac{2h\nu^3}{c^2} \times \frac{1}{(\frac{g_u}{g_l}\frac{n_l}{n_u} - 1)} \tag{2.10}$$

Narrow line limit and interaction zones

As outlined in Section 1.1.2, the outer ejecta of SNe constitute a special case of a fast-expanding atmosphere. The radiative transfer effects of line interactions are thus markedly different from the static-atmosphere case. In a star, a photon in resonance with an atomic line is exposed to the line's opacity until it leaves the star or is destroyed. The opposite holds for a photon out of the line's frequency range. In a homologously-/freely-expanding SN atmosphere a photon propagates through matter with a velocity field $v = r \times t$, in which any two particles move away from each other. Thus, the photon appears redder and redder (more Doppler-shifted) at each particle it passes by with time respectively. As a consequence, **every** photon sent out by an atom in the ejecta is shifted into resonance with **every** line redder than its (*co-moving-frame*) emission wavelength, until it has escaped, i.e. reached a radius where densities become negligible.

The derivative of the velocity field along the photon path $\mathrm{d}v/\mathrm{d}s$ and the line width $\delta\nu$ due to the locally active broadening mechanisms determine the extent of the zone in which a photon is in resonance with a line:

$$\delta s = \frac{\delta\nu}{\nu_0} \times c \times \left(\frac{\mathrm{d}v}{\mathrm{d}s}\right)^{-1} \propto t \tag{2.11}$$

i.e. in velocity coordinates simply:

$$\delta v = \frac{\delta\nu}{\nu_0} \times c. \tag{2.12}$$

If the properties of the matter do not change over this lengthscale, and if the lengthscale is small compared to the other lengthscales relevant for the transport problem, one can calculate the line transfer in the *narrow line limit*, using the *Sobolev / escape-probability formalism*, which we will explain below.

Validity of the narrow line limit implies that the width of observed line features is controlled by the global expansion of the atmosphere (cf. Sec. 1.1.2). The strength of the absorption in the observed P-Cygni profile at some wavelength λ_{obs} corresponds to the state of the atoms/ions within the zone where photons and atoms resonate. In the narrow line limit, this zone (for a given photon) narrows down to a point $\vec{r}$ – the point at which the equation

$$\lambda_0 \doteq \lambda_{\mathrm{obs}} \times \left(1 - \frac{\hat{n} \cdot \vec{v}(\vec{r})}{c}\right)$$

holds ($\hat{n}$: unit vector in the direction of propagation; the $\doteq$ sign indicates that this treatment is only correct to first order in v/c). In complicated velocity fields, two or more points can fulfill this condition; in our standard case $\vec{v} = \vec{r} \times t$ the interaction points are unique if one photon and one line are considered. In the commonly used $p-z$ *coordinate system* (cylindrical coordinate system with the z axis – the symmetry axis – parallel to the line of sight; p is the distance to the axis and $(p, z) = (0, 0)$ is the centre-of-mass of the ejecta), the point of interaction is determined by z only:

$$\lambda_0 \doteq \lambda_{\mathrm{obs}} \left(1 - \frac{z}{ct}\right)$$

This is visualised in Fig. 2.1, together with the observational consequence: the photons of a beam (which extends over some δp), all with the same frequency and propagating in

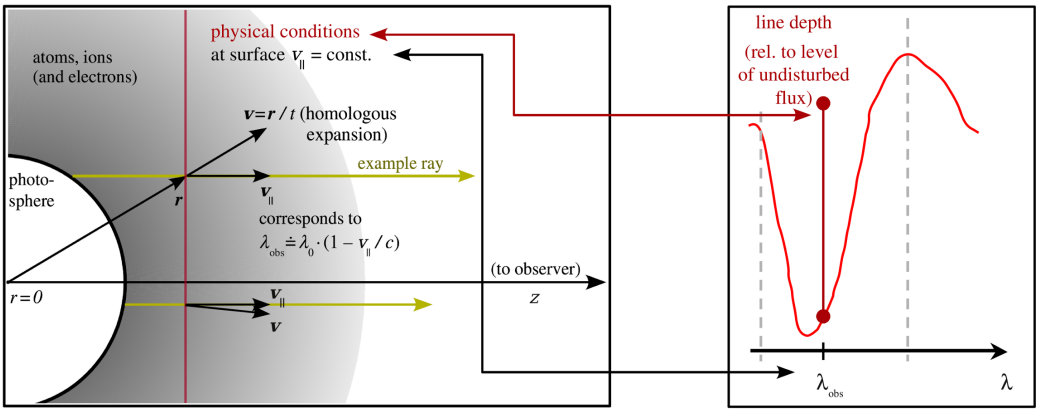

Figure 2.1: Interaction of photons (with observer-frame wavelength $\lambda_{\rm obs}$) with an atomic line (wavelength λ_0 in the co-moving frame, i.e. the atoms' frame) for a velocity field $v \propto r$. All interactions of the photons with the line happen within a thin interaction region (left panel, red line) where the ray-parallel velocity $v_{||}$ is such that resonance occurs. Within the P-Cygni profile (right panel), the line depth at $\lambda_{\rm obs}$ corresponds (approximately, neglecting any effects due to re-emission) to the physical conditions in the back-illuminated part of the interaction region.

the same direction, interact with the ejecta exactly on a plane perpendicular to the beam (surface of constant ray-parallel velocity).

If several lines are to be treated in the narrow-line limit, the interaction zones must in principle be disjoint (i.e. the width of each interaction zone must be much smaller than the free path between the respective zones), so that the effect of the zones on a photon can be treated separately. In most simulations of SN radiative transfer this is not strictly fulfilled (in particular in the UV), but additional transport effects due to line overlap are assumed to be insignificant and ignored (e.g. Mazzali 2000; Kromer et al. 2010; this work).

Sobolev formalism: Interaction of radiation with a line; effect on the atoms

The Sobolev / escape-probability formalism (Sobolev 1958, 1960; Castor 1970) provides an analytic description of the interaction of photons with atoms and ions in a thin interaction zone. Here, we present the basic ideas for a velocity field $v \propto r$.

We assume again an atmosphere with one atomic line; below, a photosphere at $r_{\rm ps}$ generates an outgoing intensity constant in angle[a)] and frequency:

$$I_{\nu,\rm ps} \;=\; I_c \text{ for } \mu > 0, \;\; 0 \text{ otherwise.}$$

After entering the thin interaction zone, a photon will (due to the Doppler shift) be presented a variable opacity, increasing first and decreasing later according to the line profile. We neglect opacities due to other processes for now, and only consider the line opacity χ^{bb} (cf. Eq. 2.7):

$$\chi^{bb}(r, z, \nu_{\rm obs}) = \chi_0^{bb}(r)\; \phi(f(z, \nu_{\rm obs})) \qquad \left(\int \phi(f)\, {\rm d}f = 1 \right).$$

[a)] I = const. implies that neither *limb-darkening* (i.e. a decrease of the intensity with decreasing μ) nor *limb-darkening* occurs.

Here, with $\nu_{\rm obs}$ being the observer-frame frequency of the radiation,

$$f \doteq \nu_{\rm obs} - \frac{\nu_{\rm obs}}{c}\frac{z}{t} - \nu_0 \doteq \nu_{\rm obs} - \frac{\nu_0}{c}\frac{z}{t} - \nu_0$$

is the radiation's frequency offset from the line centre in the co-moving frame at z in a $p-z$ coordinate system (where the photon propagates along the z-axis). ϕ is symmetric about $f = 0$. As $v \ll c$, no distinction has been made between the (isotropic) opacity in the co-moving frame and the rest-frame opacity. Furthermore, we assumed radially symmetric ejecta; hence only r appears as a spatial coordinate in χ_0^{bb}. t is a fixed point of time ($r = v \times t$); with respect to changes in t, photons are assumed to propagate instantaneously.

As a first result, the total optical depth which the photon (starting from z_0) encounters until it reaches an observer can be calculated as follows:

$$\begin{aligned}\tau(\nu_{\rm obs}, p, z_0) &= \int_{z_0}^{\infty} \chi_0^{bb}(r(\tilde{z}, p))\ \phi\left(\nu_{\rm obs} - \frac{\nu_{\rm obs}}{c}\frac{\tilde{z}}{t} - \nu_0\right)\ \mathrm{d}\tilde{z} = \\ &= \int_{f(z_0)}^{f(\infty)} \chi_0^{bb}(\tilde{f})\ \phi(\tilde{f}) \left[\left(\frac{\mathrm{d}f}{\mathrm{d}z}\right)^{-1}\right]_{\tilde{f}} \mathrm{d}\tilde{f}.\end{aligned}$$

We demanded conditions (see previous section) such that the properties of the plasma do not change strongly inside the zone where ϕ is significantly larger than 0. Therefore $\chi_0^{bb}(\tilde{f})$ can be drawn out of the integral (*Sobolev approximation*); the same is anyway true for $\frac{\mathrm{d}f}{\mathrm{d}z} = -\nu_0/(ct)$. In the end we obtain:

$$\begin{aligned}\tau(\nu_{\rm obs}, p, z_0) &= \tau_l \times \Phi\left(\nu_{\rm obs} - \frac{\nu_0}{c}\frac{z_0}{t} - \nu_0\right), \\ \text{with:}\qquad \Phi(f) &:= \int_{f(z=\infty)\equiv-\infty}^{f(z_0)} \phi(\tilde{f})\,\mathrm{d}\tilde{f}. \qquad (2.13)\\ \text{and:}\qquad \tau_l &:= \left[\chi_0^{bb}(f) \times \left(-\frac{\mathrm{d}f}{\mathrm{d}z}\right)^{-1}\right]_{f=0} = \left[\chi_0^{bb}(r)\left(\frac{\nu_0}{ct}\right)^{-1}\right]_{r(f=0)}\end{aligned}$$

$\tau_l := \tau(\nu, p, -\infty)$ is the *Sobolev optical depth* or *line optical depth* – the optical depth a photon encounters when propagating from $z = -\infty$ through the interaction region. For some optical depth value τ_l, a fraction

$$1 - e^{-\tau_l} \qquad (2.14)$$

of the photons does not survive the transition through the interaction zone, i.e. it is absorbed and re-emitted (or scattered).

Once the optical depth $\tau(z_0)$ is known, the intensity $\bar{J}$ averaged over the interaction region and over angle can be calculated. This quantity determines the effect of the radiation on the matter. We only give a sketch on the derivation here. One uses the formal solution of the TEQ (Eq. 2.6):

$$I_\nu^+(\tau_{\nu,p}, p) = I_\nu^+(\tau_{0,\nu,p}, p)\, e^{-(\tau_{0,\nu,p} - \tau_{\nu,p})} + \int_{\tau_{\nu,p}}^{\tau_{0,\nu,p}} S_\nu(\tilde{\tau}, p)\, e^{-(\tilde{\tau} - \tau_{\nu,p})}\, \mathrm{d}\tilde{\tau}.$$

for rays with different p values up to the photospheric radius (which is equivalent to different emission angles). $\tau_{0,\nu,p}$ corresponds either to the photosphere (if the ray intersects

the photosphere), or to $z = -\infty$ (otherwise). The integral over the source function gets its main contribution from the interaction region, where $\frac{\mathrm{d}\tau}{\mathrm{d}z}$ is largest; with S drawn out the integral, $I_\nu(\tau_\nu, p)$ or $I_\nu(f, p)$ can readily be evaluated. Integrating this times $\phi(f)$ over different f and p, one obtains as a good approximation (Castor 1970):

$$\bar{J}_\nu = \beta W_\mathrm{g} I_c + (1-\beta) S. \tag{2.15}$$

Here, S is the value of the line source function (Eq. 2.10) in the interaction region

$$S = \frac{2h\nu^3}{c^2} \times \frac{1}{(\frac{g_u}{g_l}\frac{n_l}{n_u} - 1)}$$

and β is defined as:

$$\beta := \frac{1 - e^{-\tau_l}}{\tau_l}.$$

W_g is the *geometrical dilution factor*:

$$W_\mathrm{g}(r) := \frac{1 - \sqrt{1 - (r_\mathrm{ps}/r)^2}}{2}.$$

The quantity β is usually interpreted as a probability for photons (at ν_obs) entering or leaving the interaction zone (*penetration / escape probability* – note that in general these need not be the same, but they are e.g. for $v \propto r$). Looking at the first term $\beta W_g I_c$ in Eq. 2.15, which represents the photons entering the interaction zone from the outside, the notion of a *penetration probability* immediately becomes clear: the term is β times the angle-averaged intensity coming from the photosphere (W_g accounts for the solid angle subtended by the photosphere as seen from the interaction zone). As an *escape probability*, β will appear in the effective downwards rate (Eq. 2.17, upper part).

Having mentioned this, we now discuss the atomic transition rates. The atoms or ions in the interaction zone will undergo bound-bound processes as determined by the atomic structure, the occupation numbers (n_u, n_l – i.e. the number densities in the upper and lower state, respectively), and the mean intensity in the interaction zone. We start by inserting the $\bar{J}_\nu$ value from above into the usual expressions for upwards and downwards rates (number of transitions per unit volume and time) due to bound-bound processes

$$\begin{aligned} R_{ul} &= A_{ul} n_u && \text{(downwards rate)} \\ R_{lu} &= B_{lu} \bar{J}_\nu n_l \times (1 - \frac{n_u}{n_l}\frac{g_l}{g_u}) && \text{(upwards rate diminshed by stimulated emission).} \end{aligned} \tag{2.16}$$

After re-grouping the terms such that the absorption of locally generated or reprocessed photons (represented by the terms including the local source function) is subtracted from the downwards rate, we obtain an *effective downwards rate* (emitted, escaping photons) and an *effective upwards rate* (incoming, penetrating photons):

$$\begin{aligned} R_{ul,\mathrm{eff}} &= A_{ul} n_u - B_{lu} n_l \;\; S \times (1-\beta) \times (1 - \tfrac{n_u}{n_l}\tfrac{g_l}{g_u}) \;\; = \;\; A_{ul} n_u \beta, \\ R_{lu,\mathrm{eff}} &= B_{lu} n_l \;\; I_c W \;\; \beta \times (1 - \tfrac{n_u}{n_l}\tfrac{g_l}{g_u}). \end{aligned} \tag{2.17}$$

For rate equation computations, we will later (see Sections 2.1.3.3, 2.2.4) use yet another grouping of the rates, which we already give here:

$$\begin{aligned} \mathcal{R}_{ul,\mathrm{eff}} &= \left(A_{ul} - \frac{g_l}{g_u} B_{lu} \; J_{\nu,\mathrm{in}} \right) \beta n_u \\ \mathcal{R}_{lu,\mathrm{eff}} &= B_{lu} J_{\nu,\mathrm{in}} \; \beta n_l. \end{aligned} \tag{2.18}$$

In this notation, the upwards rate only depends on n_l and the downwards rate only on n_u, *if* β can be assumed constant (e.g. in the limit of very low line strength). $I_c W$ has been replaced by the angle-averaged intensity $J_{\nu,\mathrm{in}}$ of photons (with the appropriate frequency) that are about to enter the interaction zone.

We conclude the discussion summarising what we have obtained using the Sobolev formalism: we have a solution for the number of photons surviving a localised interaction with an atomic line in a fast-expanding atmosphere, and a solution for the effect of this interaction on the atoms. In the formulae for the effective rates, all transport effects in the interaction zone are expressed in terms of one quantity β, the escape/penetration probability. Therefore we can avoid to compute the detailed transport within an interaction zone in our radiative transfer simulations.

2.1.2.2 Radiative bound-free / free-bound processes

Ionisation and recombination (bound-free and free-bound) processes lead to a continuous absorption and emission. The energy gained or lost by the radiation field equals the ionisation potential of the atom plus the kinetic energy of the free electron which has been removed from the atom or which is about to recombine, respectively.

In the atmospheres of Type I and IIb SNe[b)], these processes are merely relevant for the state of the plasma. The radiation field in these SNe is commonly assumed to be shaped by line opacities and emissivities (Sauer et al. 2006). Therefore, bound-free processes are not considered in our radiative transfer routine, but the bound-free opacity

$$\chi_\nu^{bf} = \sigma_\nu \left(1 - \left(\frac{n_l}{n_e n_I}\right)^* \frac{n_e n_I}{n_l}\right) \times n_l \tag{2.19}$$

plays a role in our NLTE module (Sec. 2.2.4). In the formula, σ_ν is the ionisation cross section, n_l and n_I are the number densities in the bound and ionised states considered, and n_e is the electron number density. $\left(\frac{n_l}{n_e n_I}\right)^*$ is the LTE ratio of the number densities, as it can be obtained for the respective states from the Saha-Boltzmann equation (see Sec. 2.1.3.2). The term including this ratio is the correction for stimulated processes – in this case stimulated recombinations. For completeness, we also give the free-bound emissivity:

$$\eta_\nu^{fb} = \frac{2h\nu^3}{c^2}\, \sigma_\nu \exp\!\left(-\frac{E_{\mathrm{phot}}}{k_B T_e}\right) \times \left(\frac{n_l}{n_e n_I}\right)^* n_e n_I. \tag{2.20}$$

Here, E_{phot} is the energy of the emitted / absorbed photon, T_e is the electron temperature, and all other symbols have their usual meaning.

The upwards (ionisation - lI) and downwards rates (recombination - Il) between a state l and an ionised state I are:

$$\begin{aligned}
\mathcal{R}_{lI} &= 4\pi \int_{\nu_\mathrm{T}}^{\infty} \frac{\sigma_\nu\, J_{\nu,\mathrm{cmf}}}{h\nu}\, \mathrm{d}\nu \times n_l \\
\mathcal{R}_{Il} &= 4\pi \int_{\nu_\mathrm{T}}^{\infty} \frac{\sigma_\nu}{h\nu} \left(\frac{2h\nu^3}{c^2} + J_{\nu,\mathrm{cmf}}\right) \exp\!\left(-\frac{E_{\mathrm{phot}}}{k_B T_e}\right)\, \mathrm{d}\nu \times \left(\frac{n_l}{n_e n_I}\right)^* n_I n_e
\end{aligned} \tag{2.21}$$

In these formulae, ν_T is the ionisation threshold frequency. The recombination rate, as given here, can be calculated from the ionisation rate using the *Einstein-Milne relations*,

[b)] In classical Type II SNe, this does not hold – e.g. the H ionisation opacities are expected to significantly influence the UV radiation field, as line opacities are low in the envelope.

which are analogous to the bound-bound Einstein relations. Ionisation to excited states or recombination from excited states of the ion is not considered in most practical calculations; only different lower states l are considered. We adopt this procedure, as it will give a reasonable approximation to the total ionisation and recombination rate in our case: we solve the rate equations only for H and He (see Sec. 2.2.4). In the H II ion, excited states do not exist. In the He II ion, they are at relatively large energies, implying large photon energies needed for ionisation from He I to these states and thus low ionisation rates; recombination from these states as the reverse process is not relevant as they are not strongly populated.

The continuous nature of ionisation processes implies that the interaction region of a photon with an ionisation continuum is not "thin". Escape probability formalisms for this problem have been developed (e.g. Canfield & Ricchiazzi 1980), but have a limited scope of applicability. A detailed computational treatment of continuum opacities can, however, be implemented in simulations if needed (e.g. Kromer et al. 2010).

2.1.2.3 Radiative free-free processes

A *free-free process*, often also termed *(inverse) Bremsstrahlung* process, is an absorption of a photon by a free electron which moves in an atom's field, or the inverse process. Free-free processes with optical photons are generally considered relatively unimportant in Type I and IIb SNe, for the radiation field as well as the plasma. We do not consider them in our calculations.

2.1.2.4 Thomson scattering

Continuum electrons are not only responsible for free-free absorption and emission, but also for the scattering of radiation (*Thomson scattering*, as long as the photon energies are low enough; *Compton scattering* in general). Thomson scattering contributes significantly to the opacity in a SN. It can considerably increase the mean time for a photon to escape (see the case of Type II-L / -P SNe), leading to a stronger thermalisation of the radiation.

The opacity due to Thomson scattering (in the co-moving frame) does not depend on frequency or angle:

$$\chi^{Th} = \sigma_T \times n_e = \frac{8\pi}{3}\frac{e^2}{m_e c^2} \times n_e \tag{2.22}$$

Here, n_e is the electron number density, m_e is the electron mass and all other symbols have their usual meaning. The emissivity is usually approximated to be proportional to the opacity:

$$\eta_\nu^{Th} = \chi_{T,\nu} \times J_\nu, \tag{2.23}$$

assuming that the photons experience an uniform random reshuffling in angle. In reality, forward and backward scatterings are preferred, i.e. sideways scatterings occur less often. Practically all radiative transfer calculations in astrophysics ignore this, assuming it only has a small net effect (Rutten 2003).

2.1.3 The state of the plasma

The state of the plasma can be calculated from atomic structure data and the physical conditions using different assumptions and approximations. We now describe those which are relevant for our work.

2.1.3.1 Basic assumptions underlying different approximations

The simplest assumption for calculating the plasma state is *local thermodynamic equilibrium* (*LTE*), which holds if matter and radiation are strongly coupled by absorption and emission at all frequencies. As a difference to (complete) thermal equilibrium, in LTE the temperature is allowed to vary smoothly in space. Energy transport will then occur between different locations, but it is assumed to be weak enough that the excitation/ionisation pattern is thermal, as are the electron velocities. The dominant part of the radiation field is isotropic and follows a Planck law $B_\nu(T)$ (black body):

$$I_\nu = \frac{2h\nu^3}{c^2}\frac{1}{e^{\frac{h\nu}{k_B T}} - 1} =: B_\nu(T) \text{ (with the usual symbols).} \tag{2.24}$$

A "next order" non-isotropic contribution to the radiation field is responsible for the energy transport.

If LTE does not hold, one usually assumes a *statistical equilibrium* of upwards/downwards rates to and from each energy state of each ion species possibly present, and solves for the stationary occupation numbers. This *rate equilibrium in NLTE* is much more expensive to calculate than an LTE state; we perform full NLTE calculations only for He and H.

For most chemical species, our treatment in this thesis will make use of the *nebular approximation*, which mimics some principal effects of NLTE. In the nebular approximation, radiation and electrons can have different temperatures T_R and T_e. The mean intensity is assumed to vary over frequency like a black body, but the overall amplitude is set by an *equivalent dilution factor* W:

$$J_\nu = W \cdot B_\nu(T_\mathrm{R}).$$

The use of a *dilution factor* is inspired by the concept of an optically-thin atmosphere which is illuminated by a "spherical black body" from below (*Schuster-Schwarzschild* concept). Going outwards through such an atmosphere and looking back, the photosphere subtends an angle smaller and smaller with radius. If one assumes most of the radiation to stream outwards freely, the radiation covers a smaller and smaller solid angle, so that the mean intensity is reduced by a *geometrical dilution factor* W_g, which we have already introduced in Section 2.1.2.1.

In the following we specify how the state of atoms and ions can be calculated in LTE, in statistical equilibrium and in the nebular approximation.

2.1.3.2 LTE

In LTE, the local temperature, the results of equilibrium thermodynamics (equilibrium distributions), abundances and densities and atomic level data suffice to calculate the state of the plasma.

The *Saha-Boltzmann equation* gives the occupation numbers of all (excited / ionised / excited+ionised) states of a chemical species with respect to one reference state. With the ground state "1" of some ion $j+1$ as reference, the usual form of the equation allows one to calculate the occupation numbers of any states i in the ion j:

$$\left(\frac{n_e n_{1,j+1}}{n_{i,j}}\right)^* = \frac{2g_{1,j+1}}{g_{i,j}} \left(\frac{2\pi m_e k_B T}{h^2}\right)^{3/2} \exp\left(-\frac{h\nu_T - E_{i,j}}{k_B T}\right). \tag{2.25}$$

Here, the electron number density n_e must be given (however it can be numerically calculated if the chemical composition of the plasma is specified – see. Sec. 2.2.4.1). The numbers $g_{0,j+1}$ and $g_{i,j}$ are the statistical weights of the respective states. $E_{i,j}$ is the excitation energy of level i in the ion j and ν_T is the respective ionisation threshold frequency. In order to calculate the number ratio of all j-ions (regardless of the excitation level) to $n_{1,j+1}$, one sums up the respective Saha-Boltzmann equations. The sum of the weights and exponential factors over all excitation states i, which appears in the resulting equation, is called *partition function* of the ion j:

$$U_j = \sum_i g_{i,j} \exp\left(-\frac{E_{i,j}}{k_B T}\right).$$

This sum normally diverges, but very slowly; thus in practice one stops considering further states after some highly excited state. The truncated states are assumed to "dissolved" into the continuum due to the interference with neighbouring particles (cf. Hummer & Mihalas 1988). Different truncation methods are used in practice, but fortunately all of these usually give very similar results for the partition function.

In LTE, every (excitation, ionisation, ...) process occurs exactly as often as its reverse process (*detailed balance*). This follows from basic considerations about processes in thermal equilibrium (see Mihalas 1978, Ch. 5-3 and references therein).

2.1.3.3 NLTE rate equations; collisional rates

In full NLTE calculations, one solves the equations of statistical equilibrium (*rate equations*), which for each chemical species can be written as:

$$\sum_{i=1...N} (\Lambda_{ij} n_i - \Lambda_{ji} n_j) = b_j \quad (\forall\, j = 1...N)$$

Here, $i, j = 1...N$ are all excitation/ionisation states, $\Lambda_{ij} n_i$ and $\Lambda_{ij} n_j$ are the rates to and away from state j, respectively, and b_j are rates which are not proportional to an occupation number (number density) n_i or n_j. For calculating the rates, the electron density n_e shall again be assumed given; in Sec. 2.2.4.1 we outline how we can calculate n_e numerically without prior knowledge. Often, the rate equations are abbreviated as:

$$A\vec{n} = \vec{b} \tag{2.26}$$

where A is the *rate matrix*. The row vectors of A, as written down here, are linearly dependent, so that one rate equation per chemical species can be replaced by an equation of species conservation (sum of number densities in all states = total number density of the species); any sensible $\vec{b}$ will be consistent with this replacement which finally makes the matrix A full-rank.

Besides the radiative rates $\mathcal{R}_{ij}n_i$ discussed above, and dielectronic rates which we neglect in our approximate calculations (just as the poorly known charge-exchange rates), collisions between thermal electrons and atoms / ions are responsible for a significant part of the free-bound / bound-free and bound-bound processes. The rates for these *collisional* processes (usually denoted as $\mathcal{C}_{ij}n_i$, analogously to the radiative rates) depend on complicated cross sections and the density and temperature of the free electrons. Compared to the respective radiative rates, collisional rates vary much stronger with the electron density ($\propto n_e$ instead of $\propto 1$, $\propto n_e^2$ instead of $\propto n_e$). Usually, in the relatively dilute ejecta of SNe I and IIb, these rates are therefore only important in the densest core region. Collisions with thermal electrons drive the occupation numbers into the direction of LTE at the temperature T_e of the electron gas; there is a simple relation between up- and downwards rates:

$$n_j\mathcal{C}_{ji}^{bb} = (n_i/n_j)^* \, (n_j/n_i) \, n_i\mathcal{C}_{ij}^{bb}. \tag{2.27}$$

for collisional bound-bound processes, and also for collisional bound-free processes:

$$n_j\mathcal{C}_{jI}^{bf} = \left(\frac{n_I n_e}{n_j}\right)^* \left(\frac{n_j}{n_I n_e}\right) n_I n_e \mathcal{C}_{Ij}^{fb} \quad \text{(symbols as above).} \tag{2.28}$$

Non-thermal electrons can have a marked influence on the plasma state in SNe, driving atoms out of LTE. In SN ejecta at the epochs considered in this work, such electrons can mainly be produced when the gamma rays from the decay of ^{56}Ni and ^{56}Co deposit their energy by Compton scattering[c)]. The non-thermal electrons have typical energies of $\gtrsim 1$ keV. When scattering and losing energy in the plasma, they accelerate other electrons and excite or ionise atoms. This is mainly relevant for species which have low radiative excitation or ionisation rates, which motivates why we use an NLTE solver in this thesis especially for He: For the He I atom, which has extremely large excitation and ionisation energies, nonthermal collision processes dominate over radiative excitation and ionisation (from the ground state). This has long been recognised as crucial for the appearance of spectral lines (Harkness et al. 1987). The non-thermal electrons are taken into account in our NLTE solver (2.2.4) in the right-hand side of the rate equations ($\vec{b}$). The occupation numbers in the presence of non-thermal excitation often deviate by factors $\gg 10^5$ from the LTE ones.

2.1.3.4 Nebular approximation

Mazzali & Lucy (1993) and Mazzali (2000) have used variants of the so-called *nebular approximation* for calculating the excitation and ionisation state in SNe. They give formulae for ionisation and excitation which can practically be evaluated at LTE costs. The basic idea behind these approximations is to fit the actual (angle-averaged) radiation field J_ν (e.g. in some computational cell) with a function including two fit parameters W (equivalent dilution factor) and T_R (radiation temperature):

$$\tilde{J}_\nu = W \cdot B_\nu(T_R) \ \text{(dilute blackbody).} \tag{2.29}$$

Here, Mazzali & Lucy (1993) determine T_R such that the mean frequency of $\tilde{J}_\nu$ and J_ν are the same, and then adapt W so as to match the total (frequency-integrated) intensity.

They then consider only a subset of levels for each atom/ion:

[c)] The heating contribution of positrons is negligible at the early epochs simulated in this work.

- Metastable states which are connected (by radiative transitions) to the ground state via two subsequent transitions (with a higher-lying intermediate state).
- "Normal" states which are connected to the ground state or a metastable state via a single permitted transition.

Approximating the system of the ground state 1 and a normal excited state as a "two-level atom", and neglecting stimulated emission as well as collisional processes, one obtains (from the rate equations for this case) the following occupation numbers for normal excited states u:

$$\frac{n_u}{n_1} \overset{\text{Eqn. (2.29), Wien appr.}}{=} W \times \frac{g_u}{g_1} e^{-h\nu_{1u}/k_B T_R} \,. \tag{2.30}$$

Likewise, for metastable states m one calculates, considering an appropriate "three-level atom":

$$\frac{n_m}{n_1} \overset{\text{as above}}{=} \frac{g_m}{g_1} \times e^{-h\nu_{1m}/k_B T_R} \,, \tag{2.31}$$

which equals an LTE excitation pattern at T_R.

Ionisation can be calculated from an equation similar to the Saha-Boltzmann equation. A basic form of this "nebular ionisation equation" can be derived assuming the dilute black-body radiation field given above (Eq. 2.29) and a negligible influence of collisions, **if** the ionisation cross section has a ν^{-2} or ν^{-3} frequency dependence right above the ionisation threshold (Mihalas 1978, Equation 5-46). The version which is specifically used in Mazzali & Lucy (1993) and Mazzali (2000) is:

$$\frac{n_e n_{1,j+1}}{n_{1,j}} = \frac{2g_{1,j+1}}{g_{1,j}} \times W\zeta \left(\delta + W\left(\frac{1}{\zeta} - 1\right)\right) \times \sqrt{\frac{T_e}{T_R}} \times \left(\frac{2\pi m k T_R}{h^2}\right)^{\frac{3}{2}} \times e^{-\frac{h\nu_{\mathrm{T}(1j)}}{k_B T_R}} . \tag{2.32}$$

The factor $\zeta[\delta + W(\frac{1}{\zeta} - 1)]$ has been added here with respect to Equation 5-46 of Mihalas (1978) in order to account for ionisation from and recombination to excited states (with $\zeta \neq 1$), and for a modified radiation field at UV wavelengths (with different values for δ). For further details, we refer to Mazzali & Lucy (1993) and Hachinger (2007), where a complete derivation of the equation can be found.

2.2 Radiative transfer / spectrum synthesis code

In this thesis, we use and extend a Monte-Carlo (MC) code for stationary radiative transfer in spherical symmetry (Abbott & Lucy 1985, Mazzali & Lucy 1993, Lucy 1999, Mazzali 2000 and Stehle et al. 2005). We compute SN spectra from given density and abundance profiles. The aim (see Chapters 3 and 4) is to infer densities and abundances such that we can explain observed SNe; in this way, we obtain information about the structure of the explosions.

2.2.1 Concept of the code

The code computes the radiative transfer from an assumed photosphere through the SN ejecta (atmosphere). Imposing a black-body outwards flux at the lower boundary, we

avoid a lengthy simulation of the optically thick inner zones of the SN, where most of the radiation is generated. For the atmosphere, *radiative equilibrium* is assumed to hold – no net energy is be removed or added to the radiation field or the matter, except for a "kinematic" energy loss of the photons due to scattering. This is a decent approximation as long as the photosphere in the model is not too far inside the ^{56}Ni-rich zone of the ejecta. The SN envelope, or more specifically its density, is calculated from an initial density profile in homologous, force-free expansion. No back-reaction of the radiation on the fluid elements is considered (cf. Sec. 1.4).

From the photosphere, which is located at an adjustable $v_{\rm ph}$, continuous black-body radiation at a photospheric temperature ($T_{\rm ph}$) [$I_\nu^+ = B_\nu(T_{\rm ph})$] is assumed to be emitted into the atmosphere. Notable deviations from this approximation mainly appear in the red and infrared, where the density of lines due to Fe-group elements is small, and thus no radiation can be emitted in a real SN. This sometimes leads to a discrepancy in the flux level of synthetic and observed spectra in the respective wavebands.

We simulate the propagation of *photon packets* (i.e. packets of radiative energy), which undergo Thomson scattering and interactions with lines (where we use the Sobolev approximation). A downward *branching* scheme ensures that we catch the leading-order effects of *flourescence* (cf. Sec. 2.2.5.1) when simulating bound-bound processes. Radiative equilibrium is enforced by the indivisibility of packets (Lucy 1999) in the MC simulation. Packets which are re-entering the photosphere due to backscattering are considered re-absorbed and do not contribute to the luminosity emitted.

The excitation and ionisation state of the matter is normally calculated from the radiation field statistics using the modified nebular approximation of Mazzali & Lucy (1993) and Mazzali (2000). In order to treat He and H, however, we have developed a module which calculates excitation and ionisation in full NLTE. All quantities related to the medium (abundances, ionisation, excitation) are calculated on a spatial grid of 20 – 40 shells with constant thickness in $1/r$, depending on the resolution needed.

We iterate excitation, ionisation and the radiation field in turn until the $T_{\rm R}$ values within the atmosphere are converged to the per cent level. Within these iterations, $T_{\rm ph}$ is automatically adjusted so as to match a given bolometric output luminosity $L_{\rm bol}$. Thus, the photospheric luminosity is adapted so as to compensate for the backscattering of radiation, which occurs when packets re-enter the photosphere. After the temperature iterations, the emergent spectrum is calculated by formal integration of the transfer equation (Lucy 1999), using a source function derived from the MC statistics.

Before we describe the steps of the calculation in some detail, we recap what the input data for a spectral model are:

- *Initial density profile,*
- *Abundances.* Radial shells (typically 1-15) with different abundance mixes can be set up as needed above the photosphere. This abundance grid is then mapped onto the spatial grid used for the computations.
- *Time t from explosion onset.* The time is used by the code e.g. to scale the density profile. t depends on the time offset from the observationally determined B maximum, and the assumed rise time $t_{\rm r}$ needed from explosion onset to reach maximum light.
- *Photospheric velocity v.* The optimum position for an assumed photosphere is far enough inside in order not to artificially impose a (quasi-)continuous flux in

the outer layers of the atmosphere, but far enough outside so that the atmosphere considered does not contain a major fraction of the ^{56}Ni in the SN.

- *Bolometric luminosity* $L_{\rm bol}$.

2.2.2 Main loop of the code and MC transport loop

We now mention the main steps according to which our code proceeds in order to produce the output spectrum (Fig. 2.2). We also give some details on how the transport of the radiation packets is implemented (Figure 2.3). Each step (as marked with numbers / letters in the figures) will be briefly described; we follow the discussion in Hachinger (2007).

The code runs several times through the loop depicted in Figure 2.2 (after an initialisation), with the aim of determining the atmospheric temperature structure and the temperature of the photospheric black body. Convergence of the temperature structure is assumed when the change from one to the next iteration is $\lesssim$1% in all shells (of the spatial grid), or 2% in case the temperatures in all shells show an alternating (up-and-down) behaviour during the last few cycles. The loop is then stopped, and the final spectrum is calculated from the MC statistics by the *formal integral* routine described in Section 2.2.3.

2.2.2.1 Line selection and initialisation (1)

In order to start the cycle in Figure 2.2, initial values have to be given; this are in our case the temperatures and the dilution factor in each shell of the grid.

After this, the ionisation and excitation equations are solved and the Sobolev optical depths (Equation 2.13) for all atomic lines available in the code's line list are calculated. Lines which are below a certain optical depth threshold $10^{-6.5}$...$10^{-3.5}$, depending on the actual model, are not considered any further – except for H and He lines which are always included, as their strength in NLTE, as calculated later, is difficult to predict. Typically, $\gtrsim 10^5$ lines are included in a model. Discarding weak lines mostly results in a weaker overall line opacity in the UV (Khokhlov et al. 1993), which can be compensated for by (a bit) larger abundances of Fe-group elements inserted in the model (as long as the abundances of these elements need not be inferred to extremely high accuracy).

2.2.2.2 MC radiative transfer (2)

As the envelope structure is set now [either after step (1) or after step (4)], the photon packet propagation through the envelope can be simulated (Figure 2.3). This propagation proceeds as follows (the lower-case list indices refer to the steps in Figure 2.3; z denotes a random number freshly drawn at each use, with a uniform random distribution between 0 and 1):

(a) Creation of packets. Packets, each one carrying the same energy[d)], are created. The frequency distribution of the packets is determined by sampling the photospheric black body emission function. The emission angle μ is determined by

[d)] Using equal energy packets leads to better sampling in blue wavelength regions, where then a smaller number of photons is sampled by a each packet. Note that in the exact technical implementation each packet does actually not represent an energy, but a part of the total luminosity; this makes sense because a stationary radiation flow through the atmosphere is simulated.

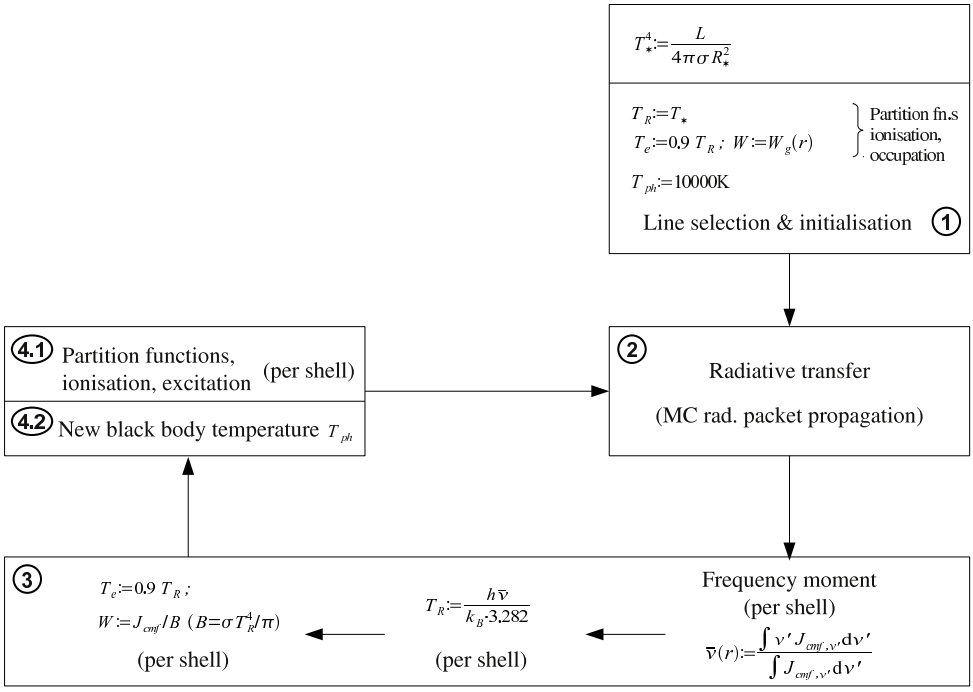

Figure 2.2: Code: Scheme of the iterative determination of physical conditions and the data flow (adapted from Hachinger 2007). For details about the MC step (2) see Figure 2.3; details on the ionisation/excitation step (4.1) are given in Sec 2.2.4.1.

$\mu = \sqrt{z}, z \neq 0$. Taking the square root maps the uniformly-distributed random numbers onto random numbers $\tilde{z}$ with a distribution proportional to $\tilde{z}$ in the interval $(0, 1]$. This is the appropriate distribution for emission with zero limb darkening.

(b) New event opt. depth & opt. pathlength record. In order to simulate the fate of a propagating photon, we first recap the following: if a bunch of photons is sent through an opaque medium, the optical depth increments ($\delta\tau = |\tau - \tau_0|$) at which they interact are distributed like $e^{-\delta\tau}$ (exponential decay in optical pathlength: $\frac{dn_{ph}}{d\tau} \propto n_{ph}$). This distribution can be sampled by random numbers $\tau_{\text{event}} := -\ln(z), z \neq 0$.
Therefore, we proceed by drawing a τ_{event} (*event optical depth*) for each photon packet in order to determine at which point of its path it will undergo an interaction. Simultaneously, the recorded optical depth increment the packet has gone through (pathlength record) is set to zero.

(c) Determination of next event. Now the code decides what the assignment of τ_{event} means for the photon, i.e. which type of event occurs next. The code sums the Sobolev optical depths of those lines line whose interaction zones are to be crossed by the photon, and adds the optical depth due to electron scattering encountered on the way to each interaction zone. Note that the line interaction zones are assumed to be infinitely thin, so that they do not overlap; each photon of some co-moving frame frequency encounters the same lines (one after another, from the bluest

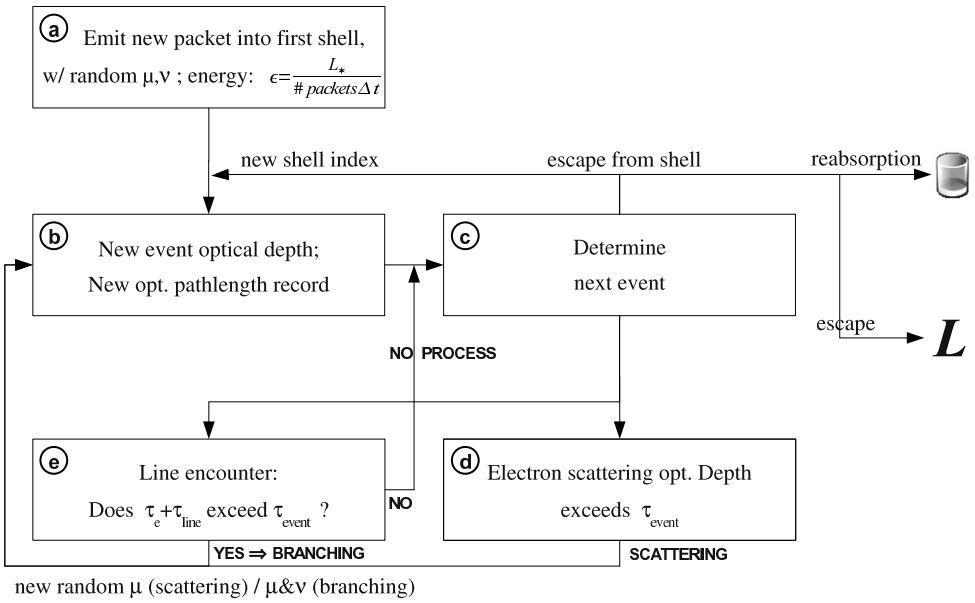

Figure 2.3: Code: Radiation propagation scheme (from Hachinger 2007).

to the reddest line). During the optical depth summation, three things can occur: τ_{event} can be exceeded within an interaction zone, or it can be exceeded on the way to an interaction zone due to the Thomson opacity, or τ_{event} is not reached before the photon approaches the shell boundary. The packet is treated accordingly:

- If the shell boundary is reached, the photon is put into the new shell and the code starts out again with (b), unless the photon was in the first or last shell. In the latter cases the photon is destroyed or counted into the luminosity, respectively.
- If the Thomson scattering optical depth is exceeded (d), the photons are Thomson-scattered (retaining their frequency in the co-moving frame); they propagate on in the same shell (and keep their optical pathlength record) but with a new random μ [go to (b)].
- If a line interaction occurs, the line is excited and de-excites with a new energy packet being sent out [branching / flourescence process, (e)].

(e) Line encounter and branching. If a line is excited, it may de-excite through different lines according to their effective downwards rates (branching). The code assigns a downward transition to the whole packet (by a random choice with appropriate probabilities), making it emerge from the process with a new co-moving frame frequency, direction and pathlength record. The co-moving frame energy of the packet, however, remains the same as before (i.e. the number of photons in the packet changes inversely to the frequency). This *indivisible packet* approach (Lucy 1999) ensures conservation of radiative energy in the co-moving frame, and in the limit of large packet numbers yields the same effect as if the packets were split between different downwards transitions.

Note that the total co-moving frame energy of a photon packet is assumed to remain constant during all the propagation, while the energy in the star's frame can change by a few per cent depending on the scattering/interaction history.

2.2.2.3 Frequency moment and other data collection; T_R and W (3)

During the MC run, the code has collected information, including packet counts at the shell midpoints (separated by angle and frequency), the emergent packets, and the packets which have come to resonance with each line in a shell. Lucy (1999) has devised a variety of *MC estimators* for the radiation field quantities, based on packet counts; here it is crucial how the packet statistics are computationally treated in order to obtain the most reliable results. For details, we refer to the original publications (Mazzali & Lucy 1993; Lucy 1999; Mazzali 2000).

The information from the MC estimators is used later in the formal integral procedure, but also in the next step of the the main loop to calculate the new ionisation and excitation state of the medium (T_R, W, and/or an NLTE solution).

2.2.2.4 Update of the excitation and ionisation state (4.1)

The new excitation and ionisation state of the plasma is calculated from the quantities collected in step (3). Some details of this step are described in Sec. 2.2.4.1. While the original version of the code exclusively used the nebular approximation, the code can now also calculate selected ions in full NLTE with a rate equation solver. The electron temperature is – in any case – not calculated in detail, but always set to $0.9 \times T_R$, which very approximately mimics a situation in which the electron temperature is mostly controlled by the radiation (Mazzali & Lucy 1993, and references therein). As long as collisional rates are not extremely important, moderate deviations in this estimate do not have much of an effect on the calculation.

2.2.2.5 Update of the photospheric black-body temperature (4.2)

At the end of each iteration, the temperature of the photospheric black body is regulated such that the light output of the model will match the luminosity $L_{\rm bol}$ better and better. Let the output luminosity in the current iteration i be $L_{{\rm bol},i}$ (which is different to the luminosity of the photospheric black body in that iteration because of backscattering). A straightforward way to come closer to the "right" photospheric temperature is then to calculate an estimate $\tilde{T}_{{\rm ph},i+1}$ such that the new photospheric black-body luminosity[e)] is $L_{\rm bol}/L_{\rm bol,i}$ times the old one. If the backscattering rate would not change between the iterations, taking $\tilde{T}_{{\rm ph},i+1}$ would immediately make the model's output luminosity right. In practice, large changes in the rate occur at least in the first iterations. This can make the iterates $T_{{\rm ph},i}$ oscillate or diverge, which one avoids by damping the iteration and calculating the new temperature as:

$$T_{{\rm ph},i+1} = \alpha \tilde{T}_{{\rm ph},i+1} + (1-\alpha) T_{{\rm ph},i}$$

with an automatically adapted damping factor $\alpha = 0.6...1.0$.

[e)] $T_{\rm ph}$ and the photospheric luminosity are related to each other by the Stefan-Boltzmann law, Eq. 1.5.

2.2.3 Formal integral procedure

When the iteration cycles have ended, the output spectrum must be calculated. Starting from the code version of Mazzali (2000), we have not been using the escaping packets to calculate the flux received by the observer any more. Instead, we numerically evaluate the formal solution of the transfer equation (Eq. 2.6), using a source function derived from the MC estimators (Lucy 1999; Mazzali 2000). This source function is usually much more well-sampled by the packet transport than the spectrum by the emerging packets; therefore the formal integral procedure significantly reduces the MC noise in the output spectrum.

The code calculates the emergent intensity, $I_\nu^+(z = \infty, p, \nu)$ (in the $p - z$ coordinate system as introduced in Section 2.1.2.1) for a grid of p and ν values, effectively performing the integration over the source function in Eq. (2.6). For details on this procedure and the appropriate boundary values, please see the discussion in Lucy (1999) or Hachinger (2007).

Finally, the luminosity an observer (at $z = \infty$) sees is calculated using the equation:

$$L_\nu = 4\pi \int_0^\infty I_\nu^+(z = \infty, p, \nu)\, 2\pi p \, \mathrm{d}p, \tag{2.33}$$

where p and z are again the usual coordinates.

2.2.4 The NLTE extension to the code

We programmed an extension module to the Monte-Carlo spectrum synthesis code which allows us to calculate the excitation and ionisation state of selected species in NLTE. The solver has a flexible structure which allows for a coupling to other radiative transfer codes and for the treatment of different ions by just providing atomic structure data. While we first used the solver only for He, we have meanwhile added data for H, albeit for this atom the distinct NLTE effects in SNe are much smaller than for He.

In the concept for the NLTE solver, we mostly followed Lucy (1991) who programmed one of the first NLTE simulations for He-rich SN atmospheres; we have re-implemented and significantly extended his method. Below, we first describe how we prepared the ionisation/excitation routine of the spectrum synthesis code for the use of the NLTE module. We then discuss additional input data and some technical details of the solver.

2.2.4.1 Ionisation/excitation loop of the spectrum synthesis code – preparation for NLTE calculations

The spectrum synthesis code calculates the ionisation and excitation state [step (4.1) of the main loop, Sec. 2.2.2] in an iteration (Fig. 2.4), during which the final electron density is determined.

We first explain a purely nebular ionisation/excitation calculation, consisting of the steps (I), (II) and (IIIa) in Fig. 2.4. These steps are iterated starting from an initial guess for the electron density n_e. In LTE or in the nebular approximation, one could also derive an algebraic equation for n_e from species conservation and the nebular ionisation/excitation equations applied to subsequent ionisation stages. However, this equation would be of too high an order to be solved in a closed form.

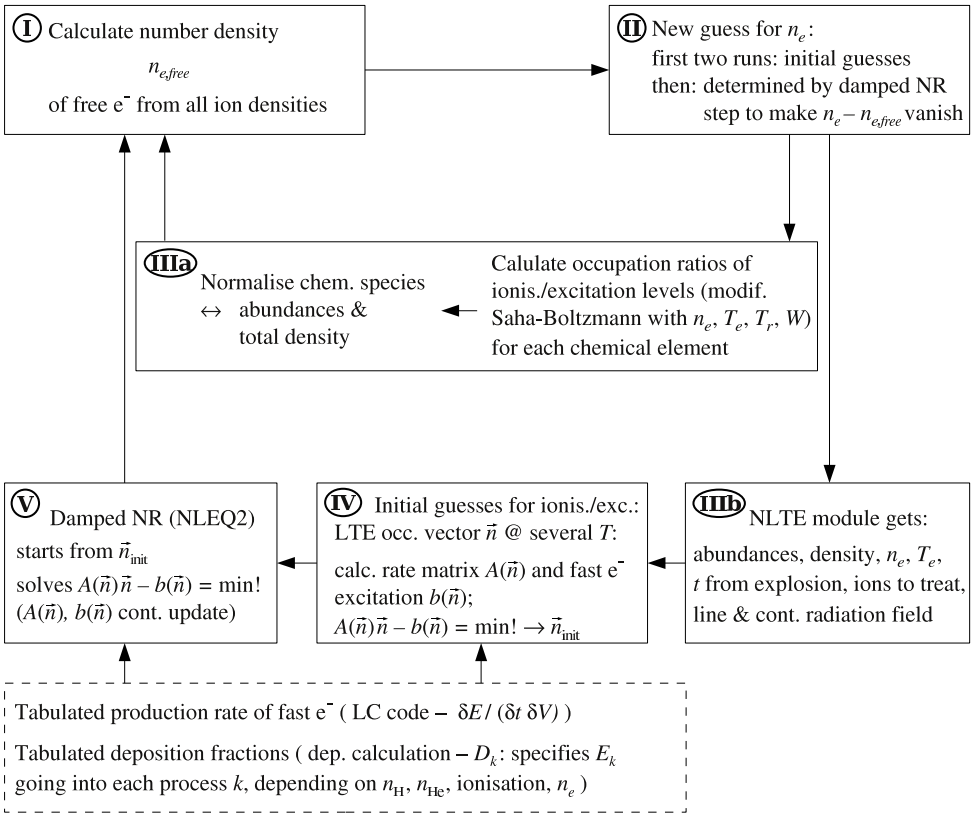

Figure 2.4: Ionisation/excitation loop of the spectrum synthesis code; integration of the NLTE module. The cycles are initialized by inserting two times an initial guess for n_e in step (II) and executing the subsequent steps (see text), respectively. As soon as two values for $n_{e,\text{free}}$ have been calculated [step (I)], the NR method can be used in step (II).

The spectral synthesis code in previous versions (Mazzali 2000; Stehle et al. 2005) has employed a damped fixed-point iteration to obtain n_e. The nebular ionisation equilibrium is calculated from the initial/current guess for n_e, giving a density of electrons "lost" by the (singly, doubly,...) ionised species, which we call $n_{e,\text{free}}$. A new iterate is then calculated as

$$n'_e = \alpha n_{e,\text{free}} + (1-\alpha) n_e$$

where $\alpha \in (0,1]$ is a damping factor. For a guess n_e larger than the "right" solution, $n_{e,\text{free}}$ will be lower than the realistic value (because of stronger recombination), and vice versa. If α is chosen low enough, the iteration will converge in practically every realistic case to the equilibrium value.

In order to speed up the convergence of the iterations, we replaced the fixed-point iteration by a *Newton-Raphson* solver (*NR*, e.g. Deuflhard 2004). We initialise the solver with two initial guesses n_e [Fig. 2.4, step (II), initialisation mode], for which the excitation/ionisation [step (IIIa)] and $n_{e,\text{free}}$ [step (I)] are calculated. Newton-Raphson steps are then used to make the function $f(n_e) := n_e - n_{e,\text{free}}$ vanish. In order to ensure stability, we use a moderate, adaptive damping (i.e. $n'_e = \alpha\, n_{e,\text{NR}} + (1-\alpha)\, n_e$, where $n_{e,\text{NR}}$ is the return value of the NR step and α is chosen such that the relative change from n_e to n'_e in one step does not exceed $\sim 50\%$). Convergence is assumed if

$$|n_e - n_{e,\text{free}}| < 0.005 \times n_e.$$

Within the accelerated excitation/ionisation iteration, our NLTE (rate matrix solver) module can conveniently be used for selected species in parallel to the nebular calculation for all other ions. n_e is then calculated in NR iterations just as discussed, with the $n_{e,\text{free}}$ contributions by all ions (in nebular approximation and NLTE) taken into account. Within the loop iteration, the NLTE module obtains the necessary data from the MC code [Fig. 2.4, step (IIIb)] and external sources and calculates the required occupation numbers / ionisation fractions.

The MC radiation field estimators passed to the NLTE code in step (IIIb) shall be briefly described, as different implementations are possible here. On the one hand, we need an estimator for the intensity at some line frequency, measured just before the interaction surface, for the calculation of radiative bound-bound rates (Eq. 2.18). It is computed analogous to the J_b estimator of Lucy (1999), but with an added transformation into the co-moving frame. On the other hand, for our bound-free rates we must obtain the radiation field in the co-moving frame at all frequencies; fortunately a lower resolution suffices here as the cross-sections are > 0 for a larger frequency interval. The required radiation field is "measured" by recording packets as they pass the shell midpoints. It has to be appropriately smoothed in order to avoid influences of Monte-Carlo noise; we generally use $\gtrsim 500000$ radiation packets in NLTE calculations so that a moderate smoothing suffices. At $\lambda < 1000$ Å, we impose a continuous transition to a constant mean intensity of $10^{-30}\text{erg}\,\text{Hz}^{-1}\text{s}^{-1}\text{sr}^{-1}\text{cm}^{-2}$. For $\lambda \lesssim 300$ Å, this normally exceeds the black-body intensity at the local electron temperature T_e, and we let the intensity decline following $B_\nu(T_e)$[f)].

2.2.4.2 External input data for the NLTE solver

The NLTE solver requires more detailed atomic data for the species treated than the spectral synthesis code. Furthermore, it needs data on the excitation/ionisation of atoms and ions by the local fast electron population in each cell (heating rate, deposition fractions).

Atomic data – model atoms / ions

Atomic data for H are relatively easy to calculate or obtain. We constructed a simple model for H, consisting of 13 energy levels. Each level corresponds to a principal quantum number; substates are not taken into account separately. For rate calculations, the occupation of the substates is assumed to take place in ratios according to the respective g-factors. This common assumption is true when collisions effectively redistribute the atoms among the substates which are (practically) identical in energy. Rate coefficients for our 13-level atom were taken from Maurer (2010), except for collisional ionisation and excitation cross sections used to calculate non-thermal and thermal rates, which are taken from Janev & Smith (1993).

The He I model we use is more sophisticated. It consists of 29 levels with $n \leq 5$. Substates differing only in the magnetic quantum number J are treated as one "effective" state (as described above). For each n with $6 \leq n \leq 8$, we combine all singlet states (regardless of L) into one effective state, and all triplet states into another one. All

[f)] The exact values [$10^{-30}\text{erg}\,\text{Hz}^{-1}\text{s}^{-1}\text{sr}^{-1}\text{cm}^{-2}$,$B_\nu(T_e)$] proved irrelevant for the present work, as in our simulations most ionisations of He occur by nonthermal collision processes, and H is mostly ionised by photons with $\gtrsim 900$ Å (also from excited states) so that the imposed flux does not control the rate.

effective levels are assigned an appropriate energy (weighted average over the substates). The occupation numbers of the states with $6 \leq n \leq 8$ are calculated in NLTE, but not mapped back to the MC code for simulating line absorption[g)]. We finally take into account a $n = 9$ triplet and singlet state, respectively, which we assume to be in LTE with He II. Energy levels for He I have been taken from the NIST Atomic Spectra Database (version 3.1.5, see acknowledgements).

We compiled radiative excitation rates for He from Drake & Morton (2007), Łach & Pachucki (2001) and Cann & Thakkar (2002). Photoionisation cross sections were taken from Hummer & Storey (1998); for energies where these were not available, data from Fernley et al. (1987) were substituted. Cross sections for collisional excitation by nonthermal and thermal electrons were obtained from Ralchenko et al. (2008), who give data for all transitions between states with $n \leq 4$. For collisional excitation to higher states by nonthermal electrons, we estimated cross sections using the recommended scaling laws of Ralchenko et al. (2008). Thermally averaged rates for excitation to and between levels $n \geq 5$, in contrast, were adopted from CHIANTI (Dere et al. 1997; Landi et al. 2006) and TMAD (Rauch & Deetjen 2003). Collisional ionisation cross sections were obtained from Ralchenko et al. (2008) ($n \leq 5$, using scaling laws for $n = 5$). An exception are again thermally averaged rates for $n > 5$, which we calculated according to Mihalas & Stone (1968). All de-excitation and recombination coefficients are calculated from the respective upwards coefficients with the usual formulae [see Sec. 2.1 or (Mihalas 1978)].

He II is approximately treated as one state; He III is not considered in our calculations. This is sufficient for the most relevant parts of our atmospheres – we demonstrate this explicitly in Chapter 4, Section 4.3.3. There, we re-calculate a representative SN model using a one-state He III ion and a preliminary 13-state He II ion, derived from our H atom by rescaling the rate coefficients appropriately.

Deposition of the gamma-ray energy

For each computational cell, we have to calculate the effect of gamma rays, resulting from the decay of ^{56}Ni and ^{56}Co, on the excitation and ionisation state of the atoms in NLTE. The gamma rays lead to the creation of fast electrons well above 1 keV by Compton scattering, which in turn excite and ionize atoms, or undergo Coulomb scattering with other (thermal) electrons. The creation and transport of the gamma rays is not simulated by the spectral synthesis code. Instead, we use a light-curve synthesis code including a gamma-ray transport routine [Cappellaro et al. (1997); cf. Chapter 4] to obtain the kinetic energy gain of the fast electron population per unit time (*gamma-ray deposition rate* or *Compton heating rate* H_C).

The kinetic energy of the fast electrons is assumed to be deposited locally. Now, our task is to compute what fraction D_k of the heating power H_C is deposited in each channel k, corresponding to an atomic process or to Coulomb scattering with thermal electrons. All atoms and ions are assumed to be in their ground state and only excitations/ionisations from this state are considered in the calculation of the deposition process and the nonthermal rates[h)]. The *deposition fraction* D_k is, in fact, a function of

[g)] Feeding back these (less reliable) numbers would have effects only at extremely long wavelengths.

[h)] This is a good approximation when considering the deposition process, as a small number of atoms/ions in excited states does not influence what happens. Also, it is a reasonable approximation for the atoms/ions, as thermal and radiative processes will dominate the rates from excited states.

the initial energy of the fast electrons E. Assuming all electrons which contribute to H_C to have the same initial energy E, we can write the energy going into channel k per unit time and volume:

$$H_{C,k} = D_k(E) H_C, \tag{2.34}$$

If $E \gtrsim 1$ keV, $D_k(E)$ becomes nearly constant (Lucy 1991; Axelrod 1980). Thus, in the case of an electron population with $E \gg 1$ keV for all electrons, we can write

$$H_{C,k} = D_k^+ H_C, \tag{2.35}$$

with an energy-independent value D_k^+.

We now describe how we compute $D_k(E)$ or D_k^+ for all processes k. The deposition process involves a cascade of slower and slower electrons. Besides the Compton-electrons, which gradually decelerate, additional nonthermal electrons can be created in ionisation processes or electron-electron scatterings. The steady-state energy spectrum of the electron population, and the resulting deposition fractions, can be calculated from an appropriate form of the Boltzmann transport equation (Spencer & Fano 1954). For our purposes, it is, however, more appropriate to use an integrated version of the transport equation (Xu & McCray 1991). This equation, which can also be seen as a simple energy-balance argument (Lucy 1991), makes it possible to calculate the deposition fraction $D_k(E)$ for a process k at a source energy E from the deposition fraction $D_k(E')$ at **all** lower energies $E' < E$, without explicitly solving for the electron spectrum:

$$\begin{aligned} E D_k(E) = & W_k p_k(E) + \sum_{\substack{\{j | E - W_j \geq E_k, \\ \text{one e}^-\text{-proc.}\}}} p_j(E) \cdot (E - W_j) \cdot D_k(E - W_j) \\ & + \sum_{\substack{\{i | E - W_i \geq E_k, \\ \text{two e}^-\text{-proc.}\}}} p_i(E) \cdot \int \mathrm{d}E_s \, \Pi_i(E_s) \cdot \Big[E_s \cdot D_k(E_s) \\ & \qquad + (E - E_s - W_i) \cdot D_k(E - E_s - W_i) \Big] \end{aligned} \tag{2.36}$$

Here, i ,k and j are indices of processes (channels), and $p_k(E)$ is the probability of process k to occur for the electron at energy E, which is proportional to the respective cross section. The energy loss (to an atom or to the thermal electron population) in process $i|j|k$ is denoted as $W_{i|j|k}$. Scattering on thermal electrons is treated as a discretised process (Habing & Goldsmith 1971) in which a nonthermal electron loses 5% of its initial energy to the plasma. The notion of a discrete energy loss in Coulomb scattering enables us to calculate a finite cross section from the stopping number of Gould (1972). This simplifies the inclusion of this process into our framework. The exact discrete loss assumed does not influence the result if the majority of the electrons is coming from large enough energies (Habing & Goldsmith 1971). The total energy $E D_k(E)$ deposited into channel k additionally involves contributions of electrons which first trigger processes j or i and then deposit energy into channel k. The second and third terms on the right-hand side of the equation thus relate the deposition fraction at some energy E to that at energies decreased through the primary processes j or i. The third term takes into account ionisation processes, in which secondary electrons emerge, i.e. newly-created nonthermal electrons. $\Pi_i(E_s)$ is the probability distribution for the energy of the secondary electron E_s, and integrates up to one. Following Opal et al. (1972), we assume

$\Pi_i(E_s) \propto 1/(E^2 + \mathcal{W}^2)$, where $\mathcal{W}$ is 13.8 eV for He I and the ionisation energy for other atoms/ions.

The deposition fractions are always known a priori below some small energy ϵ: Assuming that only atomic processes from the ground state are relevant, atomic processes only occur only above some energy threshold (determined by the species present). Electrons with lower energies lose all their energy in scatterings on thermal electrons. With initial values set up accordingly, we integrate the system up to an energy of 10 keV on an energy grid with cell sizes increasing somewhat with energy. The deposition fractions thus obtained are then adopted as D_k^+. We have tabulated these values for different H /He mixes, ionisation states, fractions $n_{\text{H I+He I}}/n_e$ (where all atoms/ions are assumed to be in the ground state) and absolute values of n_e (although the dependence on the latter is very weak, cf. Kozma & Fransson 1992). The tables are read in by the NLTE module depending on the actual local composition. If other elements than H and He are present, we calculate the deposition rate assuming an $n_{\text{H+He}}$ as large as the total number density of atoms n_{tot}, and then scale down the value for each process by $n_{\text{H+He}}/n_{\text{tot}}$ – an approximation which gives only a small error for zones in which H and He dominate, and for other zones ensures that at least the order of magnitude of the rates is right.

2.2.4.3 NLTE solver

The "NLTE solver" has to find the occupation numbers solving the rate equations (Eq. 2.26) with a given n_e. This is complicated by the fact that the coefficients of the rate matrix A depend on the plasma state in our case (escape probabilities β, which depend on the occupation numbers, enter the effective radiative rates), and also the right-hand side $\vec{b}$ depends on ionisation. For each ion, the entries b_k for the excited states k are calculated as:

$$b_k = D_k^+ H_C / W_k$$

where W_k is the work for the excitation process, and also the other symbols are as in Sec. 2.2.4.2. Each of these coefficients represents a rate between the respective ground state and excited state, which does **not** depend linearly on the ground state occupation number; it rather depends on the **mix** (i.e. number ratios) of atom/ion species and of free electrons. This is a consequence of the assumption of complete local energy deposition by the fast electrons. The rate from/to each ground state 1 of an ion is determined by non-thermal excitations and ionisations bringing atoms/ions away from the ground state, and by ionisations bringing less ionised atoms/ions to the ground state (except for the case of atoms – here b_1 is always negative):

$$b_1 = \frac{D^+_{\text{ionis, lower ion}} H_C}{W_{\text{ionis, lower ion}}} - \sum_{k=2}^{k_{\text{max}}} \frac{D_k^+ H_C}{W_k} - \frac{D^+_{\text{ionis}} H_C}{W_{\text{ionis.}}}$$

Here, k_{max} is the number of states in the ion, and all coefficients / work values refer to that ion – except for those from the lower ion which are named accordingly.

The resulting rate equations

$$A(\vec{n})\vec{n} - \vec{b}(\vec{n}) = 0$$

are highly nonlinear especially when the optical depths are large ($\beta \to 0$ for strong transitions). We therefore use [as Lucy (1991)] a Newton-Raphson solver which seeks

the root of the left-hand side of the equation as written down here. The NLTE occupation numbers usually depart strongly from the LTE values especially for He I, and therefore initial guesses are difficult to obtain. For this reason we use the adaptive-damping Newton-Raphson solver NLEQ2 (Nowak & Weimann 1991; Deuflhard 2004) which has an extremely large convergence radius and converges fast due to a sophisticated damping strategy. The NLEQ2 package internally uses a linear solver which can handle also ill-conditioned Jacobians, which appear relatively frequently in our case. Generally, one has to be careful in this respect when replacing one of the rate equations by species conservation; we implemented a routine which automatically selects the row with the smallest dynamical range in the coefficients (in the initial rate matrix) for the replacement. In our experience this has led to a significant stabilisation of the procedure.

The initial guess for the occupation numbers (Fig 2.4, step IV) in order to start the Newton-Raphson procedure (Fig 2.4, step V) is obtained by calculating LTE values at a grid of temperatures and taking those for which $\|A(\vec{n})\vec{n} - \vec{b}(\vec{n})\|$ (euclidean norm) is minimum.

When the internal convergence estimator of the NLEQ2 solver indicates convergence to 0.1 per mille, the solution is checked by considering the current matrix A and vector $\vec{b}$ and re-calculating the solution to the rate equation with a quadruple precision linear solver. The result $\vec{n}'$ is then compared to the NLEQ2 result $\vec{n}$; if the maximum entry of $|(\vec{n}' - \vec{n})/\vec{n}|$ (component-wise division and absolute value) is larger than 0.5 per mille, additional Newton-Raphson iterations are executed. The high precision here is required in order to ensure good numerical derivatives for the outer NR procedure (which determines n_e), and only produces small additional costs because of the locally quadratic convergence of the NR method.

As a last note to the discussion, we emphasize that we do **not** adapt the temperature T_e of the thermal electron population to balance the heating due to downscattering of the non-thermal electrons. As long as elements other than He are present, which is the case in every zone of our simulated atmospheres, very moderate changes in T_e will suffice to restore the energy balance of the electron gas by increased cooling (I. Maurer, private communication). We therefore chose to retain the estimate $T_e = 0.9\,T_R$ which is normally used in our Monte-Carlo radiative transfer code.

2.2.5 Spectral models: principles, modelling, abundance tomography

Before we present our spectral analyses and results, we discuss – in the last part of this chapter – the effect of the code's input parameters on our radiative transfer models in some generality. We also explain our spectral fitting technique and the abundance tomography method which we use to infer abundances from observed SN spectra.

2.2.5.1 The effect of Fe-group material: Line blocking, backwarming and flourescence

In the atmospheres of Type I and IIb SNe, the radiation is emitted and mostly reprocessed by Fe-group ions with their large opacity. This reprocessing shapes the global spectrum of the SNe.

The Fe-group lines have a large total opacity in the blue and UV. This blocks optical radiation, once it is generated, from escaping [*line blocking*, e.g. Mihalas (1978), Sauer et al. (2006)], and leads to a flux increase in the lower layers of the SN (*back-*

warming). Photons are scattered and redshifted in the co-moving frame until they escape, preferentially in *opacity windows*, i.e. wavelength regions where the opacity is low (Mazzali & Lucy 1993; Mazzali 2000). The opacity distribution, which drops towards the redder bands, thus favours a relatively red spectrum of escaping photons compared to what is generated in the lower layers. A large role in the radiative transfer in SNe is played by *flourescence*, i.e. absorption of radiation by atoms and re-emission at other wavelengths. Especially Fe-group ions are excited from well-populated low-lying states, and then often de-excite via redder transitions between higher energy levels. This process allows photons to shift to the red and escape very efficiently. All these effects are (in decent approximation) taken into account in our code with the *branching* treatment implemented by Lucy (1999) and applied to SNe by Mazzali (2000).

Fe-group elements tend to leave no particularly clear signatures in the spectra; the features they contribute to are usually blends due to several elements (Fe-group elements and IME). The main effect of Fe-group elements is rather to modulate the UV blocking. Spectra extending at least into the near-UV are thus very valuable if constraints on the Fe-group mass fractions have to be given.

2.2.5.2 The effect of IME and lighter elements

The abundances of intermediate-mass elements often influence the strength of individual spectral features. In the respective model spectra, we usually mark the features which are used to constrain the mass fractions of the different elements.

The relatively abundant lighter elements Ne, O and C have only relatively small effects on the spectra; O can sometimes be constrained from an O I feature in the IR, and C from the C IIλ6580 feature. He and H, if abundant enough and excited to the right state, again show distinct and strong spectral lines.

2.2.5.3 Influence of other input parameters on models and spectra

The spectra which result from our simulations are not only influenced by abundances, but also by the ionisation and excitation state in the atmosphere, and in part by the lower boundary spectrum. These additional factors cannot be directly controlled, but are strongly influenced by the luminosity $L_{\rm bol}$, the time t and the photospheric velocity $v_{\rm ph}$. These input parameters influence the self-consistent solution for the stationary radiation flow found by the code.

A lower $v_{\rm ph}$ or a lower t generally leads to a bluer radiation field at the lower boundary, as the emitting surface shrinks (outwards black-body emission without limb darkening – cf. Stefan-Boltzmann law, Eq. 1.5). If this radiation field is not attenuated in the zones above, radiation temperatures will increase somewhat within the entire atmosphere, and with them ionisation and excitation. The photospheric velocity $v_{\rm ph}$ not only affects the temperature, but also constitutes a lower limit to the velocity (blueshift) of the absorption parts of the spectral features.

A higher luminosity $L_{\rm bol}$ clearly also leads to a higher excitation and ionisation state, and a bluer spectrum at the photosphere (again: Stefan-Boltzmann law).

2.2.5.4 Spectral modelling

We now describe, in increasing order of complexity, our paradigms for spectral modelling which we apply in the next Chapters.

One-zone models

As a starting point, we explain the one-zone modelling approach, where one observed spectrum of a SN is to be fitted by a spectral model with homogeneous abundances in the atmosphere. Throughout the process, a fixed density profile is assumed – in most cases the outcome of an appropriate hydrodynamic simulation. We also assume a fixed time from explosion onset t, calculated from the observational epoch with respect to B maximum and an assumed B-band *rise time* (i.e. the time it takes the SN to reach B maximum).

The process of modelling (or fitting) a spectrum starts with assuming a typical abundance mix for the SN type investigated. $L_{\rm bol}$ as well as $v_{\rm ph}$ are adjusted to reach a first optimum fit. Here, we do not only take care that the overall luminosity and line velocities are well fitted: we also try to match the ionisation degree of the observed spectrum (which the ratio of Si III to Si II line strengths is often a good indicator for). Then, we continue with an iteration of those abundances which influence individual line strengths on the one hand, and parameters that influence the temperature structure, the line velocities and the UV blocking on the other hand ($L_{\rm bol}$, $v_{\rm ph}$, Fe-group abundances). We finish when no significantly better match of the spectral features and the overall flux can be obtained by varying the parameters within reasonable borders. In cases where lines and the continuum cannot be fitted perfectly at the same time, we put somewhat more emphasis on a good fit to the lines.

The parameter changes within the optimisation process are done **by hand**; we partially log these changes in order to ensure that all possibilities to optimise the spectrum have been explored. The best fit is judged **by eye**. This means that we generally just try to minimise the absolute deviation between observed spectrum and model; if a mismatch in the continuum level cannot be avoided for some wavelength range[i)], we try to fit the fractional depth of the spectral lines, i.e. the percentage of flux missing relative to the respective continuum. Degeneracies, i.e. equally good fits with different parameter sets, are the most important source of uncertainty in this manual optimisation process. To lift degeneracies, we sometimes constrain the abundances to match typical nucleosynthesis patterns within standard SN models (e.g. Iwamoto et al. 1999). Alternatively, we can use constraints on similar SNe derived with other methods in the literature.

Abundance tomography

The method of "abundance tomography" (Stehle et al. 2005) extends the approach of fitting an individual spectrum with a one-zone model. It aims at inferring the abundance profile of a SN step by step from the outer to the inner layers (again assuming a fixed density profile). To this end, one fits a time series of photospheric spectra, in which different layers of the ejecta leave their imprint. As in a one-zone model for an early-phase spectrum, one can assume that at each epoch some core of the ejecta is optically thick at most wavelengths[j)]. The spectral features are then only sensitive to what happens in the atmosphere above the core. As time progresses, the core comprises a smaller and smaller part of the ejecta (by mass, or likewise in velocity space). Therefore, later

[i)] Technically, a match of the continuum over a constrained wavelength range is always possible, but if this would make the model physically much less reasonable (e.g. wrong ionisation regime), we regard mismatches unavoidable.

[j)] This approximation breaks down especially in the infrared, where large parts of the ejecta are transparent due to a low line opacity.

spectra are more and more sensitive to central layers, while the influence of the outer layers on them is smaller.

In order to create a model for the outermost ejecta of an object, we fit the earliest spectrum available. Generally, we first create an optimized one-zone model for that spectrum. We then check whether introducing one or two additional zones with different abundances in the outermost ejecta significantly improves the fit, and whether one can determine optimum borders and abundances for these zones reasonably well. This is often successful.

The spectrum at the next epoch carries the imprint of the material in the outer envelope and additionally that of the layers inside which the photosphere has receded. As the outer abundance structure is already constrained, the new photospheric velocity and the abundances of the newly-visible layers are now the primary fitting parameters. In all other respects, the optimisation is carried out as in the one-zone case. If the abundances of the outer layers have a significant impact on the quality of the fit, and no decent fit is possible with the values used for fitting the earlier spectrum, those values are revised (normally up to $\sim$ 30% of their initial value, as needed) to equally optimise the fit to all observations. The procedure is continued with later spectra until the complete time series is fitted.

In the tomography approach, abundances which are not well constrained by an early spectrum due to degeneracies can sometimes be constrained when fitting a later spectrum. The respective abundances may then undergo significant revision ($>$ 30% of their initial value). Otherwise, we lift degeneracies as in the one-zone case by matching typical nucleosynthesis patterns or using literature results obtained applying different analysis methods to similar SNe. When discussing our models, we indicate this whenever relevant.

We emphasise that our manual fitting procedure, which has been used since our codes became available (Mazzali 2000; Stehle et al. 2005), should in the future be replaced by an automatic optimisation algorithm and code. The development of such codes is under way, but has proven unexpectedly difficult (cf. Chapter 5, outlook). For the present work, however, we can safely assume that the manual fitting process introduces smaller errors into our studies than the various approximations which are still made in numerical SN radiative transfer.

Optimisation of the density profile

The SNe Ia we study are markedly different from normal objects as they were discussed by Stehle et al. (2005) or Mazzali et al. (2008). Thus, not only the abundance distribution within the ejecta is unknown: in addition, the density profiles for them can deviate significantly from standard models. Therefore, for each object we repeat the abundance tomography procedure (or parts of it) several times with different density profiles. We then apply quality criteria to the optimum-abundance synthetic spectra in order to judge the applicability of different density profiles.

Chapter 3

SNe Ia: spectral analysis of peculiar objects

In this Chapter we analyse Type Ia SNe. Despite their "leading-order" homogeneity, which makes them standardisable candles (Phillips 1993), we find significant diversity in SN Ia spectra and light curves (Benetti et al. 2005, Taubenberger et al. 2008). We have to analyse what this diversity tells us about the explosion scenarios leading to SNe Ia. There may be multiple progenitor channels even for normal SNe Ia, and these may make varying contributions to the total rate at different redshifts.

One approach to this problem is the analysis of peculiar SNe Ia. Explaining such objects, we accumulate knowledge on what can cause extreme variations in the observables. Gaining knowledge about the nature of peculiar SNe means gaining knowledge on what normal SNe *are not*. Thus, an analysis of extreme objects contributes to a general understanding of SNe Ia.

In terms of numerical radiative transfer, analyses of SNe Ia (and Ic) are simpler than those of SNe containing He or H: we do not use the NLTE module presented in Chapter 2, Sec. 2.2.4. In the simultaneous iteration of the gas state with the radiation field, only the nebular approximation is used to describe the state of the gas (cf. 2.1.3.4). This makes the code very fast and allows us to run a large number of models for each observed object we analyse.

3.1 SN 2005bl

First, we analyse the 91bg-like SN 2005bl (Taubenberger et al. 2008). SNe Ia of the 91bg subclass are dim and decline rapidly [Fig. 3.1, see also Filippenko et al. (1992), Leibundgut et al. (1993), Turatto et al. (1996) and Garnavich et al. (2004)]. They were used, with other SNe, to infer the slope of the relation between luminosity and decline rate of SNe Ia (Phillips 1993), but later it became clear that dim SNe decline even more rapidly than expected from a linear luminosity−decline-rate relation for normal SNe (Phillips et al. 1999; Taubenberger et al. 2008). Spectroscopically, 91bg-like SNe show characteristic peculiarities, such as low line velocities around B maximum (e.g. Filippenko et al. 1992) and clear spectral signatures of Ti II, indicating lower ionisation (Mazzali et al. 1997). All these properties together are consistent with a low mass of newly-synthesised ^{56}Ni. Before our investigation, no elaborate explosion models have convincingly reproduced 91bg-like SNe Ia.

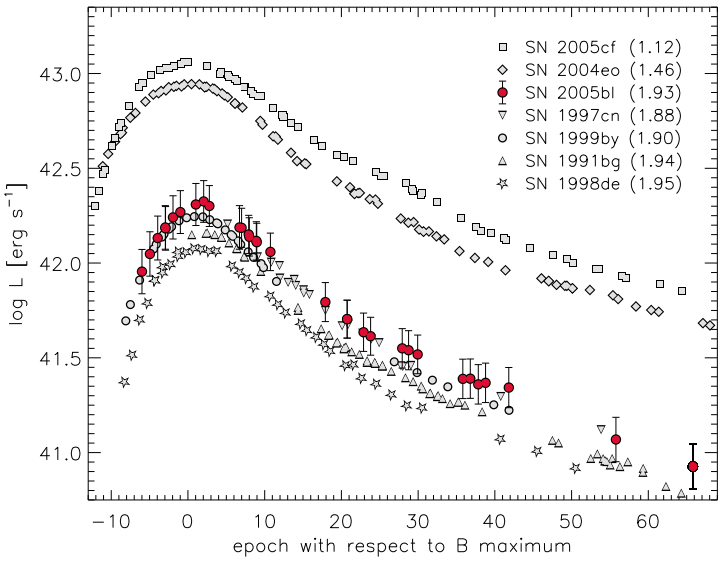

Figure 3.1: Light curve of the 91bg-like SN 2005bl compared to normal (SN 2005cf, SN 2004eo) and 91bg-like (SN 1997cn,SN 1999by,SN 1991bg,SN 1998de) SNe Ia. Plot: Taubenberger et al. (2008) – data sources: see their paper.

Table 3.1: Density models used in this work, and their total kinetic energy $E'_{\rm k}$ and mass M'. The models are named according to the scaling factors for kinetic energy and mass with respect to W7 $\left(\frac{E'_{\rm k}}{E_{{\rm k},W7}}\right.$ and $\left.\frac{M'}{M_{W7}}\right)$, and sorted according to their kinetic energy $E'_{\rm k}$.

Model	$E'_{\rm k}/E_{{\rm k},W7}$	M'/M_{W7}	$E'_{\rm k}$ [10^{51} erg]	M' [$M_\odot$]	$\frac{E'_{\rm k}}{M'}\Big/\left(\frac{E_{\rm k}}{M}\right)_{W7}$
w7e0.35	0.35	1.00	0.47	1.38	0.35
w7e0.5m0.5	0.50	0.50	0.66	0.69	1.0
w7e0.5m0.7	0.50	0.70	0.66	0.97	0.7
w7e0.5	0.50	1.00	0.66	1.38	0.5
w7e0.5m1.25	0.50	1.25	0.66	1.73	0.4
w7e0.7m0.7	0.70	0.70	0.93	0.97	1.0
w7e0.7	0.70	1.00	0.93	1.38	0.7
w7e0.7m1.25	0.70	1.25	0.93	1.73	0.6
w7e0.7m1.45	0.70	1.45	0.93	2.00	0.5
w7m0.7	1.00	0.70	1.33	0.97	1.4
w7	1.00	1.00	1.33	1.38	1.0
w7m1.25	1.00	1.25	1.33	1.73	0.8
w7m1.45	1.00	1.45	1.33	2.00	0.7
w7e1.45m1.45	1.45	1.45	1.93	2.00	1.0

Modelling a time series of spectra, we infer the abundance profile from the outer envelope to as deep a layer as possible. We then test whether variations in mass or explosion energy are needed to explain the differences between spectra of normal and dim SNe Ia. This is done performing abundance tomography with various density profiles, and assessing the quality of the resulting spectral fits.

3.1.1 Density profiles

As a first step, we adopt the density structure of the standard explosion model W7 (Nomoto et al. 1984) as a basis for our calculations. We then repeat the abundance tomography with modified density profiles, representing explosions with a different to-

tal mass and kinetic energy. To obtain the modified profiles, the values for each grid point in the W7 velocity-density structure are scaled uniformly (i.e. all velocities by one scaling factor, and all densities by another one) according to:

$$\rho' = \rho_{W7} \times \left(\frac{E'_{\rm k}}{E_{{\rm k},W7}}\right)^{-3/2} \times \left(\frac{M'}{M_{W7}}\right)^{5/2} \quad (3.1)$$

$$v' = v_{W7} \times \left(\frac{E'_{\rm k}}{E_{{\rm k},W7}}\right)^{1/2} \times \left(\frac{M'}{M_{W7}}\right)^{-1/2} . \quad (3.2)$$

Here, ρ' and v' are the density and velocity coordinates of each grid point after the scaling. $E'_{\rm k}$ and M' are the new total kinetic energy and mass.

The scaled density models used in this work are listed in Table 3.1, which gives an overview of the respective $\frac{E'_{\rm k}}{E_{\rm k}}$ and $\frac{M'}{M}$ ratios. The range in masses and energies sampled by the modified models starts at $0.5\times M_{\rm Ch,non\text{-}rot}$ / $\sim 5\times 10^{50}$erg and extends to $1.45\times M_{\rm Ch,non\text{-}rot}$ / $\sim 2\times 10^{51}$erg ($M_{\rm Ch,non\text{-}rot}$: Chandrasekhar mass for non-rotating WDs, $1.38 M_{\odot}$). This choice has been motivated by parameters inferred for observed extreme SNe Ia of all kinds (Mazzali et al. 1997; Howell et al. 2006). We have however not implemented every possible energy-mass combination within these limits. Instead, we first constrained ourselves to a few test cases. Then, we sampled the $E'_{\rm k}-M'$ plane more densely in the region where models of acceptable quality emerged (see Sec. 3.1.3.1).

W7 naturally shows some differences with respect to more recent and realistic hydrodynamical simulations, and the scaled density profiles can also be expected to do so. However, it is possible to obtain good fits to spectra of "normal" SNe Ia like SN 2002bo (Stehle et al. 2005) using the W7 density structure. The results for the scaled profiles should therefore bring out possible differences between dim SNe Ia and normal ones.

3.1.2 Models

We analyse five spectra of SN 2005bl, taken at -6 d, -5 d, -3 d, $+4.8$ d and $+12.9$ d with respect to B maximum. Observational data and one-zone spectral models have already been presented in Taubenberger et al. (2008). As in that paper, we assume a total reddening of $E(B-V)$=0.20 and a B-band rise time of 17 d to calculate the time t from the onset of the explosion.

Later spectra were not modelled, as the photosphere has already receded to $v_{\rm ph}<3500$ km s^{-1} at $+12.9$ d [for comparison, Mazzali et al. (2008) found $v_{\rm ph}$=4700 km s^{-1} at $+14$ d and $v_{\rm ph}$=2800 km s^{-1} at $+21$ d in SN 2004eo]. As the photosphere reaches the ^{56}Ni-rich zone, some energy deposition should realistically take place above the photosphere itself. This is is not taken into account in our code. Thus, to explore the innermost layers one would need to model nebular spectra (which are not available for SN 2005bl) at least as a consistency check.

The outermost ejecta of SNe Ia may partly consist of unburned material (cf. Mazzali et al. 2007). As the one-zone models for SN 2005bl (Taubenberger et al. 2008) showed too much absorption by burned material at high velocities, we introduced a zone with strongly reduced abundances of burning products above $v\gtrsim 15000$ km s^{-1}. This was done limiting the mass fractions of burning products in this zone to $\lesssim\frac{1}{10}$ their value at the photosphere at -6 d. The unburned material at $v\gtrsim 15000$ km s^{-1}, which then constitutes $\gtrsim 98\%$ by mass at these velocities, is assumed to consist of carbon and

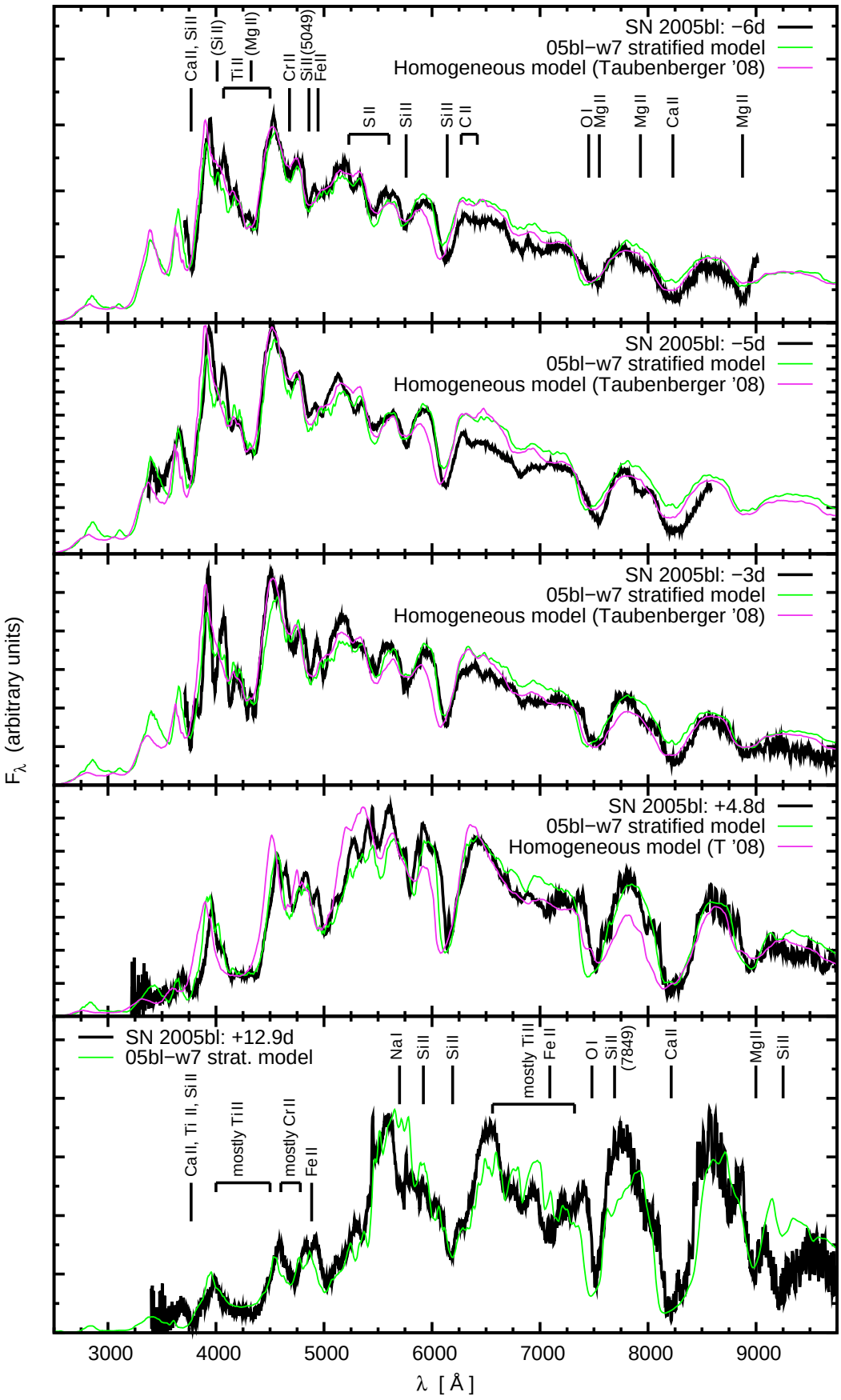

Figure 3.2: Model sequence based on the W7 density profile (05bl-w7 sequence, green lines). Observed spectra (black lines) and one-zone model spectra (magenta lines) from Taubenberger et al. (2008), which only extend to +4.8 d, are shown for comparison. Identifications of the most prominent features are given at the beginning and the end of the sequence. Especially in the +12.9 d spectrum, many blends appear, so that the identifications are only approximate.

oxygen in a $\sim$1:1 ratio. In a preliminary stratified-abundance model, this was found clearly to improve the synthetic spectra, also with respect to the one-zone models (cf. Sec. 3.1.2.2). Consequently, we implemented such a zone in all our stratified-abundance models (except when using the w7e0.35 density profile, which has negligible densities in the outer layers).

Below, we first discuss an abundance tomography experiment based on the original W7 density structure. We compare our synthetic spectra with the observed ones and with the one-zone model spectra of Taubenberger et al. (2008). After discussing the abundance profile, we then present models with different total mass and kinetic energy. Parameters (abundances, photospheric velocities, etc.) of all models are compiled in Appendix 3.1.2.9.

3.1.2.1 Abundance tomography based on W7

The spectral models discussed here are shown in Fig. 3.2, where the most important spectral features are marked.

2005 April 16: -6 d, v_{ph}=8400 km s^{-1}

At this epoch, the supernova shows a spectrum dominated by singly-ionised species. In normal SNe, usually also doubly-ionised species are detected at such early epochs (e.g. Mazzali et al. 2008). The zone between 8400 and 15000 km s^{-1} is dominated by oxygen. The absence of the Si II λ 6355 emission peak suggests absorption by C II λ 6580. However, the mass fraction of C between 8400 and 15000 km s^{-1} must be $<10\%$; otherwise the C II feature would become too deep. Burned material (oxygen as a burning product excluded) makes up for no more than $\sim$15% in mass according to the observed line depths.

While numerous lines of intermediate-mass elements (IME) are visible, there are no absorptions that can unambiguously be attributed to Fe. We determined an upper limit to the Fe abundance of 0.01%, avoiding the appearance of a spurious Fe II feature at $\sim$4950 Å. Yet, some burning products heavier than Si and S are seen in the spectra: some per mille of Ti and Cr are necessary to model the absorption trough at $\sim$4100 Å and the feature at $\sim$4700 Å, respectively. These elements also contribute significantly to line blocking in the UV (Sauer et al. 2008).

2005 April 17: -5 d, v_{ph}=8100 km s^{-1}

The April 17 spectrum is very similar to the previous one. As the material directly above the photosphere is highly ionised, many features in this spectrum depend strongly on the abundances above 8400 km s^{-1}.

At $\sim$4950 Å, the stratified model has an absorption trough too deep. This is mostly due to the Si II λ 5049 line, whose strength largely depends on the Si abundance above v=8400 km s^{-1}. We chose this abundance so as to match the Si II λ 5972 line of this and the previous spectrum, and a simultaneous match of the Si II λ 5049 line was not possible. Apart from this and some flux mismatch in the red, the observations are fitted well.

2005 April 19: −3 d, v_{ph}=7500 km s^{-1}

This model again matches the observed spectrum nicely in most regions. The Ti-dominated trough at ∼4100Å is now deeper than in the earlier spectra, and relatively hard to fit. A good model requires Ti abundances of the order of a few percent at the photosphere, and relatively large Ti abundances in the zones above. Thus, we set the Ti mass fraction to 1% between 8100 and 8400 km s^{-1}. At larger velocities, the abundances are sharply constrained to some per mille by the features in the −6 d spectrum.

There is still no evidence for significant amounts of Fe in the spectrum. Fe mass fractions of a few per cent in the layers between 7500 and 8400 km s^{-1} are compatible with the observations, but not strictly required.

2005 April 26: +4.8 d, v_{ph}=6600 km s^{-1}

In order to fit this spectrum with its low flux in the UV and blue, the model atmosphere must contain sufficient amounts of Ti, Cr and Fe. The layers at v>8400 km s^{-1} contain relatively small amounts of these elements, as dictated by the pre-maximum spectral features and UV flux. To compensate for this, large amounts are needed close to the photosphere. While the flux-blocking in the UV is quite sensitive to the abundances close to the photosphere, the depth of individual features (such as Si II λ 5972) is still more strongly influenced by the composition at >8400 km s^{-1}.

The most notable deviation the model from the observed spectrum occurs in the blue wing of O I λ 7773, where there is too much absorption. In the outermost zone, O could only be replaced by C, but we already have a ∼1:1 C-O mixture there. If we wanted to reduce the O I absorption strength by a factor of 2 in these layers, we would have to postulate a ∼3:1 C-O mixture, which would seem quite ad-hoc. In the layers between 8400 and 15000 km s^{-1}, the amount of oxygen cannot be reduced (cf. discussion of the April 16 spectrum). In Sec. 3.1.2.6, we will show that a reduction of the density in the outer layers can cure this problem.

There is some mismatch around 5700 Å, which seems to be caused by a low pseudo-continuum. This impression is however also due to Na I D absorption at the peak between the S II trough and the Si II λ 5972 feature. We introduced a small amount of Na above 8100 km s^{-1} to obtain at least some Na I D absorption at +12.9 d. The spurious absorption appearing at +4.8 d then indicates inaccuracies in the Na ionisation profile and its evolution with time, a common issue with synthetic spectra (Mazzali et al. 1997).

2005 May 04: +12.9 d, v_{ph}=3250 km s^{-1}

This model carries some conceptual uncertainty, as a possible energy deposition by ^{56}Ni above the photosphere is not simulated in our code. Yet, the overall fit is satisfactory. Some incompatibilities with the abundances inferred for the outer layers could not be resolved. It was, for example, impossible to get rid of the absorptions at ∼6500 and ∼7700 Å, which are due to Ti II $\lambda\lambda$ 6680,6718,6785 and Si II λ 7849, respectively. These lines were not visible in the earlier spectra.

The photosphere is now deep inside the Si-dominated zone. The extended red wing of the observed feature at ∼9000 Å, caused mostly by Si II λ 9242, indicates a large Si mass fraction. On the other hand, the small flux in the blue and UV already demands a larger fraction of Fe-group elements. While the exact amounts of Fe, Co and Ni are somewhat uncertain, their sum can be estimated to be ∼30%. The exact number depends

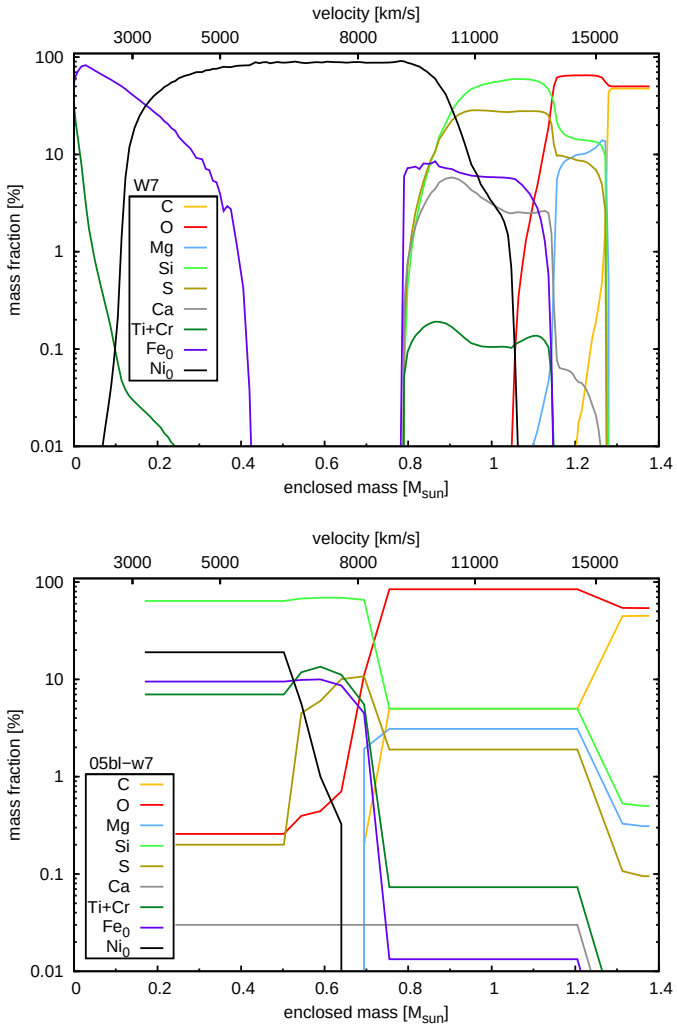

Figure 3.3: Abundances of W7 nucleosynthesis calculations (Iwamoto et al. 1999, top panel) vs. abundance tomography of SN 2005bl, based on the original W7 density profile (05bl-w7 model, bottom panel).

on the abundances of other elements blocking UV flux (mostly Ti and Cr) between 3250 and 6600 km s^{-1}, which are somewhat uncertain.

3.1.2.2 Comparison to one-zone models

Compared to one-zone models [Taubenberger et al. (2008), shown in Fig. 3.2 as the magenta line], the stratified model sequence clearly constitutes an improvement in fitting the observations. The main reason for this is the C/O-dominated shell introduced at v>15000 km s^{-1}, which makes spectral lines of burned material narrower. The changes with respect to the one-zone model are especially apparent in the pre-maximum spectra: the Ca II H&K and Si II λ 6355 lines absorb less at high velocities, so that in the blue wings of the features only small mismatches are left. The Ti II-dominated trough around 4100 Å now has more structure. Some deviations, even a bit more apparent then in the one-zone models, remain in the red wing of Si II λ 6355 in the earliest spectra. This is largely due to re-emission in this wavelength range, caused by elements such as Ti and

Cr which block and redistribute UV flux. These elements are, however, necessary to model the spectral features (see Sec. 3.1.2.1).

3.1.2.3 Abundance profile

In Fig. 3.3, we compare the abundance profile derived in our tomography experiment to the nucleosynthesis in W7 (Iwamoto et al. 1999), which approximately represents a normally-luminous SN Ia (Nomoto et al. 1984). In our models, unburned material (counting in all of the oxygen) constitutes a much larger fraction of the ejecta, almost the outer $\sim 0.7 M_\odot$. Our analysis of the outer layers is still a bit coarse. A better-resolved analysis, yielding more exact results e.g. for the amount of IME between 8400 and 15000 km s^{-1}, would be possible if spectra at earlier epochs were available (see Sec. 3.1.3.4).

Below the outer $\sim 0.7 M_\odot$, the ejecta of SN 2005bl are dominated by IME. The transition happens in the zone between 6400 and 8400 km s^{-1}. The exact transition velocity is difficult to infer, as the post-maximum spectra show only a limited sensitivity to the Si abundances below 8400 km s^{-1}. Mazzali et al. (1997) have conducted a fine analysis of the O I λ 7773 line profile in SN 1991bg, and found a lower cut-off velocity of 8600 km s^{-1} for O. We thus implemented a relatively sharp decrease of the O abundance in favour of Si below the -6 d photosphere.

The layers between 6400 and 8400 km s^{-1} already consist of $\sim 100\%$ ^{56}Ni in W7. We, in contrast, find (besides IME) comparatively large abundances of Ti and Cr as products of incomplete burning at these velocities (peak values in the order of some per cent). These elements contribute to the formation of the observed trough around $\sim$4200 Å which is characteristic of 91bg-like objects past maximum, but also to the line blocking in the UV. To some extent, their effects can also be mimicked by Fe, Co and Ni. With overly large amounts of Fe, however, individual lines in the optical may show up, and the flux distribution in the UV and blue may deviate from what is observed. Large abundances of ^{56}Ni or its decay product ^{56}Co outside the centre would be in conflict with the nebular spectra of dim SNe Ia, which show very narrow lines (Mazzali et al. 1997).

The deepest zones that we reach with our analysis are still dominated by IME. However, there are signs of a transition to the NSE-burning zone: the large amount of line blocking and flux redistribution needed to fit the $+12.9$ d spectrum clearly points towards Fe-group abundances of several 10%.

Compared to the one-zone models of Taubenberger et al. (2008) epoch by epoch, the abundances of burning products at the respective photospheres are larger. In a model with homogeneous composition, the inferred abundances will always be some average between those at the photosphere and those further outwards, where less burning products are present.

3.1.2.4 Models with modified density profiles

We now show some representative spectral models based on modified density profiles (Sec. 3.1.1). The reader interested in the abundances is referred to subsection 3.1.3.3 and Appendix 3.1.2.9. Here, we focus on the differences in the spectra with respect to the W7-based models. To facilitate the understanding of these differences, we first discuss the properties of the scaled density models.

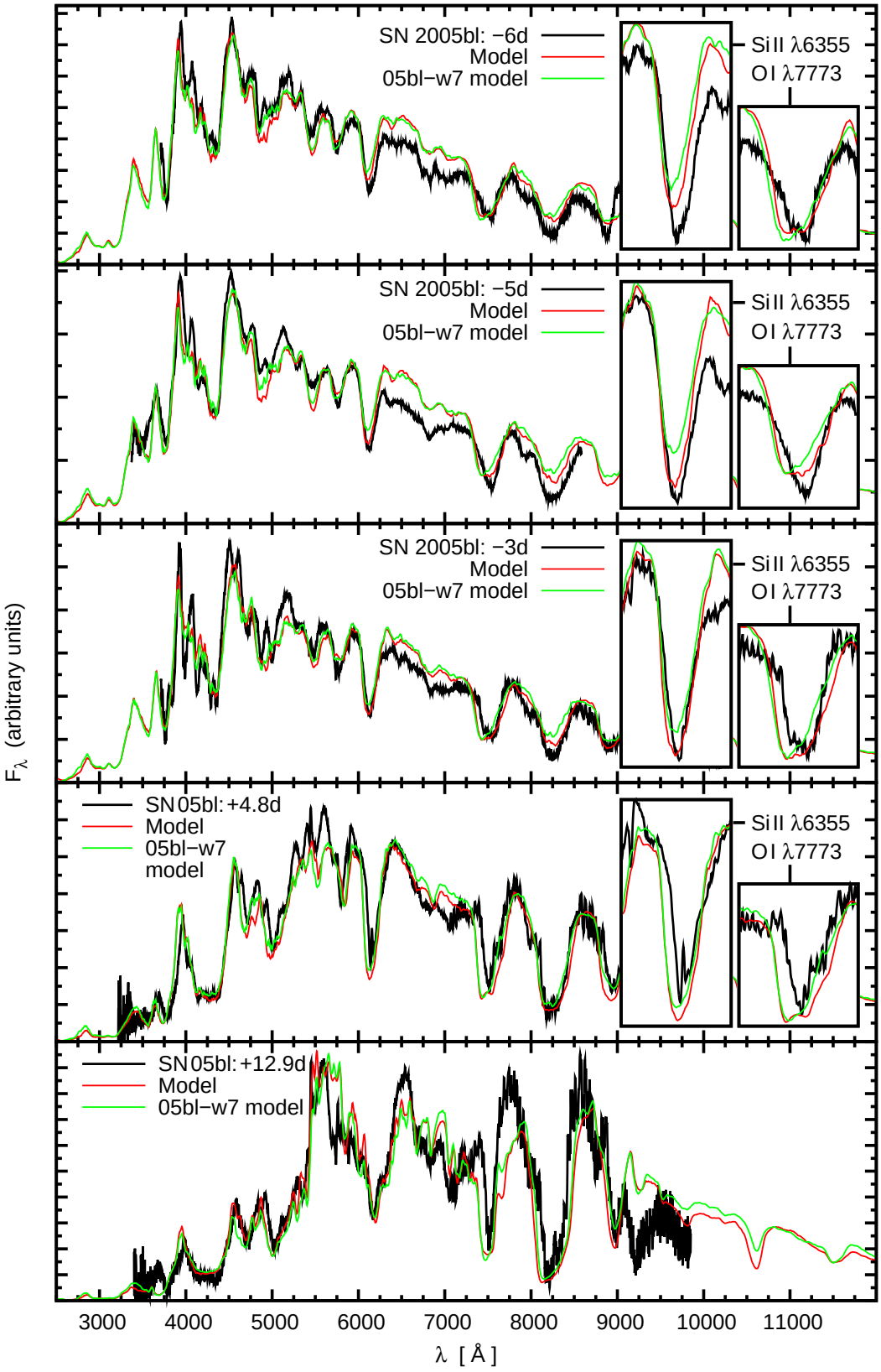

Figure 3.4: 05bl-w7e0.7m0.7 model sequence, based on the w7e0.7m0.7 density profile (red lines). Observed spectra (black lines) and 05bl-w7 spectra from Fig. 3.2 (green lines) are given for comparison. For all epochs except the last one, insets show the Si II λ 6355 and O I λ 7773 features in detail. Changes in the density profile usually manifest themselves most clearly in these two features (see also Sec. 3.1.3.1).

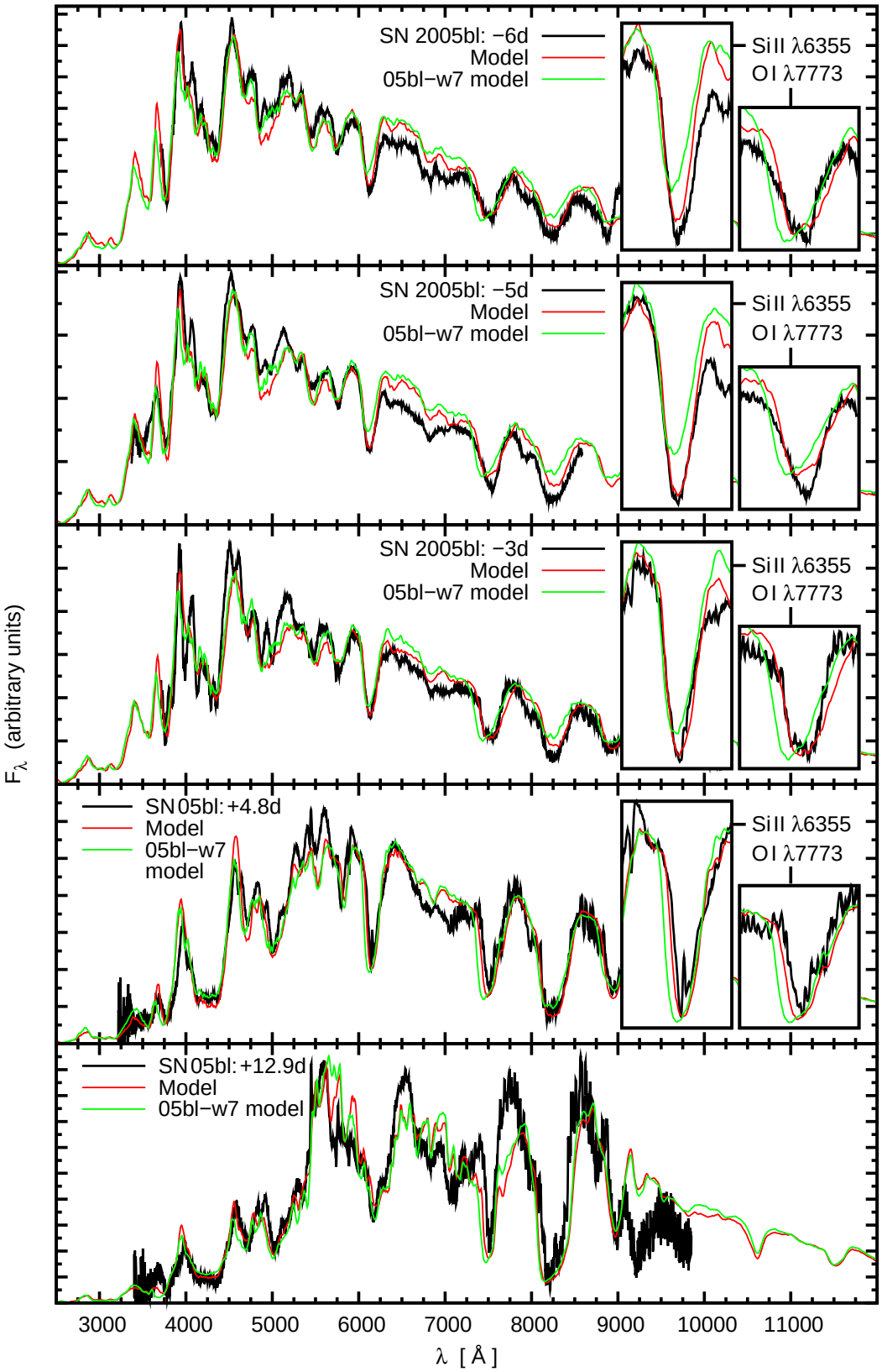

Figure 3.5: 05bl-w7e0.7 model sequence (red lines); plot analogous to Fig. 3.4.

Our scaled density models span a range of masses and kinetic energies (see Table 3.1). Scaling the total mass and energy, the amplitude and/or form of the W7 density structure is changed. What exactly happens depends on the $\frac{E'_{\rm k}}{M'}$ ratio of the final profile with respect to $\frac{E_{W7}}{M_{W7}}$. Here, we distinguish the following three cases, which result in three classes of scaled density profiles:

$\frac{E'_{\rm k}}{M'} = \frac{E_{W7}}{M_{W7}}$: In this case, the scaled velocity-density profile is obtained from W7 by reducing the density at each velocity by a uniform factor. The form of the density profile in velocity space is thus left unchanged.

$\frac{E'_{\rm k}}{M'} < \frac{E_{W7}}{M_{W7}}$: Here, the energy per unit mass is reduced. This means that mass elements are "shifted" towards lower velocities. The density profile becomes steeper in velocity space, and the relative amount of mass at high velocities is smaller.

$\frac{E'_{\rm k}}{M'} > \frac{E_{W7}}{M_{W7}}$: Increasing the energy per unit mass "shifts" material outwards, opposite to the case before. As the spectra of 91bg-like SNe Ia lack absorption at high velocities in *all* lines, this is generally disfavoured. Thus, we calculated only one model sequence with such a density profile (w7m0.7).

The models we discuss below are exemplary for these three scaling types. They are named after the underlying density models (e.g. 05bl-w7m0.7 is based on w7m0.7).

3.1.2.5 Reduced mass and energy, $\frac{E'_{\rm k}}{M'} = \frac{E_{W7}}{M_{W7}}$: 05bl-w7e0.7m0.7

In these models, the density is decreased at all radii. This leads to a slight improvement of the spectra (Fig. 3.4), as the photospheres are deeper inside the ejecta, and the absorption velocities tend to be lower. Owing to the lower densities, larger mass fractions of burned material are necessary to fit the line depths. At high velocities, however, oxygen still dominates and the high-velocity absorption in the O I λ 7773 line only becomes a bit weaker.

3.1.2.6 Reduced energy, $\frac{E'_{\rm k}}{M'} < \frac{E_{W7}}{M_{W7}}$: 05bl-w7e0.7

In the w7e0.7 density profile (Fig. 3.5), the densities are significantly increased below $\sim$6500 km s^{-1} and decreased above $\sim$13000 km s^{-1}. Thus, the spectral features become narrower compared to the W7-based sequence. Line widths and positions now generally fit the structure of the observed spectra better.

Owing to the lower densities in the outer part, there is less line blocking by heavy elements. This decreases the flux redistribution, so that the flux level in the red wing of Si II λ 6355 and redwards is matched better, especially at early times.

At the same time, the spurious high-velocity absorption is practically gone in Ca H&K and Si II λ 6355, but even more importantly in O I λ 7773. The reason for this is again the decreased density in the outer layers. As the abundances in the outer layers, especially of oxygen, are not fundamentally changed with the density modification, the decrease in density translates into weaker absorption at high velocities.

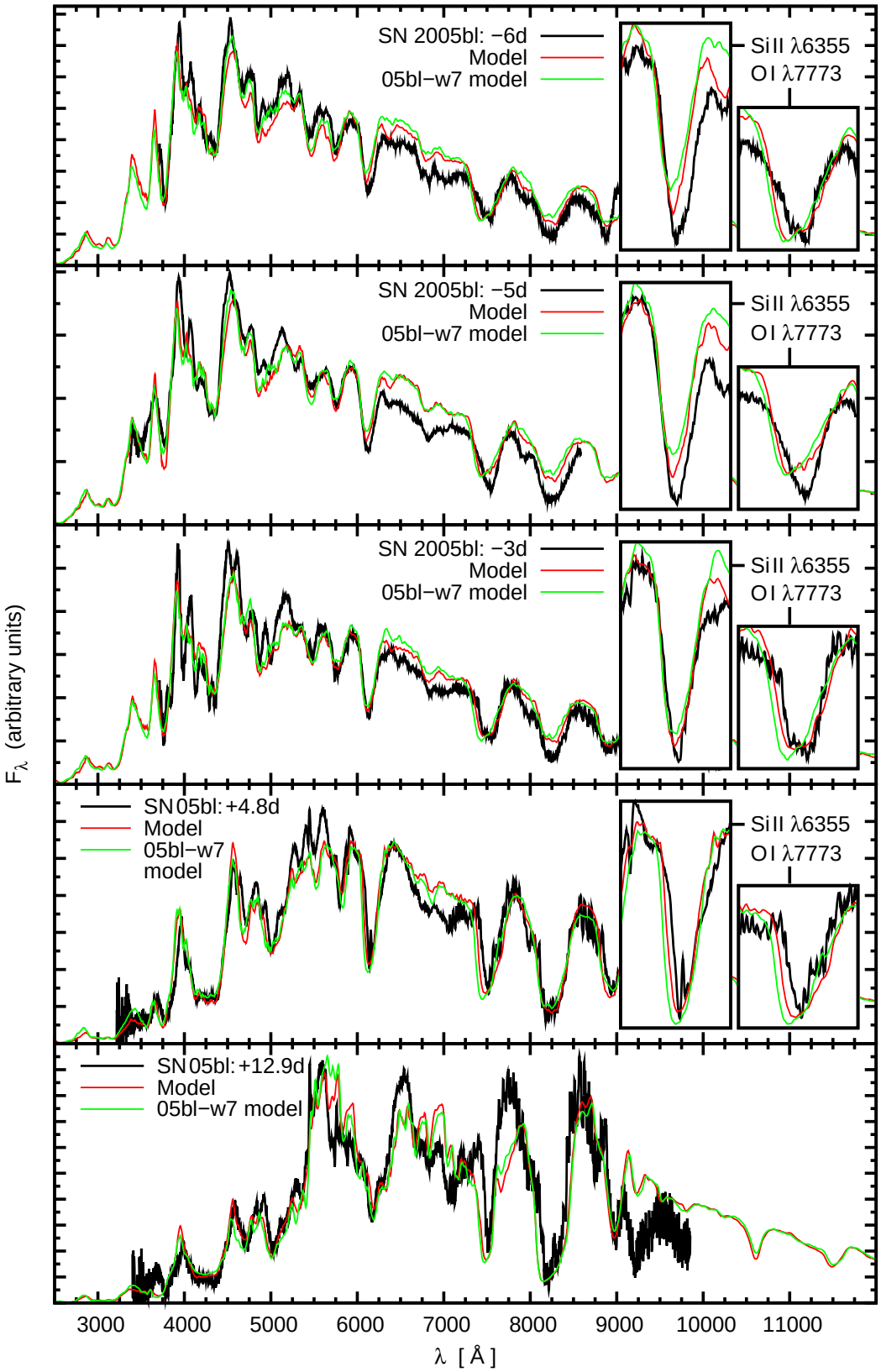

Figure 3.6: 05bl-w7m1.25 model sequence (red lines); plot analogous to Fig. 3.4.

3.1.2.7 Increased mass, $\frac{E'_{\rm k}}{M'} < \frac{E_{W7}}{M_{W7}}$: 05bl-w7m1.25

Despite the larger mass, the 05bl-w7m1.25 spectra show a somewhat improved quality compared to W7 (Fig. 3.6, see also line velocity measurements in Sec. 3.1.3.1). This illustrates that a super-Chandrasekhar total mass is not necessarily incompatible with the spectra of SN 2005bl. Note that the improvement over the W7-based sequence is due to *decreased* densities in the outermost layers ($v \gtrsim 15000$ km s^{-1}) of the warped density profile.

3.1.2.8 Reduced mass, $\frac{E'_{\rm k}}{M'} > \frac{E_{W7}}{M_{W7}}$: 05bl-w7m0.7

Here, the densities in the outermost layers are increased with respect to W7. This can directly be seen in the spectra (Fig. 3.7): all the problems which are reduced in 05bl-w7e0.7 (compared to the original W7-based model sequence) are now exacerbated.

3.1.2.9 Parameters of the models

Table 3.2 shows the code input parameters of all spectral models mentioned. Apart from the abundances, we give the photospheric velocity $v_{\rm ph}$, the time from explosion t (see main text) and the bolometric luminosity $L_{\rm bol}$. For different models of a given spectrum, these luminosities can differ a bit, depending on the model spectral energy distribution. In addition to the input values, Table 3.2 also gives the calculated temperature of the photospheric black body emission, $T_{\rm BB}$, for each model.

3.1.3 Discussion

3.1.3.1 Assessment of the models based on different density profiles – mass and kinetic energy of dim SNe Ia.

Having discussed some representative cases in subsection 3.1.2.4, we now systematically compare all models calculated on the basis of different density profiles. Our aim is to judge the quality of each model sequence in a simple and meaningful manner. To achieve this, we introduce three quality criteria:

1. *Consistency of spectra.* The main motivation to test modifications of the density were mismatches in the line velocities or widths remaining in the W7-based model sequence, especially in O I λ 7773 and Si II λ 6355. Other lines of the spectrum did not show deviations as apparent, apart from Ca II H&K, which behaves quite similar to Si II λ 6355[a)]. To assess if the lines are better fitted using different density profiles, we measured the velocities of O I λ 7773 and Si II λ 6355 in each synthetic and observed spectrum at -6 d, -3 d and $+4.8$ d. Then we calculated, for each model sequence and line, the velocity difference between the observed and the synthetic spectra, averaged over the epochs.

2. *Consistency of kinetic energy.* We calculated a hypothetical kinetic energy ($E_{\rm k,hyp}$) for each of the abundance profiles inferred. This is the nuclear energy release (assuming a pre-explosion composition of equal amounts C and O) minus the

[a)] Ca II H&K, Si II λ 6355 and O I λ 7773 are usually the strongest lines in our spectra, which therefore have the highest probability of developing high-velocity absorptions.

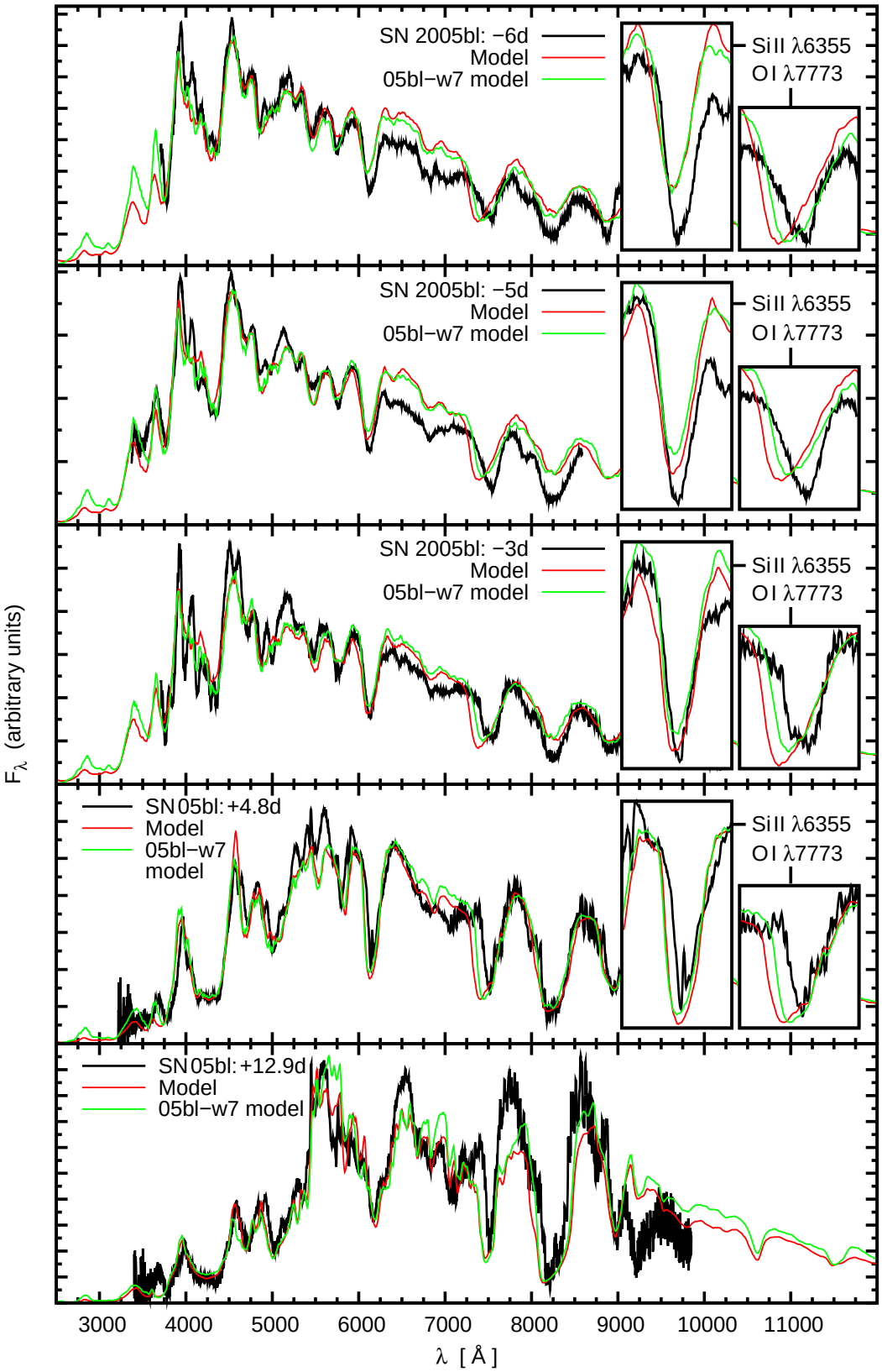

Figure 3.7: 05bl-w7m0.7 model sequence (red lines); plot analogous to Fig. 3.4.

Table 3.2: Parameters of the models for SN 2005bl. Abundances are given only for significant elements. The abundance values hold above the lower boundary $v_{\rm ph}$ of the respective layer.

Model	epochs	$\lg\left(\frac{L_{\rm bol}}{L_\odot}\right)$	$v_{\rm ph}$	$T_{\rm BB}$	Element abundances (mass fractions)											
	[d]		[km s^{-1}]	[K]	X(C)	X(O)	X(Na)	X(Mg)	X(Al)	X(Si)	X(S)	X(Ca)	X(Ti)	X(Cr)	X(Fe)$_0$[a)]	X(^{56}Ni)$_0$[a)]
05bl-w7e0.35	-6	8.520	8200	9574.5	0.05	0.87	0.0080	0.03	0.0025	0.04	0.00	0.0009	0.0016	0.0008	0.0017	0.0000
	-5	8.622	7975	10024.7	0.02	0.20	0.0050	0.03	0.0025	0.60	0.06	0.0009	0.0070	0.0035	0.0750	0.0000
	-3	8.753	7600	10377.4	0.00	0.15	0.0000	0.04	0.0015	0.50	0.13	0.0009	0.0500	0.0250	0.1000	0.0000
	4.8	8.870	7050	8658.6	0.00	0.11	0.0000	0.00	0.0000	0.55	0.04	0.0009	0.0850	0.0850	0.1100	0.0100
	12.9	8.609	3350	10611.0	0.00	0.08	0.0000	0.00	0.0000	0.65	0.00	0.0009	0.0111	0.0111	0.0800	0.1600
05bl-w7e0.5m0.5	-6	8.510	7600	9626.0	0.06	0.72	0.0080	0.13	0.0070	0.06	0.01	0.0010	0.0005	0.0007	0.0003	0.0000
	-5	8.618	7275	10220.3	0.03	0.17	0.0040	0.08	0.0070	0.60	0.01	0.0010	0.0300	0.0300	0.0400	0.0000
	-3	8.736	7000	10242.6	0.00	0.01	0.0000	0.00	0.0030	0.52	0.12	0.0010	0.1100	0.1100	0.1250	0.0000
	4.8	8.837	6400	8613.5	0.00	0.00	0.0000	0.00	0.0000	0.17	0.04	0.0010	0.2550	0.2550	0.2550	0.0100
	12.9	8.570	3250	9195.7	0.00	0.00	0.0000	0.00	0.0000	0.17	0.00	0.0010	0.2150	0.2150	0.1300	0.2600
05bl-w7e0.5m0.7	-6	8.520	7900	9734.1	0.06	0.83	0.0060	0.06	0.0025	0.03	0.01	0.0008	0.0005	0.0004	0.0004	0.0000
	-5	8.618	7600	10242.2	0.04	0.12	0.0030	0.04	0.0025	0.62	0.10	0.0008	0.0150	0.0150	0.0400	0.0000
	-3	8.740	7100	10727.9	0.00	0.03	0.0000	0.00	0.0017	0.55	0.15	0.0008	0.0750	0.0750	0.1200	0.0000
	4.8	8.845	6550	8764.9	0.00	0.00	0.0000	0.00	0.0000	0.53	0.05	0.0008	0.1225	0.1225	0.1650	0.0100
	12.9	8.590	3350	9582.3	0.00	0.00	0.0000	0.00	0.0000	0.68	0.00	0.0008	0.0400	0.0400	0.0800	0.1550
05bl-w7e0.5	-6	8.525	8300	9705.2	0.05	0.88	0.0070	0.03	0.0020	0.03	0.01	0.0004	0.0008	0.0004	0.0008	0.0000
	-5	8.625	8050	10185.4	0.02	0.12	0.0035	0.02	0.0020	0.70	0.07	0.0004	0.0300	0.0250	0.0100	0.0000
	-3	8.748	7550	10745.4	0.00	0.01	0.0000	0.00	0.0010	0.62	0.14	0.0004	0.0625	0.0625	0.1000	0.0000
	4.8	8.866	6900	8959.2	0.00	0.00	0.0000	0.00	0.0000	0.62	0.06	0.0004	0.0675	0.0675	0.1600	0.0100
	12.9	8.602	3350	10432.1	0.00	0.00	0.0000	0.00	0.0000	0.78	0.00	0.0004	0.0190	0.0190	0.0600	0.1200
05bl-w7e0.5m1.25	-6	8.517	8250	10038.1	0.05	0.87	0.0045	0.04	0.0018	0.03	0.00	0.0006	0.0010	0.0008	0.0013	0.0000
	-5	8.615	8000	10511.8	0.01	0.13	0.0045	0.04	0.0018	0.62	0.12	0.0006	0.0220	0.0220	0.0250	0.0000
	-3	8.748	7650	10658.7	0.00	0.02	0.0020	0.00	0.0010	0.64	0.16	0.0006	0.0600	0.0600	0.0600	0.0000
	4.8	8.861	7250	8628.6	0.00	0.00	0.0000	0.00	0.0000	0.65	0.07	0.0006	0.0900	0.0900	0.0850	0.0085
	12.9	8.595	3350	10835.7	0.00	0.00	0.0000	0.00	0.0000	0.82	0.00	0.0006	0.0070	0.0070	0.0500	0.1100
05bl-w7e0.7m0.7	-6	8.514	7950	9749.2	0.07	0.75	0.0050	0.10	0.0035	0.04	0.03	0.0009	0.0004	0.0004	0.0003	0.0000
	-5	8.619	7600	10346.2	0.02	0.10	0.0025	0.03	0.0035	0.70	0.07	0.0009	0.0200	0.0200	0.0300	0.0000
	-3	8.744	7100	10760.9	0.00	0.02	0.0000	0.00	0.0018	0.60	0.09	0.0009	0.0700	0.0700	0.1500	0.0000
	4.8	8.843	6550	8730.7	0.00	0.01	0.0000	0.00	0.0000	0.51	0.07	0.0009	0.1200	0.1200	0.1600	0.0100
	12.9	8.587	3250	9539.3	0.00	0.00	0.0000	0.00	0.0000	0.50	0.00	0.0009	0.0590	0.0590	0.1250	0.2500
05bl-w7e0.7	-6	8.520	8350	9764.8	0.06	0.86	0.0060	0.04	0.0025	0.02	0.01	0.0004	0.0004	0.0003	0.0003	0.0000
	-5	8.617	8100	10135.5	0.03	0.13	0.0030	0.03	0.0025	0.68	0.10	0.0004	0.0100	0.0070	0.0150	0.0000
	-3	8.745	7600	10632.8	0.00	0.01	0.0000	0.00	0.0015	0.70	0.11	0.0004	0.0533	0.0367	0.0900	0.0000
	4.8	8.861	6800	8930.6	0.00	0.00	0.0000	0.00	0.0000	0.71	0.07	0.0004	0.0550	0.0400	0.1150	0.0100
	12.9	8.594	3350	10071.5	0.00	0.00	0.0000	0.00	0.0000	0.77	0.00	0.0005	0.0167	0.0167	0.0650	0.1300
05bl-w7e0.7m1.25	-6	8.523	8700	9667.9	0.06	0.86	0.0045	0.03	0.0020	0.03	0.01	0.0006	0.0005	0.0005	0.0006	0.0000
	-5	8.623	8400	10101.1	0.03	0.13	0.0020	0.01	0.0020	0.70	0.10	0.0008	0.0100	0.0075	0.0100	0.0000
	-3	8.750	7950	10346.8	0.00	0.00	0.0000	0.00	0.0010	0.80	0.14	0.0008	0.0110	0.0080	0.0400	0.0000
	4.8	8.858	7150	8750.8	0.00	0.01	0.0000	0.00	0.0000	0.76	0.08	0.0008	0.0290	0.0240	0.0900	0.0100
	12.9	8.594	3350	10598.5	0.00	0.00	0.0000	0.00	0.0000	0.84	0.00	0.0008	0.0140	0.0140	0.0400	0.0800
05bl-w7e0.7m1.45	-6	8.519	8700	9896.0	0.09	0.82	0.0055	0.04	0.0020	0.03	0.01	0.0006	0.0006	0.0006	0.0009	0.0000
	-5	8.620	8450	10296.5	0.07	0.13	0.0030	0.04	0.0020	0.60	0.10	0.0006	0.0220	0.0220	0.0150	0.0000
	-3	8.752	8200	10222.8	0.00	0.01	0.0000	0.00	0.0010	0.76	0.12	0.0013	0.0275	0.0275	0.0450	0.0000
	4.8	8.864	7350	8761.1	0.00	0.01	0.0000	0.00	0.0000	0.78	0.07	0.0006	0.0333	0.0333	0.0700	0.0070
	12.9	8.605	3525	10682.2	0.00	0.00	0.0000	0.00	0.0000	0.87	0.00	0.0006	0.0170	0.0170	0.0250	0.0650
05bl-w7m0.7	-6	8.520	8150	9593.4	0.06	0.80	0.0060	0.05	0.0060	0.05	0.02	0.0010	0.0004	0.0008	0.0003	0.0000
	-5	8.630	7850	9927.4	0.03	0.11	0.0020	0.04	0.0050	0.72	0.07	0.0010	0.0050	0.0050	0.0050	0.0000
	-3	8.745	7475	9998.2	0.00	0.00	0.0000	0.00	0.0020	0.72	0.15	0.0010	0.0375	0.0375	0.0475	0.0000
	4.8	8.844	6550	8654.3	0.00	0.01	0.0000	0.00	0.0000	0.60	0.05	0.0010	0.0900	0.0900	0.1500	0.0100
	12.9	8.566	3250	9133.8	0.00	0.00	0.0000	0.00	0.0000	0.46	0.00	0.0005	0.0800	0.0800	0.1250	0.2500
05bl-w7	-6	8.525	8400	9845.6	0.05	0.84	0.0025	0.03	0.0032	0.05	0.02	0.0003	0.0004	0.0004	0.0001	0.0000
	-5	8.627	8100	10291.1	0.00	0.17	0.0013	0.04	0.0032	0.65	0.10	0.0003	0.0100	0.0100	0.0175	0.0000
	-3	8.754	7500	10859.7	0.00	0.01	0.0000	0.00	0.0011	0.69	0.12	0.0003	0.0500	0.0500	0.0800	0.0000
	4.8	8.859	6600	9110.3	0.00	0.00	0.0000	0.00	0.0000	0.69	0.06	0.0003	0.0675	0.0675	0.1000	0.0100
	12.9	8.594	3300	9957.4	0.00	0.00	0.0000	0.00	0.0000	0.64	0.00	0.0003	0.0350	0.0350	0.0950	0.1900
05bl-w7m1.25	-6	8.515	8800	9685.6	0.08	0.81	0.0040	0.05	0.0023	0.04	0.02	0.0003	0.0002	0.0002	0.0002	0.0000
	-5	8.622	8500	10207.5	0.05	0.12	0.0040	0.05	0.0023	0.65	0.08	0.0003	0.0160	0.0120	0.0190	0.0000
	-3	8.756	7950	10729.3	0.00	0.01	0.0000	0.00	0.0010	0.72	0.15	0.0003	0.0425	0.0400	0.0400	0.0000
	4.8	8.862	7000	8996.5	0.00	0.00	0.0000	0.00	0.0000	0.78	0.09	0.0003	0.0450	0.0450	0.0400	0.0050
	12.9	8.598	3325	10378.3	0.00	0.00	0.0000	0.00	0.0000	0.80	0.00	0.0003	0.0135	0.0135	0.0600	0.1100
05bl-w7m1.45	-6	8.520	8800	9990.6	0.06	0.83	0.0040	0.06	0.0020	0.04	0.01	0.0005	0.0003	0.0003	0.0006	0.0000
	-5	8.628	8550	10483.5	0.03	0.10	0.0020	0.04	0.0020	0.65	0.12	0.0005	0.0150	0.0150	0.0200	0.0000
	-3	8.758	8200	10562.5	0.00	0.01	0.0000	0.00	0.0010	0.78	0.10	0.0005	0.0275	0.0275	0.0525	0.0000
	4.8	8.861	7175	9017.1	0.00	0.01	0.0000	0.00	0.0000	0.78	0.08	0.0005	0.0300	0.0300	0.0700	0.0070
	12.9	8.605	3475	10418.1	0.00	0.00	0.0000	0.00	0.0000	0.87	0.00	0.0005	0.0097	0.0097	0.0350	0.0700
05bl-w7e1.45m1.45	-6	8.524	9000	10051.5	0.08	0.71	0.0043	0.10	0.0035	0.07	0.03	0.0002	0.0002	0.0003	0.0005	0.0000
	-5	8.623	8700	10534.9	0.09	0.12	0.0043	0.07	0.0035	0.55	0.10	0.0002	0.0225	0.0225	0.0200	0.0000
	-3	8.760	8100	11060.7	0.00	0.01	0.0000	0.01	0.0015	0.68	0.14	0.0002	0.0500	0.0500	0.0750	0.0000
	4.8	8.868	7000	9313.8	0.00	0.01	0.0000	0.00	0.0000	0.72	0.07	0.0002	0.0650	0.0650	0.0675	0.0067
	12.9	8.607	3450	10342.2	0.00	0.00	0.0000	0.00	0.0000	0.84	0.00	0.0002	0.0350	0.0350	0.0250	0.0600

[a)] The abundances of Fe, Co and Ni in our models are assumed to be the sum of ^{56}Ni and its decay chain products (^{56}Co and ^{56}Fe) on the one hand, and directly synthesised / progenitor Fe on the other hand. Thus, they are conveniently given in terms of the ^{56}Ni mass fraction at $t = 0$ [$X(^{56}\mathrm{Ni})_0$], the Fe abundance at $t = 0$ [$X(\mathrm{Fe})_0$], and the time from explosion onset t.

binding energy $|E_{\rm bind}|$ of the WD (gravitational energy[b)] minus thermal and, in case of rotation, rotational energy). To judge the quality of a model sequence, we then compared the kinetic energy assumed in the density scaling ($E'_{\rm k}$) to $E_{\rm k,hyp}$. The calculation of $E_{\rm k,hyp}$ depends on some assumptions, the first of which is that the mass fraction of IME in the obscured core below the $+12.9$ d photosphere is $\frac{1}{2}$ of that above the $+12.9$ d photosphere. Actually, this mass fraction may be between zero and the IME mass fraction above the $+12.9$ d photosphere. The possible error due to this is given below. The binding energy $|E_{\rm bind}|$ of the progenitors (except for the $0.69 M_\odot$ ones) was calculated following Yoon & Langer (2005), who assume a white dwarf rotation profile resulting from binary evolution. We used their "$BE(M;\rho_c)$" relation (eq. 33), assuming a central density ρ_c of $2.0\times10^9{\rm g/cm^3}$ (which is typical for WD ignition) for $M'\geq M_{\rm Ch,non\text{-}rot}$. For sub-Chandrasekhar WDs, the central densities are lower even in the absence of rotation. We assumed negligible rotation for these cases, and obtained the central density for a given mass inverting formula (22) of Yoon & Langer (2005)[c)]. Note that our energy criterion does not apply in the case of a double-degenerate progenitor system; the binding energy per unit mass is dramatically different in such a system.

3. *Expected light-curve width.* For models with good consistency based on the first two criteria, we additionally can check whether the density and abundance structure implies a width of the bolometric light curve ($\tau_{\rm LC}$) compatible with that of dim SNe Ia. We calculated an expected light curve width for each model sequence, following Mazzali et al. (2007), from the respective kinetic energy $E_{\rm k}$, ejecta mass M', and total masses of IME and NSE material $M_{\rm IME}, M_{\rm NSE}$ as:

$$\tau_{\rm LC} = \mathcal{N} \times \tilde{\kappa}^{\frac{1}{2}} E_{\rm k}^{-\frac{1}{4}} M'^{\frac{3}{4}}.$$

Here, $\tilde{\kappa} = (0.1 M_{\rm IME} + M_{\rm NSE})/M'$ is proportional to the opacity estimate of Mazzali et al. (2007), and $\mathcal{N}$ is a normalisation factor chosen so as to agree with their estimates of light-curve widths. In order to calculate $\tilde{\kappa}$, we can assume different burning efficiencies in the core, as above; additionally, we may adopt as $E_{\rm k}$ either the hypothetical value $E_{\rm k,hyp}$ or the value $E'_{\rm k}$ from the density scaling. We thus calculated again an average $\tau_{\rm LC}$ and an estimate of the error introduced by these degrees of freedom. In order to judge the models, the values $\tau_{\rm LC}$ were compared to $\tau_{\rm LC,dim}$=13.9 d, which is the average expected light curve width for the similarly dim SNe 1991bg and 1999by (Mazzali et al. 2007).

We now discuss the quality of the models in terms of the three criteria.

Line velocities – consistency of spectra

The differences in Doppler velocity of the O I λ 7773 and Si II λ 6355 lines between observed and synthetic spectra are shown in Table 3.3. In this table, the models are

[b)] By "binding energy" and "gravitational energy" we always mean the absolute values here, i.e. we treat them as positive numbers.

[c)] This formula cannot be applied for our lowest-mass models. Therefore, we inferred the binding energy of a $0.69 M_\odot$ progenitor from a WD model with constant temperature, which uses the Timmes equation of state (Timmes & Arnett 1999). This equation of state takes into account a variable degree of electron degeneracy.

Table 3.3: Time-averaged line velocity differences in Si II λ 6355 and O I λ 7773 from models to observed spectra (denoted by $\langle\Delta v(\text{Si II } \lambda 6355)\rangle$ and $\langle\Delta v(\text{O I}\lambda 7773)\rangle$, respectively). Positive differences mean that the lines are too fast (blue) in the synthetic spectra. The models are sorted according to the mean velocity difference averaged among both lines (ascending in absolute value).

Model	$E'_{\rm k}/E_{{\rm k},W7}$	M'/M_{W7}	$\langle\Delta v(\text{Si II } \lambda 6355)\rangle$	$\langle\Delta v(\text{O I } \lambda 7773)\rangle$	$\langle\Delta v\rangle$
05bl-w7e0.7	0.70	1.00	64.1	-54.7	4.7
05bl-w7m1.45	1.00	1.45	206.0	86.6	146.3
05bl-w7e0.5m0.7	0.50	0.70	-26.5	-283.8	-155.1
05bl-w7e0.7m1.25	0.70	1.25	-117.2	-386.0	-251.6
05bl-w7e0.5m0.5	0.50	0.50	292.2	222.2	257.2
05bl-w7m1.25	1.00	1.25	368.1	359.5	363.8
05bl-w7e0.7m0.7	0.70	0.70	380.4	454.9	417.7
05bl-w7e0.5	0.50	1.00	-325.5	-618.0	-471.7
05bl-w7e0.7m1.45	0.70	1.45	-223.4	-798.2	-510.8
05bl-w7	1.00	1.00	494.7	1012.4	753.5
05bl-w7e1.45m1.45	1.45	1.45	594.9	942.8	768.8
05bl-w7e0.5m1.25	0.50	1.25	-592.6	-976.9	-784.7
05bl-w7e0.35	0.35	1.00	-846.7	-1131.7	-989.2
05bl-w7m0.7	1.00	0.70	457.9	1815.7	1136.8

ranked according to the absolute value of the "mean velocity difference", which is the average over both lines and all epochs.

A decent match of line velocity is obtained especially for the 05bl-w7e0.7 model, but also, for example, for some super-Chandrasekhar mass models with $E'_{\rm k}/M'$ lower than W7. This shows that a reduced density in the outer layers is the key to a better fit in the lines. To fit the observed lines well, models near the Chandrasekhar mass need a $E'_{\rm k}/M'$ smaller by $\sim$30$-$40% with respect to W7. With too large a reduction in energy, line velocities become too low (see e.g. negative velocity differences for the 05bl-w7e0.5 model). At low masses, generally a smaller reduction in $E'_{\rm k}/M'$ suffices: 05bl-w7e0.5m0.5 (M'=0.69$M_\odot$) as an extreme model still gives a satisfactory fit with $E'_{\rm k}/M'$=$(E_{\rm k}/M)_{W7}$.

Remarkably, for all mass values probed in this work, a reasonably good model can be obtained (judged by the line velocities). The kinetic energy $E'_{\rm k}$ of all well-fitting models, however, is lower than $E_{{\rm k},W7}$.

Energetic consistency

In Table 3.4 we show our hypothetical kinetic energy values, as well as the quantities from which they were calculated. We then judge the models by the ratio of $E_{\rm k,hyp}$ to the kinetic energy assumed in the density scaling ($E'_{\rm k}$). Ideally, this ratio should be equal to one; the larger the deviation, the lower the rank of a model.

For density profiles with the same mass, but different kinetic energy $E'_{\rm k}$, the hypothetical kinetic energy $E_{\rm k,hyp}$ usually varies systematically. In density models with smaller $E'_{\rm k}$, densities are reduced in the high-velocity layers (see Sec. 3.1.2.6), which contain mostly unburned material. At the same time, densities are increased in lower layers, where the material is mostly burned. The velocity at which the transition (between unburned and burned material) happens does not vary much from model to model as it is constrained by spectral features. Therefore, the change in the density profile

Table 3.4: Energetic balance of the models (see text for a description of the quantities). The models are ordered according to the deviation of their $\frac{E_{\rm k,hyp}}{E'_{\rm k}}$ ratio from 1 (cf. last column).

Model	$E'_{\rm k}/E_{{\rm k},W7}$	M'/M_{W7}	$E'_{\rm k}$	$E_{\rm nucl}$	$E_{\rm bind}$	$E_{\rm k,hyp}$[a]	$\frac{E_{\rm k,hyp}}{E'_{\rm k}}-1$
			[10^{51}erg]	[10^{51}erg]	[10^{51}erg]	[10^{51}erg]	
05bl-w7e0.7m1.45	0.70	1.45	0.93	2.10	1.15	0.96 ± 0.10	0.03
05bl-w7e0.7m1.25	0.70	1.25	0.93	1.73	0.85	0.88 ± 0.06	-0.05
05bl-w7e0.5m0.7	0.50	0.70	0.66	0.87	0.13	0.74 ± 0.02	0.11
05bl-w7e0.7	0.70	1.00	0.93	1.26	0.49	0.77 ± 0.03	-0.17
05bl-w7e0.5m0.5	0.50	0.50	0.66	0.60	0.06	0.53 ± 0.00	-0.20
05bl-w7e0.5m1.25	0.50	1.25	0.66	1.89	0.85	1.04 ± 0.07	0.23
05bl-w7e0.7m0.7	0.70	0.70	0.93	0.80	0.13	0.68 ± 0.01	-0.27
05bl-w7m1.45	1.00	1.45	1.33	1.90	1.15	0.75 ± 0.06	-0.43
05bl-w7e0.5	0.50	1.00	0.66	1.44	0.49	0.95 ± 0.05	0.43
05bl-w7m1.25	1.00	1.25	1.33	1.56	0.85	0.71 ± 0.04	-0.47
05bl-w7	1.00	1.00	1.33	1.14	0.49	0.65 ± 0.02	-0.51
05bl-w7m0.7	1.00	0.70	1.33	0.65	0.13	0.53 ± 0.01	-0.60
05bl-w7e1.45m1.45	1.45	1.45	1.93	1.69	1.15	0.54 ± 0.04	-0.72
05bl-w7e0.35	0.35	1.00	0.46	1.55	0.49	1.07 ± 0.06	1.29

[a] The error estimate only reflects the error due to the unknown composition below the photosphere at +12.9 d.

Table 3.5: Light-curve width estimates for the spectroscopically and energetically most consistent models at each mass M'. The models are ordered according to the deviation of the ratio $\frac{\tau_{\rm LC}}{\tau_{\rm LC,dim}}$ from 1; we assume $\tau_{\rm LC,dim}$=13.9 d (see text).

Model	$E'_{\rm k}/E_{{\rm k},W7}$	M'/M_{W7}	$E'_{\rm k}$	M'	$E_{\rm k,hyp}$	$\tilde{\kappa}$[a]	$\tau_{\rm LC}$[a]	$\frac{\tau_{\rm LC}}{\tau_{\rm LC,dim}}-1$
			[10^{51}erg]	[$M_\odot$]	[10^{51}erg]		[d]	
05bl-w7e0.7	0.70	1.00	0.93	1.31	0.77	0.31 ± 0.10	13.8 ± 2.5	0.00
05bl-w7e0.5m0.7	0.50	0.70	0.66	0.97	0.74	0.34 ± 0.10	11.7 ± 1.9	-0.16
05bl-w7e0.7m1.25	0.70	1.25	0.93	1.73	0.88	0.32 ± 0.12	16.1 ± 3.4	0.16
05bl-w7e0.5m0.5	0.50	0.50	0.66	0.69	0.53	0.47 ± 0.07	11.2 ± 1.2	-0.19
05bl-w7m1.45	1.00	1.45	1.33	2.00	0.75	0.28 ± 0.11	16.9 ± 4.6	0.21
05bl-w7e0.7m1.45	0.70	1.45	0.93	2.00	0.96	0.35 ± 0.16	18.5 ± 4.5	0.34

[a] The error estimate reflects the errors due to the unknown composition below the photosphere at +12.9 d, and due to the uncertainties in $E_{\rm k}$.

results in a larger ratio of burned to unburned material and a larger $E_{\rm k,hyp}$. Similarly, when $E'_{\rm k}$ is increased, $E_{\rm k,hyp}$ decreases. Equality, i.e. consistency, between $E_{\rm k,hyp}$ and $E'_{\rm k}$ is usually reached at a reduced value of $E'_{\rm k}/M'$ with respect to W7. The required reduction varies with the mass of the models (see Sec. 3.1.3.2).

In Table 3.4, two supermassive models (05bl-w7e0.7m1.25, 05bl-w7e0.7m1.45) rank top. However, it should be noted that the energetic quality criterion again does not single out a certain mass, but sets a point of energetic consistency for each mass. All models with larger $E'_{\rm k}$ will then feature too little nucleosynthesis to explain the assumed kinetic energy. The opposite holds for models with lower $E'_{\rm k}$.

Expected light-curve width

We calculated estimates of the width of the bolometric light curve for the models ranking best in spectroscopic and energetic consistency at each mass M'. The resulting values, and those of the quantities needed for the calculation, are given in Table 3.5.

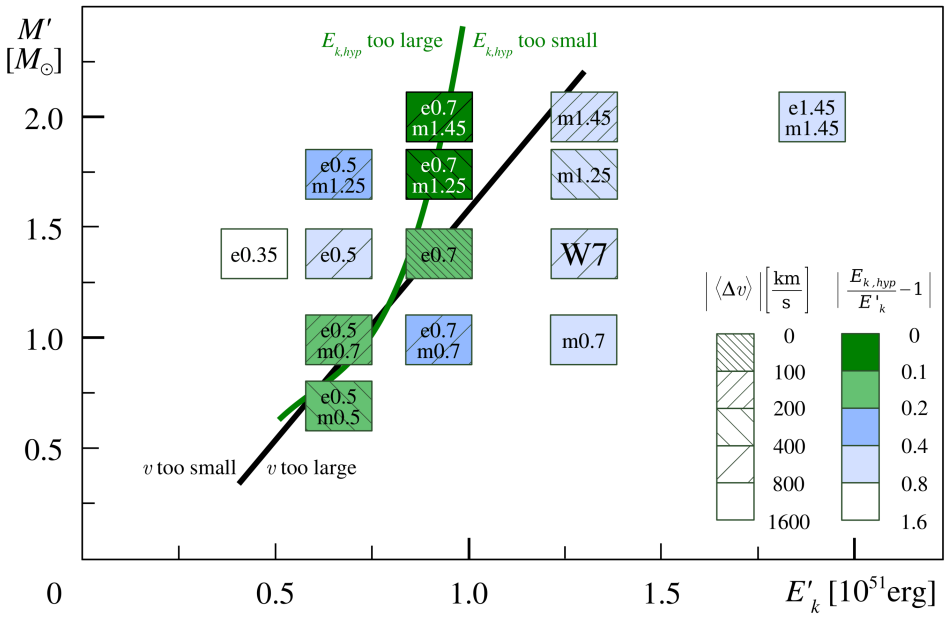

Figure 3.8: Overview of all models evaluated in this work. Colour and hatches mark the energetic and spectroscopic consistency of the models, as indicated by the quantities $\frac{E_{\mathrm{k,hyp}}}{E'_{\mathrm{k}}} - 1$ and $\langle \Delta v \rangle$, respectively (darker colours / denser hatches meaning better consistency; numerical values see Tables 3.3 and 3.4). The green line divides the regions where the models have too large and too small a hypothetical kinetic energy yield, compared to the kinetic energy assumed in the density scaling. To the left of the black line models show too low line velocities; to the right, the opposite holds.

The deviation of τ_{LC} from $\tau_{\mathrm{LC,dim}}$=13.9 d strongly depends on the mass M'. Models with larger mass clearly tend to have a larger light-curve width, although they often have lower values of $\tilde{\kappa}$, as relatively small abundances of burning products are needed to match the observed line strengths with the synthetic spectra.

Although our expected light-curve widths are quite rough estimates, one can state that the criterion disfavours masses largely deviating from the Chandrasekhar mass. The least massive model, with a mass of M'=0.5$M_{\mathrm{Ch,non\text{-}rot}}$, presumably will not produce a broad enough light curve. Likewise, the models at M'=1.45$M_{\mathrm{Ch,non\text{-}rot}}$ will probably exhibit too broad a light curve, although these models are not strictly incompatible with $\tau_{\mathrm{LC,dim}}$, as a large inaccuracy in $\tau_{\mathrm{LC,dim}}$ results from the large mass in the obscured core.

3.1.3.2 Location of consistent models in the $E'_{\mathrm{k}} - M'$ plane

Fig. 3.8 gives an overview of all models in an $E'_{\mathrm{k}} - M'$ plane. According to their quality in spectroscopic terms, the models are marked with different colours; the energetic consistency is indicated by hatches.

In the figure, we also indicate where spectroscopically and energetically consistent models can generally be expected in the plane: a black line is drawn approximately where the transition between too large and too small line velocities occurs. This line is straight and runs from massive models with low E'_{k}/M' to undermassive models with $E'_{\mathrm{k}}/M' \approx (E_{\mathrm{k}}/M)_{W7}$. A green line approximately divides the regions of too large and too small nucleosynthetic energy yields. It lies in the same region as the line of spec-

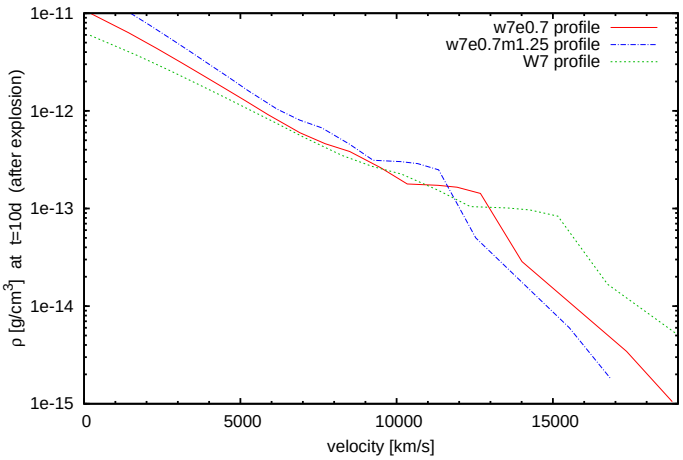

Figure 3.9: w7e0.7 compared to the standard W7 and the w7m1.25e0.7 density profiles.

troscopic consistency, but is curved because the WD binding energy shows a disproportionately strong increase with WD mass. For models up to $M' \approx 0.7 M_{\mathrm{Ch,non\text{-}rot}}$, the binding energy is negligible compared to the nuclear energy release, whereas at higher masses it is considerable, forcing the line of consistency towards smaller E'_{k} and larger nucleosynthesis yields.

Models at $M' = 1.45 M_{\mathrm{Ch,non\text{-}rot}}$ are either spectroscopically or energetically inconsistent under the assumptions made here. However, energetic consistency may be reached in a double-degenerate model with this total mass: the combination of two merging (lower-mass) white dwarfs has a significantly reduced binding energy with respect to a single white dwarf.

Criteria like those used here could give stricter limits still, if the chemical composition in the inner layers was known. This requires studies of nebular spectra of dim SNe Ia.

3.1.3.3 05bl-w7e0.7 as a "reference model"

As discussed above, our models give no clear indication for a deviation from the Chandrasekhar mass. The simplest modification leading to better spectral fits and roughly consistent energetics is simply a moderate downscaling of the energy, as in the 05bl-w7e0.7 model. We would like to give some details on this model here. In Figures 3.9 and 3.10, we show the density and abundance profiles of the 05bl-w7e0.7 model. Other spectroscopically consistent models show similar densities in the outer layers, and thus also similar abundances in that zone. This can be verified in Figures 3.9 and 3.10, where the 05bl-w7e0.7m1.25 model is also plotted for comparison.

The 05bl-w7e0.7 model features $0.46 M_{\odot}$ of unburned material (including all oxygen; C constitutes $0.04 M_{\odot}$). IME are dominant, with a total abundance of $0.55 M_{\odot}$ above 3350 km s^{-1}, the velocity of the photosphere at $+12.9$ d. Stable Fe is present in significant amounts ($0.05 M_{\odot}$). The mass of ^{56}Ni (including decay products) above 3350 km s^{-1} is $0.06 M_{\odot}$, which is a bit higher than the $0.016-0.026 M_{\odot}$ found in Mazzali et al. (1997) above 3500 km s^{-1} for SN 1991bg. However, some of the ^{56}Ni could be replaced by other UV-blocking elements without changing the quality of the

fit. Some $0.23 M_{\odot}$ of material are still hidden below the +12.9 d photosphere, where the IME abundances may still be significant (Si of the order of several 10%).

Alternative spectroscopically consistent models show similar patterns in the abundance profile in velocity space, but the exact densities and abundances below ∼10000 km s^{-1} are somewhat different. In 05bl-w7e0.7m1.25, as an example, the densities in the inner zones are larger. Thus, the abundances of Fe, Ti and Cr must be lower too keep UV opacities reasonable. For Si, moderate changes in the number density do not cause big changes in the spectra. Therefore, the smaller Fe, Ti and Cr abundances can be balanced by slightly larger Si abundances.

3.1.3.4 The need for early time and nebular spectra of dim SNe Ia

The analysis presented here could still be refined for the outermost and innermost layers. The exact abundance stratification in the outer envelope cannot be inferred from the spectrum at −6 d, whose photospheric velocity is already quite low. For the inner layers, especially the density structure and thus the abundance of Si is somewhat uncertain (see Sec. 3.1.3.3). In order to make a more precise study of dim SNe Ia possible, additional spectra in the very early and in the nebular phase are needed.

The potential of an analysis of the nebular spectra has already been shown in Mazzali et al. (1997). Here, we would like to illustrate the benefit of early time spectra, showing their sensitivity to the abundances in the outer envelope. We checked the influence of the abundances between v≈11000 km s^{-1} and 15000 km s^{-1} on the −6 d spectrum, and found that these abundances have some effects difficult to distinguish from those of the chemical composition at lower velocities. Moreover, the (small) abundances of burned material at $\gtrsim$15000 km s^{-1} cannot be exactly determined, as these only affect the extreme blue wings of the spectral features.

To explore the effect of the abundances in the outer envelope on early-time spectra, we calculated model spectra at −10 d and −15 d (Fig. 3.11). The luminosities at these epochs were crudely estimated from the luminosity at −6 d under the assumption of a quadratic light curve rise (cf. Riess et al. 1999). We first calculated spectra assuming the 05bl-w7e0.7 density and abundance structure. For each of the two epochs, the photospheric position was shifted from its value at −6 d to higher velocities, until the backscattering was reasonably reduced. This resulted in photospheric velocities of 11750 and 15200 km s^{-1}, respectively.

After calculating these initial models, we explored the effect of changes in the chemical composition, performing three additional code runs for each epoch. In the first two runs, we reduced IME and heavier elements to 20% of their original abundances, respectively. For the −15 d model, these changes were applied to the whole atmosphere. In the −10 d model, we kept the original composition at velocities >15200 km s^{-1}constant, in order to show the sensitivity to the abundances in the zone not probed by the −15 d spectrum. In the third code run, finally, we removed oxygen in favour of carbon (so that the mass fraction X(C)=80%). This change was applied to the whole atmosphere, also at -10 d, as otherwise an inverted composition (larger C abundances further inwards) would have resulted.

In Fig. 3.11, we show the resulting spectra and give line identifications to clarify the effect of the modified abundances. Moreover, it is indicated which lines do and which do not change significantly with the modifications. At −15 d, the synthetic spectrum looks vastly different from the spectrum of a normal SN Ia. We illustrate this in the upper

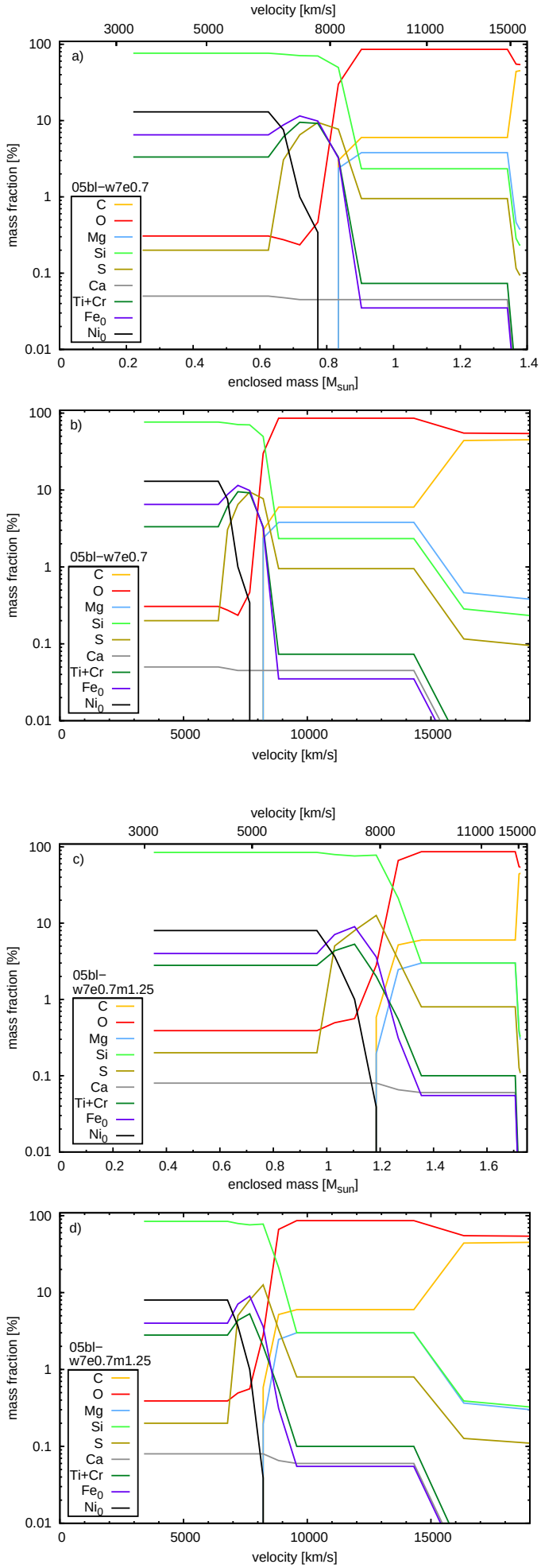

Figure 3.10: Abundance tomography of SN 2005bl based on w7e0.7. The abundances are plotted versus enclosed mass (panel a) and velocity (panel b). For comparison, we also show the 05bl-w7m1.25e0.7 abundances (panels c and d). In velocity space, the patterns of the abundance profiles are very similar.

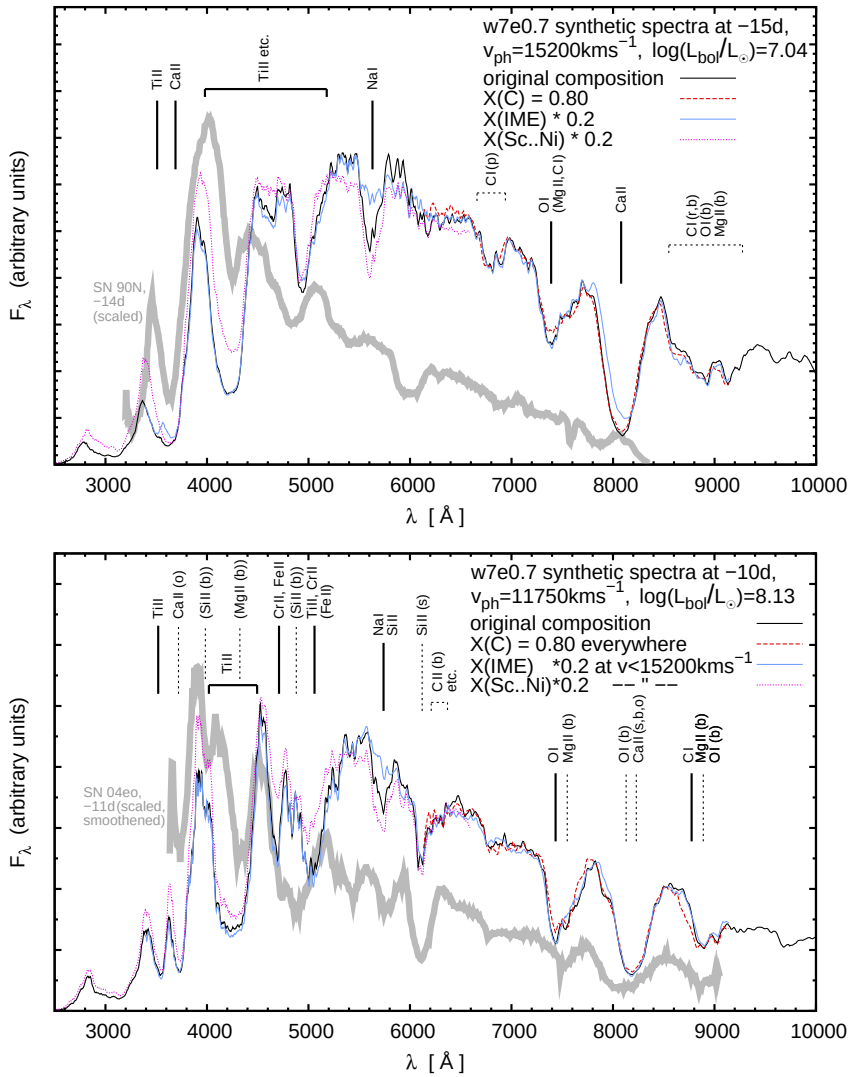

Figure 3.11: Early time synthetic spectra for 15 d and 10 d before B maximum, based on 05bl-w7e0.7. The black lines are spectra calculated with the original composition. The other lines illustrate the most notable changes which occur when setting $X(\mathrm{C})$ to 80% (red, dashed line) and when reducing IME (Mg up to Ca, blue, solid line) or heavier elements (Sc to Ni, magenta, dotted line) to 1/5 of their original abundances, respectively (in the velocity ranges indicated). For comparison, we plotted spectra of SN 1990N at -14 d and of SN 2004eo at -11 d as grey thick lines below the synthetic spectra.
Approximate identifications are given for prominent features. Weak lines are given in parentheses; lines not reacting to changes in the abundances are shown with dotted marks, with the reasons for the insensitivity indicated as follows (based on a rough analysis): (b) – line is heavily blended; (o) – line is formed mainly at $>$15000 km s^{-1}; (r) – relative change of abundance is too small; (s) – line is partially saturated.

panel of Fig. 3.11 by additionally plotting the earliest SN Ia spectrum ever observed (SN 1990N at −14 d, Leibundgut et al. 1991). Compared to spectra of normal SNe Ia, but also to the −6 d spectrum, lines of less ionised species appear owing to the low temperatures, which result from the low luminosity. Si II and S II lines, which normally characterise SNe Ia, are absent. The spectrum is especially sensitive to the abundances of Na, Ca and Fe-group elements (with Na, uncertainties in the ionisation remain a caveat, see Sec. 3.1.2.1). Furthermore, C I features are present around 6800 Å and 8700 Å. As the C abundance is already quite large in the outermost layers of 05bl-w7e0.7, these features do not react strongly to a further increase of $X(\mathrm{C})$. However, if much less carbon was present, they should gradually disappear.

At −10 d, the structure of the spectrum resembles somewhat more that at −6 d. Yet, the spectrum has little in common with that of the moderately subluminous, spectroscopically rather normal SN 2004eo at −11 d (Pastorello et al. 2007b; plotted in the lower panel of Fig. 3.11). Compared to −6 d, the −10 d spectrum still shows hints of lower temperatures: because of the scarce population of excited levels, the S II "W-trough" does not show up. For the same reason, the C II λ 6580 feature is weak. In the model with a larger C mass fraction, however, some of the strongest lines of C I begin to absorb at $\sim$ 8700Å. Furthermore, there are absorptions due to O I, Na I, Si II, Ti II, Cr II and Fe II, which should allow for an analysis of the abundances in the outer layers as soon as observations are available.

The amount of extra information which can be inferred from early-time spectra will, of course, also depend on the actual luminosity of the SN at these epochs. Larger luminosities mean higher temperatures, making lines of different ions appear. However, our results already suggest that there are interesting possibilities to infer the chemical composition of the outermost ejecta.

3.1.4 Summary – analysis of the 1991bg-like SN 2005bl

To conclude our study of SN 2005bl, a dim, 1991bg-like SN Ia, we summarise our most important findings. We conducted an abundance tomography with different density profiles, and assessed the consistency of the resulting models.

Regardless of the density profile, abundance tomography indicated that a large part of the ejecta consists of O and of IME such as Si. The abundances of burning products in the outer layers of the SN are relatively low, and complete burning to Fe-group elements has only taken place in the centre. The ejecta are not strongly mixed. All this indicates a that the explosion proceeded as a detonation at low densities.

Densities in the outer part of SN 2005bl are unusually small for a SN Ia: the photospheric spectra, as analysed by us, do not allow for material – neither for IME nor for C/O – at high velocities. Therefore, density models with a smaller E'_{k}/M' (kinetic energy over mass) ratio than W7 are preferred, unless the object has a very low overall mass.

In addition to checking whether the density profiles are consistent with the spectra (spectroscopic consistency), we investigated the consistency of our models in terms of explosion energy and in terms of the expected light-curve width. If spectroscopic consistency is demanded, the energy criterion favours models with masses somewhat smaller than the standard Chandrasekhar mass. However, this criterion does not apply to double-degenerate explosions. The light-curve criterion finally disfavours models which deviate a lot $\gtrsim$30% from the Chandrasekhar mass.

We finally remarked that more early-time and nebular spectra of 1991bg-like SNe Ia would be interesting as a basis for refined studies. We demonstrated this for the early-time case by predicting spectra with our spectral synthesis code. The potential of nebular analyses had already been shown by Mazzali et al. (1997).

3.2 SN 2009dc

3.2.1 Introduction

A SN Ia subclass very different from 1991bg-like objects, but even more "mysterious" is formed by the extremely luminous "Super-Chandrasekhar" (SC; the designation refers to $M_{\text{Ch,non-rot}}$) objects (Howell et al. 2006,Hicken et al. 2007,Scalzo et al. 2010 and references below). The early-time spectra of these SNe resemble those of normal SNe Ia; line velocities tend to be low (comparable to 1991bg-like objects). However, the light curves (Fig. 3.12) are extremely different – the maximum luminosity is about twice that of an average object (Howell et al. 2006) and the decline is slow. About a Chandrasekhar mass $M_{\text{Ch,non-rot}}$ of ^{56}Ni or more is seemingly required to generate the light-curve maximum (Taubenberger et al. 2009). Part of the peak luminosity may come from other energy sources than ^{56}Ni decay. The more conventional paradigm however is that the objects are supermassive (Taubenberger et al. 2011a). In any case, in-depth analyses of observations with radiative transfer models are needed to identify the most likely progenitor scenarios.

Here, we study the recent SC SN 2009dc. Observations with an extraordinarily good time coverage are available for this object (Yamanaka et al. 2009; Tanaka et al. 2010; Silverman et al. 2011; Taubenberger et al. 2011a).

First, we analyse the SN assuming light generation by ^{56}Ni only. The density profiles required in this case are completely uncertain. Therefore, we use the earliest observations to constrain the density structure in the outer part of the ejecta and the rise time (Sec. 3.2.3). We only calculate synthetic spectra for the earliest epoch here, which reduces the calculation costs and allows us to test a large number of models. Afterwards, we perform a full abundance tomography (taking into spectra at different epochs) with a density profile representing the explosion of $2.0 M_{\odot}$ rotating white dwarf, and with an empirically constructed $3.0 M_{\odot}$ density profile (Sections 3.2.4.1 and 3.2.4.3).

As an experiment, we finally conduct another tomography, for which we assume some light to be externally generated through interaction of the ejecta with circumstellar material (Sec. 3.2.4.4). We discuss all our models in terms of consistency and theoretical interpretation (Sec. 3.2.5). This includes a somewhat elaborate discussion of possible progenitor models for SN 2009dc, as (compared to the case of SN 2005bl, see conclusions – Chap. 5) the situation is still very unclear here.

3.2.2 Observations and observational parameters

We analyse the luminosity-calibrated spectra of SN 2009dc published by Taubenberger et al. (2011a). This data set samples the behaviour of SN 2009dc extremely well from 9.4 d before B maximum to late times.

The *galactic* extinction towards SN 2009dc is $E(B-V)_{\text{Gal}} = 0.07$ according to Schlegel et al. (1998), and $E(B-V)_{\text{Gal}} = 0.04$ according to Burstein & Heiles (1982). For the host galaxy, Taubenberger et al. (2011a) give a reddening of

$$E(B-V)_{\text{host}} = 0.10 \pm 0.08$$

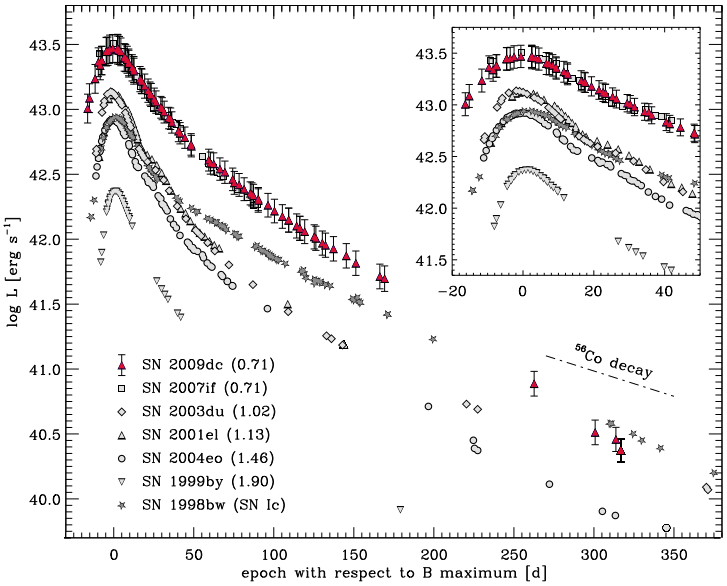

Figure 3.12: Light curve of the "Super-Chandrasekhar" Type Ia SN 2009dc compared to a similar object (SN 2007if), normal SNe Ia (SN 2003du, SN 2001el, SN 2004eo), 91bg-like SNe Ia (SN 1999by), and a Type Ic Hypernova (SN 1998bw). Plot: Taubenberger et al. (2011a) – data sources: see their paper.

Following Taubenberger et al. (2011a), we generally use the value[d)]

$$E(B-V)_{\rm tot} \sim E(B-V)_{\rm host} + E(B-V)_{\rm Gal} \sim 0.17$$

but repeat some analyses for a smaller $E(B-V)_{\rm tot} \sim 0.06$ to test the influence on the results. Apart from this, we assume the observational parameters (distance,...) given by Taubenberger et al. (2011a).

3.2.3 Density profile & rise time – early time models

We first analyse SN 2009dc assuming all luminosity to be intrinsic (i.e. generated by the decay of ^{56}Ni). Models for the earliest spectrum available to us (-9.4 d relative to B maximum) then allow us to constrain the outer part of the density profile as well as the rise time, which in turn gives clues on the ^{56}Ni mass via Arnett's rule (Arnett 1982). Observationally, the rise time has already been estimated to be shorter than $\sim$ 30 d and longer than $\sim$ 22 d (Taubenberger et al. 2011a; Silverman et al. 2011).

We show below that we can determine an optimum $t_{\rm r}$ value depending on the density profile we use: a standard SN Ia profile (W7 explosion model – Nomoto et al. 1984), a profile representative of an explosion of a rotating WD (AWD3-det model – Pfannes et al. 2010, see Figure 3.15), or empirically constructed profiles (see below). The AWD3-det model can be regarded prototypical for explosions of rotating, supermassive ($2M_{\odot}$) white dwarfs. These are probably the most intuitive progenitor candidates for SC SNe Ia (Howell et al. 2006). The thermonuclear flame in AWD3-det propagates as a pure detonation from the very beginning (Pfannes et al. 2010). Delayed-detonation

[d)] Because of the relatively short distance to the SN, we can add up the reddening values without taking redshift into account here.

models for these progenitors are not yet available in the literature. However, they probably produce roughly similar outcomes as the initial deflagration in rotators tends to be weak and burn little material (M. Fink, private communication). A pure deflagration of a supermassive WD has less of a chance to explain SN 2009dc, as it does not produce much ^{56}Ni ($\sim 0.7 M_{\odot}$) and leads to an extreme composition mixing (Pfannes et al. 2010).

After discussing the empirically inferred density profiles and the method, we calculate and assess models. Doing this, we obtain an overview on the range of densities and rise times compatible with the observations of SN 2009dc.

3.2.3.1 Empirically inferred density profiles

We construct part of the density profiles we use here employing an approach independent of explosion models. The idea is to infer the density profile from the observed time evolution of the velocities at which prominent spectral lines form. Such velocities are measurable as absorption blueshifts in the spectra.

Concept

As initial steps, we roughly assume spectral lines to *form at a density constant over time* and exploit the fact that the ejecta are in force-free expansion ($r = v \times t$). With these assumptions, the evolution of line velocities immediately gives us information on the radial density profile: in force-free expansion, the density at a space-time point (v_2, t_2) with respect to the density at another point (v_1, t_1) can directly be calculated from the radial density profile (given at some time t_0). In turn, knowledge on the ratio of the density at two points (v_1, t_1) and (v_2, t_2) allows us to constrain the shape of the density profile [i.e. $\rho(v_2, t_2)$ can be calculated from $\rho(v_1, t_1)$]. If we have velocities of line formation $v_{1...n}$ at times $t_{1...n}$, and assume a density ratio of 1.0 *(constant density)* at these points, we obtain:

$$\begin{aligned} \rho(v_i, t_i) &= \rho(v_1, t_1) \text{ (constant density) and} \\ \rho(v_i, t_1) &= \rho(v_i, t_i) \times (t_i/t_1)^3 \text{ (force-free expansion)} \\ \Rightarrow \rho(v_i, t_1) &= \rho(v_1, t_1) \times (t_i/t_1)^3 \end{aligned} \tag{3.3}$$

The time offsets t_i from explosion onset here depend on the assumed rise time $t_{\rm r}$. For each spectrum, t_i is calculated by adding the assumed rise time $t_{\rm r}$ to the observational epoch relative to B maximum. We thus obtain from our measurements a two-parameter sequence of models with $t_{\rm r}$ and $\rho(v_1, t_1)$ as free parameters.

Measurements in the spectra

We perform the necessary measurements of line blueshifts/ velocities as in Hachinger et al. (2006), determining a pseudo-continuum and taking the wavelength of maximum fractional depth as the blueshifted position. All spectra observed up to 5 days past B max are used for the measurements. With the $+5$ d limit, we avoid the epochs at which the velocities of some lines become constant (cf. Taubenberger et al. 2011a) as the photosphere moves below the zone where the respective elements are abundant. We use several prominent absorption features due to different species (Si II $\lambda\lambda$4130,6355, Si III λ4563, C II λ6580). Taking into account various ions with different ionisation

Table 3.6: Velocities measured in the Si II $\lambda\lambda$4130,6355, Si III λ4563 and C II λ6580 lines in the observed spectra of SN 2009dc up to 5 d past B max. We give the individual velocities, their average and a radial velocity of line formation $v_{\rm LF}$ (see text). The values $v_{\rm LF}$ are the v_i used in Equation (3.3).

epoch (rel. to B max.)	v (Si II λ4130)	v (Si II λ6355)	v (Si III λ4563)	v (C II λ6580)	v (line avg.)	$v_{\rm LF}$ (radial)
[d]	[km s^{-1}]	[km s^{-1}]	[km s^{-1}]	[km s^{-1}]	[km s^{-1}]	[km s^{-1}]
-9.4	8298.9	9071.6	7061.8	10142.0	8643.6	10804.5
-8.5	7906.2	9241.8	6665.3	10168.7	8495.5	10619.4
-7.5	7628.1	8754.1	6457.1	9963.1	8200.6	10250.8
-3.7	7219.0	8260.8	5853.6	9517.6	7712.7	9640.9
2.4/2.5	6224.3	7757.0	5333.7	7374.8	6672.5	8340.6
4.5	6021.9	7482.9	5197.8	7191.3	6473.4	8091.8

and excitation energies and evaluating the average velocity, we make sure that the zone of line formation we infer does not track the excitation/ionisation conditions, but the density as far as possible.

The measured velocities are given in Table 3.6. Exactly speaking, blueshifts measured in spectra give us velocity components along the line of sight. The corresponding radial velocity of line formation is somewhat larger. Thus, we calculate *radial velocities of line formation* (see Table 3.6) by multiplying the average line velocities with a factor of 1.25. These radial velocities are used as v_i in Equation (3.3).

Resulting profiles

In order to avoid kinks in the inferred density profiles, which may result from measurement uncertainties, and in order to write the inferred density profiles in a compact form, we fit exponentials

$$\rho(v,t) = a \times \exp(-bv) \times (t_0/t)^3 \tag{3.4}$$

to the measured values $\rho(v_i, t_i)$. Here, t_0 is a fixed reference time without any further meaning. As the observations do not constrain the absolute density scale, $\rho(v_1, t_1)$ is set to 1.0 for the fitting process, and the fit only gives a meaningful b which depends on the assumed rise time $t_{\rm r}$ ($t = t_{\rm r}$ + epoch rel. to B max.). For a pre-defined set of rise times $\{$21 d, 22.5 d, 25 d, 27.5 d, 30 d, 35 d and 40 d$\}$, we calculated the following values of b: 8.2×10^{-9} (km/s)$^{-1}$, 7.6×10^{-9} (km/s)$^{-1}$, 6.8×10^{-9} (km/s)$^{-1}$, 6.1×10^{-9} (km/s)$^{-1}$, 5.6×10^{-9} (km/s)$^{-1}$, 4.7×10^{-9} (km/s)$^{-1}$, and 4.1×10^{-9} (km/s)$^{-1}$.

For specifying an actual density profile, $t_{\rm r}$ and finally a have to be fixed. We therefore construct a grid of density profiles with different $t_{\rm r}$ and a. We assume rise times $t_{\rm r}$ from the grid given above (21 d...40 d), and choose scaling factors a such that our models intersect the W7 standard SN Ia model[e)] (Nomoto et al. 1984) at 9000, 10000, 12000, or 14000 km s^{-1}. As the W7 density is relatively flat in this velocity range, a smaller intersection velocity $v_\times$ results in a lower a and lower overall densities. This is illustrated in Fig. 3.13, where examples of our density profiles are plotted. The profiles are named according to a scheme reflecting the parameters (e.g. "exp9-21d" matches W7 at 9000 km s^{-1}, $t_{\rm r} = 21$ d). Our grid of profiles covers and somewhat exceeds the physical parameter space in which solutions for SN 2009dc will be found.

[e)] W7 is evaluated for the reference time t_0 we use in Equation 3.4 here.

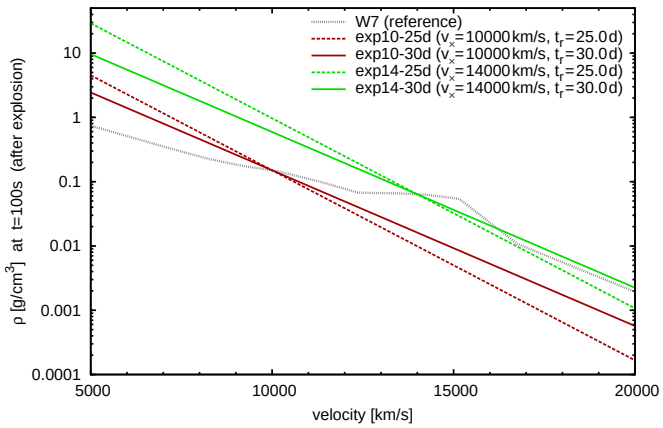

Figure 3.13: Examples of the density profiles constructed, and W7 profile as reference. All profiles are plotted for a reference time t_0 = 100 s after explosion, even though different rise times t_r are assumed in their creation.

3.2.3.2 Early time models: Setup, determination of optimum rise times

The abundance structure of the models, comprising three abundance shells, is fixed as follows to avoid an overparametrisation: The models have a zone of thickness 600 km s^{-1} above the photosphere with some Fe-group elements (up to 15% by mass; higher fractions are probably not realistic) and high IME mass fraction. Above this zone, there is a layer depleted in Fe-group elements but still rich in IME, with a thickness of 2000 km s^{-1}. It causes relatively little backscattering, such that temperatures drop quickly with radius and become ideal for the formation of prominent lines due to singly-ionised IME. Still above, the atmosphere was assumed to consist of a C-O mix only containing traces of other elements (mass fractions $\leq 10\%$ of those in the zone below). The photospheric velocities were selected such that a reasonable temperature structure (i.e. a large enough strength of Si II lines) resulted and less than 67% of the radiation packets were re-absorbed due to backscattering. If in doubt, we chose the lowest possible photospheric velocity in order not to artificially suppress the formation of lines deep inside the ejecta.

In the -9.4 d spectrum, the assumed densities and rise times influence the velocities of the spectral features. When the rise time t_r is changed, and the density distribution in velocity space is kept constant[f)], a change in line velocities occurs because of two effects:

- The energy density ε of the radiation field remains approximately constant at a given *radius* r, as the observed spectrum and intensity are fixed. ε is, crudely spoken, a function decreasing with radius. With $r = v \times t$, an *decrease* in t (due to a smaller t_r) therefore makes ε *larger at each given velocity* v. The Si II lines then form at higher v, where the radiation energy density ε is small enough (guaranteeing a low enough ionisation).

[f)]Here, we mean that the time-invariant density distribution $\frac{\mathrm{d}m}{\mathrm{d}v}(v)$, i.e. the explosion model, is kept constant. For the empirical density profiles, we do not exactly fulfil this condition: We keep $v_\times$ constant when changing t_r, but adapt the slope b to t_r. The resulting change in slope is however not significant in the current context.

- Models with a smaller t (smaller $t_{\rm r}$) usually have photospheres at larger $v_{\rm ph}$. This is necessary in order not to make the lower boundary flux too blue, and in order not to have a too large backscattering in the more compact ejecta. A larger $v_{\rm ph}$ leads to an increase of line velocities. As real SNe do not contain a sharp and wavelength-independent photosphere (Sauer et al. 2006), the velocity change in the models may be somewhat larger than in real SNe. We take this into account when we give a methodical uncertainty for our results below.

For each choice of the density, we infer an optimum rise time $t_{\rm r,opt}$ needed in order to reproduce the observed line velocities. We do this separately for the empirical profiles, W7 and AWD3-det. In the case of the empirical profiles, we infer $t_{\rm r,opt}$ for each choice of $v_\times$, while the slope b of the profile is adapted to the $t_{\rm r}$ assumed [following Eq. (3.3)]. As a measurable indicator for the fit quality we take the velocity of the Si II λ6355 feature, because observed Si II λ6355 velocities in normal SNe are known to be well fitted by our spectral models (e.g. Stehle et al. 2005).

Assuming a certain density profile, the -9.4 d spectrum is first calculated for $t_{\rm r} = 21$ d, 22.5 d, 25 d, 27.5 d, 30 d, 35 d, or 40 d. Optimised models are then calculated with the four rise times which warrant the best match to the observed Si II λ6355 line velocity. $t_{\rm r,opt}$ for the respective density profile is finally obtained fitting a regression line to the relation between $t_{\rm r}$ and the line velocity mismatch $\Delta\lambda$ in the four models, demanding $\Delta\lambda \stackrel{!}{=} 0$.

We first perform our calculations assuming low progenitor metallicity. For the outer ejecta this implies a mix of Fe-group elements dominated by decay products from ^{56}Ni and by Cr (from ^{52}Fe, Iwamoto et al. 1999). It also allows low abundances of Fe-group elements in layers with inefficient nucleosynthesis, which proves optimum for the spectral models. We then repeat the analysis assuming a higher metallicity and a lower-than standard reddening $E(B-V)_{\rm tot} \sim 0.06$ (see Sec. 3.2.1), respectively, in order to estimate the influence of these assumptions.

3.2.3.3 Results: rise time estimates based on empirical density profiles

In Figure 3.14, we plot a selection of models for $E(B-V) \sim 0.17$ and low metallicity to illustrate our method. The Si II λ6355 line, which we use to judge the quality of the synthetic spectra, is marked. For a general discussion of the characteristics and features of the -9.4 d spectrum, we refer to Section 3.2.4.1.

Table 3.7 gives for each $v_\times$ the measured line position mismatches between the observations and the four $t_{\rm r}$ test models, as well as the resulting $t_{\rm r,opt}$. Besides the results based on our standard assumptions [low progenitor metallicity, $E(B-V)_{\rm tot} \sim 0.06$], the table shows the values also for the high-metallicity and low-reddening cases.

Using a smaller $v_\times$ for the empirical density leads to smaller densities throughout the envelope. Looking from the outer layers inwards, high densities are reached later, and the zone favoured for Si II line formation tends to be deeper inside (which makes line velocities slower). Thus, the $t_{\rm r}$ values needed to reproduce the low line velocities of SN 2009dc are usually shorter for a smaller $v_\times$. If $v_\times$ is very low, the zone dense enough for line formation may be far inside where the radiation field is strong. This then favours Si III with the result that the Si II λ6355 line cannot be well formed – a condition very atypical of SNe Ia [except for 1991T-like objects, Mazzali et al. (1995)]. The exp9 and exp10 models suffer from this problem for the lower rise times tested (25.0 d, 27.5 d;

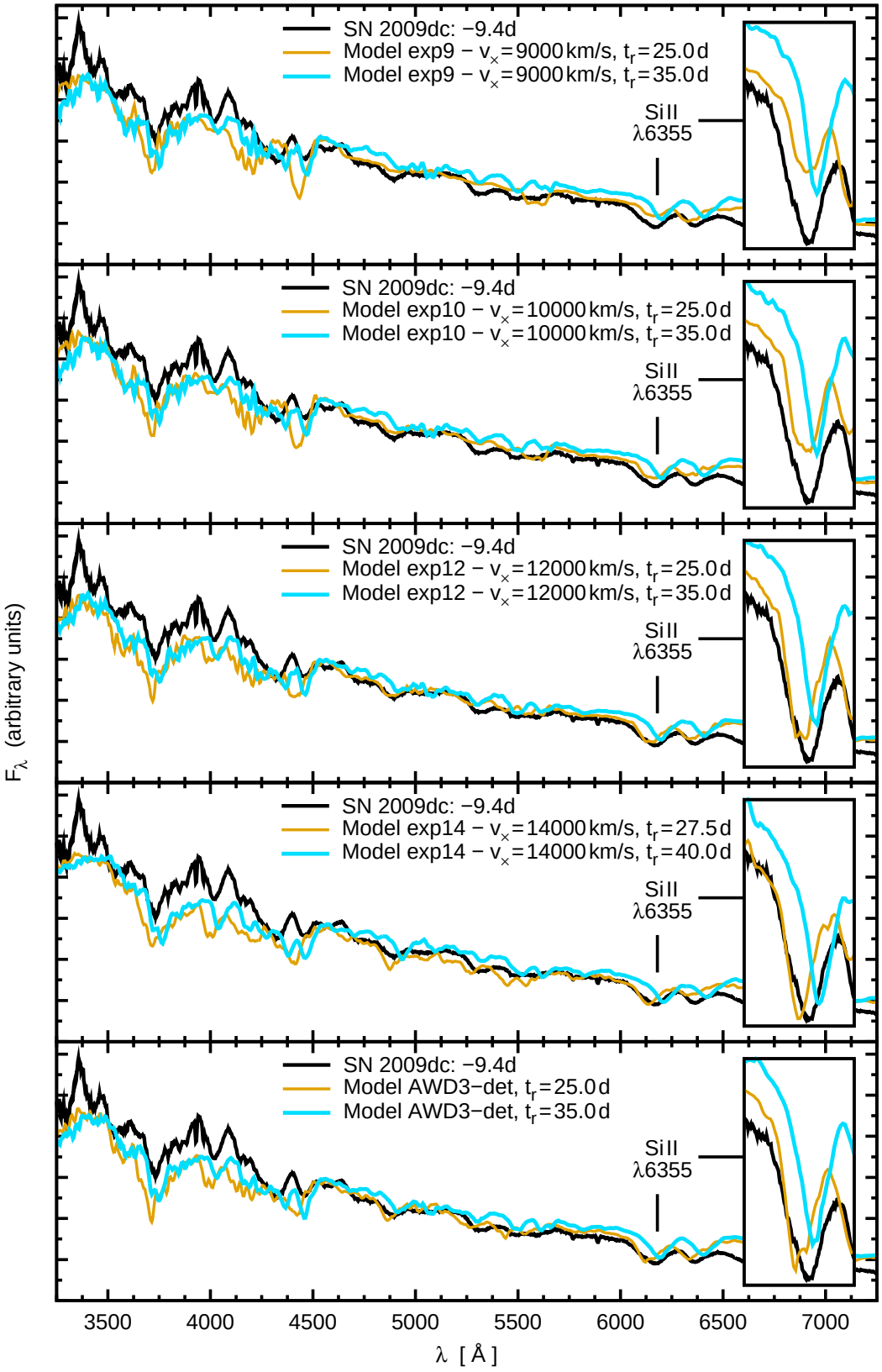

Figure 3.14: Models for the −9.4 d spectrum of SN 2009dc for low metallicity and $E(B-V)$ = 0.17. Each of the upper four panels contains two models for the same $v\times$ (empirical density profiles) and the most extreme $t_{\rm r}$ values listed in Table 3.7. The lowest panel shows AWD3-based models (see Table 3.8). An optimum model fits the velocity of the Si II λ6355 line (marks, enlarged in insets). We see too high a velocity for the short risetime, and the opposite for the long risetime – an optimum model is in between. For the exp9- and exp10-based models with $t_{\rm r}$ = 25 d, the synthetic Si II λ6355 line lacks depth due to low densities.

Table 3.7: Rise time estimates from our spectral fits using the empirical density profiles described in the text, for different values of the reddening $E(B-V)$ and metallicity. For each $v_\times$, we first give the rise times $t_{r,1\ldots4}$ for which optimised models have been calculated. We then show the wavelength deviation between the synthetic Si II λ6355 feature and the observed one $\Delta\lambda = \lambda_{\rm syn} - \lambda_{\rm obs}$ (with $\lambda_{\rm obs} = 6165.6$ Å). From the $\Delta\lambda - t_{\rm r}$ relation, we calculate an optimum rise time $t_{\rm r,opt}$ (see text).

ρ profile (name refers to $v_\times/10^3$km s^{-1})	$t_{r,1\ldots4}$ [d]	$v_{\rm ph,1\ldots4}$ [km s^{-1}]	$\Delta\lambda_{1\ldots4}$ [Å]	$t_{\rm r,opt}$ [d]
$E(B-V) = 0.17$, low metallicity				
exp9	25.0	9900	-7.1	27.8
($v_\times$ =	27.5	10100	-11.2	
9000 km s^{-1})	30.0	8640	13.2	
	35.0	7160	34.0	
exp10	25.0	10200	-10.5	27.3
	27.5	9570	-0.3	
	30.0	8560	13.5	
	35.0	7160	33.5	
exp12	25.0	10640	-21.3	29.0
	27.5	9500	-11.3	
	30.0	8630	10.4	
	35.0	7140	29.2	
exp14	27.5	10150	-30.2	31.9
	30.0	9260	-11.3	
	35.0	7450	26.4	
	40.0	6070	43.9	
$E(B-V) = 0.06$, low metallicity				
exp9	21.0	-[a]	-[a]	23.4
	22.5	-[a]	-[a]	
	25.0	8940	8.2	
	27.5	7940	21.3	
exp10	21.0	10450	-11.5	24.0
	22.5	10150	-16.8	
	25.0	8950	9.8	
	27.5	7980	18.7	
exp12	22.5	10360	-29.3	26.1
	25.0	9210	-3.3	
	27.5	8300	12.0	
	30.0	7440	24.9	
exp14	27.5	9760	-15.9	30.7
	30.0	8910	-3.5	
	35.0	7190	18.3	
	40.0	5330	56.3	
$E(B-V) = 0.17$, high (solar) metallicity				
exp9	22.5	-[a]	-[a]	28.5
	25.0	10350	-8.9	
	27.5	9650	-2.6	
	30.0	9080	4.1	
exp10	25.0	10500	28.5	29.0
	27.5	9960	-7.4	
	30.0	8880	6.2	
	35.0	7470	30.6	
exp12	25.0	11000	-24.6	29.5
	27.5	9850	-16.2	
	30.0	8950	8.1	
	35.0	7490	30.5	
exp14	27.5	10580	-35.1	32.8
	30.0	9690	-15.0	
	35.0	8010	18.3	
	40.0	6550	40.4	

[a] attempt to create model failed: densities in the outer ejecta too low/steep for decent line formation.

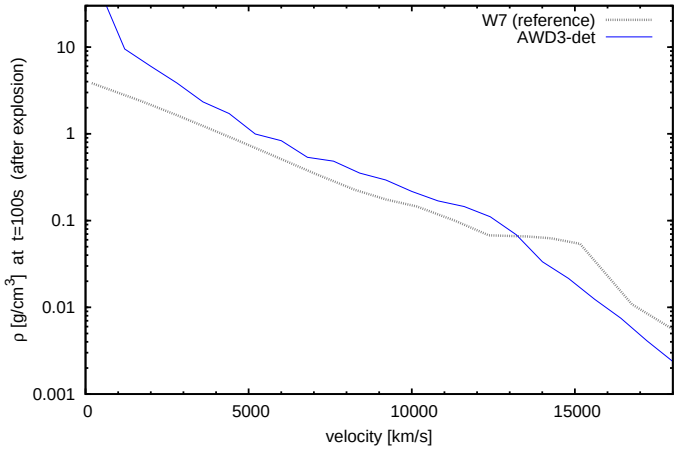

Figure 3.15: Density profiles of the explosion models AWD3-det Pfannes et al. (2010) and W7 (Nomoto et al. 1984). For our study, the original AWD3-det model has been converted into an 1-D model by adding up the cell masses in 50 radial velocity bins.

cf. Fig. 3.14). We therefore expect the actual densities in the outer layers of SN 2009dc to be no less than those in the exp9 models. The exp14 models, on the other hand, need a very long rise time to reproduce the λ6355 line (Table 3.7), and tend to have an extremely large opacity. They thus constitute an upper limit to the real densities.

The optimum rise time inferred with the exp9/exp10 profiles is a lower limit to the real rise time of the SN. For a reddening of $E(B-V) \sim 0.17$ and low progenitor metallicity, we derive (from Table 3.7):

$$t_{\mathrm{r,\,09dc}} \gtrsim 24 \text{ d}$$

Here, a possible error of $\sim$3 d (corresponding to an average step in our t_{r} grid) due to inaccuracies in the method has already been accounted for. The value also holds for high progenitor metallicity, as the high-metallicity models need somewhat longer rise times.

If one assumes a weaker reddening of $E(B-V) \sim 0.06$, the rise times needed for our models are lower. From Table 3.7, we conclude that for $E(B-V) \sim 0.06$ our rise time limit would be $t_{\mathrm{r,09dc}} > 21$ d. However, at present we see no compelling reason to prefer the low reddening.

3.2.3.4 Results: rise time estimates based on W7 / AWD3-det

We now conduct the rise-time experiment, as described in the previous subsection, with the W7 and AWD3-det density models (see Fig. 3.15).

The results indicate that the optimum rise times for both these models are $\sim$ 31 d (Table 3.8). Considering again an uncertainty in the method of $\sim$ 3 d, we conclude

$$t_{\mathrm{r,\,09dc/AWD3}} \sim t_{\mathrm{r,\,09dc/W7}} \gtrsim 28 \text{ d}.$$

This is still compatible with the observational limits, but brings up a consistency problem with W7, which we discuss below.

Table 3.8: Optimum rise time estimates $t_{\mathrm{r,opt}}$ from our spectral fits using the density profiles AWD3-det and W7, for different values of the reddening $E(B-V)$ and metallicity, analogous to Table 3.8.

ρ profile	$t_{\mathrm{r},1\ldots4}$ [d]	$v_{\mathrm{ph},1\ldots4}$ [km s^{-1}]	$\Delta\lambda_{1\ldots4}$ [Å]	$t_{\mathrm{r,opt}}$ [d]
$E(B-V) = 0.17$, low metallicity				
AWD3-det	25.0	10750	-44.4	
	27.5	9530	-25.8	
	30.0	8520	1.5	31.0
	35.0	7060	24.4	
w7	25.0	10630	-51.1	
	27.5	9300	-17.5	
	30.0	8360	2.9	30.5
	35.0	6970	29.4	
$E(B-V) = 0.06$, low metallicity				
AWD3-det	22.5	10570	-36.0	
	25.0	9050	-13.3	
	27.5	7950	6.9	27.0
	30.0	7060	20.2	
W7	22.5	9950	-41.7	
	25.0	8660	-15.4	
	27.5	7770	8.6	26.8
	30.0	6780	28.6	
$E(B-V) = 0.17$, high (solar) metallicity				
AWD3-det	27.5	10050	-22.9	
	30.0	9060	-7.8	
	35.0	7580	24.7	31.4
	40.0	6420	42.5	
W7	27.5	10130	-35.0	
	30.0	9160	-6.4	
	35.0	7640	25.1	32.0
	40.0	6460	45.4	

3.2.3.5 Inconsistency of W7-based models for SN 2009dc: Excluding a normal 1.38 $M_\odot$ WD explosion

Taubenberger et al. (2011a) already estimated that an ordinary explosion of a $\lesssim$1.38 $M_\odot$ WD can neither account for the peak luminosity of the SN, nor for the wide light curve. With the large rise time required by the spectral lines, we obtain additional support for their arguments.

A normal Chandrasekhar-mass explosion of a non-rotating WD, as it is currently understood, only shows moderate asymmetry. Therefore, its ^{56}Ni mass can be inferred from the maximum luminosity using Arnett's rule (Arnett 1982). This rule states that at maximum light the luminosity roughly equals the instantaneous energy input from radioactive decay:

$$L(t_{\text{max}}) = M_{\text{Ni-56}}(t_{\text{max}}) \times \zeta_{\text{Ni-56}} + M_{\text{Co-56}}(t_{\text{max}}) \times \zeta_{\text{Co-56}} \tag{3.5}$$

ζ_X is the energy gained from radioactive decay of an isotope X per unit mass (of this isotope) and unit time. The time-dependent masses of ^{56}Ni and ^{56}Co are calculated using the half-lifes $t_{1/2,\text{Ni-56}} = 6.077$ d and $t_{1/2,\text{Co-56}} = 77.27$ d. With a rise time of 28 d, we obtain a ^{56}Ni mass of $2.2 \pm 0.7 M_\odot$ [the error is estimated as in Taubenberger et al. (2011a) and includes uncertainties in the distance, extinction and in applying Arnett's model]. This mass is significantly larger than the Chandrasekhar mass $M_{\text{Ch,non-rot}}$.

If we continue to examine the model despite this inconsistency, it is instructive to estimate whether a fully burned $M_{\text{Ch,non-rot}}$ WD would explain a rise time of 28 d. According to (Arnett 1982), the light curve width of a Type I SN (characteristic timescale to rise and decline) can be calculated as:

$$\tau_{LC} \propto \kappa^{\frac{1}{2}} \times E_{\text{k}}^{-\frac{1}{4}} M_{\text{ej}}^{\frac{3}{4}}.$$

Here, κ is a mean opacity, E_{k} the kinetic energy and M_{ej} the ejecta mass. In W7, roughly half the SN consists of iron-group material. Thus, we estimate the mean opacity of a $1.38 M_\odot$ WD fully burned to ^{56}Ni to be $\sim 2\times$ that of W7. The explosion would have a kinetic energy of $E_{\text{k,W7}} = 1.6 \times 10^{51}$erg instead of $E_{\text{k,W7}} = 1.3 \times 10^{51}$erg. All in all, the light-curve width would increase by a factor of $(2.0/\sqrt{\frac{1.6}{1.3}})^{\frac{1}{2}} \sim 1.34$ with respect to a normal SN. However, the rise time we infer (28 – 31 d) is 1.5 – 1.6 times that of a normal SN Ia ($\sim$ 19 d , Conley et al. 2006), as is the observed light curve decline (cf. light curve comparison plot in Taubenberger et al. 2011a – compare the time to decline by 0.5 mag between SN 2003du and SN 2009dc). This indicates that a $1.38 M_\odot$ WD obviously does not trap photons efficiently enough to explain the rise time needed by our spectral models based on W7. As a word of warning we note that the τ_{LC} estimate as given here is quite rough, so that the numbers given can only be regarded indicative, but not be taken as a proof.

For AWD3-det based models, our rise-time constraints are a problem as well. However, the AWD3-det model develops significant asymmetry (Pfannes et al. 2010). In this case, it is known that Arnett's rule can not be strictly applied (Sim & Mazzali 2008).

3.2.4 Tomography models

In order to obtain further information on the properties of SN 2009dc and the applicability of different models, we infer abundance profiles. For this, we use the AWD3-det density (Section 3.2.4.1) and as an alternative an empirically-inferred density profile with

a total mass of $3.0 M_{\odot}$. Finally, we construct a tomography model with only $1.38 M_{\odot}$, assuming that part of the light of SN 2009dc is generated by interaction of the ejecta with a surrounding medium (Section 3.2.4.4). This assumption breaks the constraints which normally exclude a Chandrasekhar-mass model, and is worth at least serious consideration. All models turn out to have a similar abundance structure in velocity space, but different total nucleosynthesis yields (Section 3.2.4.3).

As the spectra only show a slow evolution of line velocities, we expect a very moderate photospheric recession for all our models (which is confirmed by our actual calculations). This has an impact on the tomography method: if the abundance zone between two subsequent photospheres is too thin, the zone has little influence on the spectrum, which implies a large uncertainty in the abundance determination. In order to avoid this, we only model the spectra at -9.4 d, -3.7 d, $+4.5$ d, $+12.5$ d, $+22.6$ d and $+36.4$ d with respect to B maximum, leaving out the other ones in between. The rise times we assume for the tomography models are adjusted so as to fit the Si II λ6355 line velocity. They may deviate a bit from the values calculated in Section 3.2.3 as the abundances in the outer layers have been adapted to also optimise the fit to later spectra (cf. Sec. 2.2.5.4). The exact code-input parameters of our tomography models are compiled in Section 3.2.4.5.

3.2.4.1 Tomography with the AWD3-det profile

The synthetic spectra based on AWD3-det are shown in in Fig. 3.16. The rise time we have used for the calculations is 30d.

-9.4 d and -3.7 d models

The observed -9.4 d spectrum of SN 2009dc extends down to 3000 Å, where it shows a flux unusually large for a SN Ia. Despite the large luminosity and blue colour, the optical spectrum shows strong signatures of singly-ionised Fe-group and IME species. The similarly luminous SN 2007if does not show clear Si II or S II lines at this epoch (Scalzo et al. 2010). This points towards smaller IME abundances or also a higher degree of ionisation in SN 2007if [cf. SN 1991T – Mazzali et al. (1995) vs. SN 1999ee – Hamuy et al. (2002), where variations in ionisation are crucial].

In the case of SN 2009dc, an optimum fit of the earliest spectra is achieved with three abundance zones in the outer ejecta, as described in Section 3.2.3.2. From the outside inwards, these zones are unburned (i.e. depleted in Fe-group elements and also IME to avoid Ca and Si high-velocity absorption), somewhat richer in IME (Si mass fraction 7% in the AWD3-det-based model) and finally in IME/Fe-group elements (Si mass fraction: 15%, Fe-group mass fraction 9% here), respectively. C II λ6580 appears as a prominent line in the spectra. It is reproduced using surprisingly low mass fractions of C (4% in the outermost zone, 2% everywhere else).

Our synthetic spectra are generally too red. A bluer colour would have implied a high $T_{\rm R}$ throughout the atmosphere. We cannot implement this, as a low enough $T_{\rm R}$ is crucial for a reasonable ionisation balance, which is needed to match e.g. the ratio between the Si III λ4563 and Si II λ6355 features.

Within the first six days covered by the observations, the spectrum of SN 2009dc does not evolve very much. For both spectra, the photospheric velocities are low (8950 km s^{-1} at -9.4 d and 8300 km s^{-1} at -3.7 d) compared to normal SNe Ia before max-

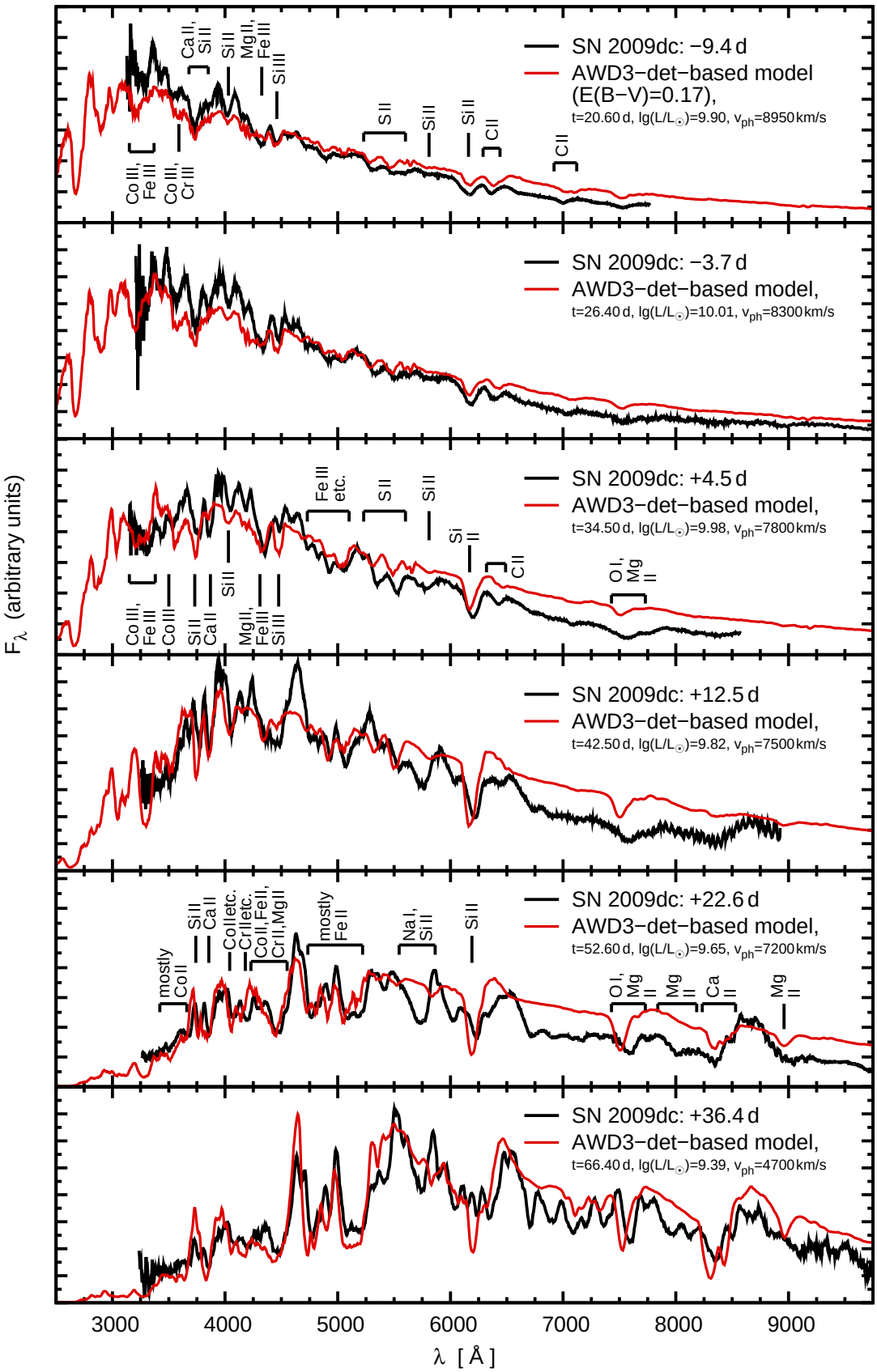

Figure 3.16: Sequence of spectral models (red graphs) for SN 2009dc, based on the AWD3-det density profile, and observations (black graphs). Identifications are given for the most prominent features.

imum. The most prominent lines due to Si II and S II are somewhat stronger at -3.7 d, but are still formed in the same atmospheric layers as before. This means that a reduction of IME in the outer layers has not only an effect on the -9.4 d spectrum, but also on later ones.

+4.5 d model

The spectrum and the model have now changed considerably. Lines made by IME gain still more strength, as temperatures drop in the outer layers of the atmosphere. The cores of the lines of singly-ionised IME (such as Si II) remain at high velocities. Only the low-velocity wings of the absorptions are caused by the lower layers of the ejecta. In Si II λ 6355 and in the S II W-feature (observed around $\sim$ 5400 Å), these low-velocity wings can unfortunately not be reproduced, regardless of the abundances assumed. This may indicate too strong an ionisation in the lower layers of the model, or too high a photospheric velocity, which however is required in order not to obtain a hot lower boundary spectrum.

The C II λ6580 feature in the observed spectrum has shifted to much lower velocities by this epoch. This clearly indicates inwards mixing of C. The line's strength at high velocities, at the same time, is automatically reduced because of lower densities and temperatures (the line originates from a highly excited level). Another feature indicating a drop in temperature is O I λ7773, which becomes deeper in the observations and in the model.

+12.5 d model

The $+12.5$ d spectrum shows a considerable drop in UV flux. Photospheric temperatures are lower, but the line blocking in the UV also increases. The Fe-group abundances are higher than at the previous epochs. Especially Co II and Cr II are now effective in suppressing the flux around $\sim$ 3500 Å: the ionisation degree is lower than at the last epoch, favouring recombination of Co III and Cr II into the singly-ionised stage. Despite the decreasing ionisation, the synthetic Fe III feature at $\sim$ 4300 Å is deep enough to reproduce the observed line, as significant amounts of ^{56}Ni have decayed into ^{56}Fe. No additional ^{54}Fe is assumed to be present in the models.

The observed features are generally well reproduced with two exceptions: At $\sim$ 4500 Å, there is a marked absorption and re-emission feature in the observations, which is reproduced only at later epochs in our models. The other exception is Si II λ5972, which is too shallow. We suggest that Na I D starts influencing the λ5972 feature around this epoch. Na is not included in our models, as past attempts to fit the feature have suffered from deviations in the ionisation of this element (Mazzali et al. 1997).

The Si II λ6355 velocity shows a mismatch between models and data, which increases with epoch. The observed line moves towards the red (lower velocities) as time progresses, while the centre of the synthetic line does not change that much. We have already removed Si from the outermost layers as far as the earliest spectra permit. Part of the velocity drop in the observed spectra may actually be caused by a feature forming bluewards, which gets stronger with time and emits into the Si II λ6355 region. This is probably a Fe II feature, but we do not reproduce it with our models.

+22.6 d model

At 22.6 d past B maximum, the photosphere recedes into a zone rich in Fe-group elements. The most prominent features in the spectrum are due to singly-ionised Fe-group elements with very strong lines (marked in Fig. 3.16). The balance of these lines is mostly a matter of temperature and density structure.

+36.4 d model

Remarkably, SN 2009dc still shows a photospheric spectrum long after maximum, with a $v_{\rm ph}$ of 4700 km s^{-1} at +36.4 d. The quality of the spectral fits is good given the late phase. The slow evolution into the nebular phase indicates larger densities in the inner part compared to normal SNe Ia.

The photospheric velocity at +36.4 d is much lower than at +22.6 d. This jump is, however, probably not physically significant, and rather an artefact of the photospheric approximation for such late epochs: An unusually low backscattering rate in the model shows that this approximation begins to break down here. We stop modelling the SN after this epoch.

Abundances

The abundance stratification of the AWD3-det-based ejecta models is shown in Fig. 3.17.

The outer zone ($v \gtrsim 9500$ km s^{-1}) only contains small amounts of IME and Fe-group elements. This corresponds to the weak line blocking and the relatively shallow features in the early-time spectra. Carbon mass fractions of some per cent suffice to fit the observed C II λ6580 line, although it is much stronger than in other SNe Ia. C must be present down to $\sim$ 7000 km s^{-1} in order to explain the observed low velocity in the post-maximum λ6580 feature. The majority of the material in the weakly burned zones, however, consists of O.

Between $\sim$ 8500 and 7000 km s^{-1}, IME are highly abundant. The mass fraction of Fe-group elements in this layer, between 10% and 50%, is constrained by line blocking of the UV flux.

Although our model sequences extend to late epochs, we mostly explore regions of incomplete burning. At velocities $<$ 7500 km s^{-1}, finally, Fe-group elements begin to be dominant. These zones are sampled by the +22.6 d and +36.4 d spectra. Due to degeneracy, the data can be fitted with different Fe-group mass fractions and mixes. We choose rather high mass fractions, consistent with the fact that we see some Fe-group elements already in the −9.4 d spectrum. ^{56}Ni, its decay products and ^{54}Fe together constitute 93% by mass at the +36.4 d photosphere. ^{54}Fe is only present deep inside our model ejecta, as our Fe-group mix mostly follows (cf. Sec. 2.2.5.4) the low-metallicity W7-based nucleosynthesis calculation W70 (Iwamoto et al. 1999).

Our models show a degree of mixing similar to tomography models of other SNe Ia Stehle et al. (2005). We need C in fairly deep layers, and Fe-group elements at the earliest photospheres. Some IME material is present in the unburned and Fe-group layers. Except for the outer layers, the sensitivity on the spectra on the IME mass fraction is only moderate. Thus, the spectra can also be reproduced with some more down-mixing of O, at the expense of Si. Strict limits on this mixing may be deduced in further studies modelling the nebular spectra. These show no marked emission lines due to oxygen

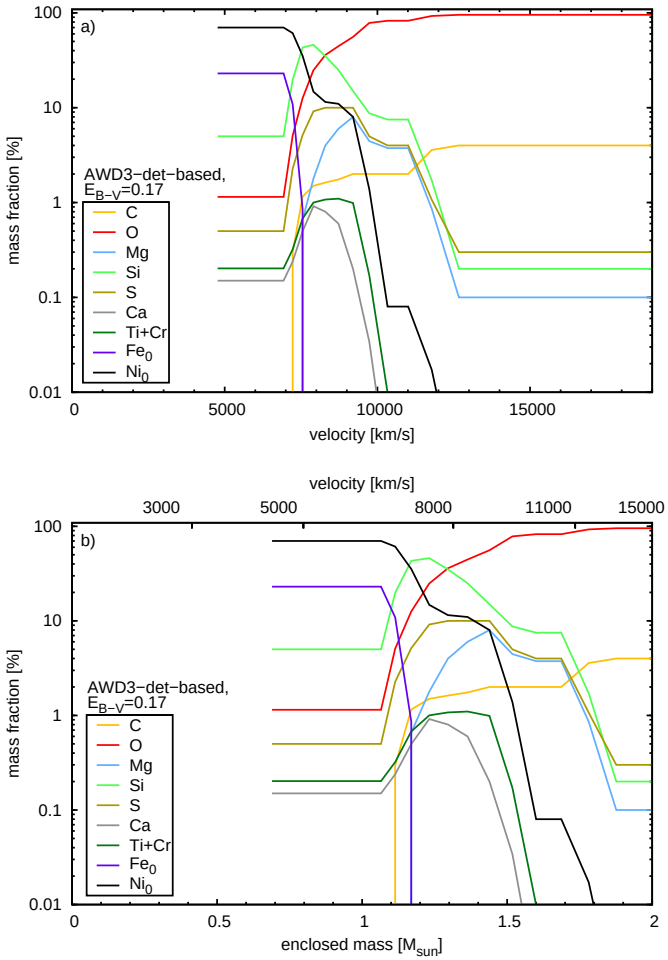

Figure 3.17: Abundance tomography of SN 2009dc based on the AWD3-det density profile. The "Ni_0" and "Fe_0" lines represent the ^{56}Ni and stable Fe abundances directly after explosion, respectively. Panel a): abundances in velocity space. Panel b): same, in mass space.

(Silverman et al. 2011), implying a separation of O and ^{56}Ni which prohibits the excitation of O atoms.

3.2.4.2 Abundance profiles and assumptions on metallicity/reddening

We repeat the AWD3-det-based tomography for a lower reddening $E(B-V) \sim 0.06$ and solar progenitor metallicity in order to examine how our results change with these assumptions.

When using a lower reddening, the models have lower luminosity and lower radiation field densities. This decreases the ionisation. The models contain more singly-ionised material, which is effective in producing lines (IME) and blocking the UV flux (Fe-group elements). Thus, we reproduce the spectra with somewhat lower abundances of IME in the outer layers of the ejecta, and lower abundances of Fe-group elements in the intermediate zones. Qualitatively, however, the abundance stratification in velocity space remains the same (Fig. 3.18b). A rise time of only 29.0 d is needed to fit continuum and lines in the early time spectra. The quality of the models is somewhat better than with the high standard reddening, which tended to exacerbate the models' flux excess in the red.

A high (solar) metallicity, on the other hand, implies that some nonvanishing Fe-group abundance is necessarily present also in the outer ejecta (Asplund et al. 2009). It also leads to a change in nucleosynthesis: significant amounts of ^{54}Fe appear in layers with incomplete burning (Iwamoto et al. 1999). We reflect this, as far as possible, in the abundances of Fe-group elements in our models (Fig. 3.18c). The resulting spectra have a slightly worse quality: the outer layers with solar Fe-group abundances block flux, heating up the atmosphere and increasing the flux excess in red, where the radiation can finally escape. Photospheric velocities are a bit larger in order to keep the backscattering reasonable and to keep the atmospheric temperatures low enough to form the spectral lines. This slightly shifts the borders of some abundance zones. Yet, the abundance stratification we infer is again qualitatively similar to the standard, low-metallicity case.

We conclude that our study is somewhat sensitive to reddening and metallicity, but not enough to compromise our conclusions.

3.2.4.3 Tomography with the 09dc-exp density profile

Density profile

The early-time models based on the empirical density profiles (Sec. 3.2.3.3) suggest a density model with $v_\times = 9000$ – 12000 km s^{-1} for the outer layers. Here, we test a relatively massive model, which we call 09dc-exp. The 09dc-exp model has a $v_\times$ of 11000 km s^{-1}, i.e. in

$$\rho(v,t) = a \times \exp(-bv) \times (t_0/t)^3,$$

t_0 and a are chosen such that W7 is matched at 11000 km s^{-1}, where it has a density of 7.2×10^{-15} g cm^{-3} (28.5 d past explosion). The slope is $b = 5.9 \times 10^{-9}$(km/s)$^{-1}$ for $t_\mathrm{r} = 28.5$ d. In the inner layers, we assumed a transition to a flatter slope. This is done by setting

$$\rho(v,t) = a_\mathrm{inner} \times \exp(-b_\mathrm{inner} v) \times (t_0/t)^3$$

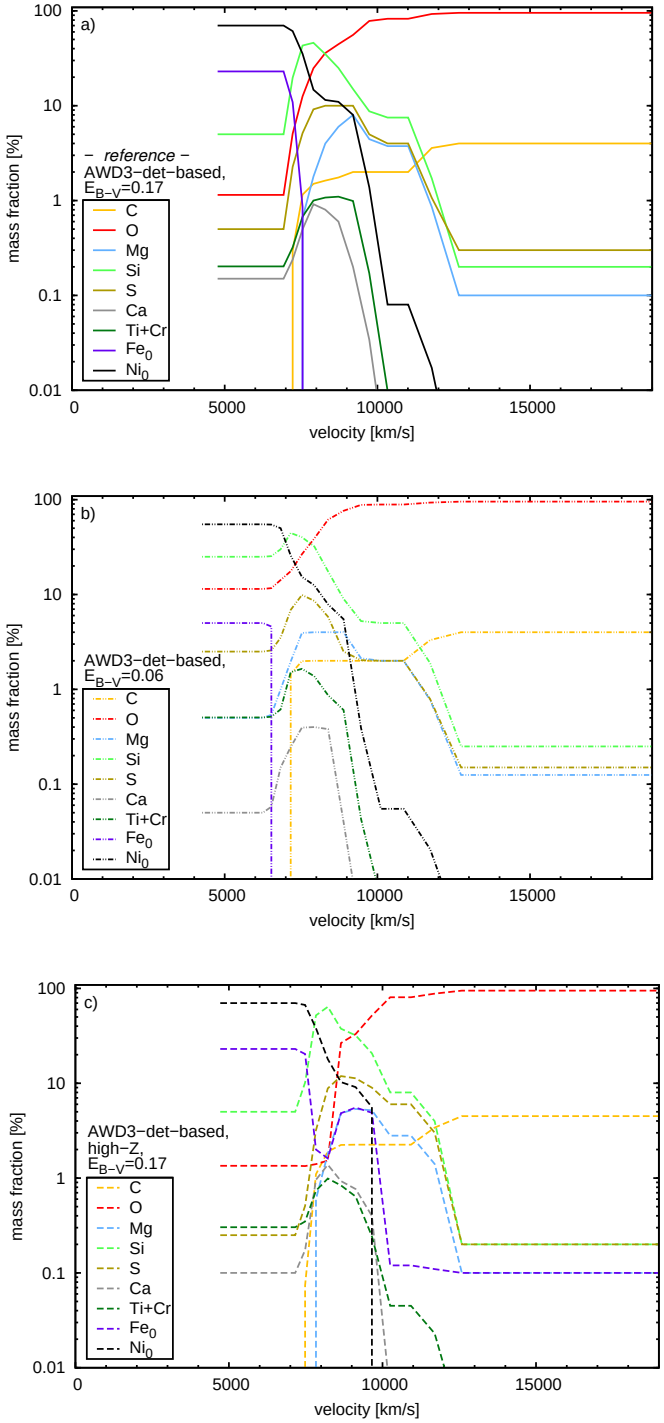

Figure 3.18: Influence of reddening and metallicity on the AWD3-det-based tomography (plots in velocity space). Panel a): standard [$E(B-V) \sim 0.17$, low metallicity] abundances (for reference). Panel b): abundances inferred for the lower limit reddening $E(B-V) \sim 0.06$ and low metallicity. Panel c): same for $E(B-V) \sim 0.17$, but solar metallicity ("high-Z").

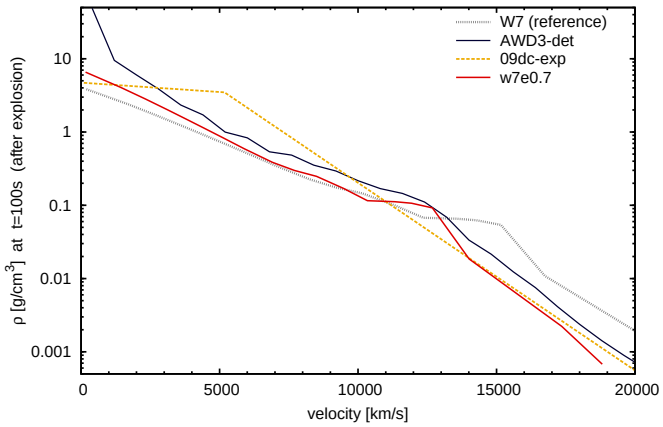

Figure 3.19: Density profiles used for abundance tomography, and W7 profile as a reference. The 09dc-exp model is shown with its slope adapted to a rise time of 28.5 d, as described in Sec. 3.2.3.1 / Eq. (3.3). In the fitting process, we adapt the slope with $t_{\rm r}$. The AWD3-det model has been converted to 1 D by adding up the cell masses in 50 radial velocity bins.

below a transition velocity, with $b_{\rm inner} = 0.1 \times b$. The resulting profile, in which the transition velocity has been chosen such that a total mass of $3.0 M_\odot$ is obtained, is shown in Fig. 3.19. The flatter slope in the inner zone leads to moderate core densities, comparable to those in core-collapse SN models [e.g. Woosley et al. (1995) – from their Fig. 12 /model 20 we obtain, for 100s past explosion, densities of ~ 2 g cm^{-3} at $v < 5000$ km s^{-1}]. We have optimised $t_{\rm r}$ (adapting the b values accordingly) once again in the fitting process to match the Si II λ6355 line velocity.

Spectral models

With the 09dc-exp density, we reproduce the observed spectra using a rise time of 28.5 d. The synthetic spectra closely resemble those calculated with the AWD3-det model (Fig. 3.16). A somewhat better fit quality is obtained with 09dc-exp for some epochs because the higher densities at $v = 3000 - 9000$ km s^{-1} decrease ionisation in that zone, and lead to a faster drop of radiation temperatures towards the outer zone.

Compared to the AWD3-det model, we need to assume significantly smaller photospheric velocities at $+22.6$ d and $+36.4$ d in order to match the spectral energy distribution. As a result, the backscattering rates are well consistent with the assumption of a photosphere at these late epochs.

Abundances

The abundance structure inferred with the 09dc-exp profile is similar to the AWD3-det standard case (Fig. 3.20), except for some shifts in the zone borders. Photospheric velocities are larger in the beginning, which is due to the smaller $t_{\rm r}$ with which the Si II λ6355 line can be fitted. As mentioned above, this situation inverts after B maximum.

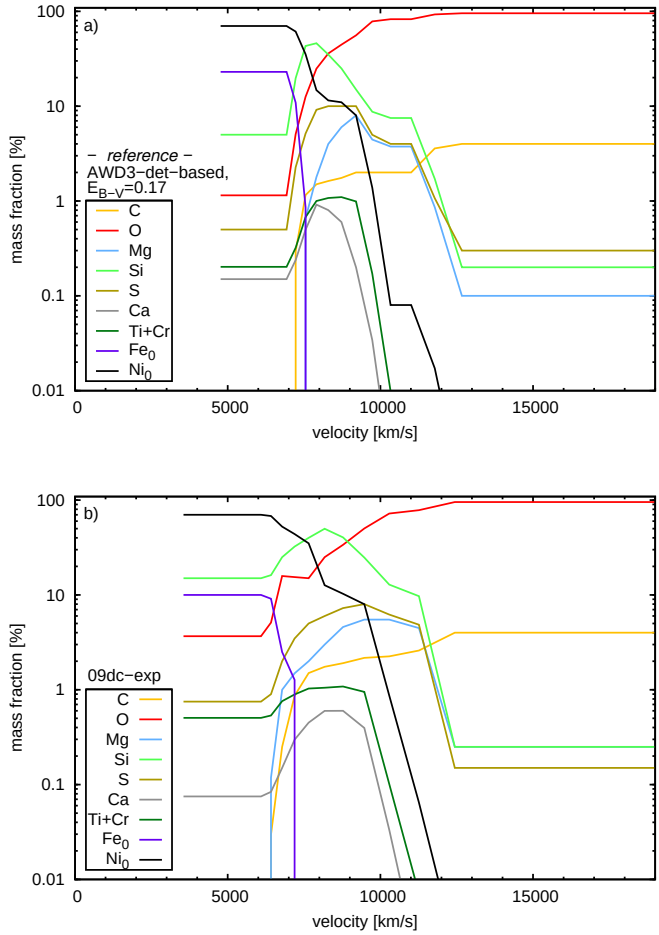

Figure 3.20: Abundance tomography of SN 2009dc based on the 09dc-exp density profile. Panel a): Abundance stratification in the AWD3-det-based model in velocity space (for reference). Panel b): abundances in the 09dc-exp model in velocity space.

3.2.4.4 Tomography assuming an external contribution to the luminosity – 09dc-int (interaction) model

As discussed in Sec. 3.2.3.5, single $M_{\text{Ch,non-rot}}$ WD models are inconsistent with SN 2009dc if all the observed light is generated internally by ^{56}Ni decay. A $M_{\text{Ch,non-rot}}$ explosion may, however, explain the SN if strong interaction of the ejecta with some circumstellar medium (CSM) generates some of the light received from the SN site. In this case, the SN only needs to contain a smaller amount of ^{56}Ni, and the long rise time may not be the result of a large progenitor mass. Instead, it may be explained by the "compression" of the ejecta when sweeping up the CSM, by scattering within the CSM, or by the light curve contribution of the interaction.

In an approach inspired by Hamuy et al. (2003), we test whether the spectra of SN 2009dc can be fitted with less luminous models, augmented by some continuous distribution of radiation. For this experiment, we reduce the bolometric luminosity in the simulation by 50% at -9.4 d (with respect to the AWD3-det based model). At the subsequent epochs, we keep the absolute luminosity reduction the same (1.5×10^{43} erg), assuming no significant increase of the continuum. From $+12.5$ d on, we begin a slow transition towards normal luminosities, so that at $+36.4$ d the simulation produces 67% of the luminosity in the models presented before. The mismatch between the observations and the model spectra with reduced luminosity is automatically fitted with a third-order polynomial[g)] after each code run in the fitting process. The final model parameters lead to an optimum fit of the observed spectrum by the sum of the model and the automatically generated polynomial.

The density profile used for these calculations is w7e0.7 (Fig. 3.19; cf. Sec. 3.1.1), a rescaled W7 model with Chandrasekhar mass, but a kinetic energy reduced to 70% of the original value. The smaller kinetic energy favours line formation at low velocities and may be interpreted in terms of a deceleration of the ejecta by the CSM.

Spectral models

Synthetic spectra for our 09dc-int model, with their respective intrinsic and continuum contributions, are shown in Fig. 3.21. The fit to the observations is very good, especially at the early epochs where the continuum contribution now allows us to perfectly match the blue colour of the observed spectra. The polynomial continua become less luminous and redder with time, which shows that the continuum luminosity and colour are reasonably coupled, although we have not enforced this on the fits. We emphasise, however, that our continua are not really thermal: At early epochs, a thermal distribution resembling the steep continuum we need would imply an unrealistically large T. We speculate that the shape may instead be explained by non-LTE emission of overlapping lines e.g. of Fe-group elements.

The most marked mismatch between synthetic and observed spectra remains in the ~ 5700 Å feature at the later epochs, where we have not attempted to fit the Na I D line. Furthermore, the Si II λ6355 line keeps too strong a blue wing at the late epochs, even more than in the AWD3-det and 09dc-exp models. This obviously depends on densities

[g)] We fit the mismatch between the observed (de-reddened) and the zero-extinction synthetic spectrum using a Levenberg-Marquardt method. The wavelength range for the fit is restricted to < 7500 Å so that the procedure is consistent for the spectra whose IR extent varies. Before further evaluation, the continua are artificially reddened with the standard total SN reddening of $E(B-V) = 0.17$.

and ionisation in the models, and is – as other, minor mismatches – not a major concern at the current stage.

Abundances

The abundance structure (Fig. 3.22) remains similar to the one obtained with the AWD3-det model, despite the physical differences. The increase of burning products from the outside inwards is a bit steeper. This is needed to fit the observed line depth as the continuum contribution makes the lines shallower in the final model (sum spectrum). We have assumed an intermediate metallicity (cf. Section 3.2.4.2), as the typical problems caused by this (redder spectrum, longer rise time needed) do not appear here.

3.2.4.5 Parameters of the abundance tomography models

The code input parameters for our abundance tomography models and the calculated temperature of the photospheric black body, $T_{\rm ph}$, for each spectrum are listed in Table 3.9.

3.2.5 Discussion

Our tomography models represent different possible explosion scenarios for SN 2009dc. Here, we comment on these scenarios and the constraints under which they are consistent with our results. We separately discuss fully-intrinsic-luminosity (Sec. 3.2.5.2) and interaction-luminosity (Sec. 3.2.5.3) models. As a starting point, we first summarise the information we obtained on the integrated nucleosynthesis yields of SN 2009dc.

3.2.5.1 Abundances

The total masses of C/O, IME, Fe-group elements and ^{56}Ni in all our tomography models are compiled in Table 3.10. The ^{56}Ni masses shown do not include the ^{56}Ni in the opaque core of the ejecta below the $+36.4$ d photosphere. The mass of this core, which is expected to contain a significant additional amount of ^{56}Ni, is also given in the Table.

Mass of Fe-group elements and ^{56}Ni in SN 2009dc

The ^{56}Ni mass allowed by each tomography model is an important indicator for the consistency with SN 2009dc, as we can compare it to what Arnett's rule (Arnett 1982) requires to produce the light-curve maximum of SN 2009dc. Applied as in Taubenberger et al. (2011a), the rule yields a ^{56}Ni mass of 2.0 ± 0.7 or $2.3 \pm 0.8 M_{\odot}$ for an assumed rise time of 26.0 d or 30.0 d, respectively. The error estimates include uncertainties in the distance, extinction and in applying Arnett's model (cf. Taubenberger et al. 2011a).

The amount and mix of Fe-group elements in our models is somewhat uncertain due to degeneracies especially at the late epochs. We have chosen large Fe-group abundances (cf. last part of Sec. 3.2.4.1) and assumed a mix of Fe-group elements favouring ^{56}Ni as far as possible. If we additionally assume the opaque core of the ejecta at $+36.4$ d to be dominated by ^{56}Ni, we can perform a consistency assessment which is conservative in the sense that we will not decline models when uncertain.

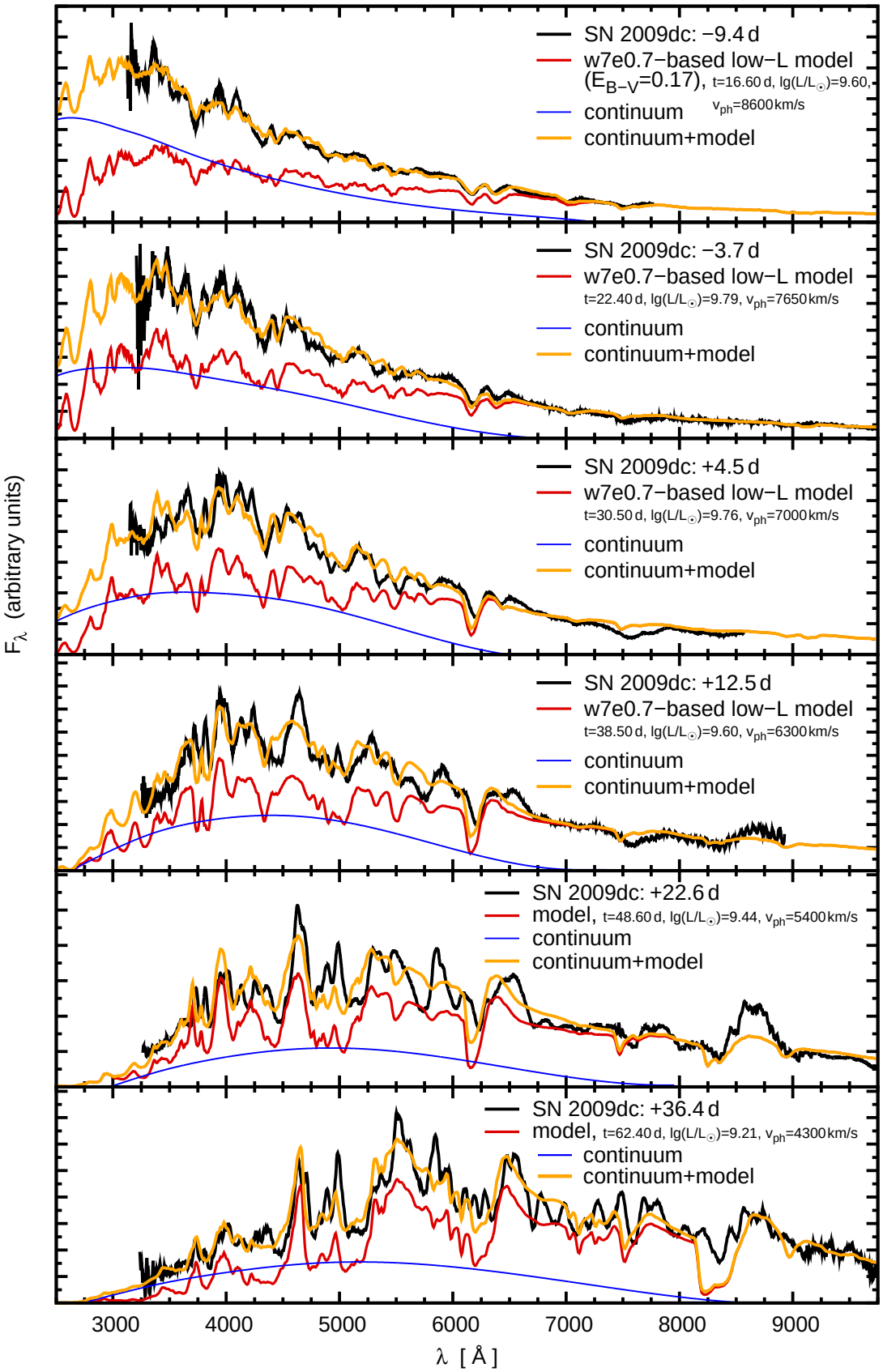

Figure 3.21: 09dc-int models for SN 2009dc. Each observed spectrum (black) is modelled as the sum (orange) of an intrinsic SN model spectrum (red) and a continuum (blue), resulting from interaction with circumstellar material. The continua (see also text) are third order polynomials which have a minimum at $\gtrsim$ 7000 Å. Contributions of the continua redwards from this minimum and contributions < 0 have been removed in the plot.

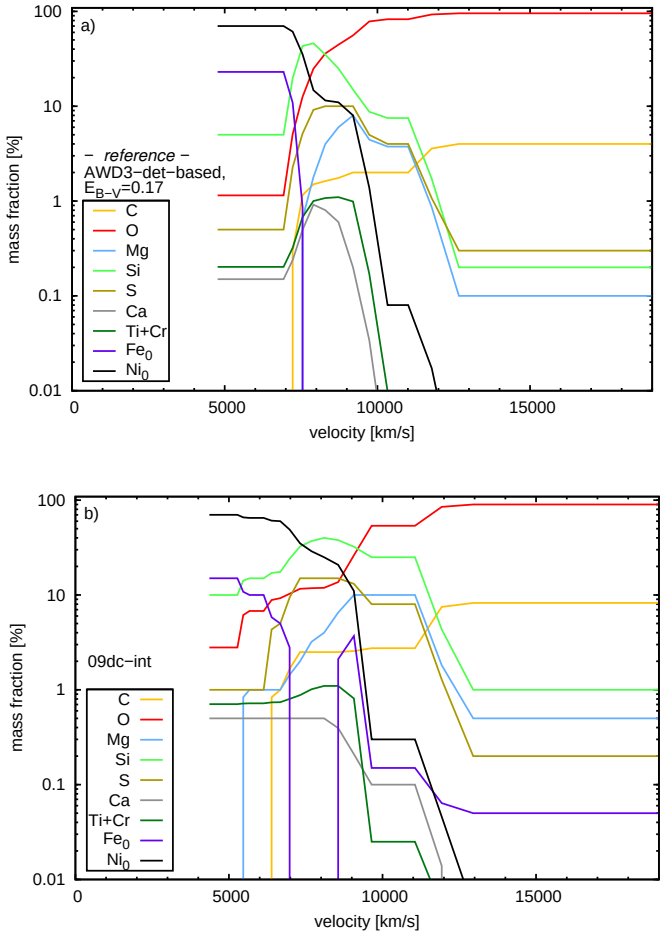

Figure 3.22: Abundance tomography of SN 2009dc assuming Chandrasekhar-mass ejecta, with some of the light generated by interaction with a CSM: 09dc-int model. Panel a): Abundance stratification in the AWD3-det-based model in velocity space (for reference). Panel b): abundances in the 09dc-int model in velocity space.

Table 3.9: Parameters of the tomography models for SN 2009dc. The abundance values, which are only given for significant elements, hold above the lower boundary v_{lowbnd} of the respective layer (up to the beginning of the next layer). The outer shells ("epoch" designations "oo", "o") improve the fit of the -9.4 d spectrum (see text).

Model	epochs	$\lg\left(\frac{L_{\mathrm{bol}}}{L_\odot}\right)$	v_{lowbnd}	T_{ph}	Element abundances (mass fractions)									
	[d]		[km s^{-1}]	[K]	X(C)	X(O)	X(Mg)	X(Si)	X(S)	X(Ca)	X(Ti)	X(Cr)	X(Fe)$_0$[a)]	X(^{56}Ni)$_0$[a)]
09dc-AWD3-det	oo	-	11550	-	0.04	0.95	0.00	0.00	0.00	0.0000	0.0000	0.0000	0.0000	0.0000
$t_{\mathrm{r}} = 30$ d	o	-	9550	-	0.02	0.83	0.04	0.07	0.04	0.0000	0.0000	0.0001	0.0000	0.0008
	-9	9.90	8950	14098.3	0.02	0.56	0.08	0.15	0.10	0.0020	0.0009	0.0090	0.0000	0.0800
	-4	10.01	8300	13586.8	0.02	0.45	0.06	0.25	0.10	0.0060	0.0010	0.0100	0.0000	0.1100
	$+5$	9.98	7800	11467.5	0.01	0.27	0.02	0.45	0.10	0.0100	0.0005	0.0100	0.0000	0.1200
	$+13$	9.82	7500	9160.4	0.01	0.15	0.01	0.50	0.06	0.0060	0.0002	0.0080	0.0000	0.2500
	$+23$	9.65	7200	7534.4	0.01	0.08	0.00	0.30	0.04	0.0030	0.0000	0.0040	0.0250	0.5500
	$+36$	9.39	4700	7295.0	0.00	0.01	0.00	0.05	0.01	0.0015	0.0000	0.0020	0.2300	0.7000
09dc-AWD3-det,	oo	-	11600	-	0.04	0.95	0.00	0.00	0.00	0.0000	0.0000	0.0000	0.0000	0.0000
$E(B-V) = 0.06$	o	-	9200	-	0.02	0.89	0.02	0.05	0.02	0.0000	0.0000	0.0001	0.0000	0.0006
$t_{\mathrm{r}} = 28$ d	-9	9.72	8600	13863.8	0.02	0.76	0.04	0.09	0.03	0.0004	0.0006	0.0055	0.0000	0.0550
	-4	9.81	8000	12769.8	0.02	0.61	0.04	0.18	0.06	0.0040	0.0008	0.0080	0.0000	0.0800
	$+5$	9.79	7350	10973.9	0.02	0.27	0.04	0.40	0.10	0.0040	0.0015	0.0150	0.0000	0.1500
	$+13$	9.66	7000	8971.0	0.01	0.18	0.02	0.45	0.07	0.0025	0.0005	0.0150	0.0000	0.2500
	$+23$	9.51	6650	7430.2	0.00	0.14	0.01	0.30	0.04	0.0015	0.0001	0.0060	0.0000	0.5000
	$+36$	9.26	4200	7401.9	0.00	0.11	0.01	0.25	0.03	0.0005	0.0001	0.0050	0.0500	0.5500
09dc-AWD3-det,	oo	-	11700	-	0.04	0.95	0.00	0.00	0.00	0.0000	0.0000	0.0000	0.0010	0.0000
solar metallicity	o	-	9800	-	0.02	0.81	0.03	0.08	0.06	0.0001	0.0001	0.0003	0.0012	0.0000
$t_{\mathrm{r}} = 31.25$ d	-9	9.89	9200	13265.0	0.02	0.42	0.06	0.25	0.10	0.0053	0.0001	0.0030	0.0650	0.0750
	-4	9.99	8450	13042.3	0.02	0.28	0.05	0.36	0.12	0.0090	0.0003	0.0080	0.0500	0.1000
	$+5$	9.97	8100	10814.0	0.02	0.02	0.02	0.65	0.10	0.0143	0.0003	0.0100	0.0200	0.1500
	$+13$	9.83	7800	8813.7	0.01	0.01	0.01	0.60	0.04	0.0120	0.0002	0.0080	0.0000	0.3000
	$+23$	9.66	7600	7264.7	0.01	0.01	0.00	0.40	0.02	0.0060	0.0001	0.0060	0.0500	0.5000
	$+36$	9.39	4650	7300.2	0.00	0.01	0.00	0.05	0.00	0.0010	0.0000	0.0030	0.2300	0.7000
09dc-exp	oo	-	11600	-	0.04	0.95	0.00	0.00	0.00	0.0000	0.0000	0.0000	0.0000	0.0000
$t_{\mathrm{r}} = 28.5$ d	o	-	9950	-	0.02	0.74	0.06	0.12	0.06	0.0000	0.0000	0.0001	0.0000	0.0008
	-9	9.90	9350	14170.7	0.02	0.56	0.06	0.20	0.08	0.0030	0.0008	0.0080	0.0000	0.0750
	-4	10.01	8700	13659.2	0.02	0.39	0.06	0.35	0.08	0.0060	0.0010	0.0100	0.0000	0.0900
	$+5$	9.97	7900	11959.4	0.02	0.25	0.03	0.50	0.06	0.0060	0.0005	0.0100	0.0000	0.1250
	$+13$	9.82	7200	9969.7	0.01	0.15	0.02	0.40	0.05	0.0045	0.0003	0.0100	0.0000	0.3500
	$+23$	9.62	6550	8230.3	0.00	0.16	0.01	0.25	0.02	0.0015	0.0001	0.0075	0.0250	0.5250
	$+36$	9.35	3500	9243.9	0.00	0.04	0.00	0.15	0.01	0.0008	0.0001	0.0050	0.1000	0.7000
09dc-int	oo	-	11600	-	0.08	0.90	0.01	0.01	0.00	0.0000	0.0000	0.0000	0.0005	0.0001
$t_{\mathrm{r}} = 26$ d	o	-	9200	-	0.03	0.54	0.10	0.25	0.08	0.0010	0.0001	0.0001	0.0015	0.0030
	-9	9.60	8600	14329.5	0.03	0.16	0.10	0.35	0.15	0.0025	0.0010	0.0100	0.0500	0.1500
	-4	9.79	7650	14374.0	0.03	0.12	0.04	0.40	0.15	0.0050	0.0010	0.0100	0.0000	0.2500
	$+5$	9.76	7000	11659.4	0.03	0.12	0.02	0.33	0.15	0.0050	0.0008	0.0080	0.0000	0.3500
	$+13$	9.60	6300	9467.7	0.01	0.09	0.01	0.17	0.05	0.0050	0.0004	0.0070	0.0500	0.6000
	$+23$	9.44	5400	8137.0	0.00	0.07	0.01	0.15	0.01	0.0050	0.0002	0.0070	0.1000	0.6500
	$+36$	9.21	4300	7143.0	0.00	0.03	0.00	0.10	0.01	0.0050	0.0001	0.0070	0.1500	0.7000

[a)] The abundances of Fe, Co and Ni in our models are assumed to be the sum of ^{56}Ni and the elements produced in the decay chain (^{56}Co and ^{56}Fe) on the one hand, and directly synthesised / progenitor Fe on the other hand. Thus, they are conveniently given in terms of the ^{56}Ni mass fraction at $t = 0$ [$X(^{56}\mathrm{Ni})_0$], the Fe abundance at $t = 0$ [$X(\mathrm{Fe})_0$], and the time from explosion onset t.

Table 3.10: Integrated yields of C/O, IME and Fe-group elements in the models. The Fe-group values include the respective amount of ^{56}Ni. For the core below the +36.4 photosphere [mass M(core)], we cannot constrain the abundances. We expect it to contain a significant amount of ^{56}Ni.

model	M(C/O) [$M_\odot$]	M(IME) [$M_\odot$]	M(Fe-group) [$M_\odot$]	$M(^{56}\mathrm{Ni})$ [$M_\odot$]	M(core) [$M_\odot$]
09dc-AWD3-det	0.67	0.24	0.48	0.37	0.68
09dc-AWD3-det-lessred	0.83	0.31	0.35	0.32	0.57
09dc-AWD3-det-highZ	0.57	0.26	0.56	0.42	0.66
09dc-exp	0.55	0.64	1.40	1.24	0.41
09dc-int	0.39	0.29	0.34	0.30	0.36

The smallest ^{56}Ni mass ($\lesssim 0.7 M_\odot$) is derived for the 09dc-int model. This model is a special case as it assumes part of the luminosity not to come from ^{56}Ni. Comparing to the ^{56}Ni mass required by Arnett's rule, one recognises that the interaction with the CSM would have to produce $\sim 2/3$ of the maximum luminosity. This is somewhat more than we assumed above, but the model is consistent within the uncertainty in the Arnett-based value.

For models assuming the luminosity to be intrinsic, we obtain sharper constraints. The AWD3-det based models only allow for a ^{56}Ni mass of $\lesssim 1.1 M_\odot$, which is a severe problem if one wants to explain SN 2009dc. We further discuss this in Sec. 3.2.5.2. The 09dc-exp model contains $\lesssim 1.7 M_\odot$, which is consistent with Arnett's rule within the error.

Minimum mass of IME and C/O in SN 2009dc

Our models correspond to a range of explosion scenarios, which imply different density structures and different conditions for ionisation and excitation in the ejecta. According to the previous subsection, their mass is too low or just enough to contain the ^{56}Ni expected in SN 2009dc. Therefore, we can regard the minimum masses of IME and C/O needed in our models as lower limits to the actual nucleosynthesis yields of the SN.

For the intermediate-mass elements, this means

$$M_{\mathrm{IME,09dc}} \gtrsim 0.24 M_\odot.$$

For the C/O mass, to which C only makes a minor contribution, we obtain

$$M_{\mathrm{C/O,09dc}} \gtrsim 0.39 M_\odot.$$

The amount of O which is included here ($\gtrsim 0.36 M_\odot$) is needed for the best possible reproduction of the observed O I λ7773 feature.

3.2.5.2 Candidate explosion models without CSM interaction

Rapidly-rotating WD models

With our AWD3-det-based models, we explored the possibility of explaining SN 2009dc with an explosion of an supermassive, rotating C-O white dwarf. Rotat-

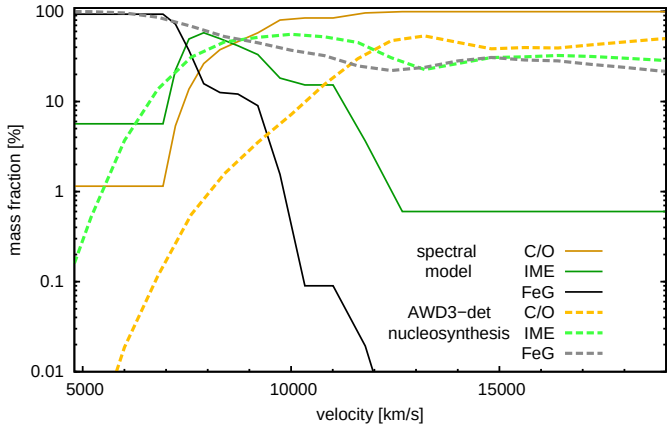

Figure 3.23: Comparison of the abundance stratification inferred from the spectra (using the AWD3-det density) with the nucleosynthesis of the AWD3-det model (Pfannes et al. 2010). We show the total abundances of three element groups (C/O, IME and FeG / Fe-group elements), as they are used in the AWD3-det calculations. The AWD3-det mass fractions have been obtained from the original 3-D model by adding up the masses of C/O, IME and Fe-group elements, respectively, in 50 radial velocity bins. The lower limit of the velocity axis corresponds to the $+36.4$ photosphere.

ing white dwarfs with up to $\sim 2M_{\odot}$ may exist (Yoon & Langer 2005), although there is no observational proof and the mass limit is a matter of debate (Scalzo et al. 2010).

Our spectral models do not allow enough ^{56}Ni in the intermediate and outer zones of the ejecta in order to explain the large ^{56}Ni masses expected for SN 2009dc (cf. Sec. 3.2.5.1). Nucleosynthesis calculations for the hydrodynamical explosion model (Pfannes et al. 2010) indicate a ^{56}Ni mass of $\sim 1.5M_{\odot}$, which would be compatible with SN 2009dc. However, such efficient nucleosynthesis within the white dwarf seems to imply that burning products, i.e. Fe-group elements and IME, are ejected with high velocities, contradicting our models (Fig. 3.23).

The major uncertainty in our analysis here is that it assumes spherical symmetry. The AWD3-det ejecta are significantly asymmetric (Pfannes et al. 2010). Therefore, we can not completely exclude SN 2009dc to be explained by a rotating WD model, although the factor ~ 2 between the ^{56}Ni mass in our model and the ^{56}Ni mass calculated with Arnett's rule (Sec. 3.2.5.1) seems difficult to overcome, and polarimetric observations disfavour asymmetry (Tanaka et al. 2010). We suggest to further analyse explosions of rotating WDs with $\sim 2M_{\odot}$ in 3 D in order to finally test whether the scenario can explain some SC SNe. This should involve modelling a set of explosions, also including delayed detonations, and simulating the radiative transfer within the predicted ejecta.

Mergers of C-O white dwarfs

The occurrence rates of WDs with $M > 1M_{\odot}$ are low (Kepler et al. 2007). Therefore, it is difficult to explain SNe with a merger of massive WDs, and more realistic to assume a merger with a massive primary and a less massive secondary (e.g. 1.1 and $0.9M_{\odot}$). In the merging or accretion process, the secondary is disrupted and its material is presumably too dilute to be converted into ^{56}Ni when the explosion occurs. This

means that the maximum ^{56}Ni mass yielded from such an explosion is limited by the mass of the primary WD at explosion, which in turn is smaller than $M_{\text{Ch,non-rot}}$. WD mergers will not explain the luminosity of SN 2009dc through an extreme ^{56}Ni production. They will rather be the progenitors of choice for a scenario with an external luminosity contribution (see Sec. 3.2.5.3).

Core collapse and Type I$\frac{1}{2}$ SNe

The 09dc-exp model, which has an ejecta mass of $3M_{\odot}$, corresponds to an explosion of an extended progenitor star instead of a WD. This would imply either core-collapse, or a thermonuclear explosion within a star (Ergma & Paczynski 1974). In any case, the explosion model has to produce an ejecta mass $\geq 3M_{\odot}$ and a ^{56}Ni mass of $> 1.5M_{\odot}$.

Umeda & Nomoto (2008) discussed the possibility of producing ^{56}Ni masses of some $M_{\odot}$ in a core collapse. Their models, based on stars with main-sequence masses of $M \geq 25M_{\odot}$, yield ^{56}Ni masses as we need them. However, the models still contain H and He envelopes ($M_{\text{H+He}} \gtrsim 10M_{\odot}$), which would have to be removed by stripping or mass loss in order for the SN to display a Type Ia spectrum. Apart from this, the (1-D) models show an abundance stratification (Fig. 5 of their paper) relatively similar to our tomography results and generally to SN Ia models. O is not significantly mixed with ^{56}Ni. This may prevent the appearance of nebular O lines, and therefore ensure compatibility with the non-detection of these lines in SC SNe Ia (Taubenberger et al. 2011a). It is necessary to explore whether abundance mixing can be sufficiently suppressed and if enough ^{56}Nican be generated also in multi-D hydrodynamic models incorporating the neutrino mechanism (e.g. Marek & Janka 2009).

Thermonuclear explosions within stars, on the other hand, have long been proposed as models for SNe (Ergma & Paczynski 1974; Iben & Renzini 1983), but never been verified using observations. Stars with a zero-age-main-sequence mass of $\lesssim 8M_{\odot}$ form degenerate C-O cores after He burning. After mass loss in the asymptotic-giant-branch (AGB) phase, the C-O core usually remains as a bare white dwarf. In the most massive AGB stars, however, the degenerate core may grow towards the Chandrasekhar limit, and an explosion may commence. The explosion would eject up to a Chandrasekhar mass of ^{56}Ni (corresponding to the entire stellar core), as well as further nucleosynthesis products and progenitor material. Iben & Renzini (1983) suggested that H and He may be visible in the spectra of such SNe, and therefore dubbed them "Type I$\frac{1}{2}$" explosions (i.e. thermonuclear with a core-collapse-like display). This must be avoided in order to explain SC SNe Ia with the model. The shocked He and H may contribute somewhat to the observed luminosity when cooling down, which is an advantage of the model as long as no H or He line emission occurs. The Type I$\frac{1}{2}$ scenario has to be simulated with recent hydrodynamic codes in order to make more definite predictions on its nucleosynthesis and observational outcome.

3.2.5.3 Candidate explosion models with CSM interaction

Finally, we discuss a scenario which involves light generation by significant interaction of the ejecta with a CSM. The 09dc-int model (Sec. 3.2.4.4) shows that the spectra can successfully be explained with an intrinsic and an external light contribution. The shape

of the external contribution in our models is a pseudo-continuum, which does not follow a strictly thermal shape, but may be generated by emitting lines which overlap.

One may thus explain "SC" objects with a $M_{\text{Ch,non-rot}}$ explosion or an explosion of a slightly supermassive WD. The CSM itself has to consist mainly of C/O, as no H and He lines are visible in the photospheric or nebular spectra of SC SNe Ia. In this context, the most promising progenitor models are those in which a primary and largely undisturbed C/O-WD accretes C and O from a secondary WD (cf. Sec. 3.2.5.2). As we discussed above, this implies a mass ratio $q \lesssim 0.8$. A mass ratio below q_{crit} would also be excluded: in this case, the primary WD might slowly grow towards $M_{\text{Ch,non-rot}}$ and explode, but the explosion is probably undisturbed by the material of the secondary, which remains a compact object. Scalzo et al. (2010) have already considered a WD merger scenario to explain SN 2007if, another SC Type Ia SN. They showed that a detailed assessment of the line velocity evolution in the spectra of this SNe may hint towards a structure involving a dense outer shell.

The CSM interaction scenario has several appealing aspects. It would not only explain the luminosity of SC SNe Ia, but also a slow-down of the ejecta which leads to low line velocities. The w7e0.7 density for the inner ejecta led to good early-time fits in the 09dc-int model. In this model, 30% of the kinetic energy yield of the explosion were assumed to be transferred to the circumstellar shells. Crudely taking the distribution of kinetic energy in the ejected mass to be uniform, this would mean that the circumstellar material would constitute 30% of the total mass $M_{\text{CSM}} + M_{\text{Ch,non-rot}}$, i.e. $0.43 \times M_{\text{Ch,non-rot}} = 0.59 M_{\odot}$.

Part of the energy lost by the ejecta, some 10^{49} erg out of $0.3 \times E_{\text{k},W7} = 0.4 \times 10^{51}$ erg, would gradually be converted into luminosity, producing the light output which distinguishes SC SNe from normal SNe Ia. Eventually the complete CSM would be dragged with the expanding ejecta, and the interaction would get less violent with time. At some point, the contribution to the luminosity would then be expected to stop. This may be an explanation for the drop in almost all colour light-curves at $\sim$ 300 d past max. found by Silverman et al. (2011) and Taubenberger et al. (2011a).

The strongest argument against an interaction model is perhaps the lack of direct evidence. No emission lines are seen as a hint. After the photospheric phase, the light-curve shows a slope compatible with ^{56}Co decay for a long time (Silverman et al. 2011). In the end, however, the scenario must be judged on the basis of radiation hydrodynamics models which are capable of simulating the explosion as well as the effects of the interaction .

3.2.6 Summary – analysis of the "Super-Chandrasekhar" SN 2009dc

In this chapter, we analysed the SN 2009dc, which is a "Super-Chandrasekhar" SN Ia. Such objects are mainly characterised mainly by an extremely high luminosity in the early phases; this either requires about a Chandrasekhar mass (or even more) of ^{56}Ni alone, or points towards an external luminosity contribution. We studied the SN spectra with our code, adopting a large ^{56}Ni mass first, and a luminosity contribution by ejecta-CSM interaction afterwards. Furthermore, we gave some speculations on possible progenitor scenarios.

In the first case, i.e. that of a large ^{56}Ni mass, very diverse explosion models (SN Ia from a rotating WD, core-collapse SN, ...) may apply. We therefore began our study using early observations to constrain the density in the outer layers and the rise time

without assuming a specific explosion scenario. Densities somewhat smaller than those of a standard W7 density model are preferred in the outer layers because of the low line velocities in the spectra (analogous to the case of SN 2005bl). In accordance with observations of the early-time light curve, we found that SN 2009dc has a rise time of $\gtrsim$ 24d[h)]. The long rise time implies that the ^{56}Ni mass calculated with Arnett's rule (Arnett 1982) is larger than a Chandrasekhar mass. A W7 density model can safely be ruled out, as it requires an even longer rise time to fit the spectra (and thus even more ^{56}Ni according to Arnett's rule).

We proceeded by conducting abundance tomography, still under the assumption of a large ^{56}Ni mass. We created tomography models using two different density profiles: one representing the detonation of a rotating $2.0M_{\odot}$ WD [AWD3-det simulation, Pfannes et al. (2010)], and another one constructed from the early-time observations (with a total mass of $3.0M_{\odot}$). The most important feature of the abundance stratification is that Fe-group elements and IME are constrained to relatively low velocities. Because of this, densities must be large in the centre of the ejecta in order to obtain ^{56}Ni masses as they are required for the light curve. The AWD3-det model has severe problems here, indicating that SN 2009dc probably was not made by a $2.0M_{\odot}$ WD (cf. Conclusions, Chap. 5). Thus, we have declined one intuitive explanation for SN 2009dc (cf. Howell et al. 2006). Our $3.0M_{\odot}$ model is compatible with a larger ^{56}Ni content. SC SNe might be core-collapse or Type I$\frac{1}{2}$ (Ergma & Paczynski 1974; Iben & Renzini 1983) explosions. However, such explosions in most cases lead to an abundance pattern different from what we find.

As an alternative, we created a tomography model in which some of the luminosity is assumed to be produced by the interaction of the ejecta with a CSM. We took a w7e0.7 profile (cf. Sec. 3.1.1) and calculated models with a luminosity reduced by 50 – 33% with respect to our other models. The synthetic spectra which resulted gave an extremely good match to the observations when augmented by a continuous, polynomial flux distribution. Our model implies that SN 2009dc would be an explosion within a C/O CSM, which slows down the ejecta and thus generates additional light. The biggest weakness of this scenario is the lacking explanation of how the continuous flux is generated. Yet, the scenario, which could correspond to a WD merger in which one WD is **accreted** onto another one, may be the most promising one.

Nebular spectra of Super-Chandrasekhar SNe are available now and will soon be analysed. This will make it possible to estimate the ^{56}Ni mass independently from previous results, and may help us to pick the right one from the SN models proposed here.

[h)] $\gtrsim$ 21d if a reddening value of $E(B-V)_{\rm tot} = 0.06$ applies, which is the lower limit according to the values and uncertainties given by Taubenberger et al. (2011a).

Chapter 4

SNe IIb/Ib/Ic: a sequence of spectral models for stripped CC SNe

In this chapter, we apply our methods to stripped-envelope core-collapse SNe (stripped CC SNe, SNe IIb/Ib/Ic). We use the NLTE code module presented in Chapter 2 to analyse the outer H and He layers of these SNe. This promises to give direct constraints on progenitor-star models.

Not much is known about the effect of different degrees of envelope stripping in core-collapse SNe on the spectra – except for the fact (Fig. 4.1) that some SNe show neither H nor He lines (SNe Ic), some show only He features (SNe Ib) and some show signs of both elements (SNe II). Here, we aim at a quantitative answer to the question: "How much He can be hidden in a SN Ic without lines showing up?" We thus begin to establish a detailed connection between observed SNe and their progenitors. We treat low- to moderate-mass SNe in this thesis as a starting point. First, we construct two tomography models (four epochs each), resembling an observed Type IIb and Ic SN, respectively. Then, we set up a sequence of "transition models". These transition models, starting from a SN IIb-like model with a somewhat truncated H envelope, have decreasing H/He envelope masses until only C and O remain. They allow us to study the connection between spectral lines and H/He abundances.

Below, we first present the SN IIb and Ic models, and then the transition sequence, giving the necessary technical details. We discuss our results focussing on the behaviour of He in NLTE; the behaviour of H may be subject to a later study. We investigate the dependence of our models on some basic assumptions, and find out whether our results fit in with current progenitor models for stripped-envelope core-collapse SNe.

4.1 Models for the SNe 2008ax and 1994I

In order to obtain reasonably realistic spectral models for low-mass SNe IIb and SNe Ic, we start out with abundances and densities from parametrised 1-D hydrodynamics/ nucleosynthesis models (cf. Introduction, Sec. 1.3.3.4) for such SNe (Shigeyama et al. 1990; Woosley et al. 1994; Iwamoto et al. 1994). Although these models are relatively old, they explain the observations of stripped core-collapse SNe reasonably well; in this respect, no significant progress has been made with more recent models. We take two well-observed supernovae [SN 2008ax, Type IIb – e.g. Taubenberger et al. (2011b); SN 1994I, Type Ic – e.g. Filippenko et al. (1995)] as reference objects.

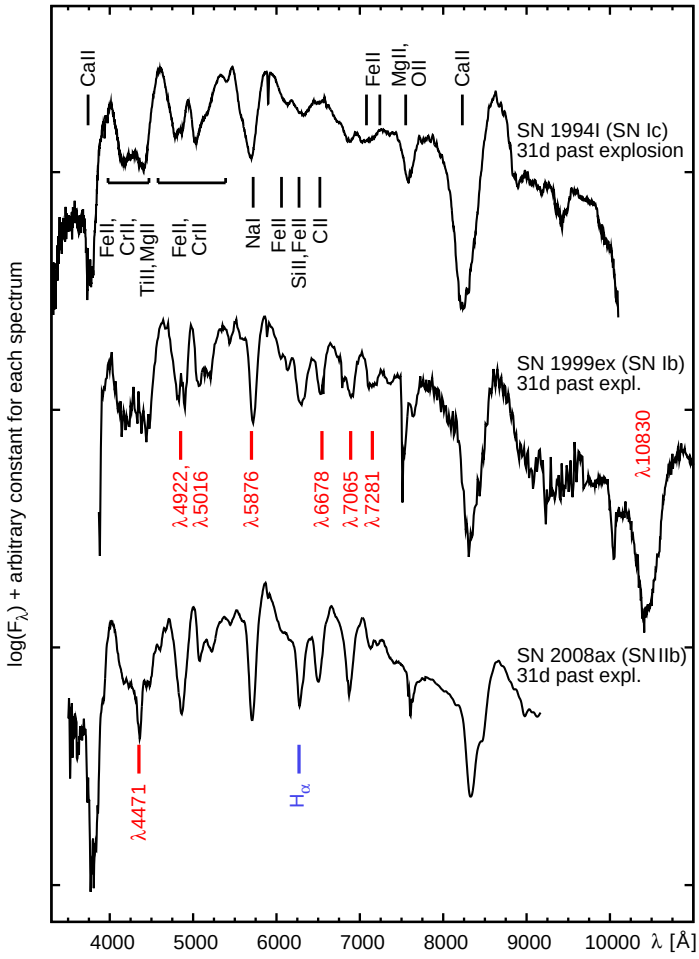

Figure 4.1: Spectra of stripped core-collapse SNe one month after explosion. Observations: SN 1994I: Filippenko et al. (1995); SN 1999ex: Hamuy et al. (2002); SN 2008ax: Taubenberger et al. (2011b). The spectra shown have been obtained by interpolation between observations with short time gap, such that the three SNe are shown for a common epoch relative to explosion (30.6 d). Line identifications are given for prominent lines – red: He I lines, blue: H lines.

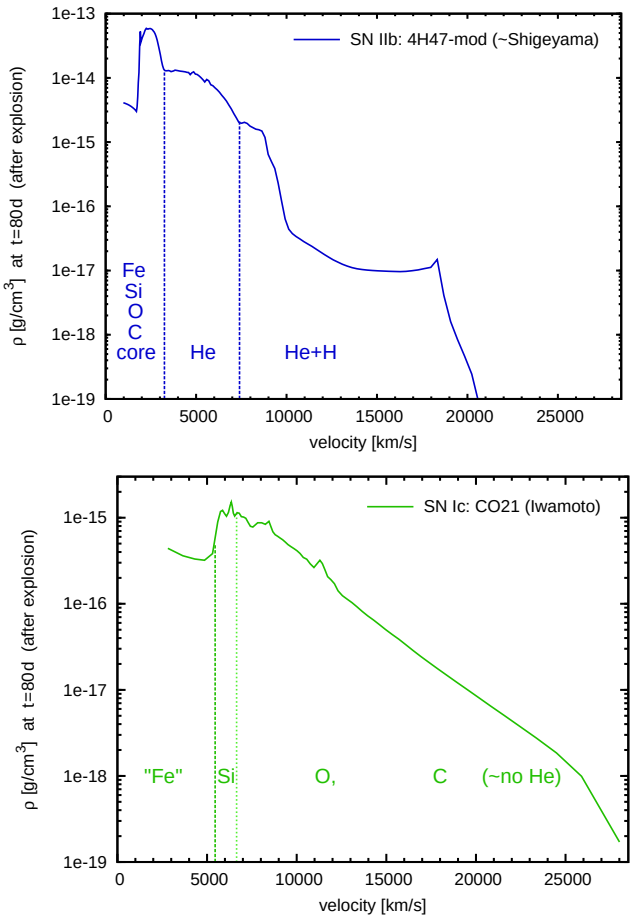

Figure 4.2: Density profiles used for the models of SN 2008ax [*upper panel*: 4H47, Shigeyama et al. (1994), with modifications as described in the text = 4H47-mod] and SN 1994I [*lower panel*: CO21, Iwamoto et al. (1994)]. Major abundance zones are indicated; we note in addition that most of the exploded C/O core consists of O in both models.

Each SN is modelled using an appropriate density profile with a kinetic energy of $\sim 10^{51}$ erg (1 *foe*). The explosions simulated to obtain the density profiles (Iwamoto et al. 1994; Shigeyama et al. 1994) use the same model for the stellar core; only the mass and composition of envelope material varies. The model used for SN 1994I [CO21, Fig. 4.2, lower panel, Iwamoto et al. (1994)] has proven to be applicable to this SN in an earlier one-zone spectrum-synthesis and light-curve study (Sauer et al. 2006). For SN 2008ax, we use the 4H47 model of Shigeyama et al. (1994), but apply some smoothing to the profile (Fig. 4.2, upper panel). The smoothing avoids narrow lines due to overdense (narrow, spherical) shells in the model. Such shells disappear naturally in (spherically-averaged) 2-D or 3-D hydrodynamic simulations[a)].

The abundance structure resulting from the original nucleosynthesis calculations (Shigeyama et al. 1994; Iwamoto et al. 1994) coupled to the hydrodynamic models is then modified to fit the observations. We choose to do this with two constraints:

- An abundance stratification typical for a core-collapse SN shall be preserved, in the sense that increasingly heavier elements dominate the ejecta going from the outside to the inside, and that only species typically dominating core-collapse ejecta (H, He, C, O, Si, Fe-group) are allowed to be dominant.
- ^{56}Ni and Fe-group abundances within the ejecta shall be such that the bolometric light curve produced with a simple light curve code (Cappellaro et al. 1997) from the ejecta model roughly matches the observed bolometric light curve.

We now discuss the models for the two SNe, after a brief digression on the observations, respectively. The code input parameters of the models are given in Table 4.3 in Sec. 4.2.1.2.

4.1.1 SN 2008ax – a SN IIb

4.1.1.1 Observed spectra used

SN 2008ax has been extensively observed by several groups (Pastorello et al. 2008; Roming et al. 2009; Chornock et al. 2010; Taubenberger et al. 2011b). The observations used for the modelling here are combined from all available sources in order to obtain a good wavelength coverage at four interesting epochs (16.0 d, 22.1 d, 30.6 d and 40.6 d after the explosion at JD 2454528.8). The spectra were chosen so as to cover the period at which the optical He I lines in SN 2008ax are strongest.

We have used the following individual observations:

- the optical spectra of Pastorello et al. (2008) and Roming et al. (2009) [and Taubenberger et al. (2011b) up to 4000Å], and the IR spectra of Chornock et al. (2010) and Taubenberger et al. (2011b), around $\sim$16.0 d;
- the combined optical-IR spectrum of Chornock et al. (2010) at $\sim$22.1 d (their Fig. 6);
- the optical spectrum of Taubenberger et al. (2011b) at 30.6 d;

[a)] In 2-D or 3-D core-collapse simulations, usually all structures are at least slightly asymmetric. Thus, after taking an average over all viewing angles, density spikes are smoothed out.

- the optical spectrum of Taubenberger et al. (2011b) at 40.6 d and their IR spectrum at 42.9 d.

The combination of optical/IR spectra taken at different epochs, between which the (logarithmic) light curve of the SN is approximately linear, is best made by performing a geometrical average, i.e.

$$\log(f_\lambda) = w_1 \times \log(f_{1,\lambda}) + w_2 \times \log(f_{2,\lambda}),$$

where the weights w_1 and w_2 add up to one and are chosen proportional to the deviations δt_2 and δt_1 of the individual epochs to the combined epoch. However, this can only be reliable if the observations are taken close to one another, as the evolution of spectral lines is sometimes unpredictable even on timescales of days.

The spectra around 16.0 d, which all cover different wavelength ranges, were first processed for the optical and IR separately. In the overlapping regions, different spectra were averaged as described. The non-overlapping parts were then attached. The optical and IR spectra thus obtained were photometrically calibrated (as in Hachinger 2007) and then combined. Note that the IR part of the 16.0 d spectrum shown is rather unreliable as the spectra used have a huge time gap of 11 d.

For the later spectra, the wavelength coverage was decent in observations by one group, respectively. We applied the usual photometric correction and combined spectra where necessary.

We assume a total reddening of $E(B-V)_{\rm tot} = 0.30$ (with a galactic contribution of 0.02) for the SN, and a distance modulus of $\mu = 29.92$ mag (all values from Pastorello et al. 2008). Models and observed spectra below are **de-reddened**.

4.1.1.2 Model calculations

The spectral models for SN 2008ax are shown in Figure 4.3 with line identifications. The lower panel of the Figure displays the heating rate of the matter by gamma rays (Compton scattering), as it is obtained running the light-curve code of Cappellaro et al. (1997) on the model (see also below).

$t = 16.0$ d spectrum

At this epoch, the SN shows a spectrum somewhat reminiscent of early SNe Ia. Apart from some Ca, Mg, Si and Fe lines in the B and V bands, however, the dominant features are made by He and H. The He I lines are relatively weak, as significant amounts of He are below the photosphere ($v_{\rm ph} = 8350$ km s^{-1}), and radiation temperatures are very high, which leads to high ionisation rates from excited states of He I (see Sec. 4.3.2). Yet, numerous He I lines can be identified (Fig. 4.3, red marks). The transitions at λ7065 and $\lambda\lambda$20581,21120,21132 are responsible for the most unambiguous features; the other features tend to be contaminated by lines of other elements.

We have inserted two additional abundance zones with lower borders at 10750 and 13000 km s^{-1}, respectively, above the photospheric abundance zone (cf. models in Chap 3). In the zone between 10750 and 13000 km s^{-1}, the abundances of C, O, IME and ^{56}Ni decrease strongly; this is needed in order to avoid high-velocity IME lines (especially Ca) and excessive line blocking (as caused by ^{56}Ni). In the outermost zone, these abundances are reduced even further and replaced by H, which contributes somewhat to the spectral lines even at these velocities.

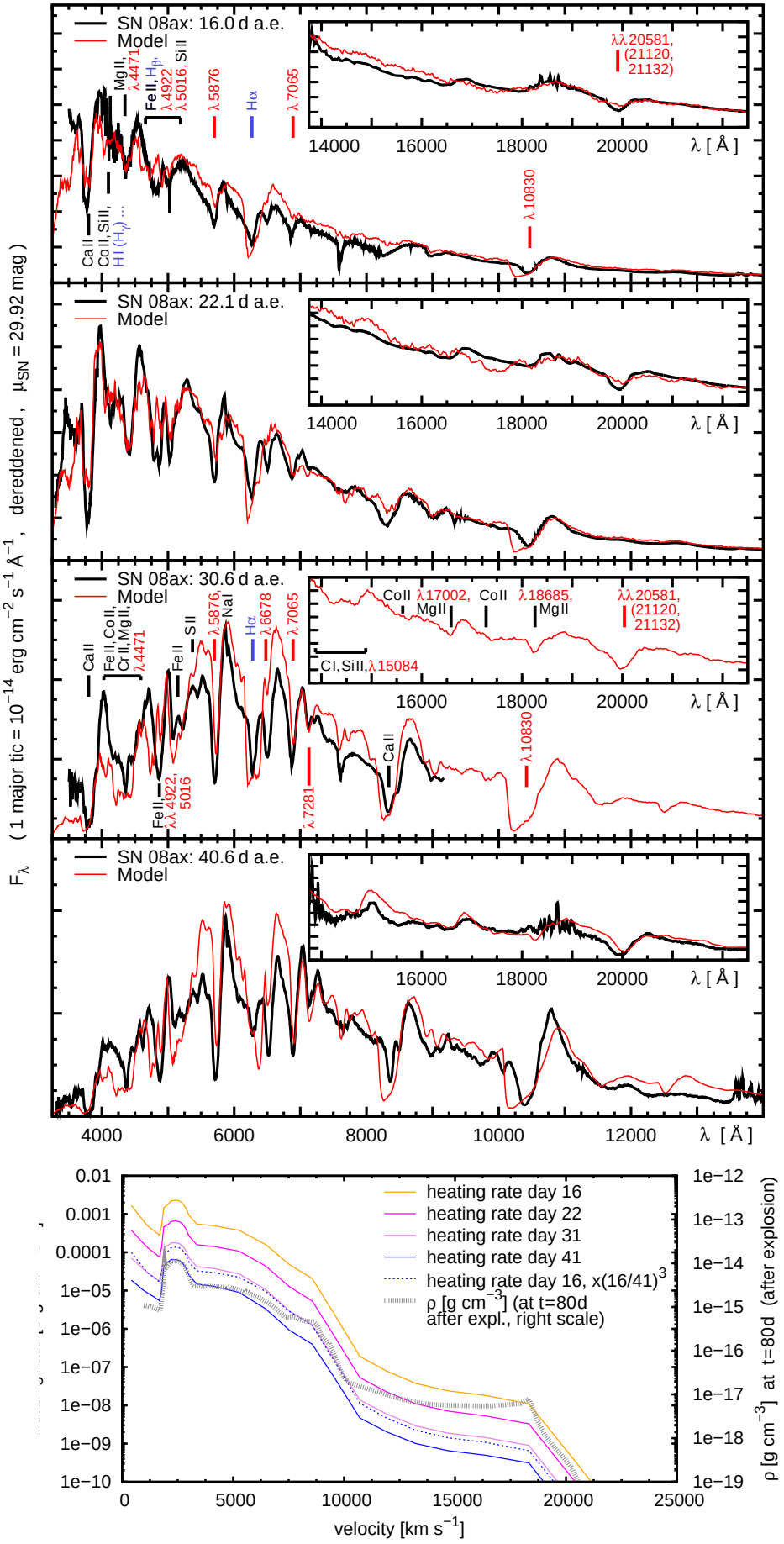

Figure 4.3: *Upper panels:* Spectral models for SN 2008ax (red lines) compared to observations (black lines). The insets show the IR. Line identifications are given for prominent lines at the first and third epoch – red: He I lines, blue: H lines. The Hα line is getting weaker with time, while He lines stay the same or gain additional strength. *Lower panel:* Density profile and heating rate (at different epochs) vs. velocity. The heating rate per unit volume, which depends on ^{56}Ni content and density, is important for exciting He so that He I features appear in the spectrum. The dotted blue line shows the earliest heating rate scaled down by the factor with which the density decreases by the latest epoch. The line is above the heating rate graph for the latest-epoch model; this means that in the latest-epoch model the heating per unit mass is weaker.

The model matches the observations well in the optical and the IR, except for the fact that H lines are generally a bit too strong and He lines a bit too weak. We accept such small mismatches here, as they depend on details of the model (gamma-ray flux due to ^{56}Ni, density distribution) and the code (charge-exchange reactions neglected for H). Around 3500 Å the flux of the model is somewhat too low, which may indicate that the ^{56}Ni abundance in the outer layers of the model is still too large; the ^{56}Ni was, however, needed to fit the light curve. Also this problem may be a consequence of the assumed density distribution and is, at the current stage, not crucial for our studies.

$t = 22.1$ d spectrum

At 22.1 d after explosion, the SN is 3 d past its B maximum. The spectrum is cooler than before and spectral features get deeper, as more material is uncovered ($v_{\rm ph} = 7300$ km s^{-1}). This is a general feature of Type II SNe: they show a more or less continuous flux distribution at early epochs, which is more and more eroded by lines with time [Sec. 1.1.2].

The high-velocity wing of the He I λ10830 feature, which is too strong in the model, is produced in the outermost regions of the ejecta. In these regions, the density in the 4H47 explosion model is probably too large to fit SN 2008ax. A reduction of the density would help to bring down the line strength (smaller He number densities). Here, also an additional effect may help: a smaller density favours ionisation, and He III may then become dominant at the expense of He II (which is dominant in our model) and He I. In the NLTE calculations shown here, He III is not included, but we have set up a test in order to show that this ion can be relevant in the outermost ejecta (Sec. 4.3.2). A smaller line strength at high velocities would only reduce the high-velocity wing of He I λ10830; the other He I lines would remain almost unchanged – these are intrinsically weaker than λ10830 and therefore do not have a significant high-velocity wing.

$t = 30.6$ d spectrum

By day 30.6, the photosphere has receded to $v_{\rm ph} = 5950$ km s^{-1}. The continuum flux in the blue/UV bands of the model is somewhat too low due to strong line blocking by Fe-group elements, which again have been inserted to fit the light curve.

In general the spectrum shows stronger lines than those at earlier epochs, and a multitude of strong He I features is visible. The redder colour and lower flux level of the spectrum leads to a lower ionisation of He. This makes the occupation numbers in He I higher, causing the lines to be stronger. The clearest He features are at $\lambda\lambda$6678, 7065, 7281 and around 20000 Å. The λ10830 feature may possibly have a contribution from C (Sauer et al. 2006); however in the nebular approximation the lower levels of the respective lines are not sufficiently populated. The λ5876 feature is extremely prominent in the optical, but has a significant contribution of Na I. The ionisation treatment for this element is commonly problematic (cf. Chapter 3). Yet, in the models shown we included some Na because the Na I D line is known to be significant in core-collapse SNe.

The IR spectrum now shows a lot of structure, not only with the marked He I feature at $\sim$ 20000 Å, but also with other features due to He, Co and Mg.

$t = 40.6$ d spectrum

40.6 days past explosion, the development described above continues and the He

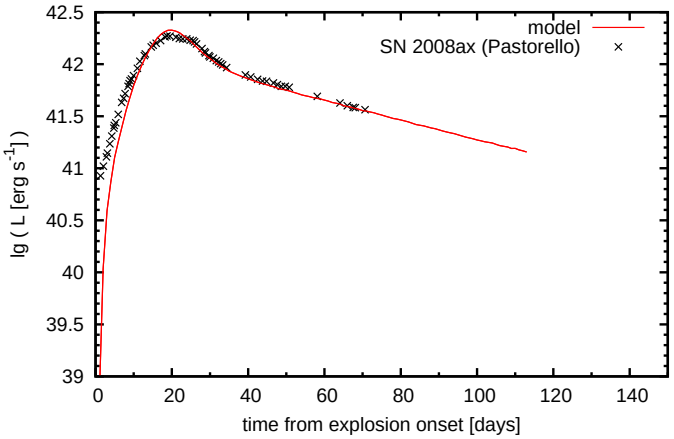

Figure 4.4: Bolometric light curve calculated from our ejecta model of SN 2008ax compared to observations (Pastorello et al. 2008). The ^{56}Ni mass is $0.08 M_{\odot}$.

lines reach their maximum strength. The photosphere has reached the bottom of the He-dominated zone ($v_{\rm ph} = 3150$ km s^{-1}). Despite the late epoch, the observed spectrum is quite well matched. Especially the match to the IR spectrum is excellent, although the models were crafted so as to primarily optimise the fit to the optical observations.

Light-curve model

The ejecta model presented here has not only been optimised to fit the spectra, but also to fit the observed light curve of SN 2008ax with the bolometric light-curve code of Cappellaro et al. (1997). Spectra and the light curve have been iterated in turn to achieve the best match. As the code of Cappellaro et al. (1997) is quite approximate, the optimisation of the light-curve fit has only been carried out as far as no extreme decrease in the quality of the synthetic spectra resulted.

The light-curve calculation[b)] only takes into account ^{56}Ni as a heating source, i.e. stored heat from shock passage is neglected. It proceeds in two steps:

- Calculation of the production and deposition of gamma rays (approximate Monte-Carlo transport). The gamma-photons deposit mostly in layers with high ^{56}Ni mass (where they are created) and with high density (where they are efficiently captured), cf. Fig. 4.3, lower panel.
- Calculation of a bolometric light curve: energy packets are created from the deposited gamma-ray energy and propagated outwards through a grey atmosphere (also with a Monte-Carlo transport routine).

In the first step, the code calculates the deposited luminosity of gamma rays (power) per unit volume (on a fine grid of radial shells). The energy is transferred to the electron gas by Compton-scattering[c)], which leads to the creation of fast electrons ($\gtrsim 10$ keV). The deposition power calculated by the light-curve code is saved and later used for

[b)] The code version used here has had some updates to the grey optical transport routine and to the opacity description [similar to Mazzali et al. (2001), but with an opacity which directly decreases when the ejecta temperature becomes lower, following the ideas of Khokhlov et al. (1993)].

[c)] Most of the energy is lost by the gamma rays in their first scatterings. Therefore the code of Cappellaro et al. (1997) only simulates one scattering per gamma quantum (where it is considered com-

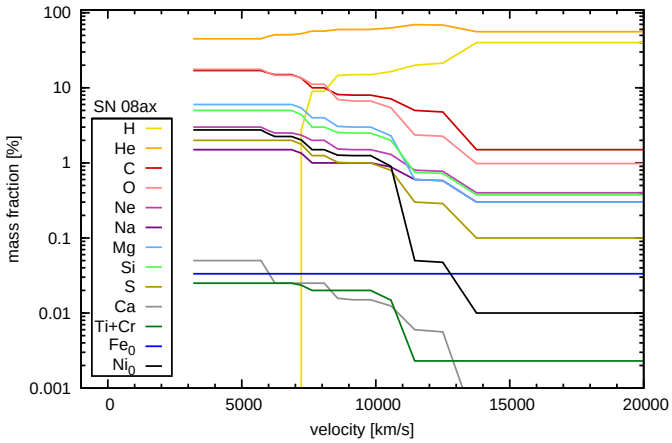

Figure 4.5: Abundance tomography plot for SN 2008ax, as derived from the fit to the spectra and the light curve.

calculating the He and H state with the NLTE module in the spectrum synthesis code. As the deposition directly influences the He and H state, the NLTE spectra can only be reliable if the density and the distribution of Fe-group elements is reasonably well known. This is ensured by our simultaneous modelling of spectra and light curves.

Our model light curve is shown with the observations of Pastorello et al. (2008) in Fig. 4.4. The match is very good; a failure to reproduce the earliest points of the light curve is expected, as these points will have a contribution from heat stored in the shocked ejecta.

Abundance stratification

The abundances in our ejecta model are plotted in Fig. 4.5. As the photosphere in our +40.6 d model is just at the border of the He envelope, only the He-dominated part of the SN is sampled. The total mass of He in the model is $\sim 1.2 M_\odot$. In the outer envelope ($v \gtrsim 7500$km s^{-1}), the H mass fraction is $\sim 10-40\%$. A larger mass fraction would lead to the formation of a deeper Hα line, which is already somewhat too strong in the models. The total H mass in our model is only $0.05 M_\odot$. Shigeyama's original 4H47 ejecta model probably contains a larger abundance of H, but another ejecta model successfully used for light-curve modelling of SN 2008ax (Tsvetkov et al. 2009), 13C (Woosley et al. 1994), has mass fractions more in line with our result.

The fact that H comes with a lot of He in the outer layers of our model has somewhat unclear implications. In the progenitor star, H may already have mixed with these amounts of He, or the mixing may have occurred in the explosion. However, one has to keep in mind a third possibility: the He in the outermost layers does not contribute strongly to the relatively low-velocity cores of the He lines. The fact that we have He in the model merely expresses that we can **not allow too much H**; thus the He fraction in the outer layers might be significantly reduced if one assumed a density profile with lower densities in the outer part. The fractions of Fe-group elements in this part of the ejecta are sub-solar ($\sim \frac{1}{3}$ of the solar values). These values have been chosen in order

pletely absorbed) with an effective opacity. This turns out to be an excellent approximation when compared to a code including the full scattering (I. Maurer, private communication).

to reduce the flux blocking in the outer layers with respect to the solar-metallicity case. In a solar-metallicity model, the blocking would cause more backwarming (a more intense, "hot" radiation field within the atmosphere), somewhat reducing the quality of the spectral fit (in particular, the He lines would be shallower because of stronger ionisation). Not only H and Fe-group elements have been reduced in the outer envelope: for Ca, a reduction to less than 10% of the solar value was required in order not to produce spurious high-velocity absorption. This may also indicate that a density reduction is needed.

The intermediate part of the ejecta ($v \sim 4000$ km s^{-1} – 12000 km s^{-1}) determines the formation of most of the lines in our spectral models. Most elements have an influence on the spectra in this velocity range, except for Si and Ne whose abundances are therefore estimates. From the model, it is evident that the composition is relatively strongly mixed, with some percent of IME and Fe-group elements almost everywhere. The right amount of outward-mixing of ^{56}Ni is especially crucial for the shape of the light curve, which shows a delayed rise if no outward-mixing is assumed, or if the abundances of Fe-group elements (which increase the opacity) are chosen too high.

4.1.2 SN 1994I – a SN Ic

4.1.2.1 Observed spectra used

SN 1994I is a very well-observed low-mass Type Ic SN (Yokoo et al. 1994; Sasaki et al. 1994; Filippenko et al. 1995; Clocchiatti et al. 1996; Richmond et al. 1996). Due to the good time coverage and quality of the observations it has already been subject to several radiative transfer studies (Iwamoto et al. 1994; Sauer et al. 2006 and references therein). We use here the observations by Filippenko et al. (1995) (spectroscopy) and Richmond et al. (1996) (photometry). These include a spectrum taken at 16 d after explosion (explosion date assumed: JD 2449438.6), i.e. matching the first epoch of SN 2008ax we investigated. We calculate four model spectra also for SN 1994I, with all epochs matching exactly those of SN 2008ax (with respect to the explosion date). For the three later spectra, this means we have to interpolate (as described in Sec. 4.1.1.1) between adjacent epochs to the desired epoch. As for SN 2008ax, the interpolated spectra are again calibrated against the photometry. IR spectra are not available for SN 1994I.

Following Sauer et al. (2006), we assume a total reddening of $E(B-V)_{\rm tot} = 0.30$ [the galactic reddening would be 0.035 (Schlegel et al. 1998)] for SN 1994I, and a distance modulus of $\mu = 29.60$ mag. However, all models and observed spectra plotted below are rescaled to the distance of SN 2008ax ($\mu = 29.92$ mag) and printed on the same scale in order to facilitate visual comparison. Again, all spectra have again been **de-reddened** prior to plotting.

4.1.2.2 Model calculations

The spectral models for SN 1994I with line identifications, and the heating rates by gamma-ray deposition, are shown in Fig. 4.6.

$t = 16.0$ d spectrum

The SN spectrum at $t = 16.0$ d – which is already ~ 5 d past maximum for this SN and corresponds to a photospheric velocity of 8850 km s^{-1} – shows a mix of O, IME

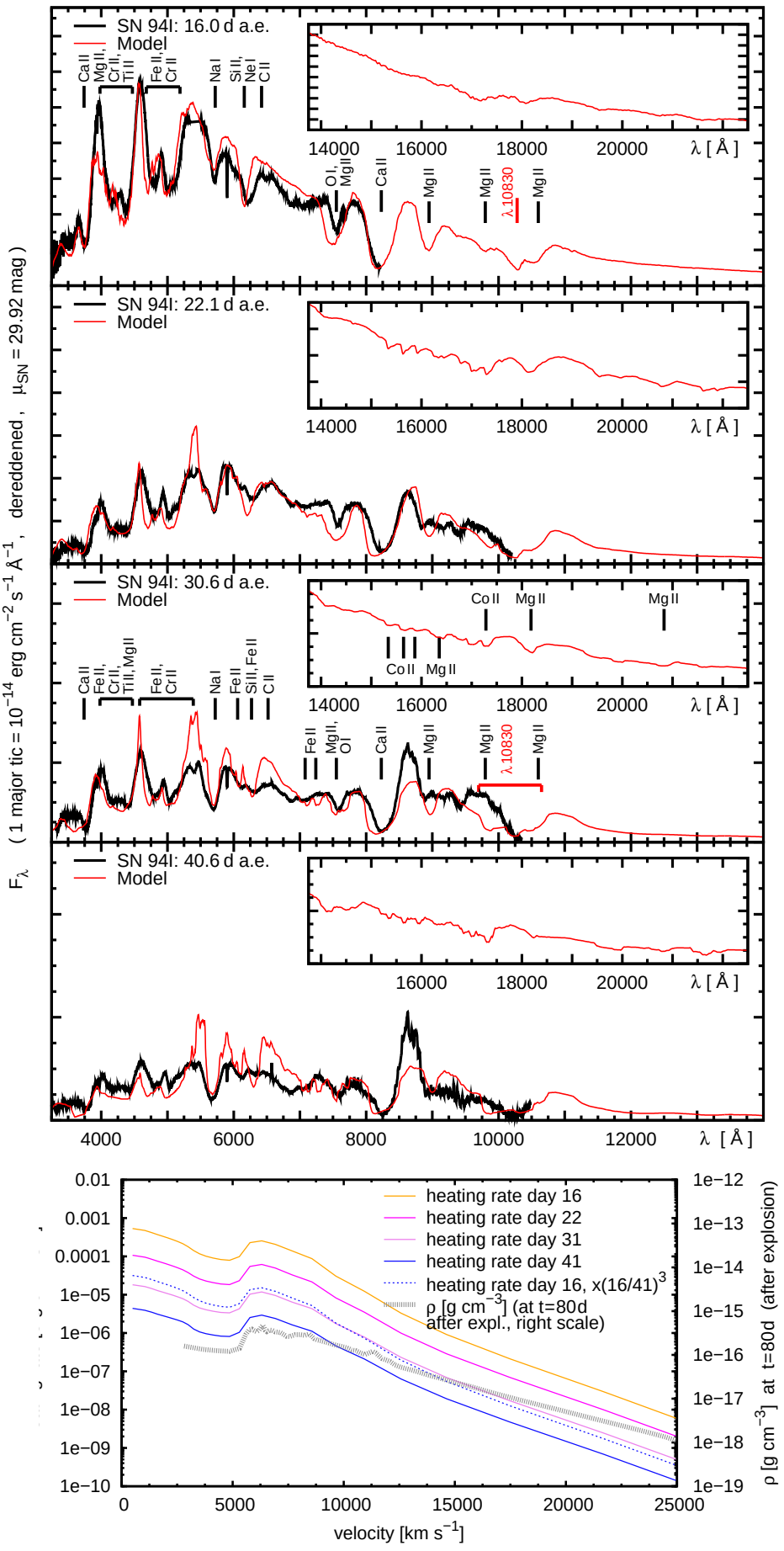

Figure 4.6: *Upper panels:* Spectral models for SN 1994I (red lines) compared to observations (black lines). The insets show the IR. Line identifications are given for prominent lines at the first and third epoch – red: He I λ10833 line. *Lower panel:* Density profile and heating rate (at different epochs) vs. velocity (analogous to the lower panel of Fig. 4.3).

and Fe-group lines. In the region around 4300 Å, the SN shows a deep trough (due to Mg II, Cr II and Ti II) similar to 91bg-like SNe Ia. Si II λ6355 is much weaker than in SNe Ia (in which the line is, in fact, usually saturated) because the Si abundance is significantly smaller. Some hint of a C II line is visible at the red edge of the Si II λ6355 line.

Line velocities in general tend to be a bit too high, which probably reflects the fact that the decline of the CO21 density is extremely shallow at high velocities.

The model includes a tiny amount of He in the intermediate and outer layers ($0.04 M_\odot$ in total); this makes the extremely strong He I λ10830 line appear, but no other He I lines. The observed spectra at later phases indicate the possible presence of the λ10830 line; unfortunately, the feature is never fully covered by the observations. Sauer et al. (2006) showed that the observations in this wavelength range may be reproduced by He I, but also by C I, **if** C I is in an NLTE excitation state [which was just assumed for testing purposes and not explicitly calculated in Sauer et al. (2006)].

Again, we have used two abundance shells above the $t = 16.0$ d photosphere (with lower borders at 15000 and $\sim$ 18900 km s^{-1}, respectively) to optimise the fit to the spectrum. In these zones we have assumed that the composition is dominated by C and contains some He, as was the case for the outer shells in the CO21 nucleosynthesis calculation of Iwamoto et al. (1994). The density of IME and Fe-group elements is reduced as in the model for SN 2008ax. This has merely been done to maintain a consistent approach (e.g. the Fe-group elements are also reduced down to $\sim \frac{1}{3}$ of the solar abundance); the exact amount of the reduction plays less of a role for the SN 1994I models. Only the Ca abundance has to be very much reduced (to practically zero) in the outer layers in order not to produce high-velocity features.

$t = 22.1$ d spectrum

The 22.1 d spectrum of SN 1994I is significantly cooler (redder), as the luminosity of the SN has declined rapidly. The photospheric velocity has decreased to the low value of $v_{\rm ph} = 3100$ km s^{-1}.

The IR spectrum begins to show a lot of structure due to lines of Co II and Mg II.

$t = 30.6$ d and $t = 40.6$ d spectra

At 30.6 d, the photosphere has receded to 1400 km s^{-1}. The limit of applicability of our code is certainly reached here, as a major fraction of ^{56}Ni is now above the photosphere, but nonetheless we have been able to calculate a decent model spectrum. We continued the calculations to $t = 40.6$ d ($v_{\rm ph} = 910$ km s^{-1}). Other models in the sequence from SN 2008ax to SN 1994I, which we construct below, do not have such a deep photosphere at these epochs and therefore will be more reliable.

The composition near the photosphere at these epochs is completely dominated by ^{56}Ni, which is required to make the light curve sufficiently bright. The sensitivity of the optical spectrum on the composition in the photospheric layers is limited. Instead, practically all elements abundant in the intermediate and also in the outer region of the ejecta contribute to line formation. This includes Na, which we have used in this model as we did for SN 2008ax.

The He in the outer layers of the model leaves a very broad λ10830 line now, with a

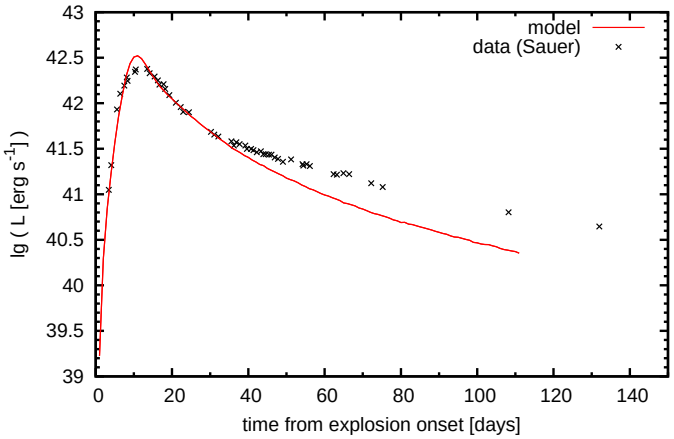

Figure 4.7: Bolometric light curve calculated from our ejecta model of SN 1994I compared to observations (as shown by Sauer et al. 2006 with his IR corrections based on SN 2002ap). The ^{56}Ni mass is $0.07 M_{\odot}$.

pronounced high-velocity component. This would possibly vanish if He III was included in our calculations (cf. Sections 4.1.1.2, 4.3.2).

Light-curve model; applicability of CO21 to SN 1994I

The light curve calculated from our SN 1994I model (Fig. 4.7) provides a decent match to the observations in the early phase. Afterwards, at 30 d past maximum and later, there is a mismatch between model and observations. We could not increase the ^{56}Ni mass in the model to improve the match because the light curve peak is already a bit too high.

The mismatch between peak and tail indicates that the CO21 model is not opaque enough to delay the escape of photons towards later epochs. This has already been noted by Sauer et al. (2006), who showed that an increased density in the innermost part significantly improves the match to the light-curve tail. Here, we refrained from making such modifications because we create models based on the same stellar core for Type IIb to Type Ic SNe.

As a final note here, we remark that the capability of SNe Ib / Ic to store photons in the ejecta and prevent them from escaping early varies strongly also among the observed objects (Clocchiatti & Wheeler 1997). The inability of CO21 to account for the observed light curve is therefore not a conceptual or qualitative problem, but rather a matter of the exact density values in the core of the SN.

Abundance stratification

The abundances with which we have been able to fit SN 1994I (Fig. 4.8) can be regarded as typical for SNe Ic. Helium appears as a trace element in the outer layers (total He mass: $0.04 M_{\odot}$); these layers are dominated by C so that C II lines can form. A hint of these lines, which are rather weak intrinsically (i.e. in terms of oscillator strength), is visible redwards of Si II λ6355 in the spectra. Below, O is the dominant element; mass fractions of IME and Fe-group elements increase further inwards.

The light curve requires a strong concentration of ^{56}Ni and other Fe-group elements

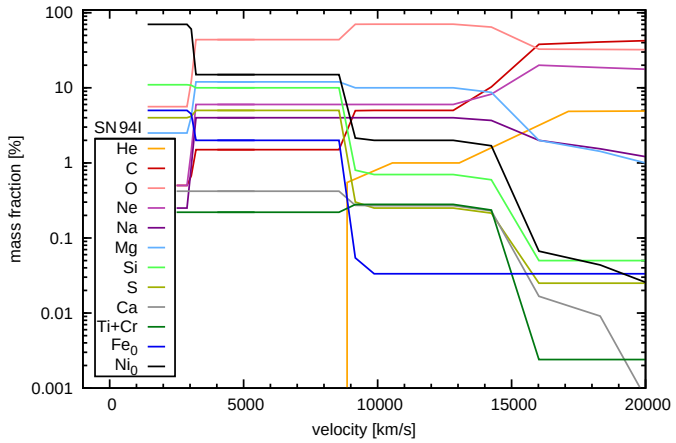

Figure 4.8: Abundance tomography plot for our SN 1994I model.

in the core, so that the escape of photons is delayed as long as possible. In our models, this is compatible with the spectra, while Sauer et al. (2006) had to reduce the Fe and ^{56}Ni mass fractions in their late-time models. This reflects the fact that Sauer et al. (2006) used one-zone models (i.e. homogeneous abundances throughout the envelope), and that a high mass fraction of Fe-group elements in the outer ejecta is incompatible with the spectra – even if the photosphere is very low and the outer layers are quite dilute at late epochs.

4.2 Model sequence

We now create a sequence of ejecta models representing SNe with different degrees of envelope stripping, but constant kinetic energy. In this context, it is helpful that the explosion models 4H47 and CO21, which we have used to model SN 2008ax and SN 1994I, represent the end points of such a sequence. Both explosion models are based on the same stellar core. Our task is now to create a finer sequence of ejecta models. From these ejecta models we then calculate spectra in order to estimate the observable consequences of the different He (and H) content.

Below, we first explain how we obtain the density and abundance structure of the transitional models, which represent steps within the model sequence. Then we show and discuss the spectra.

4.2.1 Setup

4.2.1.1 Density profiles

Ideally, one should simulate explosions with different degrees of envelope stripping to obtain density profiles of such supernovae. However, at present we have to leave this approach for future work, as the development of appropriate hydrodynamic models needs a larger collaborative effort. We therefore resort to modifying explosion models from the literature such that they fit our needs.

In the current context (models with constant kinetic energy), the step from a SN with

a massive envelope to a more stripped SN reflects also in the structure of the outer[d)] core layers: these layers, together with the remaining envelope, will carry more kinetic energy. We thus have to perform a simultaneous reduction of the envelope mass and an adequate redistribution of the remaining ejecta in velocity space. The first aim is to gradually transform the 4H47 (SN IIb) ejecta model into the "M4.0" (SN Ib) model produced from the same stellar core by Shigeyama et al. (1990). Second, we transform the M4.0 density profile analogously, such that we (approximately) obtain the model CO21 in the end. Each transformation is divided into 20 steps. We follow a fixed technical procedure to perform these transformations.

When we want to construct a model with a less massive envelope, we first generate a new model of the core of the ejecta. The new core has an energy increased by some percentage, which is achieved by scaling up the velocities of its mass shells. The relative energy increase of different shells can differ (e.g. the innermost core should remain mostly unchanged). To specify what we are doing, we define a continuous rescaling function $\eta(v) = E'(v)/E(v)$ such that the kinetic energy of a mass element δm at v increases from $E(v)$ to $E'(v)$ during the rescaling process. What function $\eta(v)$ shall be applied to our density grid? – We first infer $\eta(v)$ for a full rescaling from 4H47 to the M4.0 SN Ib model. We do this by dividing the core into five arbitrary zones and specifying mean η factors for each zone; a script programmed by us then calculates a continuous $\eta(v)$ fitting these factors. The five mean η factors and the zoning are optimised such that the rescaled result fits the M4.0 model in good approximation; data on the zones and mean η factors are given in Table 4.1. To achieve a smooth transformation from 4H47 to M4.0 in 20 steps, we apply the function $\eta(v)$ step by step: rescaling the 4H47 density with $\tilde{\eta}(v) = 1 + (\eta(v) - 1) \times \frac{n}{20}$ brings us n steps (out of 20) towards the M4.0 (SN Ib) model.

Simultaneously with each step, the envelope is replaced by an envelope with a smaller mass, which we construct following the recipes of Matzner & McKee (1999):

- We calculate a polytropic model for a pre-explosion envelope with the required mass according to Matzner & McKee (1999) (their Eq. 8). Here, we assume a polytropic index $n = 3$ for our H envelopes and of $n = 2.13$ for He envelopes; the indices have been obtained from fitting the envelopes of the progenitor stars of the 4H47 (SN IIb) and the M4.0 (SN Ib) model, respectively. The density coefficient ρ_1 appearing in Matzner & McKee (1999) is chosen so as to obtain the required envelope mass and to have a smooth transition to the outer core of the progenitor star.

- A model for the outermost (high-velocity) ejecta is then constructed inserting the coefficients of the polytropic envelope model into the lower set of formulae in Table 3 of Matzner & McKee (1999). The high-velocity model is typically valid from velocities somewhat below ~ 20000 km s^{-1} up to very high velocities.

- Below these velocities, we use a density of the form $\rho(r) = a \times \exp(-r/b) + c$ in order to connect the high-velocity ejecta to the (rescaled) outer layers of the core; here the parameters are chosen by an automatic routine such that the envelope

[d)] The innermost ejecta will be largely unaffected by the transition, as neither the inner core structure of stars, nor the kinematics of the inner layers during the explosion depend heavily on the envelope (e.g. Arnett 1974; Matzner & McKee 1999).

models (consisting of the high-velocity ejecta and the $\rho(r)$ function given above) give a reasonably smooth transition from 4H47 over M4.0 to CO21.

The mass of the "replacement envelope" is set so as to make the total kinetic energy of the ejecta model equal to 10^{51} erg. The entire procedure gives reasonable results despite the fact that the models of Matzner & McKee (1999) are a very crude approximation to the stars of Shigeyama et al. (1990, 1994) and Iwamoto et al. (1994).

Each resulting model is then smoothed with a boxcar function in order to avoid jags which often stem from small scale variations in the initial (4H47) density profile. The procedure is repeated a second time for the transformation from M4.0 to CO21 (here, however, four rescaling zones in the core have proven sufficient – Table 4.2).

A few examples of the density models we use are shown in Fig. 4.9. The evolution of different zones of the core when rescaled more and more is indicated in the figure.

4.2.1.2 Abundance, velocity and luminosity scaling – code input parameters for the models

The ejecta models for SNe 2008ax and 1994I are set up such that the abundance zones in them correspond to each other. Before discussing the scaling of the model parameters within the sequence, we explain how this set-up is performed.

Modification of the SNe 2008ax and 1994I models for the sequence set-up

For each mass shell in the C/O core of our SN 2008ax model we know where the corresponding zone must be located in our SN 1994I ejecta, and vice versa. Based on this correspondence, we have refined the abundance **zoning** in our SN 2008ax model such that

- the abundances within the original model (as far as probed by the spectral models) are not modified, and
- all zone borders within our SN 1994I model have a counterpart in the core of the SN 2008ax model (based on the zone correspondence as indicated by the rescaling script). This means that at every mass coordinate where a zone border exists in the SN 1994I model, a border must exist in the SN 2008ax model. In few cases, there was a natural match, i.e. zone borders in both models were located practically at the same mass coordinate. Otherwise, a new zone border was introduced in SN 2008ax with abundances such that the abundance structure in the model remained the same. We also had to introduce zones below the $t = 40.6$ d photosphere of SN 2008ax. The abundances of these zones have generally been chosen as in the corresponding zones in SN 1994I. Some differences appear, as we had to adapt the Fe-group abundances because the light curve of SN 2008ax required a shallower ^{56}Ni distribution than what we find in SN 1994I. The mass fraction of Fe-group elements removed or added is balanced by adjusting the O abundance.

We proceed analogously for the SN 1994I model; here we add He-rich shells with the abundances from the SN 2008ax model on the outside. The shells are at velocities[e)] so

[e)] The lower boundary velocities of the additional shells are obtained by multiplying the velocities of the SN 2008ax shells with the velocity increase of the outermost (core) mass element. This can also result in a formal velocity $v > c$.

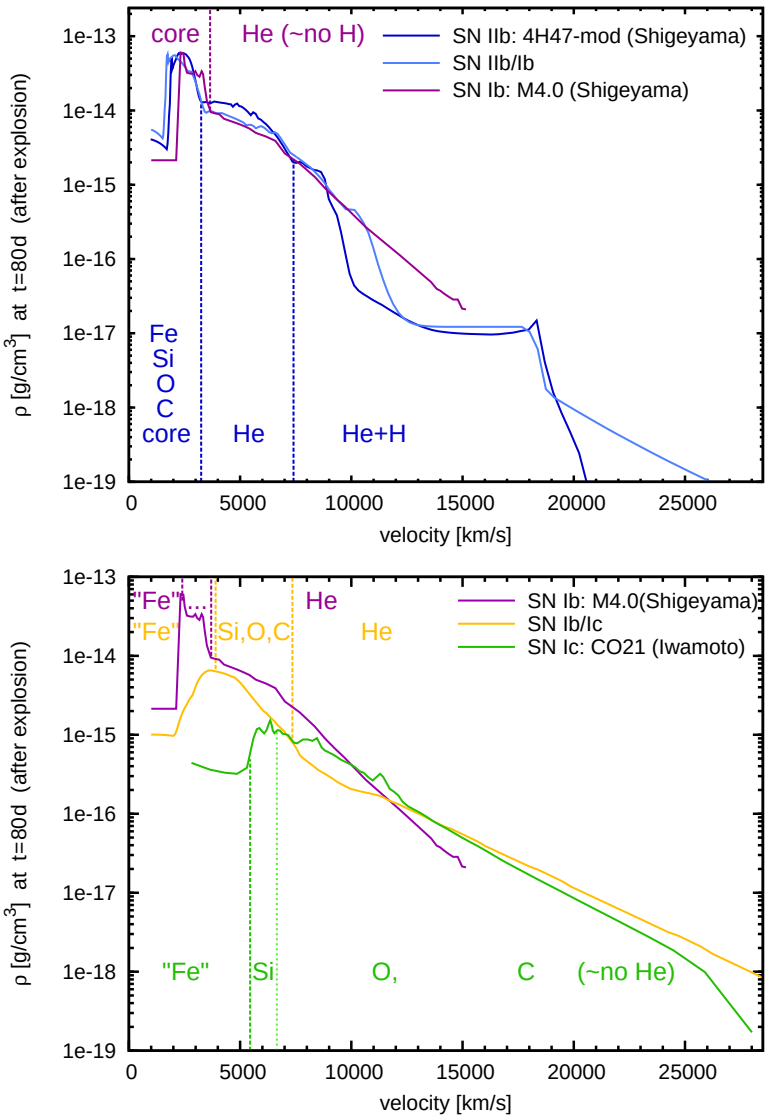

Figure 4.9: Density profiles resulting from our rescaling procedure (*upper panel:* SNe IIb and Ib, *lower panel:* SNe Ib and Ic). The hydrodynamic models used for SN 2008ax [4H47, Shigeyama et al. (1994), with modifications as described in the text = 4H47-mod] and SN 1994I [CO21, Iwamoto et al. (1994)] are included for reference. Major abundance zones are indicated. Most of the exploded C/O core of the star will consist of O in all models according to the explosion models of Shigeyama et al. (1994) and Iwamoto et al. (1994) (and also according to our spectral models).

Table 4.1: Density rescaling from the SN IIb/4H47 model to the SN Ib/M4.0 model: rescaling zones (specification and properties) and scale factors. The zone names refer to the elements dominant after explosion.

zone	Fe/Si/O/C core (with O/C/He mixed zone)	He envelope I	He env. II	He env. III	He env. IV	He/H envelope
M_{zone} (specifies zone)	$0.8 M_\odot$	$1.3 M_\odot$	$0.4 M_\odot$	$0.15 M_\odot$	$0.08 M_\odot$	$0.5 M_\odot$, decreasing
M_{enclosed}	$0.8 M_\odot$	$2.1 M_\odot$	$2.5 M_\odot$	$2.6 M_\odot$	$2.7 M_\odot$	$3.2 M_\odot$, decreasing
$E_{\text{kin,zone}}$	0.05 foe	0.30 foe	0.15 foe	0.07 foe	0.04 foe	0.40 foe, decreasing
v_{outer}	3.3×10^8 cm/s	5.9×10^8 cm/s	6.7×10^8 cm/s	7.2×10^8 cm/s	7.5×10^8 cm/s	-
mean scale factor $\eta = \frac{E_{\text{k,zone,final}}}{E_{\text{k,zone,initial}}}$	1.5	1.8	2.1	2.5	3.4	see text

Table 4.2: Density rescaling from the SN Ib/M4.0 model to the SN Ic 1994I/CO21 model: rescaling zones (specification and properties) and scale factors. The zone names refer to the elements dominant after explosion.

zone	Fe core	O core I (with Si zone at inner border)	O core II	O/C/He region	He envelope
M_{zone} (specifies zone)	$0.10 M_\odot$	$0.46 M_\odot$	$0.21 M_\odot$	$0.10 M_\odot$[a]	$1.8 M_\odot$[a], decreasing
M_{enclosed}	$0.10 M_\odot$	$0.56 M_\odot$	$0.77 M_\odot$	$0.87 M_\odot$[a]	$2.7 M_\odot$[a], decreasing
$E_{\text{kin,zone}}$	0.005 foe	0.035 foe	0.022 foe	0.014 foe	0.92 foe, decreasing
v_{outer}	2.3×10^8 cm/s	3.2×10^8 cm/s	3.5×10^8 cm/s	3.9×10^8 cm/s	-
mean scale factor $\eta = \frac{E_{\text{k,zone,final}}}{E_{\text{k,zone,initial}}}$	6.3	9.3	14.5	23.3	-

[a] Here, $0.1 M_\odot$ of the He envelope, as defined in Table 4.1, are counted as mixed O/C/He region. This is done to have the interpolated/rescaled models finally approach the mass of CO21. CO21 has a mass of $0.87 M_\odot$, somewhat larger than the pure C/O core of their stellar models, as they added a small "C+O envelope".

far outside that they do not have any effect on the spectra of SN 1994I; they just have the purpose of maintaining a 1:1 shell correspondence between the two models. The abundances of IME and Fe-group elements in the additional shells are limited to those in the outermost shells of our original SN 1994I model. The mass fraction in IME and Fe-group elements removed because of this constraint is again balanced, here by slightly adjusting the mass fraction of the most abundant element (usually He).

The complete set-up of the envelope structure is reflected in Table 4.3, where all the parameters of the zones are given, and corresponding zones of the SN 2008ax and SN 1994I models can be found in the same column.

We emphasize again that the abundance structure in each of the SN models, as far as it contributes to the formation of the respective spectra, is **not** modified by the set-up process. The photosphere at each epoch in each SN remains at the same velocity, regardless of the new abundance shells introduced.

Abundance shells, photospheres and other code input for the model sequence

Knowing the "history" of the mass elements within the density rescaling process, and having set up the abundances for SN 2008ax and SN 1994I as mentioned above (with the 1:1 shell correspondence), we are now ready to specify the input parameters for the complete model sequence. We have to consider the photospheric velocities and the abundance shells within the sequence of models as two independent things here. We explain now how this is implemented by first setting up an abundance structure, and then setting up photospheres.

We begin with defining the abundances within the envelope of a sequence model, using the data for SN 2008ax and SN 1994I given in Table 4.3. This is simply done by interpolating (for each of the shells given in the Table) in 40 equal steps between the abundance values for SN 2008ax and those for SN 1994I – one step for each step in the density rescaling process (where we had 20+20 steps, Sec. 4.2.1.1). The borders of the abundance shells are **not interpolated**, but instead set up to follow mass elements in the rescaling process. Thus, starting from SN 2008ax and going one step after another in the model sequence, the entire abundance-shell structure steadily approaches that of SN 1994I.

The photospheric velocities within the models cannot follow the mass elements when the rescaling is performed – otherwise it would not be possible that photospheres are mostly within the He envelope in SN 2008ax, while they are mostly in the O-rich zone in SN 1994I. We thus determine the luminosity L and the photospheric velocity $v_{\rm ph}$ for each model in the sequence as follows:

- L is interpolated linearly between the values for SN 2008ax and SN 1994I just as the abundances.
- The effective temperature of the photosphere, calculated from the Stefan-Boltzmann-law
$$T_{\rm ph} = \left(\frac{L}{\sigma \times 4\pi v_{\rm ph}^2 t^2} \right)^{\frac{1}{4}}$$
is interpolated linearly between the values for SN 2008ax and SN 1994I, and the new photospheric velocity is calculated from the temperature and the interpolated

Table 4.3: Abundance shells and code input parameters for the models for SN 1994I and SN 2008ax. The models are set up such that the abundance shells in SN 1994I and SN 2008ax correspond to one another (i.e. each column in the upper part of the table to the same column in the lower part). v_{lbord} is the *lower* border for each shell. Shells with epochs given correspond to observed spectra (i.e. their v_{lbord} is the photospheric velocity at that time). Shells with epoch "-" are inserted (with abundances chosen as described in the text) in order to enable a 1:1 mapping of SN 2008ax to SN 1994I (see Sec. 4.2.1.2). Shells with epochs "o" or "oo" are outer shells set up to match the $t = 16.0$ d spectrum.

SN 2008ax

epoch [d rel. to B max.]	-	-	-	-	$+21.7$	-	$+11.7$	$+3.2$	-2.9	o	oo
t [d rel. to explosion]	-	-	-	-	40.60	-	30.60	22.05	16.00	-	-
$\lg\left(\frac{L_{\mathrm{bol}}}{L_{\odot}}\right)$	-	-	-	-	8.390	-	8.530	8.745	8.695	-	-
v_{lbord} [km s^{-1}]	540	830	1820	2774	3150	3327	5950	7300	8350	10750	13000
X(H) [%]	0.0000	0.0000	0.0000	0.0000	0.0000	0.0000	0.0000	9.0000	15.0000	20.0000	40.0000
X(He) [%]	0.0000	0.0000	0.0000	1.0000	45.0000	45.0000	51.0000	57.0000	60.0000	69.5000	56.0000
X(C) [%]	0.1500	0.5000	1.5000	5.0000	17.0000	17.0000	15.0000	10.0000	8.0000	5.0000	1.5000
X(O) [%]	43.6097	43.6097	52.3597	63.1991	17.6417	17.6417	14.6667	11.1717	6.6817	2.3584	0.9791
X(Ne) [%]	0.0000	0.5000	6.0000	6.0000	3.0000	3.0000	2.5000	2.0000	1.5000	0.8000	0.4000
X(Na) [%]	0.1000	0.2500	4.0000	4.0000	1.5000	1.5000	1.5000	1.0000	1.0000	0.6000	0.3000
X(Mg) [%]	1.5000	2.5000	12.0000	10.0000	6.0000	6.0000	6.0000	4.0000	3.0000	0.6000	0.3000
X(Si) [%]	8.0000	11.0000	10.0000	5.0000	5.0000	5.0000	5.0000	3.0000	2.5000	0.7500	0.3750
X(S) [%]	2.5000	4.0000	5.0000	2.0000	2.0000	2.0000	2.0000	1.2500	1.0000	0.3000	0.1000
X(Ca) [%]	0.4200	0.4200	0.4200	0.2700	0.0500	0.0500	0.0250	0.0250	0.0150	0.0060	0.0003
X(Ti) [%]	0.0200	0.0200	0.0200	0.0800	0.0050	0.0050	0.0050	0.0050	0.0050	0.0003	0.0003
X(Cr) [%]	0.2000	0.2000	0.2000	0.2000	0.0200	0.0200	0.0200	0.0150	0.0150	0.0020	0.0020
$X(\mathrm{Fe}_0)$ [%]	3.5000	2.0000	1.0000	0.5000	0.0333	0.0333	0.0333	0.0333	0.0333	0.0333	0.0333
$X(^{56}\mathrm{Ni}_0)$ [%]	40.0000	35.0000	7.5000	2.7500	2.7500	2.7500	2.2500	1.5000	1.2500	0.0500	0.0100

SN 1994I

epoch [d rel. to B max.]	$+28.6$	$+18.6$	$+10.1$	$+4.0$	o	oo	-	-	-	-	-
t [d rel. to explosion]	40.60	30.60	22.05	16.00	-	-	-	-	-	-	-
$\lg\left(\frac{L_{\mathrm{bol}}}{L_{\odot}}\right)$	7.912	8.122	8.430	8.770	-	-	-	-	-	-	-
v_{lbord} [km s^{-1}]	910	1400	3100	8850	14800	18500	68290	113213	150803	236723	317274[a]
X(H) [%]	0.0000	0.0000	0.0000	0.0000	0.0000	0.0000	0.0000	9.0000	15.0000	20.0000	40.0000
X(He) [%]	0.0000	0.0000	0.0000	1.0000	5.0000	5.0000	65.2108	65.8558	67.0938	70.5672	56.4003
X(C) [%]	0.1500	0.5000	1.5000	5.0000	38.0000	44.0000	15.0000	10.0000	8.0000	5.0000	1.5000
X(O) [%]	0.1097	5.6097	43.8597	70.4658	32.8059	32.1225	14.9117	11.2667	6.5287	2.3054	0.9790
X(Ne) [%]	0.0000	0.5000	6.0000	6.0000	20.0000	17.0000	2.5000	2.0000	1.5000	0.8000	0.4000
X(Na) [%]	0.1000	0.2500	4.0000	4.0000	2.0000	1.0000	1.5000	1.0000	1.0000	0.6000	0.3000
X(Mg) [%]	1.5000	2.5000	12.0000	10.0000	2.0000	0.7500	0.7500	0.7500	0.7500	0.6000	0.3000
X(Si) [%]	8.0000	11.0000	10.0000	0.7000	0.0500	0.0500	0.0500	0.0500	0.0500	0.0500	0.0500
X(S) [%]	2.5000	4.0000	5.0000	0.2500	0.0250	0.0250	0.0250	0.0250	0.0250	0.0250	0.0250
X(Ca) [%]	0.4200	0.4200	0.4200	0.2700	0.0167	0.0001	0.0001	0.0001	0.0001	0.0001	0.0001
X(Ti) [%]	0.0200	0.0200	0.0200	0.0800	0.0004	0.0004	0.0004	0.0004	0.0004	0.0003	0.0003
X(Cr) [%]	0.2000	0.2000	0.2000	0.2000	0.0020	0.0020	0.0020	0.0020	0.0020	0.0020	0.0020
$X(\mathrm{Fe}_0)$ [%]	7.0000	5.0000	2.0000	0.0333	0.0333	0.0333	0.0333	0.0333	0.0333	0.0333	0.0333
$X(^{56}\mathrm{Ni}_0)$ [%]	80.0000	70.0000	15.0000	2.0000	0.0667	0.0167	0.0167	0.0167	0.0167	0.0167	0.0100

[a] see text

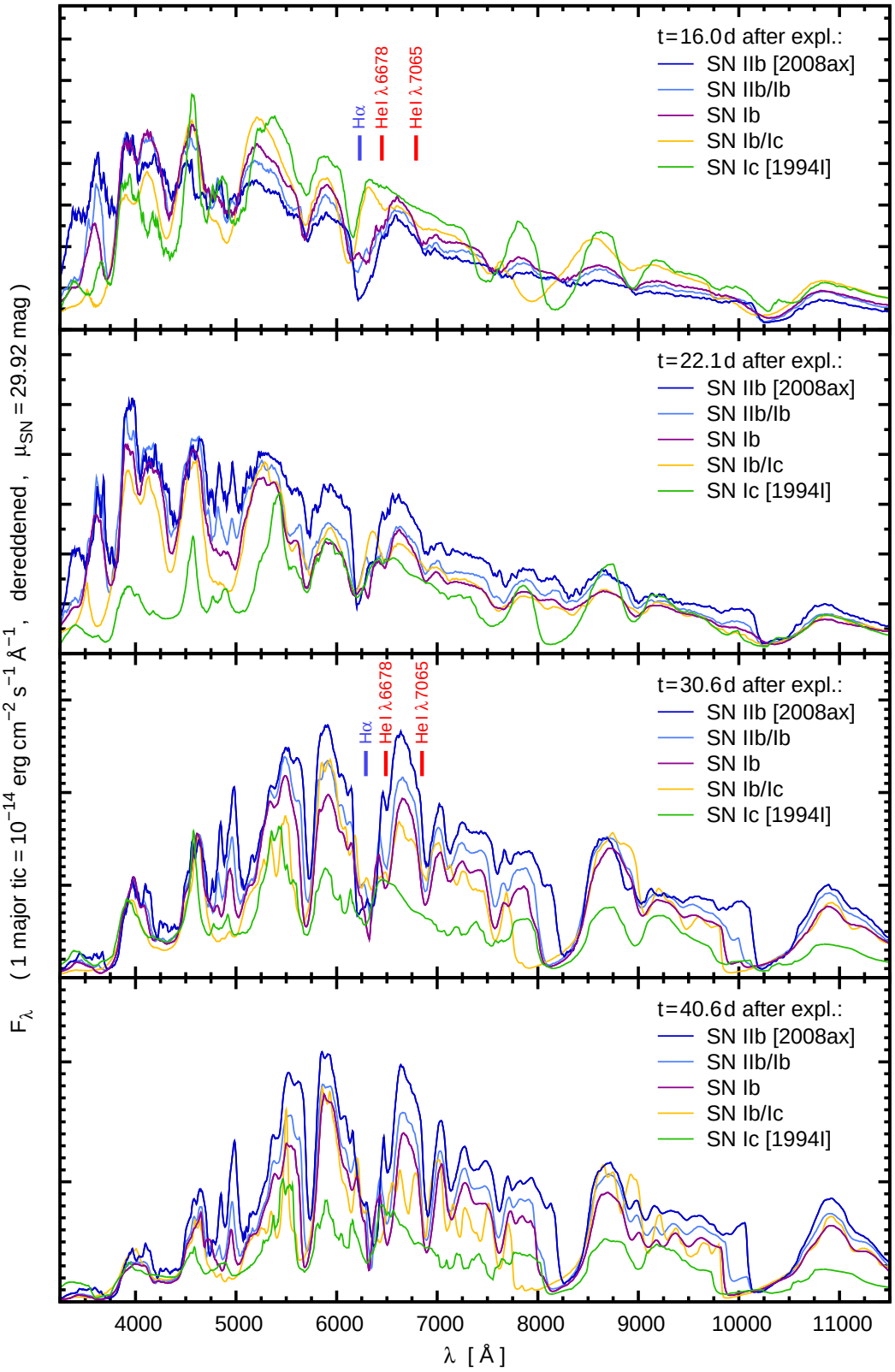

Figure 4.10: Sequence of spectral models for stripped-envelope core-collapse SNe with constant energy $E_{\rm kin} = 10^{51}$erg. The model designations refer to the SN type the respective model represents (two types in case of transitional models). Line identifications are given for the He and H lines used to determine the SN type here.

luminosity. This procedure seems awkward, but has the advantage that photospheric temperatures will not show unexpected variations within the sequence – which would happen if L and $v_{\rm ph}^2$ (see Stefan-Boltzmann law) showed a large difference in the way they vary.

The photospheres thus defined do not correspond to the abundance shells defined before. Thus, we just insert them as lower boundaries for the spectrum calculations in our sequence models, without modifying the abundance structure. The input format of our spectral synthesis code is capable of handling this without problems.

4.2.2 Results

Figure 4.10 gives an overview of the most interesting sequence models in one plot. All models have been calculated with our spectral synthesis code using the NLTE module. Before each run of the spectrum code we have run the light-curve code of Cappellaro et al. (1997) on the respective ejecta in order to obtain gamma-ray heating rates for each cell, as needed by the NLTE module.

In the Figure, we have marked the Hα line and two He lines which allow us to judge the SN type. These two lines are not strongly blended with features due to other elements in most cases. In the infrared, the λ10830 feature may partly be due to C I (Sauer et al. 2006), but the feature at $\sim$20000Å is possibly the He line with the least "contamination" by other species. The IR lines are not shown in Figure 4.10, but below (Sec. 4.2.2.2).

The Hα line gets much weaker in the sequence from the SN IIb to the SN Ib model as soon as the H mass is reduced to $0.015 M_\odot$ (SN IIb/Ib model). As the He is removed from the models, the He lines vanish. The lowest He mass for which we see He lines in the optical is $0.1 M_\odot$. The respective model is labelled "SN Ib/Ic" in the figure. Typical SNe Ic (with low mass/low energy, as simulated here), which show no signs of He lines in the optical, will contain He masses in this order or less.

We now take a closer look at two models: first, we compare the SN Ib model to observations of a SN Ib in order to make sure that our sequence matches reality. Second, we discuss the SN Ib/Ic model.

4.2.2.1 The "SN Ib" model

In Figure 4.11, the "SN Ib" model is compared to the SN Ib 1999ex (Hamuy et al. 2002; Stritzinger et al. 2002). The observed spectra have been corrected and/or interpolated in time as for the other SNe. Moreover, they have been multiplied by a factor of 0.67 to reduce the flux, as SN 1999ex was brighter than our model (i.e. it had a larger ^{56}Ni mass).

Many of the observed line features are in fact well reproduced in the model spectra. The main mismatch between model and observations is mostly a matter of the luminosity – the SN model peaks earlier (hence the larger luminosity at the first epoch) and then declines faster. Also, the high-velocity wings of the Ca II IR triplet and of He I λ10830 are stronger in the model, in particular at the later epochs.

The line at $\sim$6000 Å is mainly reproduced by Si II λ6355, without only a moderate contribution of Hα. It is somewhat unclear whether SN 1999ex contains significant amounts of H in the outer layers such as SN 2008ax; Valenti et al. (2011, in prep.) speculate that earlier spectroscopic observations might have led to a classification as

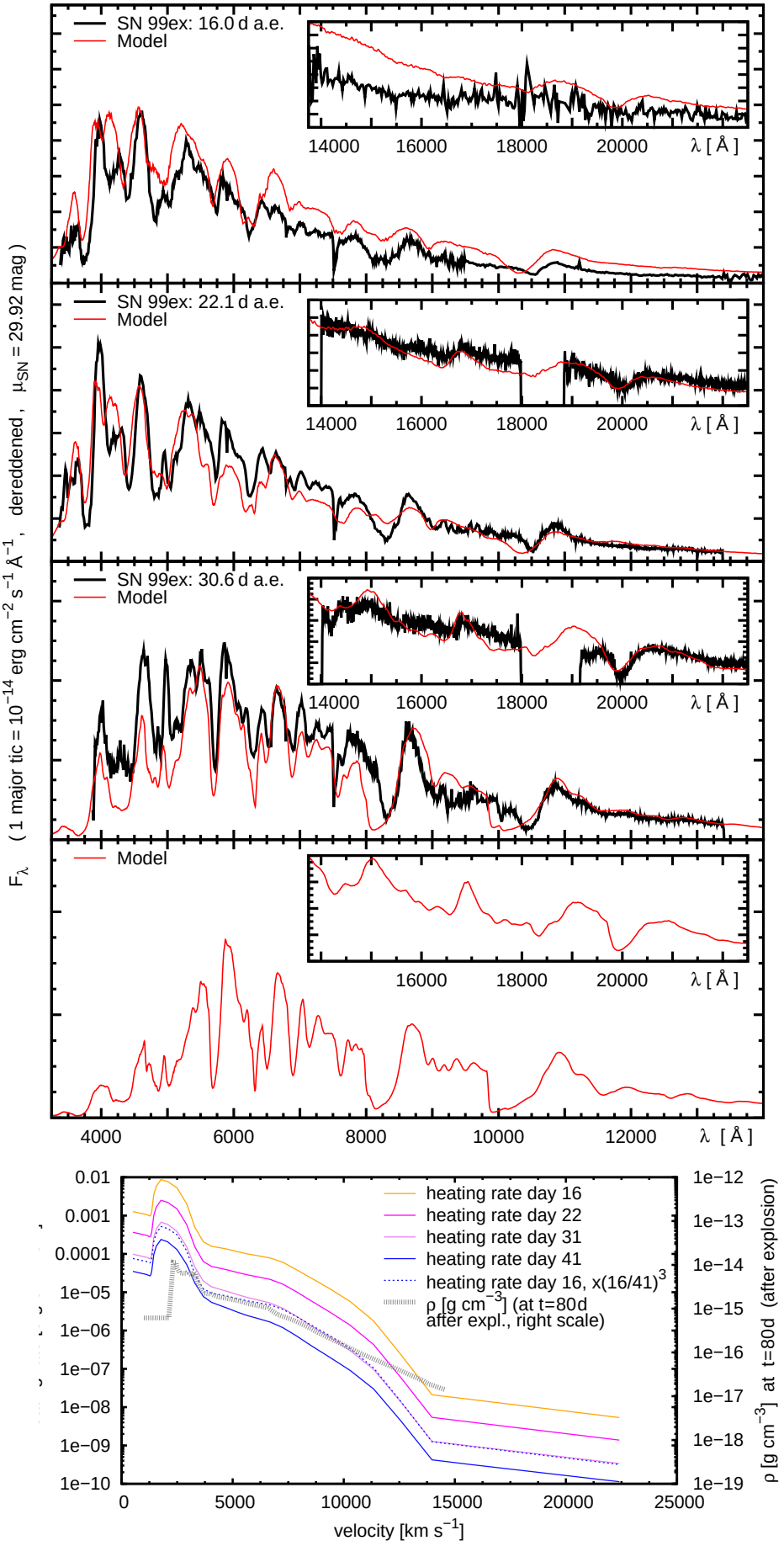

Figure 4.11: SN Ib model. The He mass in the model is $0.6 M_{\odot}$. *Upper panels:* Model spectra compared to the well-observed SN 1999ex (Hamuy et al. 2002; Stritzinger et al. 2002); for the latest epoch, there are no observations. The observed spectra have been multiplied by a factor of 0.67. There are some gaps in the IR spectra where the Earth's atmosphere has been too opaque. *Lower panel:* Density profile and heating rate (at different epochs) vs. velocity. The dotted blue line shows the earliest heating rate scaled down by the factor with which the density decreases by the latest epoch.

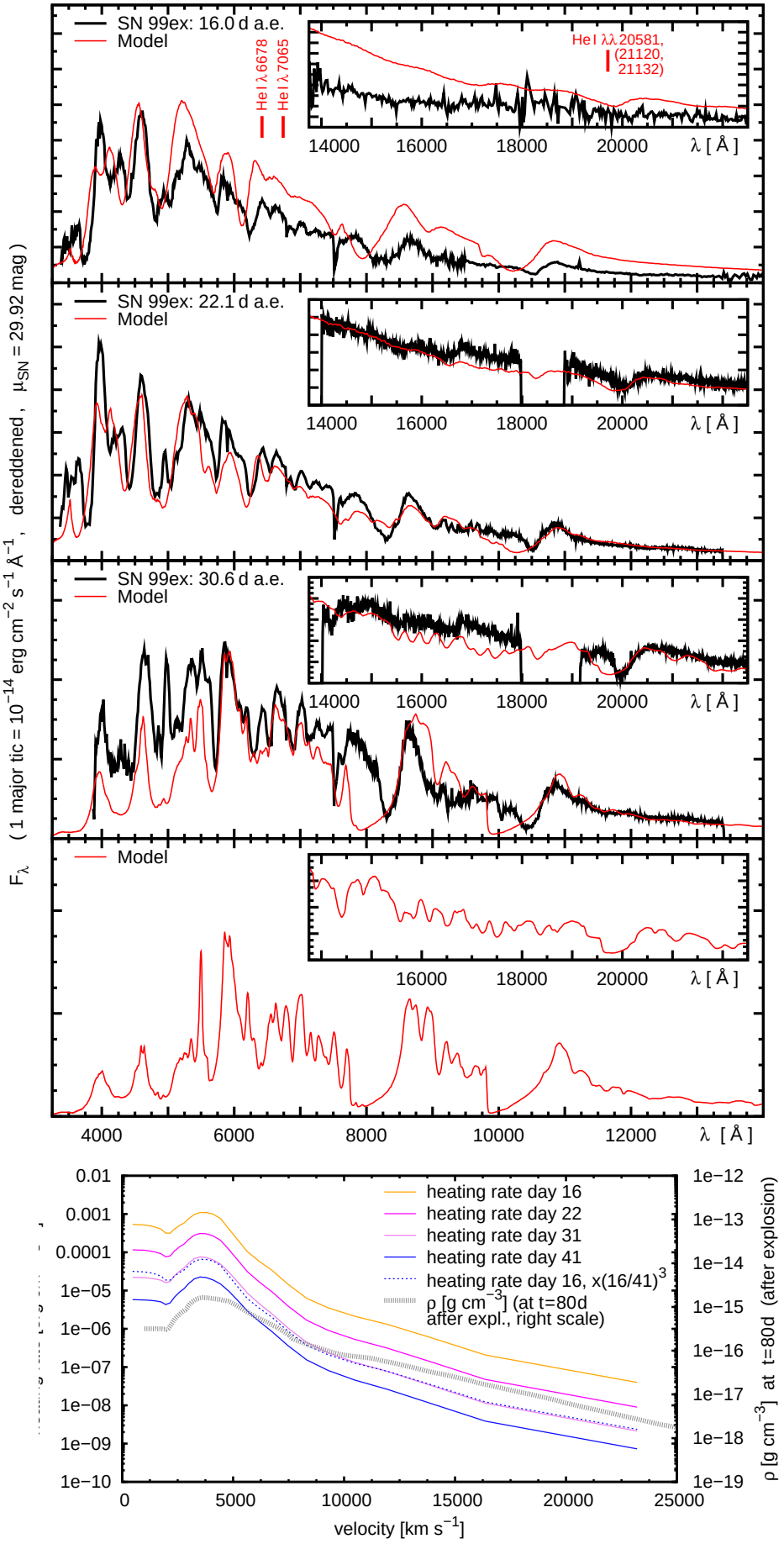

Figure 4.12: SN Ib/Ic model. The He mass in the model is $0.1 M_{\odot}$. *Upper panels:* Model spectra. SN 1999ex is again shown for comparison; the He lines we discuss in the text are marked (red marks). *Lower panel:* Density profile and heating rate (at different epochs) vs. velocity. The dotted blue line shows the earliest heating rate scaled down by the factor with which the density decreases by the latest epoch.

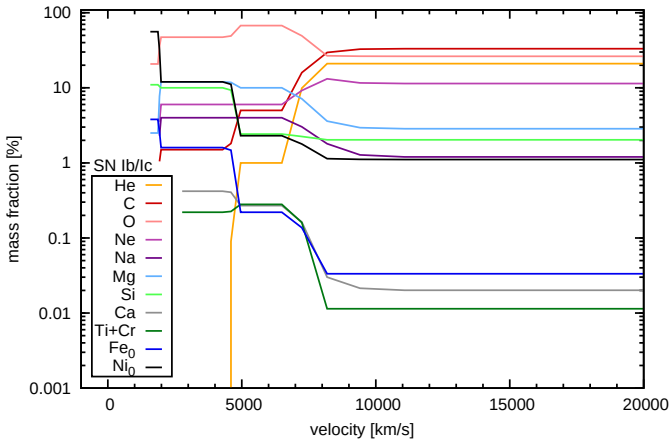

Figure 4.13: Abundance structure of the Type Ib/Ic model.

a SN IIb. However, the Hα signature in SN 1999ex is apparently weaker than that in SN 2008ax.

4.2.2.2 The "SN Ib/Ic" model

In order to obtain our "SN Ib/Ic" model, all but $0.1 M_{\odot}$ of the He have been removed from the SN Ib model.

The model (Fig. 4.12, where SN 1999ex is again shown for a rough comparison) still shows a multitude of relatively weak He lines ($\lambda\lambda$6678,7065) in the optical as well as a strong $\sim$20000 Å line (especially at late epochs) in the IR. The "λ10830" feature is also strong, but may be contaminated by other species as mentioned in Sec. 4.1.2.2). If a SN looks like our model, and decent enough observations are available, He lines can be identified.

The abundance structure of the model is shown in Fig. 4.13. The extent of the He-rich layer in mass space is smaller than it may seem from the figure, as densities drop sharply above 19000 km s^{-1}.

4.3 Discussion

After showing our model sequence, we now discuss details of the behaviour of He in SNe in general, and in the special case of our model for SNe IIb (SN 2008ax models). The SN IIb model is instructive in this context: the conditions within it vary strongly, which allows one to develop a general understanding. Finally, we run tests on the SN Ib /Ic model in order to check whether the He lines we see are due to an NLTE state of He, and in order to see whether the inclusion of He III would affect our models.

4.3.1 He atom, rate equilibria in a He I/He II-dominated plasma in SNe

The level structure of He I makes its behaviour significantly different from most other ions in SNe. A Grotrian diagram of the atom is shown in Figure 4.14. The states are divided into a singlet and a triplet system, and transitions between the two systems are (non-relativistically) forbidden. Also, the lowest excited states of both systems are metastable, i.e. there is no allowed transition from them to the ground state. There is a huge energy gap between the ground state and the first excited states.

A sparse coupling of states favours marked NLTE effects on the excitation state. This is particularly true when e.g. a He plasma is immersed in an environment with energetic nonthermal components (radiation, electrons, ...): these components can then lead to excitation and ionisation of He despite the huge energy gap above the ground state. As a result, one can obtain occupation numbers in the excited states which would occur in LTE environments only for temperatures of several 10000 K – 100000 K.

There are only a few essential processes which determine the state of He in our models (arrows and labels in Fig. 4.14). We give an overview of these processes here before discussing different regimes of He I excitation in the models (next section). For this purpose, it is in most cases appropriate to think of the plasma as two systems weakly coupled – the atoms in the ground state on the one hand, and the ions together with the atoms in excited states on the other hand.

The ground state loses atoms to the excited states and especially to the ionised states through the excitation/ionisation by nonthermal electrons (which are created when gamma rays from ^{56}Ni decay downscatter). This usually outweighs by far any other processes which may depopulate the ground state, because a huge energy gap is to be bridged to the first excited states or to the ionised state. Radiative processes and collisional processes with thermal electrons will couple the excited states to He II. Ionisation and recombination from/to the excited states are usually strong enough in our models to ensure this coupling at least for the higher excitation levels. This holds for triplet as well as singlet levels, which provides a coupling between the singlet and the triplet system as long as the matter is sufficiently ionised. The lower excited states (e.g. n = 2,3) will have some net losses to the ground state, as radiative excitation from the ground state would require extremely strong UV radiation. These losses are normally the only path to populate the ground state and compensate for the upwards rate caused by nonthermal electrons. Recombinations going directly to the ground state are mostly followed by immediate re-ionisation of another atom; Lucy (1991) implemented this by setting the radiative recombination rate to the ground state equal to zero. We have implemented a somewhat more sophisticated approximation in our solver, which diminishes the rate according to an estimate of the optical depth for continuum photons. However, also

Figure 4.14: Grotrian diagram of He I. Adapted from Bashkin & Stoner (1975).

in our "next order" approximation, direct recombination to the ground state is usually irrelevant.

The occupation numbers of the lowest excited states, which most of the observed He I lines originate from, are strongly influenced by the respective rates to the ground state. Similarly, allowed transitions from the singlet system down to the ground state (e.g. from the 2^1P state) are "self-absorbing", i.e. the effective downwards rate in the Sobolev approximation depends on the number density in the ground state, and is often so small that forbidden transitions can well compete. In this case, transitions from triplet states (2^3S, 2^3P), or two-photon transitions from the 2^1S state may be dominant in populating the ground state. At very high densities it happens that collisional downwards rates due to thermal electrons dominate, if the electron gas is cool enough.

Because of this characteristic behaviour, the occupation number of at least one (low-)excited state must be large enough that the rate from this state to the ground state balances the losses from the ground state by nonthermal processes. Usually this requires a markedly super-thermal occupation of that excited state. The other excited states and He II are then usually strongly enough coupled to this state that a significantly super-thermal occupation in all excited states and in the ionised state results. Usually a high He ionisation results from this scenario. As Lucy (1991) already observed, this is not primarily due to a strong direct ionisation by nonthermal electrons, but rather to the fact that radiative ionisation is easy from excited states, and the excited states are always overoccupied such that the non-thermal losses of the ground state can be balanced.

4.3.2 He state in the SN 2008ax model; evolution of the lines

We now take a closer look at the He in our SN 2008ax model at two different epochs ($t =$ 16.0 d and $t = 30.6$ d). Fig. 4.15 shows occupation numbers (exactly: number densities) for some important states of He as a function of radius. A hint on the correspondence to the observed line strengths is given by indicating the region where one important line (He I λ7065) has an optical depth $\tau_l > \frac{1}{3}$ (Fig 4.15, light blue vertical lines).

The behaviour of He in different zones of the ejecta at $t = 16.0$ d shall be described in some detail:

$v \lesssim 9500$ km s^{-1}: In the innermost region, densities are high. The allowed downwards transitions from the singlet system are blocked, and collisional de-excitation from the 2^3S state is the dominant channel to populate the ground state. Generally, the excited states de-excite predominantly by collisions, which leads to a lower occupation in the singlet system (as the singlet levels have higher energies than their "mirror states" in the triplet system).

9500 km s$^{-1} \lesssim v \lesssim 19000$ km s^{-1}: The ground state is more and more strongly populated by allowed radiative transition from the 2^1P state. Therefore, the occupation numbers in this state decrease more steeply towards the outside of the SN than those of the other states. Within the triplet system, the 2^3P state suffers most of the losses

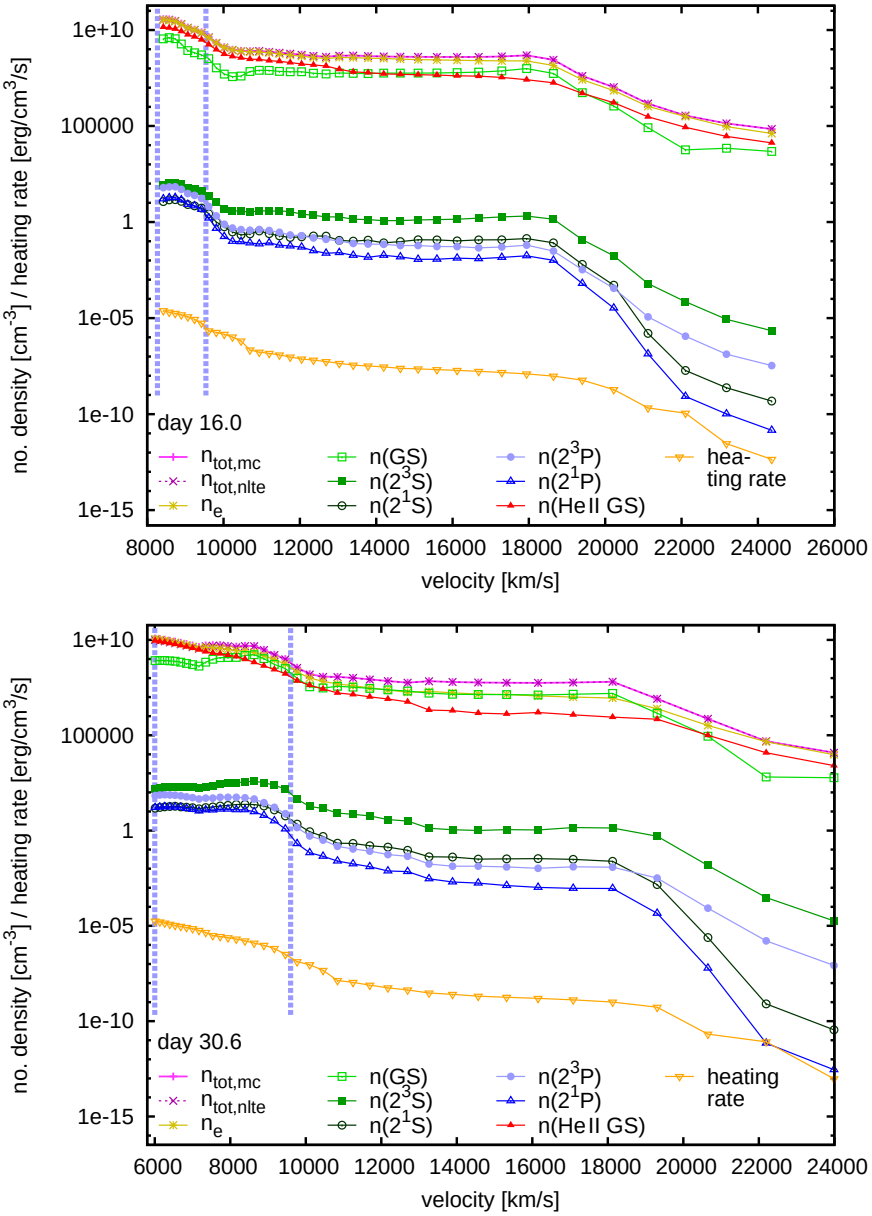

Figure 4.15: SN 2008ax model: occupation numbers in the ground state and the first few excited states of He I, and in He II (one-state ion). In addition, we show the total number density $n_{\rm tot}$, the total number density of atoms treated in NLTE $n_{\rm tot,NLTE}$, the electron number density n_e and the heating rate (cf. Fig. 4.3). The plot shows the variation with velocity/radius; the *two panels* correspond to the epochs $t = 16.0$ d and $t = 30.6$ d. The light blue, vertical (dashed) lines mark the zone in which the λ7065 multiplet has an optical depth $\tau_l > \frac{1}{3}$, respectively. This zone depends on where the 2^3P state (light blue graph and circle symbols) is strongly enough occupied – the line is an upwards transition from this state to $n = 3$.

towards the outside of the SN, as the collisional de-excitation from the 2^1S state becomes insignificant. Ionisation reaches a minimum at $\sim$ 18000 km s^{-1} (Fig. 4.15, red line vs. light green line) because of the small intensity of the (optical/UV) radiation field in the outer layers of the atmosphere.

$v \gtrsim 19000$ km s^{-1}: In the outermost layers, a large fraction of He is ionised owing to the low density. Indeed, ionisation is so strong that we will include He III (and excited states of He II) in our code in the future so as to increase the accuracy of our simulations in the outermost layers (cf. Sections 4.1.1.2, 4.3.3). Test calculations in which a full (albeit preliminary) He II model ion with ionisation to He III is included (Sec. 4.3.3) show that in the outermost layers He III may become the dominant ionisation stage if densities are slightly lower than in our models. In any case, however, we note that in the outer layers the allowed transition from 2^1P becomes increasingly transparent due to the vanishing population of the He I ground state. This drags the occupation number of the 2^1P state down, and other states of the singlet system have to follow the same trend, as they are coupled to one another by radiative transitions.

Such a discussion could also be performed for later epochs (Fig. 4.15). However, the most important points have already become clear, and we summarise them briefly. The behaviour of He deviates significantly from LTE, and the exact physical conditions determine which of the He I levels (from which spectral lines originate) are most strongly occupied. In the case of high densities, collisional downwards rates dominate and the triplet system (with its lines $\lambda\lambda$10830,7065,5876) is favoured over the singlet system (lines $\lambda\lambda$ 20581,7281,6678). At intermediate densities, this is still the case, also due to the fact that the allowed transition 2^1P – 1^1S becomes more and more transparent. However, strong differences within each of the systems appear – the states with a "bigger drain" to the ground state (i.e. 2^1P, 2^3P) become less and less occupied. Therefore, the IR lines (lines $\lambda\lambda$ 20581,10830) are favoured in each of the systems with respect to the optical lines. This may be one of the reasons why the λ10830 line in our models often seems to have the strongest high-velocity wing of all He I lines (although here also the large intrinsic strength of that line is crucial).

As a final note, we want to mention that NLTE occupation numbers are often given as "departure coefficients" (i.e. occupation numbers relative to LTE occupation numbers) in the literature. We did not follow this convention here because departure coefficients strongly depend on the reference temperature at which one calculates the LTE quantities – and in a SN the choice of a reference temperature is not straightforward. However, regardless of the temperature one can say that the departures from LTE are extremely large for all excited states of He I in SNe. We have calculated departure coefficients for the line-formation zones of several models with respect to the local radiation temperature and have practically always obtained results of the order of 10^5 – 10^{10}. Our

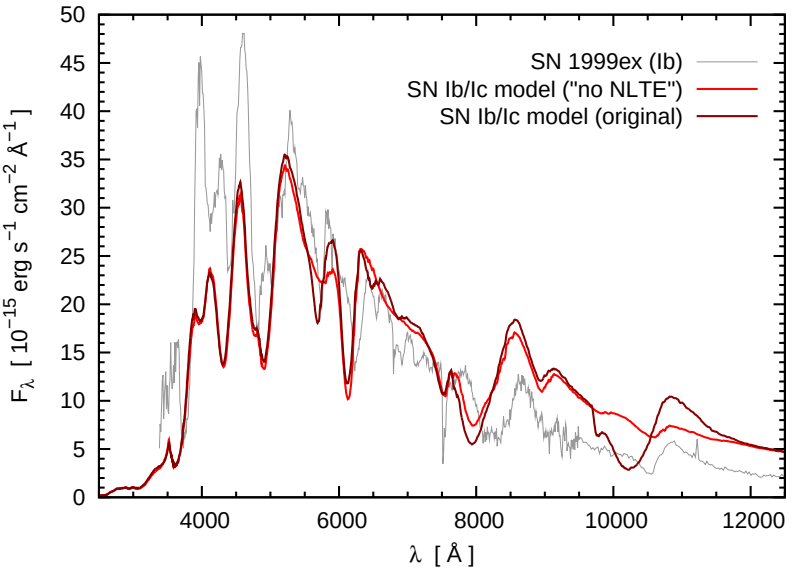

Figure 4.16: Synthetic "SN Ib/Ic" spectrum at $t = 16.0$ d: calculation of He in the nebular approximation ("no-NLTE", bright red line) compared to full NLTE calculation with excitation by fast electrons (dark red line). A spectrum of the SN Ib 1999ex is shown in grey for comparison.

results are in quite good agreement with the calculations of Lucy (1991) in the case of similar physical conditions.

4.3.3 Tests: modifications of the "SN Ib/Ic" model

Before we draw conclusions from our models, we test whether the lines we have seen in the SN Ib/Ic model spectra and interpreted as He lines, are indeed due to He in NLTE. We also test whether our models change when including He III in the calculations.

4.3.3.1 "SN Ib/Ic": deactivation of the NLTE module

We would like to confirm that the model spectra of our "SN Ib/Ic" indeed contain lines due to He in NLTE. To this purpose, we re-calculate the model at $t = 16.0$ d with the NLTE module switched off.

The result is shown in Fig. 4.16. No He lines are visible in the "no-NLTE" synthetic spectrum whatsoever. This shows that NLTE calculations, including the excitation by fast electrons, are indeed crucial for predicting the appearance of SNe containing He.

4.3.3.2 "SN Ib/Ic": removal of the outer layers

Next, we test the sensitivity of our spectrum to high-velocity absorption. If the He lines would vanish without high-velocity He absorption, our results would be very uncertain as the exact density distribution of the ejecta at high velocities is poorly known.

Fig. 4.17 shows the result of a calculation (again of the $t = 16.0$ d spectrum) in which all ejecta above 12500 km s^{-1} have been removed. This obviously results in significant changes in the spectrum, but the He lines in the optical (lines $\lambda\lambda$6678,7065) become even stronger. This is caused by a lower ionisation, which in turn is due to

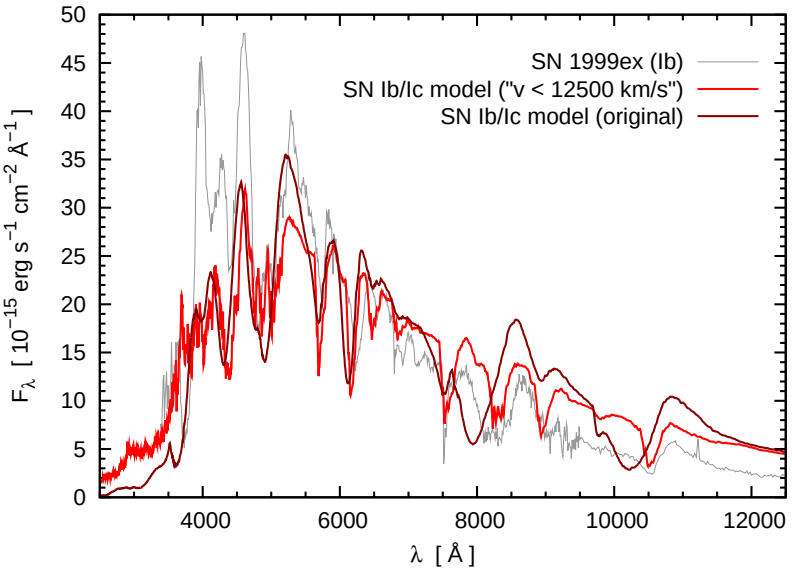

Figure 4.17: Synthetic "SN Ib/Ic" spectrum at $t = 16.0$ d: simulation without outer layers ("$v <$ 12500 km/s") compared to the full simulation. The He lines in the red ($\lambda\lambda$6678,7065, redwards from Si II λ6355) remain visible also after the removal of the outer layers.

reduced backwarming in the model: Fe-group elements are absent at high velocities in the "snipped" model.

4.3.3.3 "SN Ib/Ic": inclusion of He III

The simulations we have shown in this Chapter of the thesis include a detailed treatment only for H and He I; He II is treated as a single (ionised) state. This is justified as long as ionisation to He III does not become strong enough to affect our results. In particular, for our conclusions to be valid it is crucial that the ionisation balance between He II and He I is accurately simulated, which is the case as long as He III does not dominate over He II.

We have verified that this is the case in all but possibly the outermost layers of our atmospheres. To this purpose, we have included a preliminary, but sufficiently realistic He II ion with excited states, and He III (which only has one state), and recalculated different models. Here we show the result for the earliest "SN Ib/Ic" model (Fig. 4.18).

The result that He is extremely ionised in the outermost layers motivates us to carry out future calculations including He III by default. In cases where our models produce spurious high-velocity wings in the He I λ10830 line, the inclusion of He III together with a reduced density in the outer layers may lead to better-fitting models: both owing to the lower density and to the higher ionisation state (favoured by a low density), the number density of He I atoms will decrease. For the results in this work, He III is, however, irrelevant.

4.3.4 Summary – our results and SN Ib/Ic progenitor models

In this chapter we applied our NLTE code module, which enables us to calculate He-dominated spectra, to stripped-envelope core-collapse SNe with low to moderate ex-

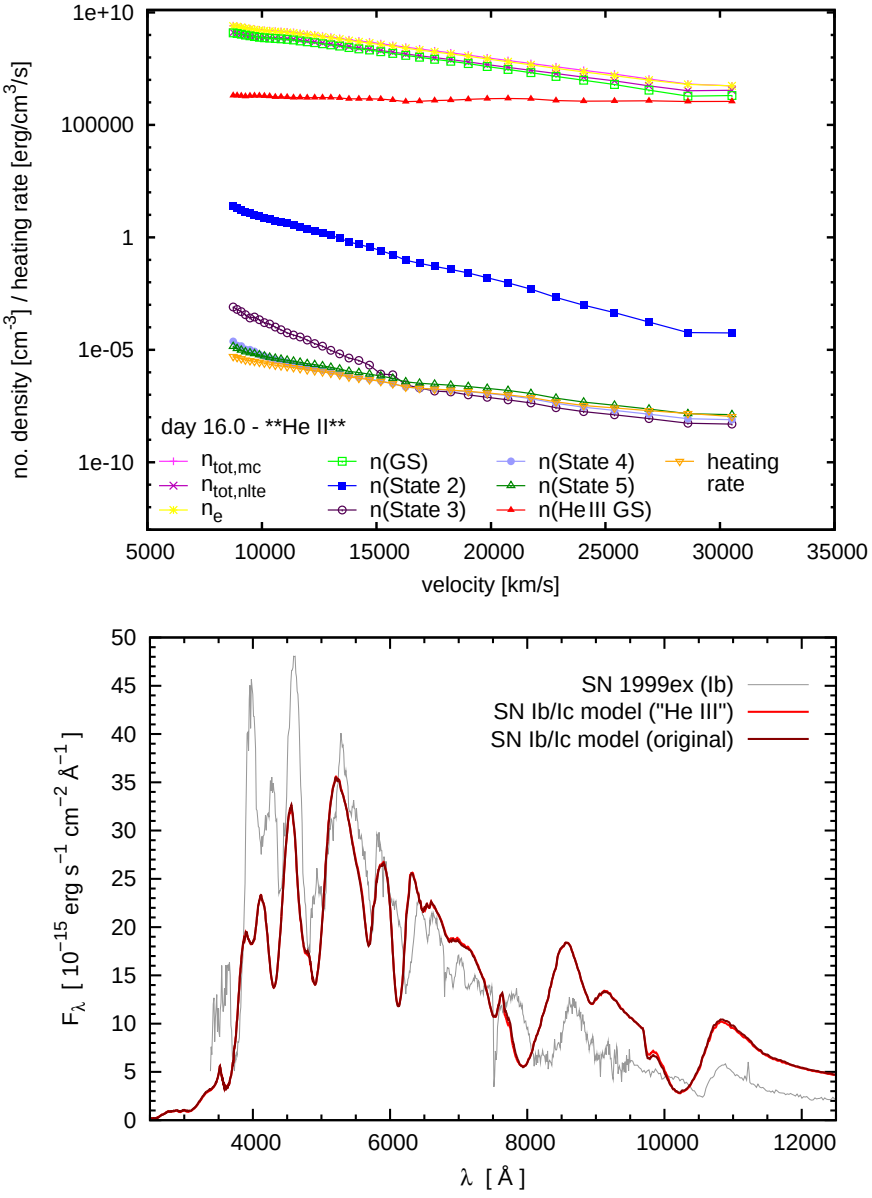

Figure 4.18: Synthetic "SN Ib/Ic" spectrum at $t = 16.0$ d: simulation including excited states of He II, and He III. The spectrum is practically unchanged (*lower panel*). The reason for this becomes apparent in the occupation number plot for He II (*upper panel*): He III becomes significant only in the outermost layers at low densities (red line).

plosion energies and ejecta masses (10^{51} erg, $1-4M_{\odot}$). We performed an abundance tomography of the Type IIb SN 2008ax, and of the Type Ic SN 1994I. The models were simultaneously processed with a light-curve code, which calculates the gamma-ray deposition rates needed for NLTE spectral synthesis. Both the light curves and the spectra of the SNe were reasonably well matched.

A key problem in spectroscopy of SNe IIb/Ib/Ic is the determination of He or H abundances from spectra. Especially for He, the NLTE state implies that it is difficult to estimate abundances from the strength of spectral lines. The NLTE module makes this possible, and thus we aimed at finding out how much He a SN must contain in order for He lines to show up. We used the tomography models for SN 2008ax and SN 1994I to construct a sequence of spectral models representing Type IIb/Ib/Ic SNe with the same core, but different degrees of envelope stripping.

We found that a SN containing $\sim 0.1 M_{\odot}$ of He shows weak He lines in the optical, and strong ones in the infrared (around 10000 Å and 20000 Å). In order to interpret this result correctly, further tests need to be run so as to estimate the influence, for example, of the ^{56}Ni distribution on the lines. However, it also needs to be observationally clarified whether some SNe Ic actually show a He line around 20000 Å.

Based on our first results presented here, and accounting for an estimated uncertainty of a factor 2, we can already say that low-mass/-energy SNe Ic may not contain more than $\sim 0.1..0.2 M_{\odot}$ of He. Otherwise, He lines would show up in the optical spectra. This estimate has interesting implications on progenitor models of these SNe.

Georgy et al. (2009) and Yoon et al. (2010) have presented state-of-the-art single- and binary-star progenitor models for SNe Ib/Ic, respectively. The progenitors of Georgy et al. (2009), which are single Wolf-Rayet stars, never have less than $0.3 M_{\odot}$ of He. The majority of their models have a larger He mass. In order to explain total SN Ic rates with their progenitors, they need to allow for He masses of $0.6 M_{\odot}$ in SNe Ic. It is therefore unlikely that these models can explain SNe Ic like SN 1994I. However, also Yoon et al. (2010), who simulated binaries with two phases of mass transfer ("case AB"), produce only a small amount of progenitors with $m_{\mathrm{He}} < 0.5 M_{\odot}$. Taken together with our results, all this seems to hint towards a binary scenario with three phases of mass transfer for low-mass Type Ic SNe. Such scenarios have already been proposed when the first models for SN 1994I were published (Iwamoto et al. 1994; Nomoto et al. 1994).

It will now be important to collaborate with explosion modellers in order to refine our density models, and with the stellar evolution community in order to investigate possible progenitor scenarios in more detail. On the other hand, we also need to repeat our analysis for higher-mass SNe Ib/c in order to obtain a comprehensive picture of the progenitors of SNe Ib/Ic.

As a by-product of our analysis, we gained experience in analysing the state of He in SN radiative transfer simulations. We characterised various regimes, in which different de-excitation channels to the ground state of He I dominate, and a characteristic occupation pattern in He I results. This will help us in the future when analysing further models in depth. Furthermore, we recognised the possible importance of He III for the outermost layers of SNe. We will therefore extend our NLTE module to include He III by default. Also, we will include additional processes (charge exchange, etc.) in the NLTE simulation in order to make the H masses we infer as reliable as the He masses.

Chapter 5

Conclusions and outlook

In this thesis, we have analysed spectra of observed Type I (and Type IIb) supernovae (SNe) in order to clarify their explosion properties and obtain information about the progenitor stars. To this end, we have used and significantly extended an efficient numerical program (Lucy 1999; Mazzali 2000; Stehle et al. 2005) which computes synthetic spectra simulating the essential physical processes. The code calculates radiative transfer (RT) in a spherically-symmetric supernova model with abundances and densities as physical parameters. Optimizing these to match observations, we inferred the abundances and density profiles of interesting observed objects.

We began with two conceptually interesting peculiar Type Ia supernovae (SNe Ia). On the one hand, we analysed the properties of the subluminous [1991bg-like, Filippenko et al. (1992)] SN 2005bl. On the other hand, we investigated the extremely superluminous SN 2009dc. For both objects, our results indicated that the progenitors differ from those of standard SNe Ia, which are supposed to originate (e.g. Hillebrandt & Niemeyer 2000) from single-degenerate systems (binary systems with one white dwarf / WD).

Next, we calculated synthetic spectra of SNe IIb/Ib/Ic, using our non–local-thermodynamic-equilibrium (NLTE) extension to the code to simulate the behaviour of He and H atoms (neutral and ionised) in detail. We first constructed models for the SN IIb 2008ax and the SN Ic 1994I. This enabled us to set up a sequence of SN IIb/Ib/Ic models with differently-massive H and He envelopes, with the aim of clarifying the effect of H and He on the spectra. From the sequence, we could predict an upper limit to the He content of (moderately massive) SN Ic progenitors, i.e. for the progenitors of core-collapse SNe in which no He lines are seen.

In the following, we summarise some of the results and give implications. Finally, we give an outlook on research which may be conducted to extend this thesis.

RT models for exotic SNe Ia: clues on structure & progenitors

SN 2005bl

In our abundance tomography of the subluminous SN 2005bl, we found that nuclear burning in dim, 91bg-like SNe Ia proceeds at lower temperatures and/or densities than in normal SNe Ia. The spectra indicate that much less burned material is present above $\sim$ 8500 km s^{-1} in SN 2005bl compared to moderately-luminous objects (Mazzali et al. 2008). From $\sim$ 8500 km s^{-1} down to $\sim$ 3300 km s^{-1}, IME dominate

the ejecta. This points towards large-scale incomplete Si-burning or explosive O burning (e.g. Woosley et al. 1973). A detonation at low densities is the most likely way to obtain such burning conditions and to preserve a pronounced abundance zoning in the explosion. Explosion models which pre-expand the star by a deflagration and then detonate (e.g. Hillebrandt & Niemeyer 2000, Badenes et al. 2003, Gamezo et al. 2004, Röpke & Niemeyer 2007, Bravo et al. 2009) produce larger amounts of ^{56}Ni. This indicates that either the pre-expansion is too weak or the amount of ^{56}Ni produced in the deflagration stage is already too large. The primary possibilities which remain to produce 1991bg-like objects are therefore either edge-lit explosions of sub-Chandrasekhar white dwarfs (which have lower densities than M_{Ch} WDs), or mergers of two WDs (where each WD is sub-Chandrasekhar).

Besides the abundances, we have obtained information about the density profile of SN 2005bl. We showed that the spectra are incompatible with the presence of significant amounts of oxygen at $v \gtrsim 13000$ km s^{-1}. Together with the low abundances of burning products, this indicates a general lack of material at high velocities, i.e. a steeply-declining density. We tested whether a good fit to the observed spectra is possible using a modified W7 density model, scaled to a different total mass and/or energy. Indeed, a reduction of $\sim 30\%$ in total kinetic energy yielded a well-fitting model (05bl-w7e0.7). Consistency with the spectra was also achieved with somewhat super- or sub-Chandrasekhar mass density profiles, provided that they were similar to w7e0.7 at $v \gtrsim 13000$ km s^{-1}. We found, however, that models with a mass deviating $> 30\%$ from the Chandrasekhar mass are somewhat disfavoured because they may produce too wide a bolometric light curve.

After our investigations, Pakmor et al. (2010, 2011) presented simulations of WD mergers with a total mass of $0.9 + 0.9 M_{\odot}$. They showed that one can indeed produce SN 1991bg-like objects from such a scenario. The ejecta simulated by them do not only show qualitative agreement with the abundances derived in this thesis, but also have a low kinetic energy so that our density constraints for the outer zones are matched. Therefore, a giant step has been made in explaining this subclass of SNe Ia. Yet, more extensive observations at very early and very late (nebular) epochs are desirable in order to further constrain the explosion models. Very early spectra are at the moment being obtained in programmes coupled to large surveys (e.g. Rau et al. 2009; P. Nugent, private communication).

SN 2009dc

As a contrast to dim SNe such as SN 2005bl, we chose to analyse SN 2009dc, a representative example of the extremely luminous "Super-Chandrasekhar" (SC) SN Ia subclass. SC SNe are characterised by an extremely large luminosity, and by spectral lines of Fe and intermediate-mass elements typical of SNe Ia. Line velocities are normal or low, and H or He lines are not present. The photospheric phase lasts unusually long, indicating dense ejecta. Due to the slow evolution, spectra up to an epoch of $+36.4$ d past B maximum can be modelled with a photospheric code.

There were (and there still are) many unknowns in a spectral analysis of SC SNe. Absolute densities and density profiles are poorly constrained, as SC SNe may not even be the result of white dwarf explosions. Furthermore, the objects may intrinsically not be as superluminous as the observations suggest, if some of the observed light is externally generated by interaction of the ejecta with material surrounding the SN ("interaction

scenario"). In this thesis, we first presented an analysis of SN 2009dc assuming that all the observed light is intrinsically generated. Later, we tested the interaction scenario by calculating model spectra with lower luminosity and an external flux component added.

In our first analysis of SN 2009dc, we aimed at models independent of specific explosion scenarios, also covering the possibility of a massive progenitor. We therefore did not test rescaled W7 densities as for SN 2005bl, but used a new approach to empirically determine the density of the outer ejecta and the rise time from the earliest spectrum of the SN (-9.4 d). We found that one can constrain the rise time of the SN to > 24 d from the spectra alone, and we specified limiting density profiles. We then conducted two abundance tomography experiments, using one of our empirically-constructed profiles and the only available hydrodynamical model possibly fitting such SNe, a detonation model for an overmassive, rotating white dwarf (AWD3-det, Pfannes et al. 2010).

In the tomography using the AWD3-det profile, we found ^{56}Ni and other Fe-group elements to be constrained to velocities $\lesssim 7500$ km s^{-1}. Therefore, the spectral models allow only ^{56}Ni masses $< 1.1 M_\odot$ with this density profile. In spherical symmetry, which has also been assumed as an approximation for the spectral models, Arnett's rule (Arnett 1982) demands the ^{56}Ni mass of the SN be $\gtrsim 2 M_\odot$. Therefore, the model can only be rescued if the radiative transfer is extremely affected by the model's intrinsic asymmetry (cf. Pfannes et al. 2010). This is, however, not indicated by polarimetric observations (Tanaka et al. 2010). Therefore, SN 2009dc is probably not explained by a model similar to AWD3-det. In general, explosion models representing overmassive WDs will have problems explaining SC SNe Ia: to allow for the ^{56}Ni to be concentrated inside, a density profile must have high densities in the core. This is probably impossible if a lot of kinetic energy is produced by burning to NSE and the total mass of the object is only $\sim 2 M_\odot$. Rotating WDs with a much larger mass probably do not exist (cf. Scalzo et al. 2010). Only in the interaction scenario, a single WD (rotating or not) may be a likely progenitor for an object such as SN 2009dc.

Our tomography with an empirically constructed density profile (with a total mass of $3 M_\odot$) produced model spectra with a similar fit quality. This showed that models which involve core collapse or a thermonuclear explosion within a star ("Type I$\frac{1}{2}$ SNe") may be an alternative. With the larger ejecta mass, possibly concentrated in the inner layers, the models are compatible with a larger ^{56}Ni content. However, it is questionable whether core-collapse or Type I$\frac{1}{2}$ models can produce the abundance stratification we find, which is similar as in our AWD3-det-based model in velocity space. Unburned material dominates at $v \gtrsim 9000$ km s^{-1}, intermediate-mass elements below, and Fe-group elements including ^{56}Ni, in the core. So far there is no self-consistent hydrodynamical model reproducing our results for these types of explosions.

Afterwards, we tested the "interaction scenario". To this purpose, we assumed a fairly normal SN Ia explosion plus interaction with some circumstellar material, and attempted to perform abundance tomography. For the SN, we used a W7 density profile rescaled to 70% of its original kinetic energy (because of the low line velocities as in SN 2005bl). We then created spectral models with a luminosity reduced by $50 - 33\%$. At each epoch, the difference between observed spectrum and model was fitted with a third-order polynomial, representing the external luminosity contribution. We obtained an outstanding reproduction of the observed spectra especially at the early epochs, with a fit quality much better than in the other approaches. Theoretically, the structure of this model would most probably correspond to a scenario where one WD is accreted onto another one in a double WD binary with a mass ratio $q_{\rm crit} < q \lesssim 0.8$ [where $q_{\rm crit}$ is be-

tween 0.2 and 0.67, Motl et al. (2007)]. The primary WD would explode roughly when reaching its Chandrasekhar mass. Due to the smaller ^{56}Ni mass the model requires, this WD would not have to rotate and be supermassive (but it may of course do so). The interaction with the surrounding material would explain why the velocities in the spectra of SN 2009dc, as those of other SC SNe Ia (cf. Taubenberger et al. 2011a) tend to be lower than for normal SNe Ia. We remark however that also this scenario leaves many serious issues to be resolved – e.g. the question how a (pseudo-)continuum, as represented by the polynomials we added to the flux, can be generated by an interaction of the ejecta with a CSM. Often, such interaction rather leads to line emission.

NLTE code module and analyses of stripped-envelope core-collapse SNe

In order to compute spectra for Type IIb, Ib and Ic SNe (stripped-envelope core-collapse SNe), we enabled our code to calculate H and He atoms/ions in full NLTE by programming an extension module. We applied the resulting code to such SNe, obtaining information on the He content of SN Ib vs. SN Ic progenitors. For this thesis, we concentrated on SNe IIb/Ib/Ic with a low to moderate mass (C-O core mass $\sim 0.8 M_{\odot}$) and energy ($\sim 1 \times 10^{51}$ erg).

First, we created abundance tomography models for the SN IIb 2008ax and the SN Ic 1994I. We assumed density profiles as they have been used in earlier studies of such objects [4H47 – Shigeyama et al. (1994); CO21 – Iwamoto et al. (1994)]; these profiles are based on the same stellar core but a different (more or less stripped) envelope. We did not make any attempts to modify the density profiles: our focus here has not been on exactly matching observed objects, but on studying this group of SNe in general. While modelling the spectra, we ran a light-curve code (Cappellaro et al. 1997) on the current version of the ejecta model from time to time. We thus obtained consistent gamma-ray deposition rates, which the NLTE module needs to calculate the state of He and H. The abundances were iteratively adapted so as to match the observed spectra and light curves. The resulting tomography models fit both SNe reasonably well and are in reasonable agreement with models for the two SNe from the literature (Sauer et al. 2006; Tsvetkov et al. 2009). The occupation numbers within He I show extremely large departures from LTE in our models (commonly by factors 10^5...10^{10}). This confirms the suggestion of Harkness et al. (1987) that an extreme NLTE occupation pattern is needed to explain He I lines in SNe.

Afterwards, we constructed a sequence of radiative transfer models which covers SNe IIb, Ib and Ic with similar stellar cores. To this purpose, we first needed to obtain density profiles. We started from the 4H47 explosion model (Shigeyama et al. 1994) used for modelling SN 2008ax, and replaced its H envelope by a lower-mass H envelope while scaling the kinetic energy of the stellar core up. We implemented this such that the end of the sequence was a H-deficient ejecta model very similar to the hydrodynamic SN Ib model M4.0 of Shigeyama et al. (1990), which is based on the same stellar core as 4H47. Afterwards, we modified the M4.0 model in a similar manner until the He envelope was removed, transforming smoothly to the CO21 model (Iwamoto et al. 1994) which fits SNe Ic. The radiative transfer code was then run with these density profiles and with an abundance structure appropriately interpolated between our models for SN 2008ax and SN 1994I.

The model sequence indicated that He I lines will realistically be detectable if a (low-mass/low-energy) core-collapse SN contains more than $\sim 0.1 M_{\odot}$ of He. This will

in particular be the case if infrared spectra are available which cover the wavelength range around 20000 Å. We will run further tests on SN Ib/Ic models with this He mass in order to pin down the exact detection threshold for He more precisely; an uncertainty of a factor ~ 2 in the threshold given can be expected, also because it depends on the data quality.

However, our result already has implications for the progenitors of low-mass SNe Ic: the progenitors of these SNe are not single Wolf-Rayet stars, as simulated for example by Georgy et al. (2009). Such stars always contain $\gtrsim 0.6 M_{\odot}$ of He at the onset of core collapse, which is far above our detection threshold. When losing parts of their He envelope, their luminosity decreases rapidly, preventing further mass loss. Also invoking binarity, it is not simple to explain low He masses. Yoon et al. (2010) presented binary models for SN IIb/Ib/Ic progenitors which involved two mass transfer episodes, and almost all their stars contain $\gtrsim 0.5 M_{\odot}$ of He when exploding. It seems that binaries undergoing three episodes of mass transfer (e.g. Nomoto et al. 1994) are needed to explain low-mass SNe Ic like SN 1994I. Detailed simulations of such systems should be conducted, also in order to obtain information about the rates at which such progenitors are possibly produced.

Besides yielding the result on the He abundance in SNe Ic, our study helped us to characterise the excitation/ionisation regimes of He in SNe Ib/IIb. We obtained information on the expected strength of various He I lines (relative to each other) under different conditions in SNe, and realized that significant amounts of He III may be present in the outermost layers of SNe Ib/IIb.

Outlook

Models for Super-Chandrasekhar SNe and other "weird" SN Ia

The SNe Ia analysed in this thesis represent two important, peculiar SN Ia subclasses. However, several such subclasses are now known, for example the extremely low-velocity 2002cx-like SNe (e.g. Sahu et al. 2008). All these SNe need to be studied and understood.

Also the analysis of SN 1991bg-like and SC SNe Ia will and should not stop with the work presented here. For SN 1991bg-like objects, it remains to be clarified whether WD mergers are the only way to produce subluminous SNe Ia. For SC SNe, explosion models have to be developed. Analyses of nebular observations may be very helpful in this process. Nebular spectra of SN 2009dc and other objects have now been processed and can be used for analyses (S. Taubenberger, private communication). With these spectra, the ^{56}Ni content of these SNe can be determined in an independent way, and a first decision (or guess) may be possible as to which of the mentioned progenitor scenarios holds.

H and He content of very massive and energetic SNe Ib/Ic

The progenitor question discussed for Ib/Ic in this thesis is just as relevant for higher-mass objects with high expansion velocities [broad-lined core-collapse SNe/hypernovae, e.g. Galama et al. (1998), Mazzali et al. (2008)]. In order to obtain a more comprehensive picture of the progenitors of core-collapse SNe, we should therefore conduct a follow-up study involving more massive and energetic models. H and He

layers on top of hypernovae also may to be relevant for explaining why these energetic explosions sometimes, but not always coincide with gamma-ray bursts of the *long/soft* type (Mazzali et al. 2008).

Continuous improvements in spectral analyses and radiative transfer methods

The analysis methods used in this thesis will be continuously refined in the next years.

One direction to follow will be the improvement of the radiative transfer methods. The NLTE module can be extended to treat "next-order" effects such as charge exchange, and to include more sophisticated H I and He II models or further species. However, there will also be updates to the Monte-Carlo spectral synthesis code itself. A promising possibility is the construction of an updated code which can handle the production of radiation within the simulated atmospheres. Such a code would improve the accuracy at epochs when some amount of ^{56}Ni is already above the photosphere. Also, it would be possible to move the photospheric boundary arbitrarily deep into the ejecta, with only a small part of the observed luminosity coming from the photosphere. This should cure the problem of the IR excess sometimes seen in our synthetic spectra due to the assumption of a black-body lower boundary.

The other direction will be an improvement of our spectral fitting techniques. Right now, we optimise the spectrum "by hand and eye", i.e. we change the abundances by hand, until the synthetic spectra fit the observed ones in a way we regard the optimum by visual judgement. This procedure will be replaced by an automatic optimisation, for which we need an optimisation algorithm as well as a suitable measure for the fit quality. The problem here is that expected deviations due to the approximations in the RT code (such as the IR excess often appearing in our current synthetic spectra) have to be neglected when determining the fit quality. When fitting "by hand and eye", we do this assessing the shortcomings and their reason in each of our models; the implementation of a fit quality function which mimics our ways to assess the fit and decide about the optimum match is an important task for the coming years.

Bibliography

Abbott D. C., Lucy L. B., 1985, ApJ, 288, 679

Arcones A., Janka H.-T., 2011, A&A, 526, A160

Arnett W. D., 1971, ApJ, 163, 11

Arnett W. D., 1974, ApJ, 193, 169

Arnett W. D., 1979, ApJ, 230, L37

Arnett W. D., 1982, ApJ, 253, 785

Arnett W. D., 1989, ApJ, 343, 834

Arnett W. D., Meakin C., 2011, arXiv:1101.5646

Arnett W. D., Truran J. W., Woosley S. E., 1971, ApJ, 165, 87

Asplund M., Grevesse N., Sauval A. J., Scott P., 2009, ARA&A, 47, 481

Astier P. et al., 2006, A&A, 447, 31

Axelrod T. S., 1980, PhD thesis, University of California, Santa Cruz

Baade W., Zwicky F., 1934a, Proceedings of the National Academy of Science, 20, 254

Baade W., Zwicky F., 1934b, Physical Review, 46, 76

Badenes C., Bravo E., Borkowski K. J., Domínguez I., 2003, ApJ, 593, 358

Barbon R., Ciatti F., Rosino L., 1979, A&A, 72, 287

Baron E., Hauschildt P. H., Branch D., Wagner R. M., Austin S. J., Filippenko A. V., Matheson T., 1993, ApJ, 416, L21

Bartunov O. S., Tsvetkov D. I., 1986, Ap&SS, 122, 343

Bashkin S., Stoner J. O., 1975. North-Holland Publ. Co., Amsterdam

Benetti S. et al., 2005, ApJ, 623, 1011

Benvenuto O. G., De Vito M. A., 2005, MNRAS, 362, 891

Bersten M. C., Benvenuto O., Hamuy M., 2011, ApJ, 729, 61

Bessell M. S., 1990, PASP, 102, 1181

Blinnikov S. I., Khokhlov A. M., 1986, Soviet Astronomy Letters, 12, 131

Blinnikov S. I., Khokhlov A. M., 1987, Soviet Astronomy Letters, 13, 364

Blinnikov S. I., Röpke F. K., Sorokina E. I., Gieseler M., Reinecke M., Travaglio C., Hillebrandt W., Stritzinger M., 2006, A&A, 453, 229

Blondin J. M., Mezzacappa A., DeMarino C., 2003, ApJ, 584, 971

Blondin S., Prieto J. L., Patat F., Challis P., Hicken M., Kirshner R. P., Matheson T., Modjaz M., 2009, ApJ, 693, 207

Bombaci I., 1996, A&A, 305, 871

Bond H. E., Bedin L. R., Bonanos A. Z., Humphreys R. M., Monard L. A. G. B., Prieto J. L., Walter F. M., 2009, ApJ, 695, L154

Borst L. B., 1950, Phys. Rev., 78, 807

Bowers E. J. C., Meikle W. P. S., Geballe T. R., Walton N. A., Pinto P. A., Dhillon V. S., Howell S. B., Harrop-Allin M. K., 1997, MNRAS, 290, 663

Brahe Tycho, 1573, De nova et nullius aevi memoria prius visa stella, iam pridem a nato Christo 1572, mense Novembri primum conspecta, contemplatio mathematica. Laurentius Benedictus, Kopenhagen

Branch D., 1986, ApJ, 300, L51

Branch D., Fisher A., Nugent P., 1993, AJ, 106, 2383

Branch D., Lacy C. H., McCall M. L., Sutherland P. G., Uomoto A., Wheeler J. C., Wills B. J., 1983, ApJ, 270, 123

Bravo E., García-Senz D., Cabezón R. M., Domínguez I., 2009, ApJ, 695, 1257

Bruenn S. W., Mezzacappa A., Hix W. R., Blondin J. M., Marronetti P., Messer O. E. B., Dirk C. J., Yoshida S., 2009, in Giobbi G., Tornambe A., Raimondo G., Limongi M., Antonelli L. A., Menci N., Brocato E., eds, AIP Conference Series Vol. 1111. AIP, Melville, pp 593–601

Burbidge G. R., Hoyle F., Burbidge E. M., Christy R. F., Fowler W. A., 1956, Phys. Rev., 103, 1145

Burrows A., Livne E., Dessart L., Ott C. D., Murphy J., 2006, New Astron. Rev., 50, 487

Burrows A., Livne E., Dessart L., Ott C. D., Murphy J., 2007, ApJ, 655, 416

Burstein D., Heiles C., 1982, AJ, 87, 1165

Canfield R. C., Ricchiazzi P. J., 1980, ApJ, 239, 1036

Cann N. M., Thakkar A. J., 2002, J. Phys. B, 35, 421

Cappellaro E., Mazzali P. A., Benetti S., Danziger I. J., Turatto M., della Valle M., Patat F., 1997, A&A, 328, 203

Cardelli J. A., Clayton G. C., Mathis J. S., 1989, ApJ, 345, 245

Carroll S. M., 2004, Spacetime and geometry. An introduction to general relativity. Addison Wesley, San Francisco, CA

Castor J. I., 1970, MNRAS, 149, 111

Catchpole R. M. et al., 1989, MNRAS, 237, 55P

Chandrasekhar S., 1931, ApJ, 74, 81

Chevalier R. A., 1976, ApJ, 207, 872

Chevalier R. A., 1981, ApJ, 246, 267

Chevalier R. A., 2005, ApJ, 619, 839

Chevalier R. A., 2010, arXiv:1011.3731

Chevalier R. A., Fransson C., 1994, ApJ, 420, 268

Chornock R. et al., 2010, ArXiv:1001.2775

Chugai N. N., 2008, Astronomy Letters, 34, 389

Clocchiatti A., Wheeler J. C., 1997, ApJ, 491, 375

Clocchiatti A., Wheeler J. C., Brotherton M. S., Cochran A L., Wills D., Barker E. S., 1996, ApJ, 462, 462

Cobb B. E., Bloom J. S., Perley D. A., Morgan A. N., Cenko S. B., Filippenko A. V., 2010, ApJ, 718, L150

Colgate S. A., 1979, ApJ, 232, 404

Colgate S. A., McKee C., 1969, ApJ, 157, 623

Colgate S. A., Petschek A. G., Kriese J. T., 1980, ApJ, 237, L81

Colgate S. A., White R. H., 1966, ApJ, 143, 626

Conley A. et al., 2006, AJ, 132, 1707

Crockett R. M. et al., 2008, MNRAS, 391, L5

Dan M., Rosswog S., Brüggen M., 2009, in Garcia-Berro E., Hernanz M., Isern J., Santiago T., eds, 16th European White Dwarfs Workshop, Vol. 172 of J. Phys. Conf. Series. p. 012034

Dere K. P., Landi E., Mason H. E., Monsignori Fossi B. C., Young P. R., 1997, A&AS, 125, 149

Dessart L., Hillier D. J., 2005, A&A, 437, 667

Deuflhard P., 2004, Newton Methods for Nonlinear Problems: Affine Invariance and Adaptive Algorithms. Springer, Berlin

Di Stefano R., 2010, ApJ, 712, 728

Di Stefano R., Kong A., Primini F. A., 2006, arXiv:astro-ph/0606364

Drake G. W. F., Morton D. C., 2007, ApJS, 170, 251

D'Souza M. C. R., Motl P. M., Tohline J. E., Frank J., 2006, ApJ, 643, 381

Eastman R. G., Woosley S. E., Weaver T. A., Pinto P. A., 1994, ApJ, 430, 300

Elias J. H., Matthews K., Neugebauer G., Persson S. E., 1985, ApJ, 296, 379

Elmhamdi A., Danziger I. J., Branch D., Leibundgut B., Baron E., Kirshner R. P., 2006, A&A, 450, 305

Ensman L., Burrows A., 1992, ApJ, 393, 742

Ensman L. M., Woosley S. E., 1988, ApJ, 333, 754

Ergma E., Paczynski B., 1974, Acta Astronomica, 24, 1

Falk S. W., Arnett W. D., 1977, ApJS, 33, 515

Fernley J. A., Seaton M. J., Taylor K. T., 1987, J. Phys. B, 20, 6457

Filippenko A. V., 1997, ARA&A, 35, 309

Filippenko A. V. et al., 1992, AJ, 104, 1543

Filippenko A. V. et al., 1995, ApJ, 450, L11+

Fink M., Hillebrandt W., Röpke F. K., 2007, A&A, 476, 1133

Fink M., Röpke F. K., Hillebrandt W., Seitenzahl I. R., Sim S. A., Kromer M., 2010, A&A, 514, A53

Fisher A., Branch D., Nugent P., Baron E., 1997, ApJ, 481, L89

Fruchter A. S. et al., 2006, Nature, 441, 463

Fryer C., Benz W., Herant M., Colgate S. A., 1999, ApJ, 516, 892

Fryer C. L. et al., 2009, ApJ, 707, 193

Fryer C. L. et al., 2010, ApJ, 725, 296

Fryer C. L., Woosley S. E., Heger A., 2001, ApJ, 550, 372

Galama T. J. et al., 1998, Nature, 395, 670

Gallagher J. S., Garnavich P. M., Berlind P., Challis P., Jha S., Kirshner R. P., 2005, ApJ, 634, 210

Gamezo V.N., Khokhlov A.M., Oran E.S., 2004, hys. Rev. Lett., 92, 211102

Garnavich P. et al., 2004, ApJ, 613, 1120

Gehrels N., Ramirez-Ruiz E., Fox D. B., 2009, ARA&A, 47, 567

Georgy C., Meynet G., Walder R., Folini D., Maeder A., 2009, A&A, 502, 611

Gilfanov M., Bogdán Á., 2010, Nature, 463, 924

Gould R. J., 1972, Physica, 60, 145

Grasberg E. K., Imshenik V. S., Nadëzhin D. K., 1971, Ap&SS, 10, 3

Grasberg É. K., Nadëzhin D. K., 1970, SvA, 13, 585

Greggio L., Renzini A., Daddi E., 2008, MNRAS, 388, 829

Habing H. J., Goldsmith D. W., 1971, ApJ, 166, 525

Hachinger S., 2007, Quantitative Analysis of Spectra of Type Ia Supernovae, Diplom Thesis, TU München

Hachinger S., Mazzali P. A., Benetti S., 2006, MNRAS, 370, 299

Hachisu I., Kato M., 2001, ApJ, 558, 323

Hachisu I., Kato M., Nomoto K., 2010, ApJ, 724, L212

Hammer N. J., Janka H.-T., Müller E., 2010, ApJ, 714, 1371

Hamuy M. et al., 2001, ApJ, 558, 615

Hamuy M. et al., 2002, AJ, 124, 417

Hamuy M. et al., 2003, Nature, 424, 651

Hamuy M. A., 2001, PhD thesis, The University of Arizona

Han Z., Podsiadlowski P., 2004, MNRAS, 350, 1301

Harkness R. P. et al., 1987, ApJ, 317, 355

Hashimoto M., 1995, Progress of Theoretical Physics, 94, 663

Hayden B. T. et al., 2010, ApJ, 712, 350

Heger A., Fryer C. L., Woosley S. E., Langer N., Hartmann D. H., 2003, ApJ, 591, 288

Hicken M. et al., 2009, ApJ, 700, 1097

Hicken M., Garnavich P. M., Prieto J. L., Blondin S., DePoy D. L., Kirshner R. P., Parrent J., 2007, ApJ, 669, L17

Hillebrandt W., Niemeyer J. C., 2000, ARA&A, 38, 191

Hoeflich P., Khokhlov A., 1996, ApJ, 457, 500

Höflich P., Schaefer B. E., 2009, ApJ, 705, 483

Howard W. M., Meyer B. S., Woosley S. E., 1991, ApJ, 373, L5

Howell D. A., 2010, Nature Communications, in press (arXiv:1011.0441)

Howell D. A. et al., 2006, Nature, 443, 308

Howell D. A., Höflich P., Wang L., Wheeler J. C., 2001, ApJ, 556, 302

Hoyle F., Fowler W. A., 1960, ApJ, 132, 565

Hubble E., 1929, Proceedings of the National Academy of Science, 15, 168

Hummer D. G., Mihalas D., 1988, ApJ, 331, 794

Hummer D. G., Storey P. J., 1998, MNRAS, 297, 1073

Iben Jr. I., Renzini A., 1983, ARA&A, 21, 271

Immler S., Weiler K., McCray R. eds,, 2007, SUPERNOVA 1987A: 20 YEARS AFTER: Supernovae and Gamma-Ray Bursters, Vol. 937 of AIP Conference Series. AIP, Melville

Imshenik V. S., Nadëzhin D. K., 1965, SvA, 8, 664

Iwamoto K., Brachwitz F., Nomoto K., Kishimoto N., Umeda H., Hix W. R., Thielemann F.-K., 1999, ApJS, 125, 439

Iwamoto K. et al., 1998, Nature, 395, 672

Iwamoto K., Nomoto K., Hoflich P., Yamaoka H., Kumagai S., Shigeyama T., 1994, ApJ, 437, L115

Jackson J. D., 1998, Classical Electrodynamics, 3rd edn. John Wiley & Sons, Inc., New York

Janev R. K, Smith J. J., 1993, Atomic and plasma-material interaction data for fusion (Supplement to the journal Nucl. F.), Vol. 4. International atomic energy agency, Vienna

Janka H.-T., Langanke K., Marek A., Martínez-Pinedo G., Müller B., 2007, Phys. Rept., 442, 38

Jha S., Riess A. G., Kirshner R. P., 2007, ApJ, 659, 122

Jones M. I. et al., 2009, ApJ, 696, 1176

Justham S., 2011, ApJ, submitted (arXiv:1102.4913)

Kasen D., 2006, ApJ, 649, 939

Kasen D., 2010, ApJ, 708, 1025

Kasen D., Nugent P., Thomas R. C., Wang L., 2004, ApJ, 610, 876

Kasen D., Röpke F. K., Woosley S. E., 2009, Nature, 460, 869

Kasen D., Woosley S. E., 2009, ApJ, 703, 2205

Kawabata K. S., Maeda K., Nomoto K., Taubenberger S., Tanaka M., Deng J., Pian E., Hattori T., Itagaki K., 2010, Nature, 465, 326

Keller S. C. et al., 2007, PASA, 24, 1

Kelly P. L., Kirshner R. P., Pahre M., 2008, ApJ, 687, 1201

Kepler Johannes, 1606, De stella nova in pede serpentarii, et qui sub ejus exortum de novo iniit, Trigono igneo. Paul Sessius, Prague

Kepler S. O., Kleinman S. J., Nitta A., Koester D., Castanheira B. G., Giovannini O., Costa A. F. M., Althaus L., 2007, MNRAS, 375, 1315

Kerzendorf W. E., Schmidt B. P., Asplund M., Nomoto K., Podsiadlowski P., Frebel A., Fesen R. A., Yong D., 2009, ApJ, 701, 1665

Khokhlov A., Mueller E., Hoeflich P., 1993, A&A, 270, 223

Khokhlov A. M., 1991a, A&A, 245, 114

Khokhlov A. M., 1991b, A&A, 246, 383

Kippenhahn R., Weigert A., 1994, Stellar Structure and Evolution (edition XVI). Springer, Berlin, Heidelberg, New York

Kirshner R. P., Kwan J., 1974, ApJ, 193, 27

Kirshner R. P., Kwan J., 1975, ApJ, 197, 415

Kitaura F. S., Janka H.-T., Hillebrandt W., 2006, A&A, 450, 345

Kozma C., Fransson C., 1992, ApJ, 390, 602

Kromer M., Sim S. A., 2009, MNRAS, 398, 1809

Kromer M., Sim S. A., Fink M., Röpke F. K., Seitenzahl I. R., Hillebrandt W., 2010, ApJ, 719, 1067

Łach G., Pachucki K., 2001, Phys. Rev. A, 64, 042510

Landi E., Del Zanna G., Young P. R., Dere K. P., Mason H. E., Landini M., 2006, ApJS, 162, 261

Large M. I., Vaughan A. E., Mills B. Y., 1968, Nature, 220, 340

Lattimer J. M., Prakash M., 2010, arXiv:1012.3208

Leibundgut B. et al., 1993, AJ, 105, 301

Leibundgut B., Kirshner R. P., Filippenko A. V., Shields J. C., Foltz C. B., Phillips M. M., Sonneborn G., 1991, ApJ, 371, L23

Leonard D. C., 2007, ApJ, 670, 1275

Leonard D. C. et al., 2006, Nature, 440, 505

Leonard D. C., Filippenko A. V., 2005, in Turatto M., Benetti S., Zampieri L., Shea W., eds, AIP Conference Series Vol. 342, Spectropolarimetry of Core-Collapse SNe. AIP, Melville, p. 330

Leonard D. C., Li W., Filippenko A. V., Foley R. J., Chornock R., 2005, ApJ, 632, 450

Li W. et al., 2011a, MNRAS, accepted (arXiv:1006:4612)

Li W. et al., 2011b, MNRAS, accepted (arXiv:1006.4613)

Lifshitz E. M., Pitaevskii L. P., 1984, Landau and Lifshitz Course of Theoretical Physics, Vol. 10: Physical Kinetics. Butterworth-Heinemann, Oxford

Litvinova I. I., Nadëzhin D. K., 1983, Ap&SS, 89, 89

Livne E., 1990, ApJ, 354, L53

Lucy L. B., 1991, ApJ, 383, 308

Lucy L. B., 1999, A&A, 345, 211

MacFayden A., 2004, Sci, 303, 45

Maeda K. et al., 2010, Nature, 466, 82

Mannucci F., Della Valle M., Panagia N., 2006, MNRAS, 370, 773

Marek A., Janka H.-T., 2009, ApJ, 694, 664

Marietta E., Burrows A., Fryxell B., 2000, ApJS, 128, 615

Mattila S., Lundqvist P., Sollerman J., Kozma C., Baron E., Fransson C., Leibundgut B., Nomoto K., 2005, A&A, 443, 649

Matzner C. D., McKee C. F., 1999, ApJ, 510, 379

Maund J. R., Smartt S. J., Kudritzki R. P., Podsiadlowski P., Gilmore G. F., 2004, Nature, 427, 129

Maurer J. I., 2010, PhD thesis, Technische Universität Müenchen

Maurer J. I., Mazzali P. A., 2010, MNRAS, 408, 947

Mazzali P. A., 2000, A&A, 363, 705

Mazzali P. A., Chugai N., Turatto M., Lucy L. B., Danziger I. J., Cappellaro E., della Valle M., Benetti S., 1997, MNRAS, 284, 151

Mazzali P. A., Danziger I. J., Turatto M., 1995, A&A, 297, 509

Mazzali P. A. et al., 2008, Sci, 321, 1185

Mazzali P. A., Lucy L. B., 1993, A&A, 279, 447

Mazzali P. A., Nomoto K., Cappellaro E., Nakamura T., Umeda H., Iwamoto K., 2001, ApJ, 547, 988

Mazzali P. A., Röpke F. K., Benetti S., Hillebrandt W., 2007, Sci, 315, 825

Mazzali P. A., Sauer D. N., Pastorello A., Benetti S., Hillebrandt W., 2008, MNRAS, 386, 1897

Meyerott R. E., 1980, ApJ, 239, 257

Mezzacappa A., 2005, Annual Review of Nuclear and Particle Science, 55, 467

Mihalas D., 1978, Stellar atmospheres, 2nd edn. W. H. Freeman and Co., San Francisco

Mihalas D., Stone M. E., 1968, ApJ, 151, 293

Minkowski R., 1941, PASP, 53, 224

Motl P. M., Frank J., Tohline J. E., D'Souza M. C. R., 2007, ApJ, 670, 1314

Narayan G. et al., 2010, arXiv:1008.4353

Nomoto K., 1980, in Wheeler J. C., ed., Texas Workshop on Type I Supernovae, Supernova explosions in accreting white dwarfs and Type I supernovae. pp 164–181

Nomoto K., 1982, ApJ, 257, 780

Nomoto K., Iben Jr. I., 1985, ApJ, 297, 531

Nomoto K., Mashimoto M., 1988, Phys. Rept., 163, 13

Nomoto K., Saio H., Kato M., Hachisu I., 2007, ApJ, 663, 1269

Nomoto K., Suzuki T., Shigeyama T., Kumagai S., Yamaoka H., Saio H., 1993, Nature, 364, 507

Nomoto K., Thielemann F.-K., Yokoi K., 1984, ApJ, 286, 644

Nomoto K., Tominaga N., Tanaka M., Maeda K., Suzuki T., Deng J. S., Mazzali P. A., 2006, Nuovo Cimento B Serie, 121, 1207

Nomoto K., Wanajo S., Kamiya Y., Tominaga N. and. Umeda H., 2009, in Andersen, J. and Bland-Hawthorn, J. and Nordström, B. ed., IAU Symposium, Vol. 254 of IAU Symposium, Chemical Yields from Supernovae and Hypernovae. pp 355–368

Nomoto K., Yamaoka H., Pols O. R., van den Heuvel E. P. J., Iwamoto K., Kumagai S., Shigeyama T., 1994, Nature, 371, 227

Nordhaus J., Burrows A., Almgren A., Bell J., 2010, ApJ, 720, 694

Nowak U., Weimann L., 1991, Technical Report TR-91-10, A Family of Newton Codes for Systems of Highly Nonlinear Equations. Konrad-Zuse-Zentrum fuer Informationstechnik Berlin

Nugent P., Phillips M., Baron E., Branch D., Hauschildt P., 1995, ApJ, 455, L147

Opal C. B., Beaty E. C., Peterson W. K., 1972, Atomic Data, 4, 209

Oppenheimer J. R., Volkoff G. M., 1939, Physical Review, 55, 374

Pakmor R., Hachinger S., R"opke F. K., Hillebrandt W., 2011, A&A, 528, A117

Pakmor R., Kromer M., Röpke F. K., Sim S. A., Ruiter A. J., Hillebrandt W., 2010, Nature, 463, 61

Pakmor R., Röpke F. K., Weiss A., Hillebrandt W., 2008, A&A, 489, 943

Pankey T. Jr., 1962, PhD thesis, Howard University

Papantonopoulos L. ed., 2007, The Invisible Universe: Dark Matter and Dark Energy, Vol. 720 of Lecture Notes in Physics. Springer, Berlin

Parthasarathy M., Branch D., Jeffery D. J., Baron E., 2007, New Astron. Rev., 51, 524

Pastorello A. et al., 2004, MNRAS, 347, 74

Pastorello A. et al., 2007a, MNRAS, 376, 1301

Pastorello A. et al., 2007b, MNRAS, 377, 1531

Pastorello A. et al., 2008, MNRAS, 389, 955

Patat F. et al., 2007, Science, 317, 924

Patnaude D. J., Loeb A., Jones C., 2009, arXiv:0912.1571

Perets H. B. et al., 2010, Nature, 465, 322

Perlmutter S. et al., 1997, in Bulletin of the AAS Vol. 29, Cosmology From Type IA Supernovae: Measurements, Calibration Techniques, and Implications. p. 1351

Perlmutter S. et al., 1999, ApJ, 517, 565

Pfannes J. M. M., Niemeyer J. C., Schmidt W., 2010, A&A, 509, A75

Pfannes J. M. M., Niemeyer J. C., Schmidt W., Klingenberg C., 2010, A&A, 509, A74

Phillips M. M., 1993, ApJ, 413, L105

Phillips M. M., Lira P., Suntzeff N. B., Schommer R. A., Hamuy M., Maza J., 1999, AJ, 118, 1766

Pinto P. A., Eastman R. G. et al., 2000, ApJ, 530, 744

Piro A. L., Chang P., Weinberg N. N., 2010, ApJ, 708, 598

Plewa T., Calder A. C., Lamb D. Q., 2004, ApJ, 612, L37

Podsiadlowski P., Joss P. C., Hsu J. J. L., 1992, ApJ, 391, 246

Raffelt G. G., 1996, Stars as laboratories for fundamental physics : the astrophysics of neutrinos, axions, and other weakly interacting particles. University of Chicago Press, Chicago

Raffelt G. G., 2010, Prog. Part. & Nucl. Phys., 64, 393

Ralchenko Y., Janev R. K., Kato T., Fursa D. V., Bray I., de Heer F. J., 2008, ADNDT, 94, 603

Rau A. et al., 2009, PASP, 121, 1334

Rauch T., Deetjen J. L., 2003, in Hubeny I., Mihalas D., Werner K., eds, Stellar Atmosphere Modeling, Vol. 288 of ASP Conference Series, Handling of Atomic Data. ASP, San Francisco, p. 103

Richmond M. W. et al., 1996, AJ, 111, 327

Riess A. G. et al., 1998, AJ, 116, 1009

Riess A. G. et al., 1999, AJ, 118, 2675

Roming P. W. A. et al., 2009, ApJ, 704, L118

Röpke F. K., Hillebrandt W., 2005, A&A, 431, 635

Röpke F. K., Hillebrandt W., Schmidt W., Niemeyer J. C., Blinnikov S. I., Mazzali P. A., 2007, ApJ, 668, 1132

Röpke F. K., Niemeyer J. C., 2007, A&A, 464, 683

Rosswog S., Kasen D., Guillochon J., Ramirez-Ruiz E., 2009, ApJ, 705, L128

Ruiter A. J., Belczynski K., Fryer C., 2009, ApJ, 699, 2026

Ruiter A. J., Belczynski K., Sim S. A., Hillebrandt W., Fryer C. L., Fink M., Kromer M., 2011, arXiv:1011.1407

Ruiz-Lapuente P., Comeron F., Méndez J., Canal R., Smartt S. J., Filippenko A. V., Kurucz R. L., Chornock R., Foley R. J., Stanishev V., Ibata R., 2004, Nature, 431, 1069

Rutten R. J., 2003, Radiative Transfer in Stellar Atmospheres, 8th edition

Sahu D. K. et al., 2008, ApJ, 680, 580

Saio H., Nomoto K., 1985, A&A, 150, L21

Saio H., Nomoto K., 1998, ApJ, 500, 388

Sasaki M., Kosugi G., Ishigaki T., Maemura H., Aoki K., Ohtani H., 1994, PASJ, 46, L187

Sathyaprakash B. S., Schutz B. F., 2009, Living Reviews in Relativity, 12, 2

Sauer D. N. et al., 2008, MNRAS, 391, 1605

Sauer D. N., Hoffmann T. L., Pauldrach A. W. A., 2006, A&A, 459, 229

Sauer D. N., Mazzali P. A., Deng J., Valenti S., Nomoto K., Filippenko A. V., 2006, MNRAS, 369, 1939

Scalzo R. A. et al., 2010, ApJ, 713, 1073

Scheidegger S., Käppeli R., Whitehouse S. C., Fischer T., Liebendörfer M., 2010, A&A, 514, A51+

Schlegel D. J., Finkbeiner D. P., Davis M., 1998, ApJ, 500, 525

Schlegel E. M., 1990, MNRAS, 244, 269

Schmidt B. P., Kirshner R. P., Eastman R. G., 1992, ApJ, 395, 366

Schmidt W., Ciaraldi-Schoolmann F., Niemeyer J. C., Röpke F. K., Hillebrandt W., 2010, ApJ, 710, 1683

Seitenzahl I. R., Taubenberger S., Sim S. A., 2009, MNRAS, 400, 531

Shigeyama T., Nomoto K., Tsujimoto T., Hashimoto M.-A., 1990, ApJ, 361, L23

Shigeyama T., Suzuki T., Kumagai S., Nomoto K., Saio H., Yamaoka H., 1994, ApJ, 420, 341

Shore S. N., Livio M., van den Heuvel E. P. J., 1993. Springer, Berlin

Silverman J. M., Ganeshalingam M., Li W., Filippenko A. V., Miller A. A., Poznanski D., 2011, MNRAS, 410, 585

Sim S. A., Mazzali P. A., 2008, MNRAS, 385, 1681

Sim S. A., Röpke F. K., Hillebrandt W., Kromer M., Pakmor R., Fink M., Ruiter A. J., Seitenzahl I. R., 2010, ApJ, 714, L52

Simon J. D. et al., 2009, ApJ, 702, 1157

Smartt S. J., 2009, ARA&A, 47, 63

Sobolev V. V., 1958. Pergamon Press, New York

Sobolev V. V., 1960

Soderberg A. M. et al., 2008, Nature, 454, 246

Spencer L. V., Fano U., 1954, Phys. Rev., 93, 1172

Spergel D. N. et al., 2007, ApJS, 170, 377

Staelin D. H., Reifenstein III E. C., 1968, Science, 162, 1481

Stehle M., Mazzali P. A., Benetti S., Hillebrandt W., 2005, MNRAS, 360, 1231

Stritzinger M. et al., 2002, AJ, 124, 2100

Stritzinger M., Leibundgut B., Walch S., Contardo G., 2006, A&A, 450, 241

Tanaka M. et al., 2008, ApJ, 677, 448

Tanaka M. et al., 2009, ApJ, 692, 1131

Tanaka M. et al., 2010, ApJ, 714, 1209

Taubenberger S. et al., 2006, MNRAS, 371, 1459

Taubenberger S. et al., 2008, MNRAS, 385, 75

Taubenberger S. et al., 2009, MNRAS, 397, 677

Taubenberger S. et al., 2011a, MNRAS, in press (arXiv:1011:5665)

Taubenberger S. et al., 2011b, MNRAS, in press (arXiv:1101:1824)

Thielemann F. K., Nomoto K., Yokoi K., 1986, A&A, 158, 17

Thompson T. A., Quataert E., Burrows A., 2005, ApJ, 620, 861

Thorne K. S., 1980, Reviews of Modern Physics, 52, 285

Timmes F. X., Arnett D., 1999, ApJS, 125, 277

Tolman R. C., 1939, Physical Review, 55, 364

Trundle C., Dufton P. L., Hunter I., Evans C. J., Lennon D. J., Smartt S. J., Ryans R. S. I., 2007, A&A, 471, 625

Tsvetkov D. Y., Volkov I. M., Baklanov P., Blinnikov S., Tuchin O., 2009, Peremennye Zvezdy, 29, 2

Turatto M., Benetti S., Cappellaro E., Danziger I. J., Della Valle M., Gouiffes C., Mazzali P. A., Patat F., 1996, MNRAS, 283, 1

Turatto M., Benetti S., Pastorello A., 2007, in S. Immler, K. Weiler, & R. McCray ed., AIP Conference Series Vol. 937, Supernova classes and subclasses. AIP, Melville, pp 187–197

Umeda H., Nomoto K., 2008, ApJ, 673, 1014

Unsöld A., Baschek B., 2001, The new cosmos : an introduction to astronomy and astrophysics. Springer, Berlin

Uomoto A., Kirshner R. P., 1986, ApJ, 308, 685

Utrobin V. P., 1997, Ap&SS, 252, 237

Vink J. S., 2011, Ap&SS, pp online first (doi:10.1007/s10509–011–0636–7)

Wagoner R. V., 1977, ApJ, 214, L5+

Walborn N. R., Prevot M. L., Prevot L., Wamsteker W., Gonzalez R., Gilmozzi R., Fitzpatrick E. L., 1989, A&A, 219, 229

Waxman E., Loeb A., 2001, Physical Review Letters, 87, 071101

Weaver T. A., 1976, ApJS, 32, 233

Weaver T. A., Woosley S. E., 1980, in Ehlers J., Perry J. J., Walker M., eds, Ninth Texas Symposium on Relativistic Astrophysics, Vol. 336 of Annals of the New York Academy of Sciences, Evolution and explosion of massive stars. pp 335–357

Webb S., 1999, Measuring the Universe. The Cosmological Distance Ladder.. Springer, Berlin, Heidelberg

Wheeler J. C., 1981, Reports on Progress in Physics, 44, 85

Wheeler J. C., Harkness R. P., 1986, in Madore B. F., Tully R. B., eds, Galaxy distances and deviations from universal expansion. Proceedings of the NATO Advanced Research Workshop, Kona, HI, Jan. 13-17, 1986. D. Reidel Publishing Co., Dordrecht, p. 45

Wheeler J. C., Meier D. L., Wilson J. R., 2002, ApJ, 568, 807

Whelan J., Iben Jr. I., 1973, ApJ, 186, 1007

Wilson J. R., Mayle R., Woosley S. E., Weaver T. A., 1985, Technical report, Stellar core collapse and supernova. NASA STI

Wood-Vasey W. M., Miknaitis G., Stubbs C. W., Jha S., Riess A. G., Garnavich P. M., Kirshner R. P., Aguilera C., Becker A. C., others, 2007, ApJ, 666, 694

Woosley S. E., Arnett W. D., Clayton D. D., 1973, ApJS, 26, 231

Woosley S. E., Bloom J. S., 2006, ARA&A, 44, 507

Woosley S. E., Eastman R. G., Weaver T. A., Pinto P. A., 1994, ApJ, 429, 300

Woosley S. E., Hoffman R. D., 1992, ApJ, 395, 202

Woosley S. E., Howard W. M., 1978, ApJS, 36, 285

Woosley S. E., Kasen D., Blinnikov S., Sorokina E., 2007, ApJ, 662, 487

Woosley S. E., Langer N., Weaver T. A., 1995, ApJ, 448, 315

Woosley S. E., Pinto P. A., Ensman L., 1988, ApJ, 324, 466

Woosley S. E., Weaver T. A., 1986, ARA&A, 24, 205

Woosley S. E., Weaver T. A., 1994, ApJ, 423, 371

Woosley S. E., Weaver T. A., 1995, ApJS, 101, 181

Woosley S. E., Weaver T. A., Taam R. E., 1980, in Wheeler J. C., ed., Texas Workshop on Type I Supernovae Models for Type I supernovae. pp 96–112

Xu Y., McCray R., 1991, ApJ, 375, 190

Yamada S., Sawai H., 2004, ApJ, 608, 907

Yamanaka M. et al., 2009, ApJ, 707, L118

Yokoo T., Arimoto J., Matsumoto K., Takahashi A., Sadakane K., 1994, PASJ, 46, L191

Yoon S.-C., Langer N., 2005, A&A, 435, 967

Yoon S.-C., Podsiadlowski P., Rosswog S., 2007, MNRAS, 380, 933

Yoon S.-C., Woosley S. E., Langer N., 2010, ApJ, 725, 940

Zampieri L., 2005, in Turatto, M. and Benetti, S. and Zampieri,L. and Shea, W. ed., 1604-2004: Supernovae as Cosmological Lighthouses, Vol. 342 of ASP Conference Series, Physical Properties of Type II Supernovae and Their Progenitors. ASP, San Francisco, p. 358

Software references

IRAF - Image Reduction and Analysis Facility - is an astronomical data reduction software. It is distributed by the National Optical Astronomy Observatory (http://iraf.noao.edu; NOAO is operated by AURA, Inc., under contract with the National Science Foundation). STSDAS / SYNPHOT and TABLES are IRAF packages provided by the Space Telescope Science Institute (http://www.stsci.edu; STSCI is is operated by AURA for NASA). IRAF with STSDAS / SYNPHOT and TABLES version 3.6 has been used for spectrophotometry and data handling in the work presented here.

For obtaining atomic data, we occasionally used online databases: The NIST atomic line database (http://physics.nist.gov/PhysRefData/ASD/index.html) is provided by the National Institute of Science and Technology, Gaithersburg, MD, USA. Individual references for the atomic data in the NIST database are available at http://physics.nist.gov/PhysRefData/ASD/Html/ref.html.

Acknowledgements

I would like to thank Paolo Mazzali and Wolfgang Hillebrandt for supervising this work and supporting me all the time. It has been a pleasure to work with them. I also thank all the colleagues of my group, but especially Stefan Taubenberger, Rüdiger Pakmor and Immanuel Maurer for their constant support and for working together. Furthermore, I thank the INAF-OAPd Supernova group, especially Stefano Benetti, for hospitality and collaboration!

I thank all the other people providing data which formed the basis of my work, or contributing ideas. These include Immanuel Maurer, Daniel Sauer, Ken'ichi Nomoto, Norbert Przybilla, Peter Storey, Markus Kromer, Stan Woosley, and all the people providing software packages and data compilations mentioned in this work.

A big "thank you" goes to my parents, who have always been there when I needed them. That is the same for my friends, especially my "gang" from university: Thank you for never leaving me lonely and for all the help! I also thank the colleagues in my office for our friendship and for solving all kinds of computer problems.

As for my education, I thank the professors, especially those who spend a lot of time on lectures and supporting material. Especially, I want to thank Prof. K. Buchner. Furthermore, I thank my teachers at school, especially those who did unusual projects with us.

Finally, I am grateful to everyone who made me have a good time and motivated me: Zhongli Zhang, Michael Fink, Monique Alvez-Cruz, Thomas M adler and Paula Jofre, Wolfgang Hayek and others from MPA who I had activities with. I thank all my friends, everyone I forgot to mention, and the Austrian radio station FM4.

Munich, 2011/05
Stephan Hachinger